Theory at a Crossroads:

An In-depth Look at Simulations of Galaxy Interactions

A DISSERTATION SUBMITTED TO THE GRADUATE DIVISION OF THE
UNIVERSITY OF HAWAI‘I AT MĀNOA IN PARTIAL FULFILLMENT OF THE
REQUIREMENTS FOR THE DEGREE OF

DOCTOR OF PHILOSOPHY

IN

ASTRONOMY

August 2019

By
Kelly Anne Blumenthal

Dissertation Committee:

J. Barnes, Chairperson
L. Hernquist
J. Moreno
R. Kudritzki
B. Tully
M. Connelley
J. Maricic

This dissertation is dedicated to the amazing administrative staff at the Institute for Astronomy: Amy Miyashiro, Karen Toyama, Lauren Toyama, Faye Uyehara, Susan Lemn, Diane Tokumura, and Diane Hockenberry. Thank you for treating us all so well.

Acknowledgements

I would like to thank several people who, over the course of this graduate thesis, have consistently shown me warmth and kindness. First and foremost: my parents, who fostered my love of astronomy, and never doubted that I would reach this point in my career. Larissa Nofi, my partner in crime, has been my perennial cheerleader – thank you for never giving up on me, and for bringing out the best in me. Thank you to David Corbino for always being on my side, and in my ear. To Mary Beth Laychack and Doug Simons: I would not be the person I am now if not for your support. Thank you for trusting me and giving me the space to grow.

To my east coast advisor, Lars Hernquist, thank you for hosting me at Harvard and making time for me. To my dear friend, advisor, and colleague Jorge Moreno: you are truly inspirational. Thank you for being unabashedly yourself in every context, for standing up for what you believe is right, and for investing so much into my success. Working with you has reminded me why I wanted to do this in the first place. Last, but certainly not least, thank you to my advisor, Joshua Barnes. We have been through quite a bit over the last five years, and you have been unwaveringly kind to me at every step of the way. Thank you for teaching me all that you have, thank you for nurturing my curiosity, and thank you for trusting me as much as you do. It is profoundly reassuring to know that people like you are still in the field. I would also like to recognize the National Science Foundation Graduate Research Fellowship (Grant No. DGE-1329626); without this financial and professional support, I would not have been able to carry out this thesis.

Though this thesis does not use any data from Maunakea Observatories, I feel it is important to recognize and acknowledge the very significant cultural role and reverence that the summit of Maunakea has always had within the indigenous Hawaiian community. As astronomers, we are incredibly fortunate to have the opportunity to conduct observations from this mountain. Without the mauna, there would be no Institute for Astronomy, and no graduate thesis today. I owe the indigenous Hawaiian community a great debt for sharing their skies and knowledge with the world.

Abstract

While cosmological simulations capture a wealth of information regarding how galaxies evolve in their large-scale environment, idealized simulations can achieve high spatial, temporal, and mass resolution. The subgrid physics models which lead to the successes of cosmological simulations are developed and perfected using idealized simulations. Idealized simulations remain valuable but need to be updated according to the findings of cosmological simulations and modern observations. The primary concern of this thesis is to explore the limitations of idealized simulations and provide suggestions to improve the methodology.

Observations have shown that the gas discs of spiral galaxies are always the same size or larger than stellar discs. Despite this, most idealized simulations of galaxy interactions employ equal-sized discs. I present a series of experiments which investigate the consequences of this assumption: the magnitude and efficiency of inflow is affected by a confluence of structural and orbital parameters.

Idealized simulations are informed by observational catalogues. These typically use the projected separation and tidal features to identify merging systems, both of which are subject to biases. To assess these biases, I create a sample of interacting pairs from IllustrisTNG. I generate mock observations of the simulated pairs and use both observational techniques and the full cosmological data to determine that ~45% of these pairs are visually identifiable as interacting. In this work, I show that local merger samples constructed from stellar features are likely to be incomplete and biased toward certain environments.

I then use the merger sample to perform a series of tests that assess the validity of the Keplerian (ideal) approximation. Many aspects are consistent with cosmological simulation, however accretion onto the halo provides a non-negligible amount of mass and momentum which has significant effects on galaxies' trajectories. I provide distributions of infall conditions as a primer for future idealized simulations, and additionally present a case study that tests the proposed methodology. Under certain circumstances, the idealized prescription is able to predict orbital parameters such as the time of first pericenter.

Table of Contents

List of Tables

List of Figures

Chapter 1

Physics Introduction

We live in the Milky Way galaxy, home to a few hundred billion stars. In nearly 4 billion years, we will collide and eventually merge with our closest neighbor: Andromeda. As with any major galaxy merger (that is, one between two galaxies of roughly equal mass), this will be a transformative event. Sweeping arms of stars and gas will form as the two galaxies interact with one another. Over time, the bulges will coalesce, the orbits of the stars will randomize, and a giant elliptical galaxy will form.

The main players in a galaxy collision are dark matter haloes, which are just that: dark. Even though they cannot be observed directly, the effect they have on stars and gas is often easily observable. We can directly observe tidal features (e.g., Figure 1.1) that manifest as “bridges" – luminous matter bridging the two galaxies – and “tails" – luminous matter trailing behind one or both of the colliding galaxies. Whereas the stars within each galaxy have a negligible chance of colliding, the galaxies’ gas clouds will strongly affect one another, and their collisions may have drastic effects. There are many parameters that might change the outcome of a galaxy collision. Among others, these include the stellar mass ratio, orbital geometry, internal structure (e.g., warped or thick disks), and the presence of nearby structures.

There is an extensive body of observational work that has detailed the role of mergers in galaxy evolution. For example, star clusters form at a higher rate in merging galaxies than isolated ones (e.g., Ashman & Zepf 1992; Whitmore & Schweizer 1995; Mihos & Hernquist 1996; de Grijs et al. 2003; Li et al. 2004; Elmegreen et al. 2005; Linden et al. 2017; Maji et al. 2017). Merging galaxies have also been shown to host heightened levels of star formation (e.g., Joseph & Wright 1985; Kennicutt et al. 1987; Mihos et al. 1991; Whitmore & Schweizer 1995; Mihos & Hernquist 1996; Vigroux et al. 1996; Mirabel et al. 1998; Hibbard & Yun 1999; Alonso-Herrero et al. 2000; Xu et al. 2000; Wang et al. 2004; Bridge et al. 2007; Ellison et al. 2011a; Patton et al. 2011; Scudder et al. 2012a,b; Rich et al. 2015; Moreno et al. 2015, 2019). Irrefutably, these

Figure 1.1 The Antennae (NGC 4038/NGC 4039) is an interacting pair of roughly equal mass galaxies. Evident in this (optical + UV composite) image are clumpy star forming regions outlining the tidal features, unstructured dust lanes, and diffuse stellar light surrounding the galaxies. A wide field view would show faint tidal features that span about 150 kpc. Image credit: NASA, ESA, and the Hubble Heritage Team (STScI AURA)-ESA Hubble Collaboration

encounters lead to significant changes in galaxy morphology (e.g., Mihos 1995; Mihos et al. 1995; Malin & Hadley 1997; Côté et al. 1998; Knierman et al. 2003; Lotz et al. 2008; Wen & Zheng 2016; Tapia et al. 2017), such as non-axisymmetric structures that affect the gas distribution on a global scale. Gravitational torques produce inflows of gas (e.g., Duc et al. 2004; Blumenthal & Barnes 2018), which may eventually feed the central black hole, leading to heightened activity of the nucleus and outflows that can extend well beyond the galaxy's disk (e.g., Cutri & McAlary 1985; Dahari 1985; Heckman et al. 1986a,b; Ellison et al. 2011b; Hewlett et al. 2017; Trakhtenbrot et al. 2017). Ultimately, mergers of all sizes are the fundamental building blocks of hierarchical structure formation (e.g., Miller 1983; Burkey et al. 1994; De Propris et al. 2005, 2007; Bridge et al. 2010; Bluck et al. 2012; Pipino et al. 2014; Robotham et al. 2014; Fan et al. 2016; Molina et al. 2017; Ventou et al. 2017; Mantha et al. 2018) as small objects come together to form larger ones throughout cosmic time. Galaxy interactions thus play a key role in everything from the smallest scales of star formation, to understanding the physics of black holes, to the overall structure of the universe.

The framework for nearly every theoretical study of interacting galaxies was developed by Toomre & Toomre (1972). In this early work, disk galaxies are approximated by a set of test particles ordered in concentric rings about a central point mass. The two “galaxies” are launched on Keplerian orbits, and the evolution of the test particles is evaluated by a fourth-order Runge-Kutta integration.

In the subsequent decades, as our observational and computational methods have advanced, galaxy evolution theory – and our understanding of the relative role of galaxy mergers – has improved. With the advent of modern computing resources and techniques, we can efficiently implement models with many orders of magnitude more particles than used in Toomre & Toomre (1972) (so called N-body simulations, see §2.1). With further technological advancements, simulations could handle the computational load associated with incorporating hydrodynamics (e.g., Gingold & Monaghan 1977; Lucy 1977; Evrard 1988; Hernquist & Katz 1989). Today, some modern codes are now able to model whole (dwarf) galaxies wherein each particle is an individual star (e.g., Bryan et al. 2014; Emerick et al. 2019), which affords us the opportunity to test star formation prescriptions with detailed IMF considerations at unprecedented mass resolution.

Although the resources and techniques have vastly improved in the last forty years, simulations are still very much idealized. Typically, galaxies’ initial orbits are assumed to be Keplerian and frequently parabolic (e.g., Barnes 1988; Barnes & Hernquist 1991, 1992, 1996; Springel 2000; Springel & Hernquist 2005; Springel et al. 2005; Cox et al. 2006; Oser et al. 2012; Hayward et al. 2014; Blumenthal & Barnes 2018; Khan et al. 2018; Pearson et al. 2018; Pettitt & Wadsley 2018), with few – but notable – exceptions (e.g., Borne 1988; Mihos & Hernquist 1996; Di Matteo et al. 2007; Cox et al. 2008; Bois et al. 2011; Bournaud et al. 2011; Villalobos et al. 2012; Moreno et al. 2015; Holincheck et al. 2016; Solanes et al. 2018; Moreno et al. 2019). The galaxy models are initialized as equilibrated objects with the baryonic components that are often not representative of the real universe (e.g., Broeils & Rhee 1997). The most far-reaching failure of these so called “idealized simulations” is their assumption of isolation, however, recent work on cosmological zoom simulations has begun to alleviate this issue (e.g., Moreno 2012; Moreno et al. 2013): galaxies are not considered inside their cosmological context (e.g., Sparre & Springel 2016).

Modern cosmological simulations, on the other hand, utilize initial conditions derived from the well-established physics of linear theory in an expanding universe to produce structures that evolve in their environmental context and eventually produces a universe that mimics reality (e.g., Hopkins et al. 2014; Torrey et al. 2017; Naiman et al. 2018; Weinberger et al. 2018; Rodriguez-Gomez et al. 2019). These simulations have driven the advancement of our theories for galaxy evolution, the formation of large-scale structure, the importance of feedback mechanisms, and many others.

However, while cosmological simulations manage to reproduce the observed universe, idealized simulations are essential to test the recipes of small-scale phenomena associated with baryonic matter. It is thus important to approach galaxy modeling in a two-handed way, wherein we consider the advantages of both cosmological and idealized simulations. That is the fundamental domain of this thesis.

In this chapter, I discuss the physical processes at play in galaxies and galaxy interactions. These span a wide range of scales, from the chemistry of atoms and molecules on dust grains in the interstellar medium (ISM), to jets from supermassive black holes that extend many kiloparsecs beyond the disk. Arguably the most fundamental – and ubiquitous – is gravity. Everything in a galaxy is subject to its gravitational potential. The motion of collisionless components (e.g., dark matter and stars) is completely governed by gravity, whereas gaseous components (e.g., the interstellar medium) are affected additionally by hydrodynamics. These systems are not static, however; they evolve dramatically over time. In order for stars to form, atomic hydrogen must undergo a process by which it forms molecules. Stellar evolution is driven primarily by the star's mass, limited by the material available for its formation: the contents of the interstellar medium. Magnetic fields from stars aggregate to form galaxy-wide magnetic environments which propel winds and gaseous fountains. Galaxies are severely affected by active galactic nuclei (AGN) through fueling and feedback processes, influencing the rate of star formation. There are other topics not mentioned here (e.g., cosmic ray heating), as our understanding of their effects on galaxy evolution is still nascent.

1.1 Galactic Dynamics

Galaxies can be considered to have two broad categories of components: collisionless matter, such as stars and dark matter, and gaseous material, represented by the various phases of the ISM. Each of these has its own method for determining the equations of motion, depending on the dominant physics involved. For dark matter, gravity is (presumably) the only force at play. Stellar dynamics are governed entirely by gravity, but stars may shed gas and become part of the interstellar medium. On the other hand, the gas is subject to hydrodynamics.

There are three cases to consider when discussing the difference between collisionless and collisional matter: (1) $t_{\rm relax} >> H_{\rm o}^{-1} > t_{\rm cross}$, wherein the relaxation time (the time it takes a system to reach equilibrium) is much larger than the Hubble time, which is in turn larger than the crossing time (or the time it takes for a star to complete an orbit). Collisionless stellar systems such as galaxies behave in this way. (2)

$H_o^{-1} > t_{\mathrm{relax}} > t_{\mathrm{cross}}$, is a slight modification of case (1), and applies to collisional stellar systems, such as globular clusters, where collisions are frequent with respect to the dynamical evolution of the cluster. (3) $H_o^{-1} > t_{\mathrm{cross}} >>> t_{\mathrm{relax}}$ describes hydrodynamic and gas-dynamic systems. In the following, I describe how collisionless and gaseous matter behave in a galaxy's gravitational potential.

1.1.1 Collisionless Systems

In collisionless systems, the dynamics are described by the distribution function (DF), $f(\mathbf{v}, \mathbf{r}, t)$. The DF represents an evolving distribution of matter within a 6-dimensional phase space of position and velocity for all particles in the system. This is then compatible with the Collisionless Boltzmann Equation (CBE), which combines continuity with the equations of orbital motion in a gravitational field $\Phi(\mathbf{r}, t)$:

$$0 = \frac{\mathrm{d}f}{\mathrm{d}t} = \frac{\partial f}{\partial t} + \mathbf{v} \cdot \frac{\partial f}{\partial \mathbf{r}} - \frac{\partial \Phi}{\partial \mathbf{r}} \cdot \frac{\partial f}{\partial \mathbf{v}} \tag{1.1}$$

The CBE (how material moves in a gravitational field) and Poisson's Equation (below; how material generates a gravitational field) are the only two components needed to solve the dynamics of a collisionless system.

1.1.2 Gaseous Systems

The primary assumption made by implementing the Hydrodynamic Equations below is that locally, the gas is in equilibrium. This need not be the case globally, however.

There are four fundamental equations that constrain the motion of gases.

1. The continuity equation:

$$\frac{\partial \rho}{\partial t} + \nabla \cdot (\rho \mathbf{v}) = 0 \tag{1.2}$$

   where ρ is the gas density and $\mathbf{v}$ is the fluid flow velocity. This equation is equivalent to the requirement of mass conservation; the flow into or out of one volume element must be balanced by the mass accumulation within that same cell. Note that this equation is an analog to the CBE: both define the conditions for mass continuity.

2. The momentum conservation equation:

$$\frac{\partial \mathbf{v}}{\partial t} + (\mathbf{v} \cdot \nabla)\mathbf{v} = -\frac{\nabla P}{\rho} - \nabla \Phi \tag{1.3}$$

   where ρ and $\mathbf{v}$ are the same as above, P is the gas pressure and Φ is the gravitational potential.

3. The energy conservation equation:

$$\frac{\mathrm{d}u}{\mathrm{d}t} = \frac{Q}{\rho} - \frac{P}{\rho}\nabla \cdot \mathbf{v} \tag{1.4}$$

   Here, u is the internal energy, and the ratio Q/ρ gives the mass heating/cooling rate, countered by the adiabatic term, $\frac{P}{\rho}\nabla \cdot \mathbf{v}$.

4. The equation of state (EOS) relates pressure and gas density to the internal energy. The simplest EOS is the ideal gas equation:

$$P = \frac{\rho k T}{\mu m_{\mathrm{H}}} \tag{1.5}$$

   where k is the Boltzmann constant, m_{H} is the mass of hydrogen, μ is the molecular mass and T is the temperature of the gas. If the gas is assumed to be ideal, then the total internal energy can be written as

$$u = \frac{n_{\mathrm{f}}}{2} P \tag{1.6}$$

   where n_{f} is the number of degrees of freedom of the system.

1.1.3 Gravity

Collisionless dynamics can be understood by approximating a whole system of discrete objects (e.g., stars) as a smoothed mean potential. This assumes that there is a continuous distribution of matter throughout the potential. In a galaxy, this is the case for the dark, stellar and gaseous material. The Poisson Equation,

$$\nabla^2 \Phi = 4\pi G \left(\rho_{\mathrm{gas}} + \int \mathrm{d}\mathbf{v} f(\mathbf{v}, \mathbf{r}) \right) \tag{1.7}$$

describes how matter creates a gravitational field. Here, ρ_{gas} is the mass density of the gaseous material, and $\int d\mathbf{v} f(\mathbf{v}, \mathbf{r})$ is the mass density of the collisionless matter. At the most basic level, Poisson's Equation, the Hydrodynamic Equations, and the Collisionless Boltzmann Equation self-consistently describe the motion of material in a galaxy. The background physics that follows in this section all build upon the prior knowledge of these three fundamental sets of equations.

Keplerian Dynamics

When two bodies (e.g., stars, galaxies) interact with one another, their dynamics can often be modeled using Kepler's laws of motion.

1. Objects moving within a gravitational potential will have trajectories that correspond to conic sections. Bound orbits are elliptical (or circular), while unbound orbits are hyperbolic (or parabolic). The eccentricity (e) of the orbit is found from the angular momentum (L) and energy (E) of the orbit

   $$e = \sqrt{1 + \frac{2EL^2}{\mu(GM_\mathrm{p}M_\mathrm{s})^2}} \tag{1.8}$$

   where $\mathrm{M}_\mathrm{p,s}$ is the mass of the primary and secondary, respectively, and μ is the reduced mass of the system, defined as

   $$\mu = \frac{M_\mathrm{p}M_\mathrm{s}}{M_\mathrm{p} + M_\mathrm{s}} \tag{1.9}$$

   In the frame of reference where the center of mass of the system is at one of the orbit's foci, the position r of one body can be written as

   $$r(\theta) = \frac{a(1 - e^2)}{1 + e\cos(\theta)} \tag{1.10}$$

   where θ is the true anomaly (or simply, the angular position along the orbit), and a is the semi-major axis, or one-half the length of the long axis of the orbit.

2. Equal amounts of time spent along an orbit sweep out equal areas. In reality, this is a manifestation of angular momentum conservation.

3. For a closed, bound orbit, the square of the orbital period and the cube of the semimajor axis are directly proportional. The constant of proportionality depends on the total mass of the system.

These laws are exact for an isolated pair of point masses. In a cosmological setting, objects are frequently under the gravitational influence of multiple nearby bodies, and galaxies (and their dark matter haloes) are extended and may even overlap. However, a Keplerian description may still apply if the dark matter haloes: (1) are not overlapping (and thus, the galaxies "see" each other as point masses), or (2) have not interacted with other structures in the recent past.

1.2 The Interstellar Medium

The interstellar medium (ISM) is a complex system of gas and dust. Its thermodynamics are driven by several different heating and cooling processes that define its structure and overall composition. The first modern discussion of the ISM was laid out by McKee & Ostriker (1977), who developed a model of a three phase ISM. Today, we typically discuss five thermal phases of the ISM: molecular gas (H_2, $T{\sim}10$ K), the cold neutral medium (HI, $T{\sim}100$ K), the warm neutral medium (HI, $T{\sim}10^3$ K), the warm ionized medium (HII, $T{\sim}10^4$ K), and the hot ionized medium ($T{\sim}10^{6-7}$ K).

1.2.1 Atomic and Molecular Hydrogen

The ISM is filled with photons that keep hydrogen in atomic form. Thus, molecular hydrogen is found only in the densest regions of the ISM, where self-shielding and dust-shielding are sufficient to keep the molecules from dissociating. Molecular clouds are thus surrounded by a photodissociation region (PDR), which is predominantly atomic. Krumholz et al. (2008) found that the location of the transition region is determined primarily by the size of the cloud and the radiation field in which it sits. This transition from atomic to molecular hydrogen is fundamental to the regulation of star formation; it defines where, when and how many stars are formed.

1.2.2 Heating and Cooling

O and B stars are the primary source of ionizing photons in the diffuse ISM. Far UV photons of the energy distribution will ionize hydrogen atoms. If the gas is dense enough, the photoelectrons will collide with nearby ions, redistributing their kinetic energy throughout the medium. Gravitational collapse, dissipation of energy via turbulence and shocks are large-scale sources of heating that have a significant effect on the

ISM. In the dense cores of cold clouds, heating is dominated by collisions of low energy cosmic rays. In HII regions, the primary source of heating is the central stars' Lyman continuum (LYC) photons.

In an HII region, the LYC photons randomly walk through the cloud, ionizing atoms as they are absorbed. Eventually, the ions will cascade back down to a lower energy state and produce photons of a lower energy than the LYC photons, which can easily radiate away from the cloud via emission lines. This is the predominant cooling process, known as recombination emission. The Lyα photons continue to be absorbed and re-emitted as they make their way toward the edge of the cloud. If there is dust in the HII region, then the Lyα photons can be absorbed and re-emitted as thermal radiation. Even if there is no source of LYC photons, this type of cooling may still occur. Ions near the high-energy tail of the Maxwell Boltzmann distribution have sufficient energy to produce Lyα photons via collisions, which may produce a similar phenomenon. Another cooling mechanism is collisional excitation, which occurs typically in neutral hydrogen regions where temperatures are on the order of 100 K. This process is significantly more efficient than recombination emission, but the emission lines observed are typically from heavy ions such as C^+. The abundance of these heavy elements is so low that the probability of reabsorption is negligible. Thus, the collisionally excited ion will decay to lower energy states, resulting in photon emission that leaves the region. The final significant avenue for cooling is Bremsstrahlung Radiation. Though it is most efficient in high densities, it may also play a significant role if the gas is sufficiently hot and tenuous (i.e. in the intra-cluster medium). Above about $T= 10^8$ K, Bremsstrahlung Radiation is the only way by which the gas can cool.

1.3 Stellar Physics

1.3.1 Star Formation

Once a giant molecular cloud (GMC) reaches approximately the Jeans Mass, it will begin to collapse due to its own self-gravity. Assuming a polytropic equation of state (with $\gamma < \frac{4}{3}$), the Jeans Mass will decrease as the density increases. This causes fragmentation to occur within the GMC, and thus multiple stars may form out of a single gas cloud. The initial distribution of masses is often discussed as the Initial Mass Function (IMF; e.g., Salpeter 1955), and whether it is universal or environment-specific (e.g., Hosek et al. 2015) is still a contested topic. It has also been suggested that every star has at least one companion (e.g., Kobulnicky & Fryer 2007). This would have a significant effect on the inferred IMF (e.g., Lu et al. 2013), but is almost never included in simulations of whole galaxies. Typically, large systems of stars are assumed to follow an

IMF similar to Salpeter (1955). For a Salpeter IMF, the majority of the newly formed stars will have masses $\leq 1\mathrm{M}_{\odot}$.

Star formation has been modeled in a number of ways, one of which assumes that the local star formation rate follows the Kennicutt-Schmidt Law (Schmidt 1959; Kennicutt 1998):

$$\dot{\rho}_{\star} = A_{\star}\rho_{\mathrm{g}}^{n} \tag{1.11}$$

where $A_{\star}$ is a constant, ρ_{g} is the local gas density, and n is the slope of the power law. Previous studies (e.g., Mihos & Hernquist 1994; Mihos et al. 1991) have taken n to be between about 1.5 and 2, consistent with the empirical law. However, the Kennicutt-Schmidt Law averages over diverse conditions in star forming regions, and may not capture the physics of star formation (e.g., Parmentier 2016). Feedback processes that produce self-regulating star formation under quiescent (e.g., Springel & Hernquist 2003) and merging (e.g., Springel et al. 2005) circumstances are necessary to be consistent with observations of star formation. The Feedback In Realistic Environments (FIRE) simulations (e.g., Hopkins et al. 2014; Moreno et al. 2019) do not assume this law, but rather recover it as a consequence of their feedback models.

1.3.2 Stellar Evolution

The lowest mass stars have main sequence lifetimes on the order of the Hubble time. Stars near one solar mass will eventually expel their outer atmospheric layers, resulting in a planetary nebula with a white dwarf at its core. On the other hand, the highest mass stars (i.e. $\geq 8\mathrm{M}_{\odot}$) evolve very rapidly. Over the course of its short lifetime, a high mass star may produce stellar winds, depositing energy and momentum into the surrounding region before exploding as supernovae, thereby enriching the surrounding ISM with metals.

Metallicity

As a star fuses hydrogen into helium, and eventually forms heavier elements (such as carbon, nitrogen and oxygen), the star's metallicity is said to increase. That is, it is becoming more enriched with elements heavier than hydrogen. Gaseous material in evolving stars gets reprocessed and eventually returned into the ISM. In galaxies, the distribution of metals is used to infer their dynamical and star formation history (e.g., Zaritsky et al. 1994; Kewley et al. 2010; Rupke et al. 2010; Bresolin et al. 2012; Torrey et al. 2012; Kudritzki et al. 2015).

Stellar Winds

O, B and A stars may have radiation driven winds throughout their lifetime (e.g., Kudritzki & Puls 2000, and sources therein). Lower mass stars may develop stellar winds during the post asymptotic giant branch (AGB) phases (Pauldrach et al. 1988) if they are sufficiently hot. Stellar winds have been shown to significantly affect the surrounding ISM via momentum and energy transfer (e.g., Gabler et al. 1989; Najarro et al. 1996).

Supernovae

After about ten million years, a massive star (i.e. $M_\star \geq 8\mathrm{M}_\odot$) will fuse all of its hydrogen to helium. At that point, the core will contract, causing it to heat up and eventually ignite helium fusion in the core. This pattern of contraction and heating is moderated by hydrodynamic equilibrium, and progresses until the core is dominated by iron. At that point, nuclear fusion can no longer occur in the core, and as such the balance of radiation pressure and gravity is broken. The final gravitational collapse will cause the temperature in the core to increase rapidly, resulting in the dissociation of iron nuclei. This process is stopped by neutron degeneracy pressure, when the core's iron has been converted to a sea of neutrons. The shock wave that is produced expels the rest of the star's atmosphere into the local ISM.

Typical supernova energies are on the order of 10^{53}erg, roughly one percent of which is mechanical energy. The rest of the energy budget is in neutrinos, which can increase the pressure behind the shock wave, making the supernova's sphere of influence expand, bringing with it metals and dust to enrich the ISM. Energy and momentum from the supernova is deposited into the ambient medium, causing it to heat up. This in turn acts on the cooler gas and may result in a further heating and evaporation of cloud complexes. If most of the ambient material is hot, then the density may be hot enough that most of the energy will have radiated away by the time it can significantly affect the nearby cold medium. Supernovae explosions form structures in the ISM that can break through the disk of the host galaxy. If the galaxy's gravitational potential is sufficient to recapture this material, it flows back down to the disk in a galactic fountain. Otherwise, the material is ejected into the circumgalactic medium.

Depending on the initial mass of the star (which in turn depends on the IMF), the remnant core is either a neutron star or a black hole. Type II, Ib and Ic supernovae are all formed by this core collapse process. Type Ia supernovae, on the other hand, are the result of mass exchange between a white dwarf and its binary companion. Once the white dwarf exceeds the Chandrasenkhar mass limit, the star explodes, producing a burst of energy that can in some cases outshine its host galaxy (e.g., Quimby et al. 2011).

1.4 Galactic-Scale Physics

1.4.1 Magnetic Fields

The majority of normal matter in the universe is a plasma, and as such produces an appreciable magnetic field. Magnetic fields play a significant role in a wide variety of physical processes, including providing support against gravitational collapse in GMCs (e.g., Shu et al. 1987; Bertoldi & McKee 1992; McKee & Ostriker 2007; Crutcher 2012), stellar evolution (e.g., Kennicutt & Evans 2012, and sources therein), and the ISM (e.g., McKee & Ostriker 2007, and sources therein). On the scale of whole-galaxies, magnetic fields are formed through a complex series of dynamos that evolve with the dynamic ISM, the nuclear activity, and the galaxy's dynamical history (e.g., Widrow 2002, and sources therein). In galactic nuclei, black hole accretion produces strong magnetic fields (e.g., Colgate & Li 1999; Kronberg et al. 2001; Pariev et al. 2007) which may form conical outflows of material (so-called jets; e.g., Jorstad et al. 2005; Marscher et al. 2010). On the largest scales, magnetic fields are thought to be integral to the evolution of the early universe (e.g., Smoot et al. 1992; Kim et al. 1996; Grasso & Rubinstein 2001, and sources therein).

1.4.2 Active Galactic Nuclei

Once gas is funneled deep into the nucleus of a galaxy, it loses even more angular momentum and falls into an accretion disk around the central black hole, emitting radiation as it does so. Until recently, this was a theoretical prediction; the Event Horizon Telescope collaboration released the first image of an accretion disk around the supermassive black hole in M87 (Event Horizon Telescope Collaboration et al. 2019). Flows within accretion disks, which eventually fuel black holes, are due to magnetohydrodynamic turbulence (e.g., Balbus & Hawley 1991; Hawley et al. 1995; Krolik 1999; Agol & Krolik 2000; Balbus 2003; Reynolds et al. 2006; Penna et al. 2010).

About 10% of all galaxies are observed to have significant non-stellar activity in their nuclei (Maoz 2007), called active galactic nuclei (AGN). The mechanism by which a supermassive black hole becomes active is thought to be tied to nuclear gas inflows, and perhaps the result of galaxy interactions (e.g., Tacconi et al. 2008; Koss et al. 2010). AGN themselves may have dramatic effects on their host galaxies: it has been suggested that nuclear activity may be able to trigger and quench star formation throughout the entire disk (e.g., Rawlings & Saunders 1991; Chartas et al. 2003; Crenshaw et al. 2003; Fabian 2012, and sources therein). Winds and jets from the AGN deposit energy, gas and metals into the intergalactic and interstellar media (e.g., Jorstad et al. 2013), which helps to regulate heating and cooling in galaxies. AGN feedback is often considered in two "modes": (1) quasar mode, or high-accretion mode, during which time a large amount of gas is funneled into the central black hole, and (2) radio mode, which is characterized by relatively low accretion, and can be accompanied by massive (often bipolar) outflows (e.g., Fabian 2012; Kormendy & Ho 2013, and sources therein), or smaller-scale outflows in intermediate mass haloes (e.g., Yuan & Narayan 2014; Cheung et al. 2016).

References

Agol, E. & Krolik, J. H. 2000, ApJ, 528, 161

Alonso-Herrero, A., Rieke, G. H., Rieke, M. J., & Scoville, N. Z. 2000, ApJ, 532, 845

Ashman, K. M. & Zepf, S. E. 1992, ApJ, 384, 50

Balbus, S. A. 2003, ARA&A, 41, 555

Balbus, S. A. & Hawley, J. F. 1991, ApJ, 376, 214

Barnes, J. E. 1988, ApJ, 331, 699

Barnes, J. E. & Hernquist, L. 1992, Annual Review of Astronomy and Astrophysics, 30, 705

—. 1996, ApJ, 471, 115

Barnes, J. E. & Hernquist, L. E. 1991, ApJ, 370, L65

Bertoldi, F. & McKee, C. F. 1992, ApJ, 395, 140

Bluck, A. F. L., Conselice, C. J., Buitrago, F., Grützbauch, R., Hoyos, C., Mortlock, A., & Bauer, A. E. 2012, ApJ, 747, 34

Blumenthal, K. A. & Barnes, J. E. 2018, MNRAS, 479, 3952

Bois, M., Emsellem, E., Bournaud, F., Alatalo, K., Blitz, L., Bureau, M., Cappellari, M., Davies, R. L., Davis, T. A., de Zeeuw, P. T., Duc, P.-A., Khochfar, S., Krajnović, D., Kuntschner, H., Lablanche, P.-Y., McDermid, R. M., Morganti, R., Naab, T., Oosterloo, T., Sarzi, M., Scott, N., Serra, P., Weijmans, A.-M., & Young, L. M. 2011, MNRAS, 416, 1654

Borne, K. D. 1988, ApJ, 330, 61

Bournaud, F., Chapon, D., Teyssier, R., Powell, L. C., Elmegreen, B. G., Elmegreen, D. M., Duc, P.-A., Contini, T., Epinat, B., & Shapiro, K. L. 2011, ApJ, 730, 4

Bresolin, F., Kennicutt, R. C., & Ryan-Weber, E. 2012, ApJ, 750, 122

Bridge, C. R., Appleton, P. N., Conselice, C. J., Choi, P. I., Armus, L., Fadda, D., Laine, S., Marleau, F. R., Carlberg, R. G., Helou, G., & Yan, L. 2007, ApJ, 659, 931

Bridge, C. R., Carlberg, R. G., & Sullivan, M. 2010, ApJ, 709, 1067

Broeils, A. H. & Rhee, M.-H. 1997, A&A, 324, 877

Bryan, G. L., Norman, M. L., O'Shea, B. W., Abel, T., Wise, J. H., Turk, M. J., Reynolds, D. R., Collins, D. C., Wang, P., Skillman, S. W., Smith, B., Harkness, R. P., Bordner, J., Kim, J.-h., Kuhlen, M., Xu, H., Goldbaum, N., Hummels, C., Kritsuk, A. G., Tasker, E., Skory, S., Simpson, C. M., Hahn, O., Oishi, J. S., So, G. C., Zhao, F., Cen, R., Li, Y., & Enzo Collaboration. 2014, The Astrophysical Journal Supplement Series, 211, 19

Burkey, J. M., Keel, W. C., Windhorst, R. A., & Franklin, B. E. 1994, ApJ, 429, L13

Chartas, G., Brandt, W. N., & Gallagher, S. C. 2003, ApJ, 595, 85

Cheung, E., Bundy, K., Cappellari, M., Peirani, S., Rujopakarn, W., Westfall, K., Yan, R., Bershady, M., Greene, J. E., Heckman, T. M., Drory, N., Law, D. R., Masters, K. L., Thomas, D., Wake, D. A., Weijmans, A.-M., Rubin, K., Belfiore, F., Vulcani, B., Chen, Y.-M., Zhang, K., Gelfand , J. D., Bizyaev, D., Roman-Lopes, A., & Schneider, D. P. 2016, Nature, 533, 504

Colgate, S. A. & Li, H. 1999, Ap&SS, 264, 357

Côté, P., Marzke, R. O., & West, M. J. 1998, ApJ, 501, 554

Cox, T. J., Jonsson, P., Primack, J. R., & Somerville, R. S. 2006, MNRAS, 373, 1013

Cox, T. J., Jonsson, P., Somerville, R. S., Primack, J. R., & Dekel, A. 2008, MNRAS, 384, 386

Crenshaw, D. M., Kraemer, S. B., & George, I. M. 2003, ARA&A, 41, 117

Crutcher, R. M. 2012, Annual Review of Astronomy and Astrophysics, 50, 29

Cutri, R. M. & McAlary, C. W. 1985, ApJ, 296, 90

Dahari, O. 1985, The Astrophysical Journal Supplement Series, 57, 643

de Grijs, R., Lee, J. T., Clemencia Mora Herrera, M., Fritze-v. Alvensleben, U., & Anders, P. 2003, New A, 8, 155

De Propris, R., Conselice, C. J., Liske, J., Driver, S. P., Patton, D. R., Graham, A. W., & Allen, P. D. 2007, ApJ, 666, 212

De Propris, R., Liske, J., Driver, S. P., Allen, P. D., & Cross, N. J. G. 2005, AJ, 130, 1516

Di Matteo, P., Combes, F., Melchior, A.-L., & Semelin, B. 2007, A&A, 468, 61

Duc, P.-A., Bournaud, F., & Masset, F. 2004, A&A, 427, 803

Ellison, S. L., Nair, P., Patton, D. R., Scudder, J. M., Mendel, J. T., & Simard, L. 2011a, MNRAS, 416, 2182

Ellison, S. L., Patton, D. R., Mendel, J. T., & Scudder, J. M. 2011b, MNRAS, 418, 2043

Elmegreen, D. M., Elmegreen, B. G., & Ferguson, T. E. 2005, ApJ, 623, L71

Emerick, A., Bryan, G. L., & Mac Low, M.-M. 2019, MNRAS, 482, 1304

Event Horizon Telescope Collaboration, Akiyama, K., Alberdi, A., Alef, W., Asada, K., Azulay, R., Baczko, A.-K., Ball, D., Baloković, M., Barrett, J., Bintley, D., Blackburn, L., Boland, W., Bouman, K. L., Bower, G. C., Bremer, M., Brinkerink, C. D., Brissenden, R., Britzen, S., Broderick, A. E., Broguiere, D., Bronzwaer, T., Byun, D.-Y., Carlstrom, J. E., Chael, A., Chan, C.-k., Chatterjee, S., Chatterjee, K., Chen, M.-T., Chen, Y., Cho, I., Christian, P., Conway, J. E., Cordes, J. M., Crew, G. B., Cui, Y., Davelaar, J., De Laurentis, M., Deane, R., Dempsey, J., Desvignes, G., Dexter, J., Doeleman, S. S., Eatough, R. P., Falcke, H., Fish, V. L., Fomalont, E., Fraga-Encinas, R., Freeman, W. T., Friberg, P., Fromm, C. M., Gómez, J. L., Galison, P., Gammie, C. F., García, R., Gentaz, O., Georgiev, B., Goddi, C., Gold, R., Gu, M., Gurwell, M., Hada, K., Hecht, M. H., Hesper, R., Ho, L. C., Ho, P., Honma, M., Huang, C.-W. L., Huang, L., Hughes, D. H., Ikeda, S., Inoue, M., Issaoun, S., James, D. J., Jannuzi, B. T., Janssen, M., Jeter, B., Jiang, W., Johnson, M. D., Jorstad, S., Jung, T., Karami, M., Karuppusamy, R., Kawashima, T., Keating,

G. K., Kettenis, M., Kim, J.-Y., Kim, J., Kim, J., Kino, M., Koay, J. Y., Koch, P. M., Koyama, S., Kramer, M., Kramer, C., Krichbaum, T. P., Kuo, C.-Y., Lauer, T. R., Lee, S.-S., Li, Y.-R., Li, Z., Lindqvist, M., Liu, K., Liuzzo, E., Lo, W.-P., Lobanov, A. P., Loinard, L., Lonsdale, C., Lu, R.-S., MacDonald, N. R., Mao, J., Markoff, S., Marrone, D. P., Marscher, A. P., Martí-Vidal, I., Matsushita, S., Matthews, L. D., Medeiros, L., Menten, K. M., Mizuno, Y., Mizuno, I., Moran, J. M., Moriyama, K., Moscibrodzka, M., Müller, C., Nagai, H., Nagar, N. M., Nakamura, M., Narayan, R., Narayanan, G., Natarajan, I., Neri, R., Ni, C., Noutsos, A., Okino, H., Olivares, H., Oyama, T., Özel, F., Palumbo, D. C. M., Patel, N., Pen, U.-L., Pesce, D. W., Piétu, V., Plambeck, R., PopStefanija, A. a., Porth, O., Prather, B., Preciado-López, J. A., Psaltis, D., Pu, H.-Y., Ramakrishnan, V., Rao, R., Rawlings, M. G., Raymond, A. W., Rezzolla, L., Ripperda, B., Roelofs, F., Rogers, A., Ros, E., Rose, M., Roshanineshat, A., Rottmann, H., Roy, A. L., Ruszczyk, C., Ryan, B. R., Rygl, K. L. J., Sánchez, S., Sánchez-Arguelles, D., Sasada, M., Savolainen, T., Schloerb, F. P., Schuster, K.-F., Shao, L., Shen, Z., Small, D., Sohn, B. W., SooHoo, J., Tazaki, F., Tiede, P., Tilanus, R. P. J., Titus, M., Toma, K., Torne, P., Trent, T., Trippe, S., Tsuda, S., van Bemmel, I., van Langevelde, H. J., van Rossum, D. R., Wagner, J., Wardle, J., Weintroub, J., Wex, N., Wharton, R., Wielgus, M., Wong, G. N., Wu, Q., Young, A., Young, K., Younsi, Z., Yuan, F., Yuan, Y.-F., Zensus, J. A., Zhao, G., Zhao, S.-S., Zhu, Z., Farah, J. R., Meyer-Zhao, Z., Michalik, D., Nadolski, A., Nishioka, H., Pradel, N., Primiani, R. A., Souccar, K., Vertatschitsch, L., & Yamaguchi, P. 2019, ApJ, 875, L4

Evrard, A. E. 1988, MNRAS, 235, 911

Fabian, A. C. 2012, ARA&A, 50, 455

Fan, L., Han, Y., Fang, G., Gao, Y., Zhang, D., Jiang, X., Wu, Q., Yang, J., & Li, Z. 2016, ApJ, 822, L32

Gabler, R., Gabler, A., Kudritzki, R. P., Puls, J., & Pauldrach, A. 1989, A&A, 226, 162

Gingold, R. A. & Monaghan, J. J. 1977, MNRAS, 181, 375

Grasso, D. & Rubinstein, H. R. 2001, Phys. Rep., 348, 163

Hawley, J. F., Gammie, C. F., & Balbus, S. A. 1995, ApJ, 440, 742

Hayward, C. C., Torrey, P., Springel, V., Hernquist, L., & Vogelsberger, M. 2014, MNRAS, 442, 1992

Heckman, T. M., Beckwith, S., Blitz, L., Skrutskie, M., & Wilson, A. S. 1986a, ApJ, 305, 157

Heckman, T. M., Smith, E. P., Baum, S. A., van Breugel, W. J. M., Miley, G. K., Illingworth, G. D., Bothun, G. D., & Balick, B. 1986b, ApJ, 311, 526

Hernquist, L. & Katz, N. 1989, ApJS, 70, 419

Hewlett, T., Villforth, C., Wild, V., Mendez-Abreu, J., Pawlik, M., & Rowlands, K. 2017, MNRAS, 470, 755

Hibbard, J. E. & Yun, M. S. 1999, ApJ, 522, L93

Holincheck, A. J., Wallin, J. F., Borne, K., Fortson, L., Lintott, C., Smith, A. M., Bamford, S., Keel, W. C., & Parrish, M. 2016, MNRAS, 459, 720

Hopkins, P. F., Kereš, D., Oñorbe, J., Faucher-Giguère, C.-A., Quataert, E., Murray, N., & Bullock, J. S. 2014, MNRAS, 445, 581

Hosek, M., Lu, J. R., Anderson, J., Clarkson, W., Ghez, A., Kudritzki, R.-P., & Morris, M. 2015, IAU General Assembly, 22, 2257879

Jorstad, S. G., Marscher, A. P., Lister, M. L., Stirling, A. M., Cawthorne, T. V., Gear, W. K., Gómez, J. L., Stevens, J. A., Smith, P. S., Forster, J. R., & Robson, E. I. 2005, AJ, 130, 1418

Jorstad, S. G., Marscher, A. P., Smith, P. S., Larionov, V. M., Agudo, I., Gurwell, M., Wehrle, A. E., Lähteenmäki, A., Nikolashvili, M. G., Schmidt, G. D., Arkharov, A. A., Blinov, D. A., Blumenthal, K., Casadio, C., Chigladze, R. A., Efimova, N. V., Eggen, J. R., Gómez, J. L., Grupe, D., Hagen-Thorn, V. A., Joshi, M., Kimeridze, G. N., Konstantinova, T. S., Kopatskaya, E. N., Kurtanidze, O. M., Kurtanidze, S. O., Larionova, E. G., Larionova, L. V., Sigua, L. A., MacDonald, N. R., Maune, J. D., McHardy, I. M., Miller, H. R., Molina, S. N., Morozova, D. A., Scott, T., Taylor, B. W., Tornikoski, M., Troitsky, I. S., Thum, C., Walker, G., Williamson, K. E., Sallum, S., Consiglio, S., & Strelnitski, V. 2013, ApJ, 773, 147

Joseph, R. D. & Wright, G. S. 1985, MNRAS, 214, 87

Kennicutt, Robert C., J., Keel, W. C., van der Hulst, J. M., Hummel, E., & Roettiger, K. A. 1987, AJ, 93, 1011

Kennicutt, R. C. & Evans, N. J. 2012, Annual Review of Astronomy and Astrophysics, 50, 531

Kennicutt, Jr., R. C. 1998, ApJ, 498, 541

Kewley, L. J., Rupke, D., Zahid, H. J., Geller, M. J., & Barton, E. J. 2010, ApJ, 721, L48

Khan, F. M., Capelo, P. R., Mayer, L., & Berczik, P. 2018, ApJ, 868, 97

Kim, E.-J., Olinto, A. V., & Rosner, R. 1996, ApJ, 468, 28

Knierman, K. A., Gallagher, S. C., Charlton, J. C., Hunsberger, S. D., Whitmore, B., Kundu, A., Hibbard, J. E., & Zaritsky, D. 2003, AJ, 126, 1227

Kobulnicky, H. A. & Fryer, C. L. 2007, ApJ, 670, 747

Kormendy, J. & Ho, L. C. 2013, Annual Review of Astronomy and Astrophysics, 51, 511

Koss, M., Mushotzky, R., Veilleux, S., & Winter, L. 2010, ApJ, 716, L125

Krolik, J. H. 1999, ApJ, 515, L73

Kronberg, P. P., Dufton, Q. W., Li, H., & Colgate, S. A. 2001, ApJ, 560, 178

Krumholz, M. R., McKee, C. F., & Tumlinson, J. 2008, ApJ, 689, 865

Kudritzki, R.-P., Ho, I.-T., Schruba, A., Burkert, A., Zahid, H. J., Bresolin, F., & Dima, G. I. 2015, MNRAS, 450, 342

Kudritzki, R.-P. & Puls, J. 2000, ARA&A, 38, 613

Li, Y., Mac Low, M.-M., & Klessen, R. S. 2004, ApJ, 614, L29

Linden, S. T., Evans, A. S., Rich, J., Larson, K. L., Armus, L., Díaz-Santos, T., Privon, G. C., Howell, J., Inami, H., Kim, D. C., Chien, L. H., Vavilkin, T., Mazzarella, J. M., Modica, F., Surace, J. A., Manning, S., Abdullah, A., Blake, A., Yarber, A., & Lambert, T. 2017, ApJ, 843, 91

Lotz, J. M., Jonsson, P., Cox, T. J., & Primack, J. R. 2008, MNRAS, 391, 1137

Lu, J. R., Do, T., Ghez, A. M., Morris, M. R., Yelda, S., & Matthews, K. 2013, ApJ, 764, 155

Lucy, L. B. 1977, AJ, 82, 1013

Maji, M., Zhu, Q., Li, Y., Charlton, J., Hernquist, L., & Knebe, A. 2017, ApJ, 844, 108

Malin, D. & Hadley, B. 1997, Publications of the Astronomical Society of Australia, 14, 52

Mantha, K. B., McIntosh, D. H., Brennan, R., Ferguson, H. C., Kodra, D., Newman, J. A., Rafelski, M., Somerville, R. S., Conselice, C. J., Cook, J. S., Hathi, N. P., Koo, D. C., Lotz, J. M., Simmons, B. D., Straughn, A. N., Snyder, G. F., Wuyts, S., Bell, E. F., Dekel, A., Kartaltepe, J., Kocevski, D. D., Koekemoer, A. M., Lee, S.-K., Lucas, R. A., Pacifici, C., Peth, M. A., Barro, G., Dahlen, T., Finkelstein, S. L., Fontana, A., Galametz, A., Grogin, N. A., Guo, Y., Mobasher, B., Nayyeri, H., Pérez-González, P. G., Pforr, J., Santini, P., Stefanon, M., & Wiklind, T. 2018, MNRAS, 475, 1549

Maoz, D. 2007, Astrophysics in a Nutshell (Princeton University Press)

Marscher, A. P., Jorstad, S. G., Larionov, V. M., Aller, M. F., Aller, H. D., Lähteenmäki, A., Agudo, I., Smith, P. S., Gurwell, M., Hagen-Thorn, V. A., Konstantinova, T. S., Larionova, E. G., Larionova, L. V., Melnichuk, D. A., Blinov, D. A., Kopatskaya, E. N., Troitsky, I. S., Tornikoski, M., Hovatta, T., Schmidt, G. D., D'Arcangelo, F. D., Bhattarai, D., Taylor, B., Olmstead, A. R., Manne-Nicholas, E., Roca-Sogorb, M., Gómez, J. L., McHardy, I. M., Kurtanidze, O., Nikolashvili, M. G., Kimeridze, G. N., & Sigua, L. A. 2010, ApJ, 710, L126

McKee, C. F. & Ostriker, E. C. 2007, Annual Review of Astronomy and Astrophysics, 45, 565

McKee, C. F. & Ostriker, J. P. 1977, ApJ, 218, 148

Mihos, J. C. 1995, ApJ, 438, L75

Mihos, J. C. & Hernquist, L. 1994, ApJ, 437, 611

—. 1996, ApJ, 464, 641

Mihos, J. C., Richstone, D. O., & Bothun, G. D. 1991, ApJ, 377, 72

Mihos, J. C., Walker, I. R., Hernquist, L., Mendes de Oliveira, C., & Bolte, M. 1995, ApJ, 447, L87

Miller, G. E. 1983, ApJ, 268, 495

Mirabel, I. F., Vigroux, L., Charmandaris, V., Sauvage, M., Gallais, P., Tran, D., Cesarsky, C., Madden, S. C., & Duc, P.-A. 1998, A&A, 333, L1

Molina, J., Ibar, E., Swinbank, A. M., Sobral, D., Best, P. N., Smail, I., Escala, A., & Cirasuolo, M. 2017, MNRAS, 466, 892

Moreno, J. 2012, MNRAS, 419, 411

Moreno, J., Bluck, A. F. L., Ellison, S. L., Patton, D. R., Torrey, P., & Moster, B. P. 2013, MNRAS, 436, 1765

Moreno, J., Torrey, P., Ellison, S. L., Patton, D. R., Bluck, A. F. L., Bansal, G., & Hernquist, L. 2015, MNRAS, 448, 1107

Moreno, J., Torrey, P., Ellison, S. L., Patton, D. R., Hopkins, P. F., Bueno, M., Hayward, C. C., Narayanan, D., Kereš, D., Bluck, A. F. L., & Hernquist, L. 2019, MNRAS, 485, 1320

Naiman, J. P., Pillepich, A., Springel, V., Ramirez-Ruiz, E., Torrey, P., Vogelsberger, M., Pakmor, R., Nelson, D., Marinacci, F., Hernquist, L., Weinberger, R., & Genel, S. 2018, MNRAS, 477, 1206

Najarro, F., Kudritzki, R. P., Cassinelli, J. P., Stahl, O., & Hillier, D. J. 1996, A&A, 306, 892

Oser, L., Naab, T., Ostriker, J. P., & Johansson, P. H. 2012, ApJ, 744, 63

Pariev, V. I., Colgate, S. A., & Finn, J. M. 2007, ApJ, 658, 129

Parmentier, G. 2016, ApJ, 826, 74

Patton, D. R., Ellison, S. L., Simard, L., McConnachie, A. W., & Mendel, J. T. 2011, MNRAS, 412, 591

Pauldrach, A., Puls, J., Kudritzki, R. P., Mendez, R. H., & Heap, S. R. 1988, A&A, 207, 123

Pearson, S., Privon, G. C., Besla, G., Putman, M. E., Martínez-Delgado, D., Johnston, K. V., Gabany, R. J., Patton, D. R., & Kallivayalil, N. 2018, MNRAS, 480, 3069

Penna, R. F., McKinney, J. C., Narayan, R., Tchekhovskoy, A., Shafee, R., & McClintock, J. E. 2010, MNRAS, 408, 752

Pettitt, A. R. & Wadsley, J. W. 2018, MNRAS, 474, 5645

Pipino, A., Cibinel, A., Tacchella, S., Carollo, C. M., Lilly, S. J., Miniati, F., Silverman, J. D., van Gorkom, J. H., & Finoguenov, A. 2014, ApJ, 797, 127

Quimby, R. M., Kulkarni, S. R., Kasliwal, M. M., Gal-Yam, A., Arcavi, I., Sullivan, M., Nugent, P., Thomas, R., Howell, D. A., Nakar, E., Bildsten, L., Theissen, C., Law, N. M., Dekany, R., Rahmer, G., Hale, D., Smith, R., Ofek, E. O., Zolkower, J., Velur, V., Walters, R., Henning, J., Bui, K., McKenna, D., Poznanski, D., Cenko, S. B., & Levitan, D. 2011, Nature, 474, 487

Rawlings, S. & Saunders, R. 1991, Nature, 349, 138

Reynolds, C. S., Garofalo, D., & Begelman, M. C. 2006, ApJ, 651, 1023

Rich, J. A., Kewley, L. J., & Dopita, M. A. 2015, ApJS, 221, 28

Robotham, A. S. G., Driver, S. P., Davies, L. J. M., Hopkins, A. M., Baldry, I. K., Agius, N. K., Bauer, A. E., Bland-Hawthorn, J., Brough, S., Brown, M. J. I., Cluver, M., De Propris, R., Drinkwater, M. J., Holwerda, B. W., Kelvin, L. S., Lara-Lopez, M. A., Liske, J., López-Sánchez, Á. R., Loveday, J., Mahajan, S., McNaught-Roberts, T., Moffett, A., Norberg, P., Obreschkow, D., Owers, M. S., Penny, S. J., Pimbblet, K., Prescott, M., Taylor, E. N., van Kampen, E., & Wilkins, S. M. 2014, MNRAS, 444, 3986

Rodriguez-Gomez, V., Snyder, G. F., Lotz, J. M., Nelson, D., Pillepich, A., Springel, V., Genel, S., Weinberger, R., Tacchella, S., Pakmor, R., Torrey, P., Marinacci, F., Vogelsberger, M., Hernquist, L., & Thilker, D. A. 2019, MNRAS, 483, 4140

Rupke, D. S. N., Kewley, L. J., & Barnes, J. E. 2010, ApJ, 710, L156

Salpeter, E. E. 1955, ApJ, 121, 161

Schmidt, M. 1959, ApJ, 129, 243

Scudder, J. M., Ellison, S. L., & Mendel, J. T. 2012a, MNRAS, 423, 2690

Scudder, J. M., Ellison, S. L., Torrey, P., Patton, D. R., & Mendel, J. T. 2012b, MNRAS, 426, 549

Shu, F. H., Adams, F. C., & Lizano, S. 1987, Annual Review of Astronomy and Astrophysics, 25, 23

Smoot, G. F., Bennett, C. L., Kogut, A., Wright, E. L., Aymon, J., Boggess, N. W., Cheng, E. S., de Amici, G., Gulkis, S., Hauser, M. G., Hinshaw, G., Jackson, P. D., Janssen, M., Kaita, E., Kelsall, T., Keegstra, P., Lineweaver, C., Loewenstein, K., Lubin, P., Mather, J., Meyer, S. S., Moseley, S. H., Murdock, T., Rokke, L., Silverberg, R. F., Tenorio, L., Weiss, R., & Wilkinson, D. T. 1992, ApJ, 396, L1

Solanes, J. M., Perea, J. D., & Valentí-Rojas, G. 2018, A&A, 614, A66

Sparre, M. & Springel, V. 2016, MNRAS, 462, 2418

Springel, V. 2000, MNRAS, 312, 859

Springel, V., Di Matteo, T., & Hernquist, L. 2005, MNRAS, 361, 776

Springel, V. & Hernquist, L. 2003, MNRAS, 339, 289

—. 2005, ApJ, 622, L9

Tacconi, L. J., Genzel, R., Smail, I., Neri, R., Chapman, S. C., Ivison, R. J., Blain, A., Cox, P., Omont, A., Bertoldi, F., Greve, T., Förster Schreiber, N. M., Genel, S., Lutz, D., Swinbank, A. M., Shapley, A. E., Erb, D. K., Cimatti, A., Daddi, E., & Baker, A. J. 2008, ApJ, 680, 246

Tapia, T., Eliche-Moral, M. C., Aceves, H., Rodríguez-Pérez, C., Borlaff, A., & Querejeta, M. 2017, A&A, 604, A105

Toomre, A. & Toomre, J. 1972, ApJ, 178, 623

Torrey, P., Cox, T. J., Kewley, L., & Hernquist, L. 2012, ApJ, 746, 108

Torrey, P., Vogelsberger, M., Marinacci, F., Pakmor, R., Springel, V., Nelson, D., Naiman, J., Pillepich, A., Genel, S., Weinberger, R., & Hernquist, L. 2017, arXiv e-prints, arXiv:1711.05261

Trakhtenbrot, B., Lira, P., Netzer, H., Cicone, C., Maiolino, R., & Shemmer, O. 2017, ApJ, 836, 8

Ventou, E., Contini, T., Bouché, N., Epinat, B., Brinchmann, J., Bacon, R., Inami, H., Lam, D., Drake, A., Garel, T., Michel-Dansac, L., Pello, R., Steinmetz, M., Weilbacher, P. M., Wisotzki, L., & Carollo, M. 2017, A&A, 608, A9

Vigroux, L., Mirabel, F., Altieri, B., Boulanger, F., Cesarsky, C., Cesarsky, D., Claret, A., Fransson, C., Gallais, P., Levine, D., Madden, S., Okumura, K., & Tran, D. 1996, A&A, 315, L93

Villalobos, Á., De Lucia, G., Borgani, S., & Murante, G. 2012, MNRAS, 424, 2401

Wang, Z., Fazio, G. G., Ashby, M. L. N., Huang, J. S., Pahre, M. A., Smith, H. A., Willner, S. P., Forrest, W. J., Pipher, J. L., & Surace, J. A. 2004, The Astrophysical Journal Supplement Series, 154, 193

Weinberger, R., Springel, V., Pakmor, R., Nelson, D., Genel, S., Pillepich, A., Vogelsberger, M., Marinacci, F., Naiman, J., Torrey, P., & Hernquist, L. 2018, MNRAS, 479, 4056

Wen, Z. Z. & Zheng, X. Z. 2016, ApJ, 832, 90

Whitmore, B. C. & Schweizer, F. 1995, AJ, 109, 960

Widrow, L. M. 2002, Reviews of Modern Physics, 74, 775

Xu, C., Gao, Y., Mazzarella, J., Lu, N., Sulentic, J. W., & Domingue, D. L. 2000, ApJ, 541, 644

Yuan, F. & Narayan, R. 2014, Annual Review of Astronomy and Astrophysics, 52, 529

Zaritsky, D., Kennicutt, Jr., R. C., & Huchra, J. P. 1994, ApJ, 420, 87

Chapter 2

Introduction to Computational Methods

2.1 The N-Body Method

The N-body method represents a distribution function (DF; see Section 1.1.1) as a collection of particles. If all of the particles have the same mass, then the three-dimensional position and velocity are drawn from the distribution function. To initially set up a simulation of N particles, the DF is treated as a probability function and sampled accordingly. The so-called method of characteristics is used to evolve this in time: each particle moves along the trajectory it would otherwise take in the original potential. As the particles move, they iteratively change the potential and their motions are altered accordingly. Solving the collisionless Boltzmann Equation thus becomes an N-body problem.

2.1.1 Hierarchical Force Calculation (Barnes-Hut Tree)

Summing over all particles in an N-body code is computationally expensive. The Barnes-Hut tree algorithm (Barnes & Hut 1986) is an approximation to full N-body force calculations which greatly decreases the computing time. Simply put, at each time step, this algorithm regroups nearby collections of particles such that they may be approximated by their collective center of mass.

Consider, for example, a localized distribution of particles, and suppose that we wish to calculate the force of gravity on a test mass some distance, d, away. If the ratio of the diameter, d, of the cloud of particles to the distance, r, is below some threshold value, θ, then the cloud's gravitational field may be approximated as a single particle located at its center of mass. If $d/r < \theta$ is satisfied, then the test mass experiences a $1/r$ potential, as if the cloud of particles was a point mass. On the other hand, if $d/r > \theta$, the cloud is split into sub-clouds and the same test is applied to each.

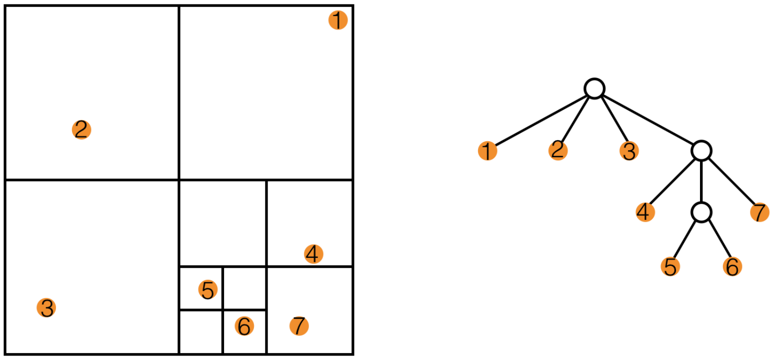

Figure 2.1 The Barnes-Hut tree algorithm, used in approximating N-body force calculations.

This is shown in more detail in Figure 2.1. Each of the seven bodies in Figure 2.1 inhabits its own cell (note that not all cells need to be filled). The right image diagrams the tree structure. The open circles represent parent cells and orange circles are bodies. At the top of the tree is the primary parent cell, which represents the space in which all bodies exist. The fourth quadrant is the first with child branches (i.e. more than one body within the branch). The parent cells are split into child branches until there is only one body per cell. Consider the body in the primary parent node's first quadrant, labeled 1. To calculate the force on 1, we first look across at its siblings, or external cells 2 and 3. The forces of these two bodies on 1 will simply add to its net force. The last quadrant in the primary tree contains four other bodies (4, 5, 6 and 7). If the ratio of the size of the grid box at this level to the distance between its center of mass and body 1 is below a threshold value, then we can simply approximate this grid box as a single body. This approximated body will have a total mass equal to the sum of the body masses within the parent cell and will be located at the center of mass of the cell. If that ratio is above the threshold value, then we must recursively calculate the force on 1 due to the parent's children.

2.1.2 Particle-Mesh Algorithm

Another method for reducing the computation time on N-body problems is the particle-mesh (PM) (Hockney & Eastwood 1981). Instead of iterating over individual particles and their mutual interactions, the PM method approximates the potential as a volume-filling field. This is accomplished by defining a mesh of points (e.g., Figure 2.2), with assigned field quantities based on the corresponding value of the nearest particle. Poisson's equation, Equation 1.7, is then applied directly on the mesh. Interpolation over the field mesh allows the user to output desired quantities for each particle's position. While it is fast, PM suffers from a coarse resolution,

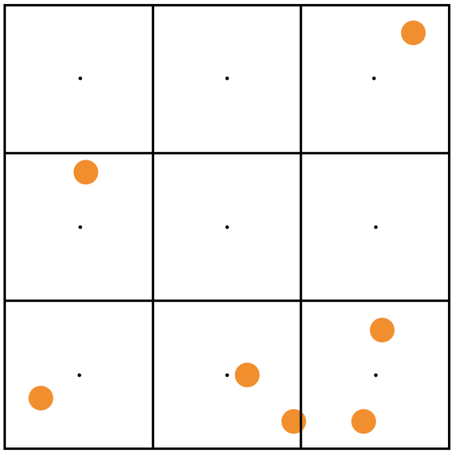

Figure 2.2 In the particle mesh method, a grid is placed over a distribution of particles (orange circles), and the potential is measured at each mesh point (small black points).

and as such is not ideal for e.g., high density calculations. In recent years, this has been paired with the BH tree (known as TreePM; e.g., Xu 1995; Bagla 2002; Springel 2005) to coarsely sample long-range forces, while maintaining the high resolution of short-range calculations with the BH tree.

2.2 Hydrodynamic Methods

2.2.1 Smoothed-Particle Hydrodynamics

Just as the N-body method uses particles to sample a smooth gravitational potential, Smoothed-Particle Hydrodynamics (SPH) models a smooth fluid flow as a set of discrete particles. SPH codes use smoothed kernels, defined by a particle's smoothing parameter, h. The kernels generally contain a set number of particles that define its mass and overall direction of motion. This methodology allows for an adaptive resolution; the kernels will be smallest where the fluid density is highest. This interpolation method is used to obtain the continuous approximation. In this case, the fluid particles are collisional gas particles. The i^{th} smoothed kernel will have associated with it a sound velocity, c_i, that is the average of its constituent particles.

Figure 2.3 illustrates how an SPH code generates kernels with a fixed number of neighbor particles. In this case, the kernel sizes, h_i, are defined such that each kernel contains six neighbors. If allowed to step through time, h_i would be iteratively redefined, according to the changing particle density.

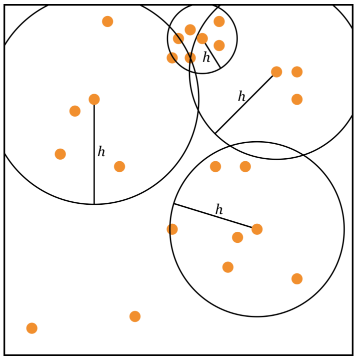

Figure 2.3 Smoothed-particle hydrodynamics, after Dale (2015)

2.2.2 Moving-Mesh Hydrodynamics (AREPO)

Prior to AREPO (Springel 2010a), there were two frameworks used for evolving and tracking gas in simulation: (1) the Lagrangian method (e.g., smoothed-particle hydrodynamics; SPH), in which individual kernels of fluid are tracked (and can change size) over time, and (2) the Eulerian method (e.g., adaptive mesh refinement; AMR), in which the fluid itself is not tracked, but its effect on the volume elements of a structured and fixed grid could be accurately measured. Though the former enables careful tracking of the fluid over time, the process of smoothing over many particles to form a kernel suppresses instabilities, discontinuities and shocks. AREPO is a novel technique which combines the benefits of both Lagrangian and Eulerian methods, while minimizing the drawbacks, particularly for large cosmological simulations. It is a Galilean-invariant: AREPO provides consistent results for both a moving reference frame (e.g., SPH) and a fixed frame (e.g., AMR). The code generates an unstructured mesh based on the Voronoi tessellation of a set of fluid particles that is allowed to evolve continuously. In this way, AREPO provides sufficient resolution to accurately represent shock instabilities and other discontinuities, while also tracking fluid flow.

2.3 Zeno

Zeno is a software package that combines SPH (e.g., Springel 2010b) and N-body algorithms to initialize and implement numerical simulations. It has a series of programs that will build the individual pieces of a galaxy: the gas disk, stellar disk, stellar bulge and dark matter halo. These four pieces are stacked to form a single file which acts as the initial data input file for the encounter model.

To generate the initial conditions of the encounter, Zeno places the two disks on parabolic trajectories with some Keplerian (or, ideal) pericentric separation. Though the dark matter haloes extend out to infinity, they taper at a characteristic radius such that the initial overlap between the two haloes involved in a merger is insignificant. Hence, the two haloes initially interact as if they were both point masses (i.e. each halo will experience a 1/r potential) and move along Keplerian orbits. As the dark matter haloes move closer to one another and gravitationally interact, their orbits will decay via dynamical friction, and will spiral inward toward their mutual center of mass until final coalescence.

2.4 IllustrisTNG

IllustrisTNG is an N-body/hydrodynamic cosmological simulation suite. There are three cosmological boxes (TNG300, TNG100 and TNG50) which have progressively higher resolution. The TNG100 and TNG300 volumes are each run with three initializations using the full physics model, and a separate dark matter only set. TNG50 was initialized with four sets of initial conditions using the full physics model only (i.e. there is no corresponding dark matter only run). These are often referred to as e.g., TNG100-1 or TNG300-2-Dark. In all cases, gravity is solved using a Tree-PM algorithm, which uses a particle mesh on large scales and a tree code (as described above) on small scales. Gas is treated as an ideal fluid on an unstructured mesh (AREPO; Springel 2010b, and see below for a brief description). Gas cooling occurs via metal-lines and radiation, while the gas may be heated radiatively by exposure to a redshift-dependent radiation field (e.g., Katz et al. 1996; Faucher-Giguère et al. 2009). With sufficiently high optical depth, high density gas can self-shield (Vogelsberger et al. 2013). The interstellar medium (ISM) is modeled in two phases: cool clouds that are in pressure equilibrium with a hot diffuse medium (Springel & Hernquist 2003b, see §2.4.2 for a detailed description of this subgrid model).

Each star particle represents a stellar population, not an individual star. These particles obey empirical models that include stellar evolution, enrichment, mass and metal returns and supernova rates (Pillepich et al. 2018a). Star formation and supernovae drive outflows in galaxies. Gas mass is ejected from star forming regions such that the wind velocity is proportional to the dark matter velocity dispersion. Due to resolution limitations, outflowing material is initially hydrodynamically decoupled, and are re-coupled at some density threshold. The winds carry their metal content out of the galaxy, in a way that is tuned to match the mass-metallicity (or, M-Z) relation. Magnetic fields have important implications for galaxy formation and evolution over a wide range of physical scales (as demonstrated in e.g., Marinacci et al. 2015; Marinacci & Vogelsberger 2016; Hull et al. 2017; Mocz et al. 2017; Ehlert et al. 2018; Marinacci et al. 2018). In

IllustrisTNG, they are implemented using an ideal magnetohydrodynamic (MHD) solver that acts directly on TNG's unstructured mesh within the framework of AREPO (Pakmor et al. 2011; Pakmor & Springel 2013). The MHD equations are solved in each gas cell to arrive at a magnetic flux. In this way, IllustrisTNG is able to determine the magnetic field over a large dynamical range. Black holes – and the feedback due to AGN – are a key part of TNG's success.

The previous iteration of the cosmological suite, Illustris (Vogelsberger et al. 2014a,b; Genel et al. 2014; Sijacki et al. 2015), underproduced quiescent galaxies in large part due to the poor implementation of AGN feedback (Nelson et al. 2018). This was significantly updated for IllustrisTNG (Weinberger et al. 2018, and see below for a detailed discussion), resulting in a more reliable set of galaxy morphologies (Rodriguez-Gomez et al. 2019). Additionally, IllustrisTNG improves upon the original treatment of supernovae and subsequent chemical evolution (Naiman et al. 2018), and includes an ideal treatment of magnetohydrodynamics (Pakmor et al. 2011, 2016). In this thesis, I utilize the TNG100-1 run for the following reasons: (1) it uses the same set of initial conditions as the original Illustris run; (2) it has the largest number of resolution elements for its volume; and (3) the volume is large enough to contain many examples of interacting galaxies (c.f., TNG50), but not too large that these galaxies are poorly resolved (c.f., TNG300).

The IllustrisTNG model (Weinberger et al. 2017; Pillepich et al. 2018b) has succeeded in many ways. For example, Nelson et al. (2018) show that the the suite of simulations recovers the color bimodality, and suggest that this is due to the particular black hole feedback implementation used. Rodriguez-Gomez et al. (2019) look at simulated images of galaxies in TNG100 and find that they have very similar morphologies to an analogous sample of objects from Pan-STARRS. Other derived relations, such as chemical evolution (Naiman et al. 2018), the galaxy mass-metallicity relations (Torrey et al. 2017), and the present day quasar luminosity function (Weinberger et al. 2018) have been shown to be consistent with observations. Despite its relative successes over the original Illustris simulation, the IllustrisTNG model deviates significantly from what is observed. It has been shown that the IllustrisTNG model may inhibit bulge growth, and overproduce both red discs and blue spheroids (e.g., Huertas-Company et al. 2019; Rodriguez-Gomez et al. 2019). The early universe is also a point of contention: the high-redshift luminosity function (Habouzit et al. 2018; Weinberger et al. 2018) and H_2 gas fraction in galaxies (Popping et al. 2019) seen in the IllustrisTNG suite of simulations disagree with observations.

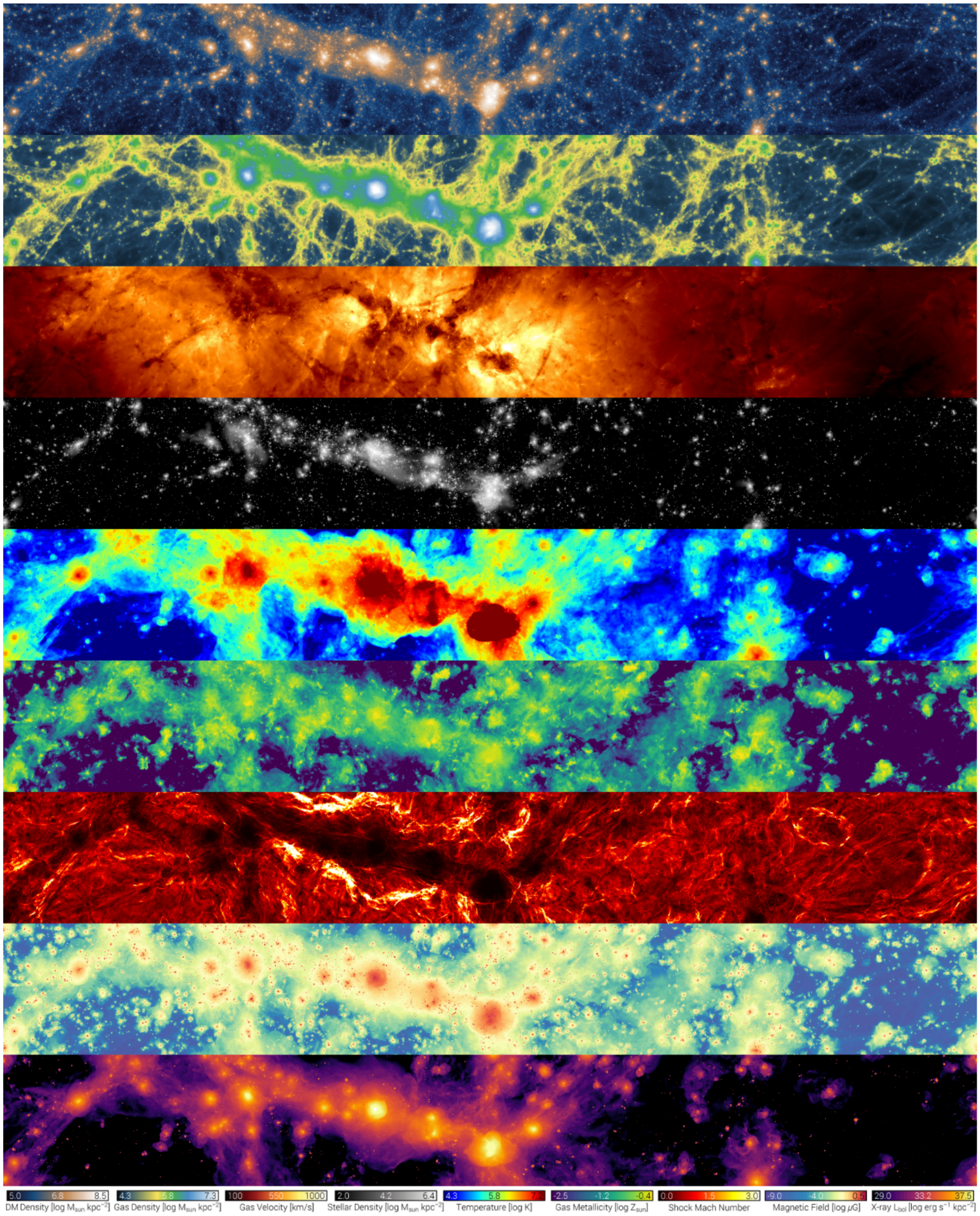

Figure 2.4 This shows a subset of the information that can be derived from TNG100-1 snapshot data. Each panel shows the same volume at $z = 0$. They are, from top to bottom: the dark matter density, gas density, gas velocity, stellar mass density, gas temperature, gas-phase metallicity, shock mach number, magnetic field strength, and X-ray luminosity. Image credit: TNG Collaboration

2.4.1 Coordinate systems

Cosmological simulations, such as Illustris and IllustrisTNG, use comoving coordinates as a way to simplify distance measurements within a volume that is expanding due to Hubble flow. The physical coordinates ($\mathbf{r}$, e.g., in units of kiloparsecs) is related to the comoving coordinate ($\mathbf{x}$) via

$$\mathbf{r} = a(t)\mathbf{x} \tag{2.1}$$

where a(t) is the scale factor at a particular time. Taking the time derivative of this equation gives us a similar relation for the velocities

$$\begin{align} \dot{\mathbf{r}} &= a(t)\dot{\mathbf{x}} + \dot{a}(t)\mathbf{x} \tag{2.2} \\ &= a(t)\dot{\mathbf{x}} + H(t)\mathbf{r} \tag{2.3} \end{align}$$

where the first set of terms is the peculiar velocity, $\mathbf{v}_{\rm pec}$. Here we introduce the Hubble parameter, $H(t) = \dot{a}/a$, which when applied to the physical distance, as in the second set of terms, defines a recessional velocity. This radial expansion is independent of position: all points expand away from one another at the same rate regardless of their placement within the volume. When added to the peculiar velocity, the Hubble term provides an instantaneous velocity correction corresponding to the expansion rate at a given time. All velocities and positions reported in this work are in physical coordinates.

2.4.2 Simulation Algorithms

Multiphase ISM

Springel & Hernquist (2003a, hereafter SH03) devised a model for self-regulating star formation and feedback. Typically, gas in galaxies is treated as a single-phase medium (that is, isothermal; e.g., Barnes 2004), and stars form on a characteristic timescale, $t_\star$. In the SH03 model, the authors instead incorporate a two-phase ISM: a hot ambient gas ($T \geq 10^4$ K) with cool clouds ($T=10^3$ K). The cold phase exists at the sub-resolution level: SH03 cannot capture the internal structure of cold clouds, and so these are a statistical treatment of the cites of star formation. The dynamics of the ambient hot gas are integrated using the hydrodynamics equations, whereas the clouds are only subject to gravity, and as such, do not contribute significantly to the pressure of the galaxy's gas (thus these two components can be treated independently).

If the relaxation time is much shorter than the crossing time, gaseous material tends to remain in, or close to, equilibrium. SH03 exploit this fact by bypassing an explicit treatment of mass transfer between the gaseous and stellar phases within their hybrid SPH particles. Each hybrid SPH particle is tagged with an abundance fraction of the cold and hot material. The relative amount of material in each phase at any given point in time is defined by the following two equations

$$\frac{\rho_{\mathrm{c}}}{\rho} = y\frac{\rho_{\mathrm{h}}}{\rho} \tag{2.4}$$

$$y \equiv \frac{t_\star \Lambda_{\mathrm{net}}(\rho, u_{\mathrm{h}})}{\rho\,(\beta u_{\mathrm{SN}} - (1-\beta)u_{\mathrm{c}})} \tag{2.5}$$

In this way, the transfer of material between the phases is driven by the cooling rate, Λ_{net}, and the internal energy of the hot, u_{h}, and cold, u_{c} media and the heat injection energy due to supernovae, u_{SN}. The β parameter is derived from the IMF, and can be considered a mass fraction of the highest mass stars which will undergo a supernova. Energy from the supernova is deposited into the ambient medium, causing it to heat up. At a sub-resolution level, this is equivalent to clouds within some radius of the supernova evaporating as a result of the explosion, and returning their material to the ambient hot gas.

If the density of the gas exceeds a star formation threshold (in the IllustrisTNG model, this threshold is $n_{\mathrm{H}} \simeq 0.1\mathrm{cm}^{-3}$, see e.g., Pillepich et al. 2018a), the hybrid SPH particle may shed star particles at a rate

$$\dot{M}_\star = \frac{\rho_{\mathrm{c}}}{\rho}\frac{m}{t_\star}(1-\beta) \tag{2.6}$$

if the probability

$$p_i = \frac{m}{m_\star}\left(1 - \exp\left\{-(1-\beta)\frac{\rho_{\mathrm{c}}}{\rho}\frac{\Delta t}{t_\star}\right\}\right) \tag{2.7}$$

is greater than a random number drawn from a uniform distribution between 0 and 1. In this equation, the total mass in the hybrid SPH particle (including stars) is m, the mass of the shed stellar particles is $m_\star = m_{\mathrm{o}}/N_{\mathrm{G}}$; m_{o} is the initial mass of the SPH particle at time Δt and N_{G} is the number of generations of stars that SPH particle has produced. This methodology ensures that the stellar and gaseous material are not artificially coupled, and also incorporates supernovae. In effect, at each star formation event, some fraction of that material (determined by the β parameter) instantaneously and completely gets returned to the gaseous phase.

This ongoing exchange of material between the cold and hot gas and stellar material naturally results in a change in the metallicity of the ISM. At each time step, this change is calculated by the following equation:

$$\Delta Z = (1 - \beta) y_\star \frac{\rho_c}{\rho} \frac{\Delta t}{t_\star} \tag{2.8}$$

where $y_\star$ is the yield, or fractional amount of metals returned to the ISM at any point in time. The above accounts for the metallicity change due to supernovae and stellar winds. Each star particle generated at a given point in time is tagged with the metallicity of the gas from which it was formed.

Star Formation and Feedback

In SPH codes, star formation is generally treated probabilistically. That is, for a SPH kernel at each point in time, a probability is calculated based on the local gas conditions. If the probability exceeds some pre-defined value, then the kernel sheds star particles.

For example, in Barnes (2004), the star formation rate is given by

$$\dot{\rho}_\star = C_\star \, \rho_g^n \, \mathrm{MAX}(\dot{u}, 0)^m \tag{2.9}$$

where $C_\star$ is a constant, ρ_g is the local gas density and $\dot{u}$ is the rate of heating due to shocks. The probability for each particle, i, is then

$$p_i = C_\star \, \rho_i^{n-1} \, \mathrm{MAX}(\dot{u}_i, 0)^m \, \Delta t \tag{2.10}$$

In this prescription, the probability is calculated at each time step and compared to a number randomly selected from a uniform distribution between 0 and 1. If at a given time step, the probability is greater than this random number, then the gas particle instantly and completely enters the "stellar phase." Its motions are from then on treated collisionlessly.

There are two key choices for n and m. In the case $n > 1$ and $m = 0$, the rate of star formation is completely driven by the gas density. On the other hand, if $n = 1$ and $m > 0$ then the probability is entirely dependent upon the shock induced heating, and star formation will only occur at the location of shocks.

A choice of $n > 1$ and $m > 1$ would allow for star formation throughout the disk, but has not yet been implemented.

As stellar evolution undoubtedly takes place on a spatial scale much smaller than the typical resolution of simulations, artificial effects may present problems for interpreting the results. In the specific case discussed above, a choice of $m = 1$ allows for star formation which is approximately independent of the spatial resolution of the simulation.

AGN Fueling and Feedback

Black holes – and the feedback due to active galactic nuclei – are a key part of this simulation, in particular the production of quiescent galaxies. Given the resolution of the simulation, black hole formation cannot be self-consistently modeled, so once a galaxy reaches a certain size, a seed black hole particle is inserted at its center, which then acts as a sink particle. The black hole is thus tied to the potential minimum, which is also how the galaxy centers are tracked. Black holes grow by subsequent mass accretion via Eddington-limited Bondi-Hoyle accretion (Springel et al. 2005).

Accretion onto a central black hole is typically treated in a similar manner to star formation. In Springel et al. (2005), a probability is calculated at each time step for each particle, i:

$$p_i = \frac{w_i \; \dot{M}_{\rm BH} \; \Delta t}{\rho_{\rm g}} \tag{2.11}$$

where w_i is a constant weighting parameter, $\dot{M}_{\rm BH}$ is the accretion rate, and $\rho_{\rm g}$ is the approximate local gas density at the location of the accretion disk. Just as in Barnes (2004), this probability is compared to a number randomly selected from a uniform distribution between 0 and 1. If the probability is less than this random number, then the particle's mass and momentum will be accreted onto the black hole.

The channel of AGN feedback (Sijacki et al. 2007; Weinberger et al. 2018) depends on the ratio of the accretion rate to the Eddington rate. Gas around the black hole mimics photoevaporation at lower accretion rates, which includes a wind and jet (radio or kinetic) mode. In this regime, kinetic energy is deposited into the gas around the black hole, and the duty cycle ensures star formation does not become bursty. At higher accretion rates, the galaxy enters the thermal (quasar) mode; the strength of this feedback mode is a function of the black hole mass.

2.4.3 Post-Processing Methods

Friends-of-Friends (FoF) Algorithm

Haloes, or equivalently FoF groups, are constructed via the Friends-of-Friends algorithm (Davis et al. 1985). FoF is a percolation algorithm in which dark matter particles are linked together based on the mean particle separation of the simulation, l, and the linking length, b, which is left as a free parameter. Gas and star particles are assigned to a FoF group based on the membership of the closest dark matter particle. This methodology has been applied to many different astrophysical scenarios, including observational studies of galaxy distributions and groupings (e.g., Press & Davis 1982; Einasto et al. 1984; Eke et al. 2004; Yang et al. 2005, 2007; George et al. 2011), and halo finding in cosmological simulations (see Knebe et al. 2011, for an extensive list). For IllustrisTNG, and most halo finders, the linking length is $b = 0.2$.

There are many different methods for identifying structure in cosmological simulation particle data. For example, the bound density maximum method (e.g., Klypin & Holtzman 1997) locates density maxima and defines a halo based on a fixed spherical radius about the density peak. The AHF method (e.g., Gill et al. 2004; Knollmann & Knebe 2009) also uses particle overdensity to identify potential haloes, but particles are considered within a defined isodensity contour and removed from the structure if they are unbound. More recently, ROCKSTAR (Behroozi et al. 2013) was developed to use the six-dimensional phase-space (plus time) to refine and track FoF-defined (sub)haloes. For a comprehensive evaluation of the various halo finders, refer to Knebe et al. (2013).

SUBFIND Algorithm

The SUBFIND algorithm was developed by Springel et al. (2001) to identify substructure (i.e. haloes and galaxies) within relatively small-scale cosmological simulations of galaxy clusters. The algorithm acts on FoF haloes to identify these substructures, creating a hierarchical grouping of particles within the simulation data. Substructure candidates are initially indicated by the position (and by extension, the local number density) of the particles, and are iteratively stripped of particles that are not physically bound. This is achieved by entering into a frame of reference centered on the candidate subhalo's most bound particle and removing those which are unbound. If at the end of this process, a subhalo candidate has more than a minimum number of particles, it is considered a true subhalo of the FoF group. As a result of this "unbinding" process, there are some particles which are physically associated with the FoF group based on

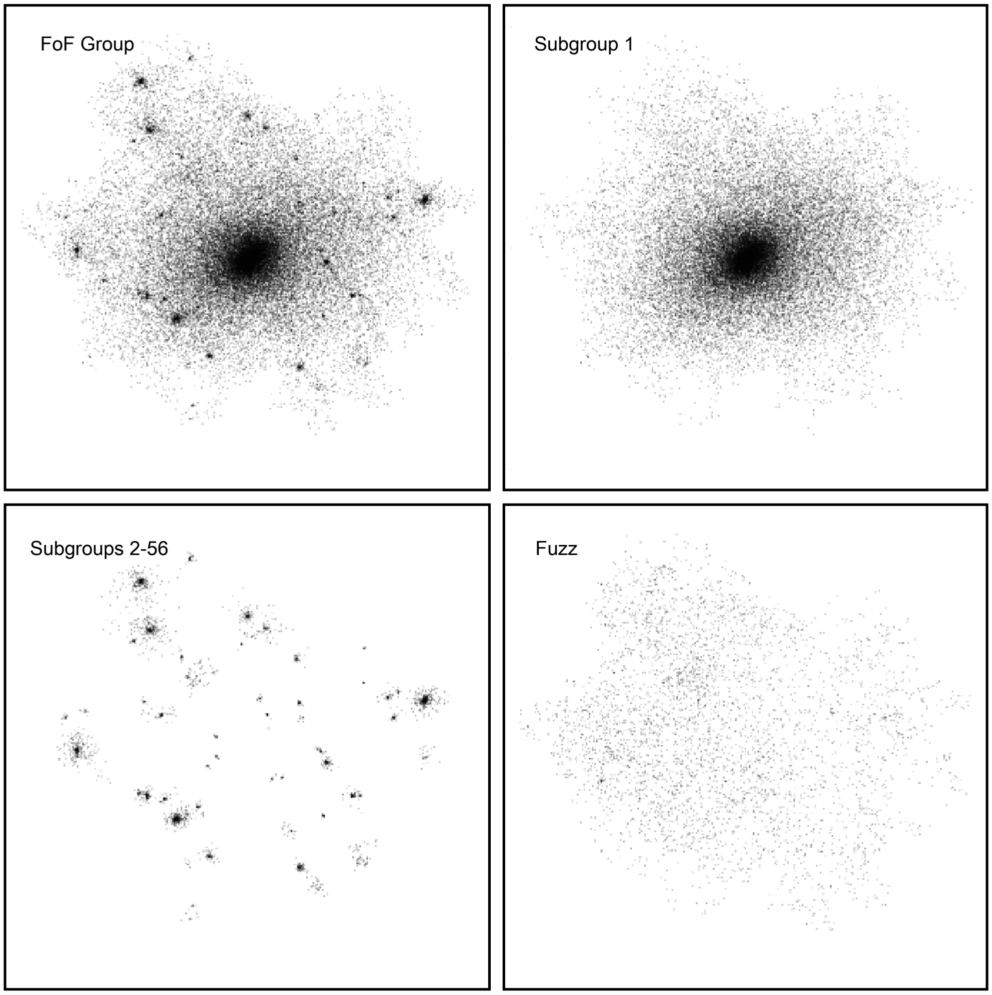

Figure 2.5 The hierarchy of particle groupings in IllustrisTNG. The FoF group corresponds roughly to the haloes of massive clusters of galaxies. The substructure within these haloes are galaxies, or smaller unpopulated dark matter haloes, known as subhaloes. Unbound particles physically associated with the FoF group are considered “(inner) fuzz”. Not shown are the so-called “outer fuzz” particles, which are not bound to any FoF group. This is Figure 3 in Springel et al. (2001), and has been reproduced here with the author’s permission.

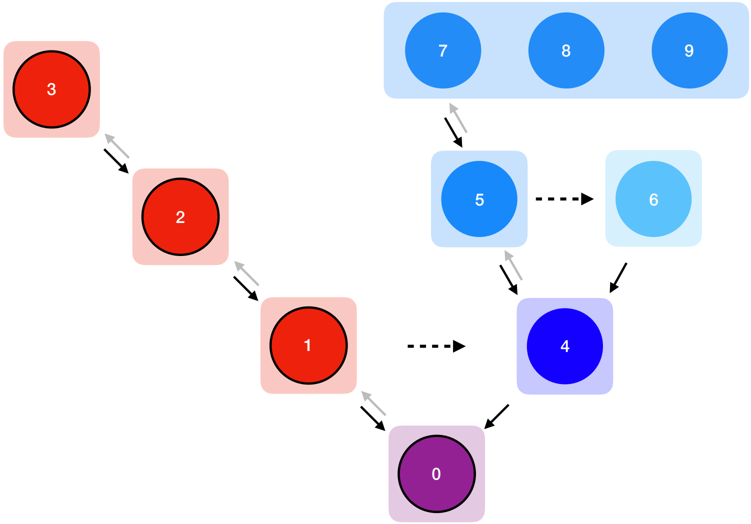

Figure 2.6 A schematic of merger tree structure. Here, time progresses downward. Each individual circle represents a subhalo within a group, or FoF halo (shaded rectangles). The subhaloes are numbered according to their mass: subhalo 0 is the most massive and 7 the least massive. Black solid arrows point toward the Descendant; grey solid arrows point at the FP; dotted black arrows point toward the NP. The MPB is outlined in black. As an example, subfind haloes 5 and 6 merge to form subfind halo 4, which in turn merges with subfind halo 1 to form subfind halo 0. Were we to only consider the MPB, we would not get any information regarding subfind halo 8 or 9, as they are not directly linked to the subfind haloes outlined in black.

proximity, but are not bound to any particular substructure. These are designated as "inner fuzz", and make up approximately 8% of the TNG volume at the present day. Nearly three-fourths of that exists in low-mass haloes with no substructure (i.e. dark haloes). Counting only those FoF haloes which have a subhalo, the fraction of "inner fuzz" reduces to about 2.7%. The particles that make up this value are nearly entirely dark matter, with a small contribution from diffuse gas.

There are, however, known problems with the SUBFIND algorithm. Muldrew et al. (2011) found that the mass recovered by SUBFIND depends on the subhalo's proximity to the center of the parent halo: the subhalo will be artificially truncated due to the relative high density of the halo near its core. It has been suggested (e.g., Onions et al. 2012; Muldrew et al. 2011) that using the six-dimensional phase space (as in e.g., Maciejewski et al. 2009; Behroozi et al. 2013) to define the subhalo structure would improve the accuracy of this method.

Merger Trees

Merger trees (Rodriguez-Gomez et al. 2015) use information about the baryonic material within subfind haloes to trace galaxies back as a function of time. The merger tree is constructed from three fundamental links: the Descendant, First Progenitor (FP), and Next Progenitor (NP). A subfind halo always has a Descendant and a FP; their definitions are related. The descendant link tracks subfind haloes through time. The FP is thus the most massive subfind halo of a given Descendant. The NP is the next most massive subfind halo of a that Descendant. A merger occurs when two subfind haloes share a Descendant. Put another way, a merger occurs when a Descendant has both a First and Next Progenitor. When parsing a merger tree, it is often useful to consider only the Main Progenitor Branch (MPB), which can be considered the "trunk" of the tree. This provides information only directly linked to the MPB. A schematic of this network is shown in Figure 2.6. Parsing a merger tree requires at least two identifiers: the identification (ID) numbers of the First and Next Progenitors. Walking back along the MPB, each FP is defined by its index in the subhalo catalog at that snapshot until a FP can no longer be defined. If the FP ID number is -1, then you have reached the end of the FP branch. For each FP, there is a network of Next Progenitors (NP) which were involved in a merger. Similarly, when there are no more Next Progenitors for a given FP, the NP ID is -1.

2.5 Dissertation Outline

This thesis attempts to reconcile idealized simulations of galaxy interactions with what is "observed" in the cosmological simulation IllustrisTNG. To do this, I first considered idealized simulations of galaxy encounters within the context of gaseous inflows (Chapter 3). Inflows are driven by the intricate tug-o-war between gravitational and hydrodynamic torques (e.g., Barnes & Hernquist 1991, 1996; Mihos & Hernquist 1996; Blumenthal & Barnes 2018). The dominance of one over the other depends on parameters such as the orbit geometry (gravity) and the relative size of the gas disks (hydrodynamics). Most simulations of galaxy encounters naively (and inaccurately) assume that the stellar and gas disks are the same physical size. The primary focus of the first part of my thesis is: if we apply observationally motivated gas-to-stellar size ratios, how does the merger-driven inflow change? Put a different way, how do the hydrodynamical torques change when the size of the gas disk is altered?

On the other side of this tug-o-war, the gravitational torque's magnitude can be altered by the interaction geometry. This includes the orbital eccentricity, disk inclinations, and width of the orbit. Although approximations to these parameters are often derived from observational catalogues, the observable universe does not reveal a galaxy's entire dynamical history. Further, merger catalogues are likely to be biased toward certain kinds of interactions. To understand the extent to which our merger samples (and by extension, our small-scale simulations) are affected, I generated a sample of binary pairs in the local ($z = 0$) TNG100-1 volume (Chapter 4). With mock Sloan Digital Sky Survey (SDSS) images and the true trajectory information from the cosmological volume, I split this sample into pairs which were visually identified (VIP) and those which were not (nonVIP). We can then ask the question: when using morphological indicators (e.g., tidal features and stellar debris fields) to identify merging galaxies, what fraction of the whole interacting sample do we select? Toward what kinds of interactions are these catalogues biased?

At present, the initial conditions of idealized merger simulations are based on a series of presumptions that may not be truly representative of reality because they are themselves based on potentially biased merger catalogues. In Chapter 5, I present cosmologically derived initial conditions: I characterize the orbits of the TNG100-1 pairs sample and provide distributions for the eccentricity, disc inclinations, (sub)halo total angular momentum, first pericentric separation, in addition to the relative position and velocity at infall. I also present fits to the dark matter and stellar particle distributions. In this way, future idealized simulations will be able to utilize parameters that are cosmologically motivated. I discuss the Keplerian approximation, and ways in which it might fail. I present a case study in idealized simulations in which we employ several different methods to model one system from the TNG100-1 interacting pairs sample. With this, we ask the questions: can cosmologically motivated initial conditions sufficiently improve the idealized method? In the era of high-resolution cosmological simulations, are idealized simulations obsolete?

In the chapters that follow, I present the branches of my thesis that touch on each of the three topics discussed above. These are followed, in Chapter 6, by a brief discussion of my cumulative results, my conclusions, and potential future directions.

References

Bagla, J. S. 2002, Journal of Astrophysics and Astronomy, 23, 185

Barnes, J. & Hut, P. 1986, Nature, 324, 446

Barnes, J. E. 2004, MNRAS, 350, 798

Barnes, J. E. & Hernquist, L. 1996, ApJ, 471, 115

Barnes, J. E. & Hernquist, L. E. 1991, ApJ, 370, L65

Behroozi, P. S., Wechsler, R. H., & Wu, H.-Y. 2013, ApJ, 762, 109

Blumenthal, K. A. & Barnes, J. E. 2018, MNRAS, 479, 3952

Dale, J. E. 2015, New A Rev., 68, 1

Davis, M., Efstathiou, G., Frenk, C. S., & White, S. D. M. 1985, ApJ, 292, 371

Ehlert, K., Weinberger, R., Pfrommer, C., Pakmor, R., & Springel, V. 2018, MNRAS, 481, 2878

Einasto, J., Klypin, A. A., Saar, E., & Shandarin, S. F. 1984, MNRAS, 206, 529

Eke, V. R., Baugh, C. M., Cole, S., Frenk, C. S., Norberg, P., Peacock, J. A., Baldry, I. K., Bland-Hawthorn, J., Bridges, T., Cannon, R., Colless, M., Collins, C., Couch, W., Dalton, G., de Propris, R., Driver, S. P., Efstathiou, G., Ellis, R. S., Glazebrook, K., Jackson, C., Lahav, O., Lewis, I., Lumsden, S., Maddox, S., Madgwick, D., Peterson, B. A., Sutherland, W., & Taylor, K. 2004, MNRAS, 348, 866

Faucher-Giguère, C.-A., Lidz, A., Zaldarriaga, M., & Hernquist, L. 2009, ApJ, 703, 1416

Genel, S., Vogelsberger, M., Springel, V., Sijacki, D., Nelson, D., Snyder, G., Rodriguez-Gomez, V., Torrey, P., & Hernquist, L. 2014, MNRAS, 445, 175

George, M. R., Leauthaud, A., Bundy, K., Finoguenov, A., Tinker, J., Lin, Y.-T., Mei, S., Kneib, J.-P., Aussel, H., Behroozi, P. S., Busha, M. T., Capak, P., Coccato, L., Covone, G., Faure, C., Fiorenza, S. L., Ilbert, O., Le Floc'h, E., Koekemoer, A. M., Tanaka, M., Wechsler, R. H., & Wolk, M. 2011, ApJ, 742, 125

Gill, S. P. D., Knebe, A., & Gibson, B. K. 2004, MNRAS, 351, 399

Habouzit, M., Volonteri, M., Somerville, R. S., Dubois, Y., Peirani, S., Pichon, C., & Devriendt, J. 2018, arXiv e-prints, arXiv:1810.11535

Hockney, R. W. & Eastwood, J. W. 1981, Computer Simulation Using Particles (McGraw-Hill)

Huertas-Company, M., Rodriguez-Gomez, V., Nelson, D., Pillepich, A., Bernardi, M., Domínguez-Sánchez, H., Genel, S., Pakmor, R., Snyder, G. F., & Vogelsberger, M. 2019, arXiv e-prints, arXiv:1903.07625

Hull, C. L. H., Mocz, P., Burkhart, B., Goodman, A. A., Girart, J. M., Cortés, P. C., Hernquist, L., Springel, V., Li, Z.-Y., & Lai, S.-P. 2017, ApJ, 842, L9

Katz, N., Weinberg, D. H., & Hernquist, L. 1996, ApJS, 105, 19

Klypin, A. & Holtzman, J. 1997, arXiv e-prints, astro

Knebe, A., Knollmann, S. R., Muldrew, S. I., Pearce, F. R., Aragon-Calvo, M. A., Ascasibar, Y., Behroozi, P. S., Ceverino, D., Colombi, S., Diemand, J., Dolag, K., Falck, B. L., Fasel, P., Gardner, J., Gottlöber, S., Hsu, C.-H., Iannuzzi, F., Klypin, A., Lukić, Z., Maciejewski, M., McBride, C., Neyrinck, M. C., Planelles, S., Potter, D., Quilis, V., Rasera, Y., Read, J. I., Ricker, P. M., Roy, F., Springel, V., Stadel, J., Stinson, G., Sutter, P. M., Turchaninov, V., Tweed, D., Yepes, G., & Zemp, M. 2011, MNRAS, 415, 2293

Knebe, A., Pearce, F. R., Lux, H., Ascasibar, Y., Behroozi, P., Casado, J., Moran, C. C., Diemand, J., Dolag, K., & Dominguez-Tenreiro, R. 2013, MNRAS, 435, 1618

Knollmann, S. R. & Knebe, A. 2009, ApJS, 182, 608

Maciejewski, M., Colombi, S., Springel, V., Alard, C., & Bouchet, F. R. 2009, MNRAS, 396, 1329

Marinacci, F. & Vogelsberger, M. 2016, MNRAS, 456, L69

Marinacci, F., Vogelsberger, M., Mocz, P., & Pakmor, R. 2015, MNRAS, 453, 3999

Marinacci, F., Vogelsberger, M., Pakmor, R., Torrey, P., Springel, V., Hernquist, L., Nelson, D., Weinberger, R., Pillepich, A., Naiman, J., & Genel, S. 2018, MNRAS, 480, 5113

Mihos, J. C. & Hernquist, L. 1996, ApJ, 464, 641

Mocz, P., Burkhart, B., Hernquist, L., McKee, C. F., & Springel, V. 2017, ApJ, 838, 40

Muldrew, S. I., Pearce, F. R., & Power, C. 2011, MNRAS, 410, 2617

Naiman, J. P., Pillepich, A., Springel, V., Ramirez-Ruiz, E., Torrey, P., Vogelsberger, M., Pakmor, R., Nelson, D., Marinacci, F., Hernquist, L., Weinberger, R., & Genel, S. 2018, MNRAS, 477, 1206

Nelson, D., Pillepich, A., Springel, V., Weinberger, R., Hernquist, L., Pakmor, R., Genel, S., Torrey, P., Vogelsberger, M., Kauffmann, G., Marinacci, F., & Naiman, J. 2018, MNRAS, 475, 624

Onions, J., Knebe, A., Pearce, F. R., Muldrew, S. I., Lux, H., Knollmann, S. R., Ascasibar, Y., Behroozi, P., Elahi, P., Han, J., Maciejewski, M., Merchán, M. E., Neyrinck, M., Ruiz, A. N., Sgró, M. A., Springel, V., & Tweed, D. 2012, MNRAS, 423, 1200

Pakmor, R., Bauer, A., & Springel, V. 2011, MNRAS, 418, 1392

Pakmor, R. & Springel, V. 2013, MNRAS, 432, 176

Pakmor, R., Springel, V., Bauer, A., Mocz, P., Munoz, D. J., Ohlmann, S. T., Schaal, K., & Zhu, C. 2016, MNRAS, 455, 1134

Pillepich, A., Nelson, D., Hernquist, L., Springel, V., Pakmor, R., Torrey, P., Weinberger, R., Genel, S., Naiman, J. P., Marinacci, F., & Vogelsberger, M. 2018a, MNRAS, 475, 648

Pillepich, A., Springel, V., Nelson, D., Genel, S., Naiman, J., Pakmor, R., Hernquist, L., Torrey, P., Vogelsberger, M., Weinberger, R., & Marinacci, F. 2018b, MNRAS, 473, 4077

Popping, G., Pillepich, A., Somerville, R. S., Decarli, R., Walter, F., Aravena, M., Carilli, C., Cox, P., Nelson, D., Riechers, D., Weiss, A., Boogaard, L., Bouwens, R., Contini, T., Cortes, P. C., da Cunha, E., Daddi, E., Díaz-Santos, T., Diemer, B., González-López, J., Hernquist, L., Ivison, R., Le Fevre, O., Marinacci, F., Rix, H.-W., Swinbank, M., Vogelsberger, M., van der Werf, P., Wagg, J., & Yung, L. Y. A. 2019, arXiv e-prints, arXiv:1903.09158

Press, W. H. & Davis, M. 1982, ApJ, 259, 449

Rodriguez-Gomez, V., Genel, S., Vogelsberger, M., Sijacki, D., Pillepich, A., Sales, L. V., Torrey, P., Snyder, G., Nelson, D., Springel, V., Ma, C.-P., & Hernquist, L. 2015, MNRAS, 449, 49

Rodriguez-Gomez, V., Snyder, G. F., Lotz, J. M., Nelson, D., Pillepich, A., Springel, V., Genel, S., Weinberger, R., Tacchella, S., Pakmor, R., Torrey, P., Marinacci, F., Vogelsberger, M., Hernquist, L., & Thilker, D. A. 2019, MNRAS, 483, 4140

Sijacki, D., Springel, V., Di Matteo, T., & Hernquist, L. 2007, MNRAS, 380, 877

Sijacki, D., Vogelsberger, M., Genel, S., Springel, V., Torrey, P., Snyder, G. F., Nelson, D., & Hernquist, L. 2015, MNRAS, 452, 575

Springel, V. 2005, MNRAS, 364, 1105

—. 2010a, MNRAS, 401, 791

—. 2010b, ARA&A, 48, 391

Springel, V., Di Matteo, T., & Hernquist, L. 2005, MNRAS, 361, 776

Springel, V. & Hernquist, L. 2003a, MNRAS, 339, 289

—. 2003b, MNRAS, 339, 312

Springel, V., White, S. D. M., Tormen, G., & Kauffmann, G. 2001, MNRAS, 328, 726

Torrey, P., Vogelsberger, M., Marinacci, F., Pakmor, R., Springel, V., Nelson, D., Naiman, J., Pillepich, A., Genel, S., Weinberger, R., & Hernquist, L. 2017, arXiv e-prints, arXiv:1711.05261

Vogelsberger, M., Genel, S., Sijacki, D., Torrey, P., Springel, V., & Hernquist, L. 2013, MNRAS, 436, 3031

Vogelsberger, M., Genel, S., Springel, V., Torrey, P., Sijacki, D., Xu, D., Snyder, G., Bird, S., Nelson, D., & Hernquist, L. 2014a, Nature, 509, 177

Vogelsberger, M., Genel, S., Springel, V., Torrey, P., Sijacki, D., Xu, D., Snyder, G., Nelson, D., & Hernquist, L. 2014b, MNRAS, 444, 1518

Weinberger, R., Springel, V., Hernquist, L., Pillepich, A., Marinacci, F., Pakmor, R., Nelson, D., Genel, S., Vogelsberger, M., Naiman, J., & Torrey, P. 2017, MNRAS, 465, 3291

Weinberger, R., Springel, V., Pakmor, R., Nelson, D., Genel, S., Pillepich, A., Vogelsberger, M., Marinacci, F., Naiman, J., Torrey, P., & Hernquist, L. 2018, MNRAS, 479, 4056

Xu, G. 1995, The Astrophysical Journal Supplement Series, 98, 355

Yang, X., Mo, H. J., van den Bosch, F. C., & Jing, Y. P. 2005, MNRAS, 356, 1293

Yang, X., Mo, H. J., van den Bosch, F. C., Pasquali, A., Li, C., & Barden, M. 2007, ApJ, 671, 153

Chapter 3

Inflow Mechanisms in Idealized Simulations of Galaxy Collisions

3.1 Preamble

This chapter contains the figures and text of my paper which was published in the Monthly Notices of the Royal Astronomical Society, entitled Go with the Flow: Understanding Inflow Mechanisms in Galaxy Collisions. The article can be found at DOI: `10.1093/mnras/sty1605`

3.2 Abstract

Dynamical interactions between colliding spiral galaxies strongly affect the state and distribution of their interstellar gas. Observations indicate that interactions funnel gas toward the nuclei, fueling bursts of star formation and nuclear activity. To date, most numerical simulations of galaxy mergers have assumed that the gaseous and stellar disks initially have the same distribution and size. However, observations of isolated disk galaxies show that this is seldom the case; in fact, most spirals have as much or more gas beyond their optical radii as they do within. Can gas in such extended disks be efficiently transported to the nuclei during interactions?

To address this question, we examine the effect of various parameters on the transport of gas to the nuclei of interacting galaxies. In addition to the relative radii of the gaseous and stellar disks, these parameters include the pericentric separation, disk orientation, fractional gas mass, presence of a bulge, treatment of gas thermodynamics, and the spatial resolution of the numerical simulation. We found that gas accumulates in

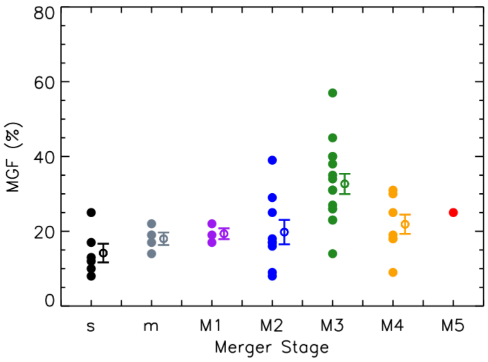

Figure 3.1 Reproduced from Larson et al. (2016). Molecular gas fraction, $M_{H_2}/(M_* + M_{H_2})$, as a function of merger stage: single galaxies (s), minor mergers (m), and major mergers (M1−M5). At each stage, the mean molecular gas fraction and corresponding uncertainties are shown as filled circles and empty circles with error bars, respectively. The increase in molecular gas content between M1 and M3 may be a direct result of inflows.

most of our simulated nuclei, but the efficiency of inflow is largely dependent upon the encounter geometry. Dissipation alone is not enough to produce inflows; an efficient mechanism for extracting angular momentum from the gas is necessary. Several different mechanisms are seen in these experiments. Aside from mode-driven inflows (such as, but not limited to, bars) and ram-pressure sweeping, both of which have been previously described and well studied, we supply the first quantitative study of an often-seen process: the formation of massive gas clumps in Jeans-unstable tidal shocks, and their subsequent delivery to the nuclei via dynamical friction.

3.3 Introduction

When two galaxies collide, the luminous matter responds to the merging gravitational potentials, which are largely generated by the invisible dark matter haloes. Tidal effects manifest in “bridges” – luminous matter bridging the two galaxies – and “tails” – luminous matter trailing behind one or both of the colliding galaxies. Individual stars within each galaxy have a negligible chance of colliding. However, the galaxies’ gas disks are strongly affected by one another; the interaction may trigger galaxy-wide or nuclear bursts of star formation (e.g., Alonso-Herrero et al. 2000; Barnes 2004; Evans et al. 2008; Chien & Barnes 2010) or accretion on to a central supermassive black hole (e.g., Kormendy & Gebhardt 2001; Springel et al. 2005a; Hopkins & Quataert 2010; Gaspari et al. 2013; Rich et al. 2015).

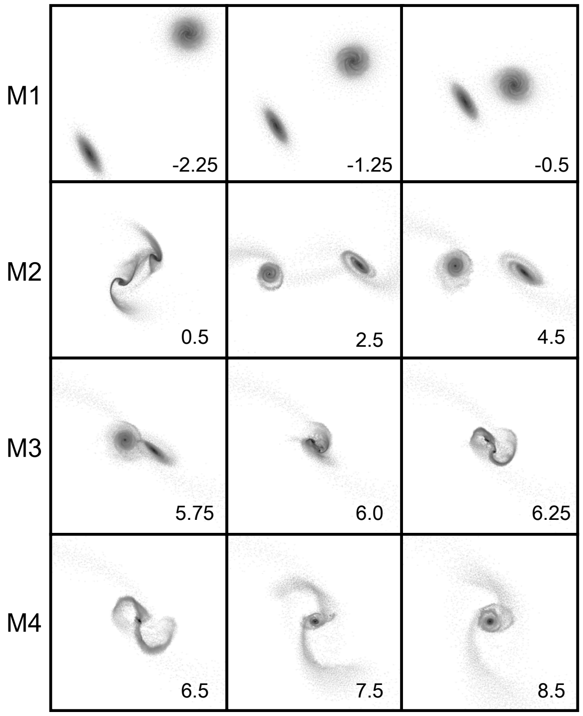

Figure 3.2 Simulation snapshots showing only the gas particles, organized in the merger stage sequence defined by Larson et al. (2016) for M1 through M4. This is encounter B1 (see §3.4.2 for details). Each snapshot is labelled with the time relative to pericenter (in simulation units; see §3.4.1). M1: Galaxies are well separated and on their initial approach. M2: Tidal features (bridges and tails) are clearly visible, and prior to second passage. M3: Two individual nuclei are visible in highly disturbed overlapping disks. The tidal tails are still well defined. M4: The two nuclei have now coalesced, but the tidal tails are still visible. For full animations of the encounters presented here, please refer to: `kelblu.weebly.com/animations.html`

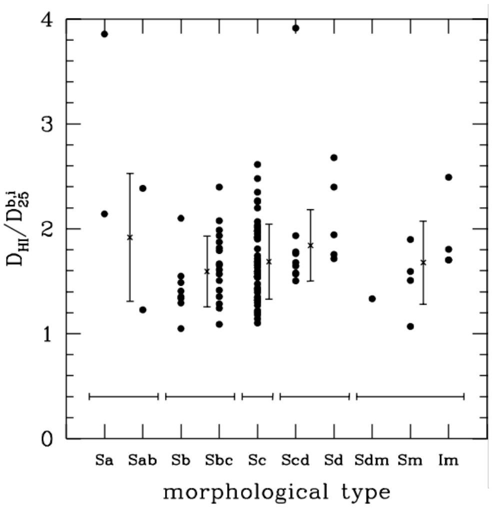

Figure 3.3 After Broeils & Rhee (1997), Figure 3a. This figure shows the ratio of D_{HI} to $D_{25}^{b,i}$, the HI and optical diameters, respectively, as a function of morphology type. In this work, the HI diameter is defined as the point at which the surface density of gas reaches 1 $M_\odot pc^{-2}$, and the optical diameter is taken as the isophote at 25 mag arcsec^2. Within each morphology group, the average is represented as an x, with its corresponding 1σ dispersion. It is clear that the HI disk is typically larger than the stellar disk.

An important tool for probing these changes is the molecular gas: the material from which stars form. Larson et al. (2016) devised a merger stage classification scheme that included non-interacting single galaxies (s), minor mergers (m), and major mergers, ranging from before first pericentric passage through final coalescence and post-merger remnant (M1−M5; see Figures 3.1 and 3.2). They also derived the molecular gas mass fraction (MGF) as a function of merger classification stage, and found that there appears to be a significant increase in the MGF during M3−M4, as seen in Figure 3.1. Interestingly, the increase in molecular gas content between M1 and M3 corresponds to an increase in the mean IR luminosity. Larson et al. (2016) posit that this increase is a direct result of inflows: atomic hydrogen from the outskirts of the galaxy is swept into the central regions and converted to H_2, which fuels a burst of star formation, and naturally results in an increase of the IR luminosity.

One assumption often made by previous simulations is that the stellar and gaseous disks are initially similar in size. However, using 21cm line observations of about 100 galaxies, Broeils & Rhee (1997) showed that the HI disks of spiral galaxies are always equal to or larger than that of the stellar disks (Figure 3.3). They found that on average there is just as much gas outside the stellar disk as there is inside.

This work was motivated by two key questions:

1. Can the gas in extended gas disks be efficiently transported into the nuclei during interactions?

2. How does the merger-driven inflow mechanism depend on the galaxy structure?

We vary the relative sizes of the gaseous and stellar disks to understand how this parameter affects the nuclear gas fraction. To maintain consistency with observations, we will alter the size of the gas disk within the range of Broeils & Rhee (1997) results (that is, $\alpha_\star/\alpha_g = 1 - 2$, where $\alpha_\star$ and α_g are the inverse scale length of the stellar or gas disks, respectively). Given that the most drastic changes to the state of the gas appear to occur between M2 and M4 (Figure 3.1), we will focus only on the time between first and second pericentric passage.

3.4 Methods

In this study, we use N-body/smoothed particle hydrodynamics (SPH) simulations similar to those described in e.g., Barnes (2004). Two identical galaxies are set on initially Keplerian, parabolic ($e = 1$) orbits. As the galaxies approach one another, their dark matter haloes will undergo gravitational friction, causing their orbits to decay, as seen in Figures 3.2 and 3.4. The two galaxies gradually coalesce, eventually forming a single galaxy.

SPH codes model fluids using smoothed kernels, defined by a kernel smoothing radius, h. This radius is adjusted to contain a fixed number of 40 gas particles, which collectively define the kernel's hydrodynamic properties. This methodology allows for an adaptive resolution; the kernels will be smallest where the fluid density is highest. For a characteristic density of about $0.015 M_\odot pc^{-3}$, $h \simeq 120pc$. The smoothing length will scale as $\rho^{-1/3}$, so this value will naturally change depending on disk substructure. For more details on the SPH code, see Appendix A. Energy is conserved to within 1% between first and second pericenter, at which point it fails due to the high densities reached when star formation is not included.

It is important to note that this work does not include the effects of star formation, winds, supernovae or feedback due to an active galactic nucleus. The purpose of this study was to examine the simplest scenario possible, in which only gravitational dynamics and hydrodynamics are considered. To that end, we assume an isothermal equation of state (see §3.4.1 for more details). A good deal of how we currently think we understand fueling comes from decades-old calculations using isothermal gas (e.g., Hernquist & Katz 1989; Barnes & Hernquist 1991). It is thus appropriate to revisit this assumption, but with more accurate galaxy models and better resolution.

This work makes several other assumptions consistent with other studies of idealized simulations. We use a perfectly spherical NFW halo that is truncated at a certain radius, an exponential stellar disk with constant scale height, and a pair of identical galaxies, each of which is initially in near perfect equilibrium. We are exploring the simplest scenario in which only gravitational dynamics and a simplified version of hydrodynamics are considered. In future work, we will assess the validity of the aforementioned assumptions within the context of what is "observed" in state-of-the-art cosmological simulations, such as IllustrisTNG (Marinacci et al. 2018; Naiman et al. 2018; Nelson et al. 2018; Pillepich et al. 2018; Springel et al. 2018). In such simulations, we would anticipate the stellar disk to be smaller than the gas disk, as stars are formed from the gas disk based on a density criterion. It is thus important to understand how the relative sizes of stellar and gas disks plays a role in the inflow mechanics of idealized calculations, before we investigate similar questions in much more complex systems.

3.4.1 Galaxy Models

In these models, each galaxy is constructed from four discrete components: a central bulge, a stellar disk, a gas disk, and a dark matter halo. We usually assume a baryon fraction, $(\mathrm{M}_{\mathrm{bulge,b}} + \mathrm{M}_{\mathrm{gas,g}} + \mathrm{M}_{\mathrm{stars},\star})/\mathrm{M}_{\mathrm{total}}$, of 10%, consistent with current predictions of ΛCDM (e.g., Planck Collaboration et al. 2014). A full account of the parameters used in our galaxy models is given in Table 3.1. We typically assume a gas mass fraction of 25%, although two cases adopt 12.5% gas mass (see Table 3.2). Most of our galaxy models are derived from the suite described by Barnes (2016). For comparison with earlier simulations of galaxy encounters, like those of Barnes & Hernquist (1991), we ran a few simulations with a baryon fraction of 20%.

The components of each model are:

1. **a bulge**

   The mass density of the galaxy bulge is modeled according to Jaffe (1983),

   $$\rho(r) = \frac{a_b M_b}{4\pi r^2 (a_b + r)^2} \tag{3.1}$$

   where M_b is the total bulge mass and a_b is the scale radius of the bulge.

   The Jaffe model is a good representation of a spherical galaxy, and thus serves well to model the galactic bulge. The bulge contains 25% of the baryons (that is, $\mathrm{M_b}/(\mathrm{M_b} + \mathrm{M_g} + \mathrm{M}_\star) = 0.25$), but is compact with respect to the stellar disk ($a_{\mathrm{b}}\alpha_\star \approx 0.5$).

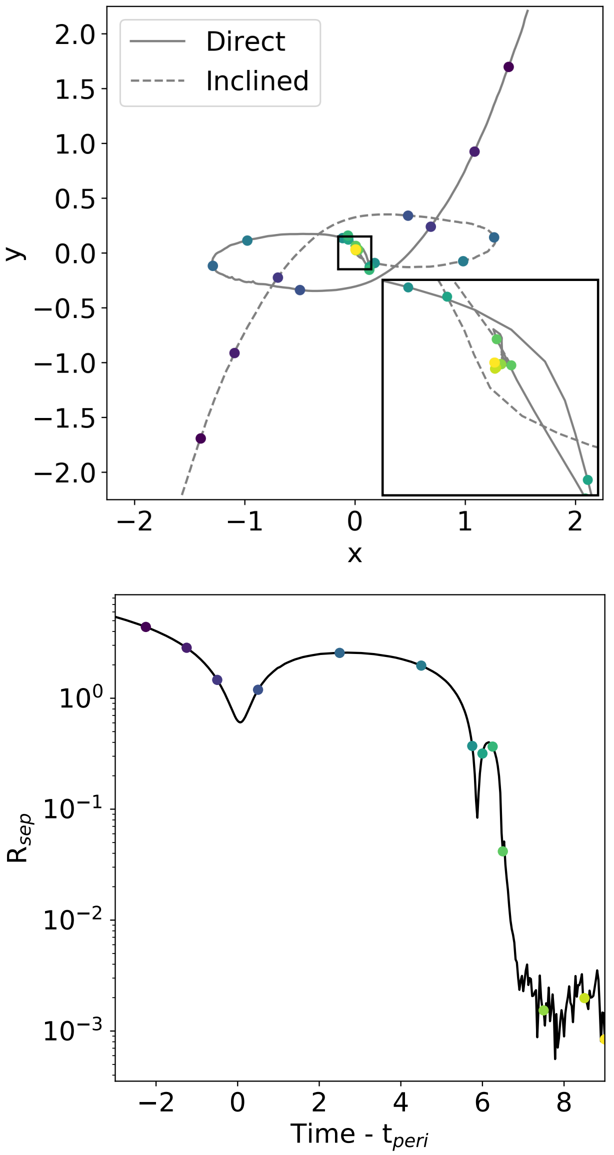

Figure 3.4 *Top:* The trajectories of the interacting galaxies in a single encounter simulation. The inset of the top panel shows the details of post-second pericentric passage. Colors indicate a time sequence similar to that of Figure 3.2. *Bottom:* The magnitude of the separation between the two galaxies in the encounter shown in the top panel.

ID	$\alpha_\star/\alpha_g$	**Bulge**			**Disk**						**Halo**			ϵ
					Gas			Stars						
		M_b	a_b	N_b	M_g	α_g	N_g	$M_\star$	$\alpha_\star$	$N_\star$	M_h	a_h	N_h	
A-D	[1.0, 1.25, 1.6, 2.0]	0.0625	0.04	16384	0.046875	[12.0, 9.6, 7.5, 6.0]	49152	0.140625	12.0	36864	2.25	0.25	147456	0.0025
E	1.0	0.0625	0.04	16384	0.046875	12.0	49152	0.140625	12.0	36864	1.0	0.25	65536	0.0075
E'	1.0	0.0625	0.04	16384	0.0234375	12.0	24576	0.1640625	12.0	43008	1.0	0.25	65536	0.0075

Table 3.1 This table provides the specific parameters, in simulations units, used for each of the disks modeled here. $M_{b,g,\star,h}$ are the bulge, gas disk, stellar disk and halo masses, respectively. $a_{b,h}$ are the bulge and halo length scales, while $\alpha_{g,\star}$ are the gas and stellar disk inverse length scales. $N_{b,g,\star,h}$ are the number of particles used for each component of the model. The smoothing length, ϵ, is also given. Note that the gas disk size increases with $\alpha_\star/\alpha_g$.

2. **a single-component exponential/isothermal stellar disk**

   The stellar disk has an exponential density distribution,

$$\rho(R, z) = \rho_o \text{sech}^2(z/z_o)\text{e}^{-R\alpha_\star} \tag{3.2}$$

   where, Σ_o is the central surface density, R is the polar radial coordinate, and $\alpha_\star$ is the inverse scale length of the stellar component of the disk. The vertical distribution of the stellar disk is approximated as an isothermal sheet, with constant scale heigh z_o.

3. **a single-component exponential gas disk**

   The gas is distributed with a similar density distribution as the stellar disk, as shown in Eqn. 2, but with a different scale length, α_g. The gas abides by an isothermal (T $\approx 2 \times 10^4$ K) equation of state. This temperature is chosen to allow for non-thermal pressure sources (e.g., magnetic fields) (e.g., Barnes 2002). We assume also that the gas disk is thinner than the stellar disk, and solve the equations of hydrostatic equilibrium to derive its vertical structure.

4. **a dark matter halo**

   The dark matter halo is a Navarro et al. (1996) model,

$$\rho(r) = \frac{a_h^3 \rho_o}{r(a_h + r)^2} \tag{3.3}$$

   where a_h is the scale radius of the halo and ρ_o is a constant that depends on the halo parameters. This model has $\rho \propto r^{-1}$ as $r \to 0$ and $\rho \propto r^{-3}$ as r tends to large radii. The halo tapers off exponentially at the virial radius (Springel & White 1999).

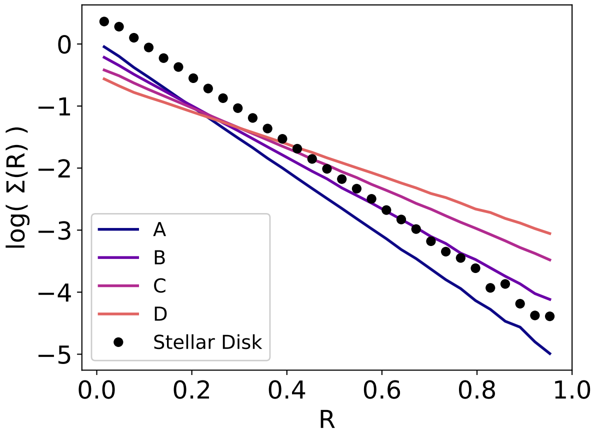

Figure 3.5 The initial gas disk surface mass density distributions for each model described in Tables 3.1 and 3.2. Also shown is the stellar disk surface mass density (black dots) for comparison.

Simulation Units

All simulated quantities quoted in this study are in units where the gravitational constant, $G = 1$. That is, we set

$$G = 6.67 \times 10^{-11} kg^{-1} m^3 s^{-2} = 1 \mathcal{M}^{-1} \mathcal{L}^3 \mathcal{T}^{-2} \tag{3.4}$$

to constrain simulation units of mass, length and time: $\mathcal{M}, \mathcal{L}$ and $\mathcal{T}$. Another condition, based on the specific internal energy of the gas, fixes the velocity scale

$$u_{int} = \frac{3}{2}\left(\frac{k_B T}{\mu m_H}\right) \simeq 2.0 \times 10^8 m^2 s^{-2} = 0.014 \mathcal{L}^2 \mathcal{T}^{-2} \tag{3.5}$$

where k_B is the Boltzmann constant, μ is the molecular mass, T is the temperature of the interstellar medium (ISM), and 0.014 is the value for u_{int} chosen in simulation units. Note that the constant $\frac{3}{2}$ in this equation is appropriate for a monatomic gas. We also assume that the ISM is comprised of 75% H and 25% He by mass (for this composition, and assuming a totally unionized ISM, $\mu \simeq 1.23$). If we choose a scale for the length, then the time unit follows from Equation 3.5. Using those two values, we can easily derive a mass unit from Equation 3.4. For example, if we take $\mathcal{L} = 30$ kpc, then $\mathcal{T} = 2.5 \times 10^8$ yrs, and $\mathcal{M} = 1 \times 10^{11}$ $M_\odot$.

Galaxy Mass Models

Each galaxy mass model is assigned a letter (A through E). The first four models differ only in the relative size of their gas and stellar disks: the stellar and gas disks of model A are the same size, while the gas disk scale length of the D model is twice that of its stellar disk. Models B and C lie within this range. This is illustrated in Figure 3.5, which shows the initial gas surface density distributions for each of the galaxy models. The ratio of the gas disk size to the stellar disk size (i.e., $\alpha_\star/\alpha_g$) ranges from 1.0 to 2.0.

After completing several encounters using mass models A-D, we found that none of our simulations formed bars. In an attempt to reproduce bars as seen in earlier simulations (e.g., Barnes & Hernquist 1991; Springel et al. 2005b; Hayward et al. 2014), we ran two "legacy models." These E models are similar to those of Barnes & Hernquist (1991), which were known to form bars. The prime (i.e., E') in Table 3.2 indicates a lower gas fraction.

We used Plummer smoothing when computing the gravitational potential (e.g., Aarseth 1963; Barnes 2012). That is, the canonical r^{-1} potential becomes $(r^2 + \epsilon^2)^{-1/2}$, where ϵ is the smoothing parameter. Typically, the gravitational smoothing parameter is $\epsilon = 0.0025$ (or, roughly 75 pc). The legacy models use a larger smoothing length: $\epsilon = 0.0075$ (or, roughly 225 pc). These values are the same for all particle types, and are also listed in Table 3.1. The legacy models also contain a less massive halo.

As a test of our galaxy models, we allowed four isolated galaxies (one for each of the original mass models, A-D) to evolve for the entire encounter time. We measured the amount of gas within a defined nuclear radius (details in §3.5) and found that little material flows into the nucleus. The inflow rate is nearly constant, with about 0.15% to 0.375% of the gas reaching the centre per unit of simulation time (see the bottom panel of Figure 3.7 for the inflow of both the A and D isolated control galaxies). This slow inflow is due to weak torques provided by transient spiral patterns and artificial viscosity. We see no clump formation in these control models, which indicates that the clumps found in our encounters are indeed a byproduct of galaxy interactions.

3.4.2 Encounter Models

The encounters in this work are described in Table 3.2. To better understand how the ratio of gaseous and stellar disk scales affect dynamical inflows, we tested the effects of several other parameters. These include (1) the disk orientation, (2) the pericentric separation, (3) the fractional gas mass, and (4) the spatial resolution of the simulation.

In Table 3.2, the ID letters from Table 3.1 are given modifiers to describe the interaction in more detail. The numbers tell us about the pericentric passage: wide (1; $r_p = 0.5$), intermediate (2; $r_p = 0.2$ or 3; $r_p = 0.25$) or close (4; $r_p = 0.125$).

Encounter	r$_p$	$\alpha_\star/\alpha_g$	$i_1°$	$i_2°$	f_{gas}
A1	0.5	1.0	0	72	0.25
A1$_r$	"	1.0	180	109	"
B1	"	1.25	0	72	"
C1	"	1.6	0	72	"
D1	"	2.0	0	72	"
D1$_r$	"	2.0	180	109	"
A2	0.25	1.0	0	72	0.25
D2	"	2.0	0	72	"
E3	0.2	1.0	0	72	0.25
E3'	"	1.0	0	72	0.125
A4	0.125	1.0	0	72	0.25
D4	"	2.0	0	72	"

Table 3.2 The above table summarizes the encounters studied. Here, r$_p$ is the pericentric separation, $i_{1,2}$ are the two galaxies' inclinations with respect to the orbital plane in degrees, and f_{gas} is the fractional amount of gas defined as f$_{gas}$ = $M_{gas}/(M_\star + M_{gas})$.

Previous studies, from Toomre & Toomre (1972) on, have shown that prograde encounters of two galaxies in the same orbital plane elicit the strongest response from the disks, forming pronounced tidal features. To the extent that the dynamics of the two disks are largely decoupled at early times, we can explore the effects due to collision geometry on the outcome of the interaction by studying an encounter with one in-plane galaxy (inclination, $i = 0°$) and an inclined galaxy (in this case, $i = 72°$). Similarly, we can do the same for retrograde disks ($i = 180°$) and inclined retrograde disks ($i = 109°$). The subscript r denotes a retrograde encounter.

3.5 Analysis

When two galaxies collide, their haloes spiral toward one another and eventually merge to form a single galaxy. Tidal and hydrodynamic effects disrupt the stellar and gas disks, producing torques which drive material into the galaxies' nuclei. In most of the encounters listed in Table 3.2, we observe substantial amounts of gas flowing into the centre of each galaxy between first and second pericentric passage. In the following sections, we will look at the inflow of material over time in select cases, and then discuss the different mechanisms driving that inflow.

In order to accurately track the inflows, we must be careful of how we define the nucleus of a galaxy. Here, we chose the inner $\alpha_\star R = 0.15$, or roughly the central kiloparsec in diameter, which is consistent with observational definitions (e.g., Querejeta et al. 2016). Visual inspection showed that this choice was reasonable throughout the interaction history for all collision realizations.

3.5.1 Inflow

Figure 3.6 shows the fractional amount of gas within the nucleus as a function of time for the direct disk (top) and inclined disk (bottom) of the encounter models A1, A4, D1, and D4. The times shown are well before first pericenter until just before second pericenter. These encounters are selected to compare the gas inflows for extreme values of the $\alpha_\star/\alpha_g$ ratio and pericentric separation. Sharp increases in nuclear gas fraction reflect the arrival of massive clumps of material.

Inflow is fastest in the $\alpha_\star/\alpha_g = 1.0$ disks, with large amounts of gas accumulating regardless of pericentric distance or disk inclination. Hereafter we consider encounter D1 as the "canonical" encounter, because observations (e.g., Figure 3.3) indicate that gas disks are on average nearly twice as extended as stellar disks. The D1 encounter produces somewhat more modest inflow in both the direct and inclined disks, but much later: several time units after pericentric passage. The direct and inclined disks of B1 and C1 behave as one might expect from the bounds created by A1 and D1, showing a clear correlation of nuclear inflow with decreasing size gas disk. Remarkably, there is virtually no inflow in the direct D4 encounter, despite the violent tidal interaction of the galaxies.

In a similar vein, the inclined retrograde disks ($i = 109°$) also show almost no inflow (Figure 3.7). The gradual inflows seen in the inclined retrograde disks are likely due to the same process driving inflow in the isolated galaxies: torques associated with the spiral pattern slowly drive material inward. The bottom panel of Figure 3.7 compares the relevant isolated disks (also our control sample) to the inflow experienced by the inclined retrograde disks. These gradual increases in the nuclear gas fraction seen in Figure 3.7 are visible largely because the vertical scale is significantly smaller compared to Figures 3.6 and 3.8; modest upward trending plateaus can also be seen in other figures (e.g., in the bottom panel of Figure 3.6, for $t - t_{peri}$ between 3 and 5).

When inflow does occur, however, the retrograde passages behave very differently than the prograde encounters. Here, extended gas disks are *more* effective at producing inflows (see the top panel of Figure 3.7). The retrograde disks appear also to react to the encounter faster, likely due to the strong hydrodynamic interaction that occurs near pericenter (as seen in e.g., Capelo & Dotti 2017).

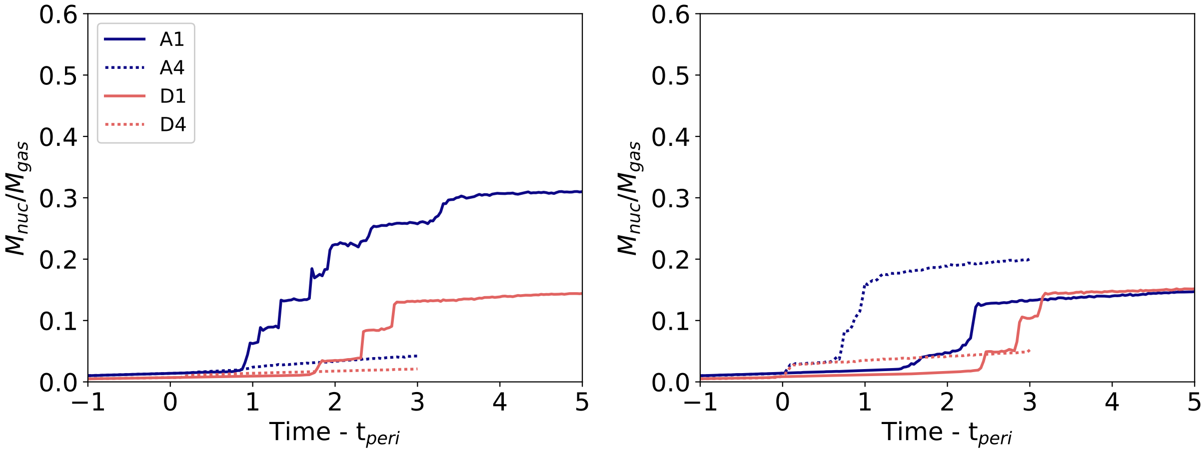

Figure 3.6 The fractional amount of gas in the nuclear region is plotted as a function of time for the A1, A4, D1 and D4 models, both the direct (top) and inclined (bottom) disks.

Comparing the top and bottom panels of Figures 3.6 and 3.7, we can easily note the complex relationship between inflow and orbital geometry (e.g., inclination and pericentric separation). Closer passages reduce inflow in the direct disk and increase inflow in the inclined disks. This trend is generally followed by intermediate pericentric passages. A strong tidal interaction does not necessarily imply a large inflow; hydrodynamic forces counter the tidal reaction of an interaction with varying success, depending on the properties of the encounter.

Figure 3.8 shows the nuclear inflow for the legacy models (recall, these models are those which have a larger smoothing length than the models previously discussed). These produce prompt and substantial inflows that are nearly 2-3 times larger than the modern models. Comparing the inflow of E3’ to that of D1 (shown in grey), we note that the curve is much more smooth, indicating that clumps are not driving inflow in this case. These inflows are remarkably sensitive to gas content; the encounter with 12.5% gas drives a larger absolute amount of gas inward than does its gas-rich counterpart. The bottom panel of Figure 3.8 shows that the inclined disk of the 12.5% gas legacy model is also more effective at producing inflow, while the inflow in the 25% gas legacy model does not appear to be as sensitive to geometry.

As the cases described above make clear, the accumulated nuclear gas has a complex relationship with encounter parameters such as inclination angle and pericentric separation. Toomre & Toomre (1972) showed that the tidal response is strongest in a direct prograde disk. We might naively assume that inflow is strongest in the encounters with the strongest tidal response (e.g., direct and close encounters; Barnes & Hernquist 1996; Mihos & Hernquist 1996). We have shown here that this is not necessarily the case. In fact, the rate and

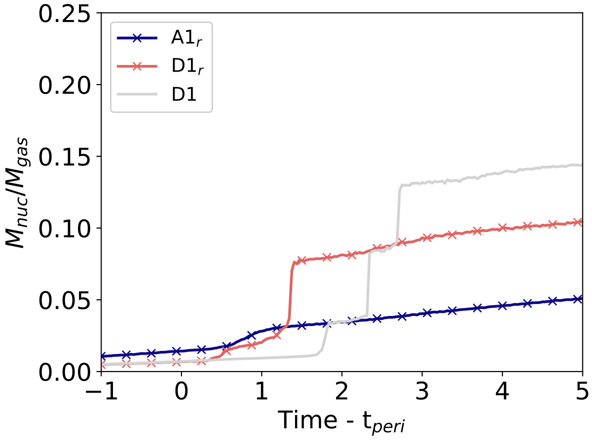

Figure 3.7 Here, the nuclear inflow is shown for the A1$_r$, and D1$_r$ models. The retrograde disk is shown on the top, while the retrograde inclined disk is shown in the bottom panel. The D1 encounter model is also shown for scale to Figure 3.6. Also shown in the bottom panel is the inflow for the A and D isolated galaxies. The inflow seen in the inclined retrograde passages is very nearly what one might expect from an isolated galaxy.

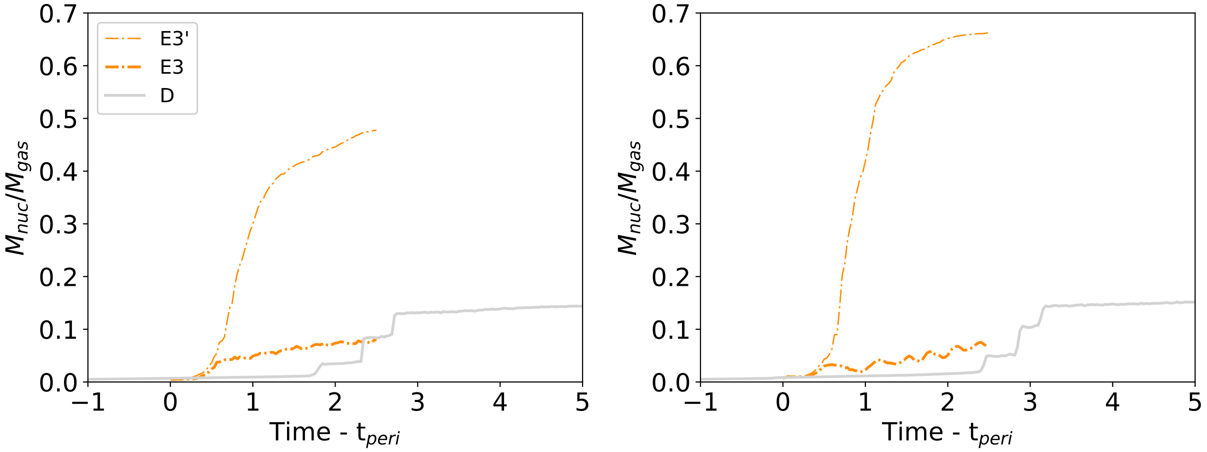

Figure 3.8 Here, the nuclear inflow is shown for the legacy E3 and E3’ models. The top panel shows the inflow for the direct disk, and the bottom panel shows the same for the inclined disk. The D1 encounter model is also shown for scale to Figure 3.6.

magnitude of the inflow exhibits a complex and somewhat counter-intuitive dependence the circumstances of an encounter. This trend is also seen in the studies of e.g., Renaud et al. (2014) and Di Matteo et al. (2007). This suggests that there must be a competing force which compensates for a weak tidal response, thereby drawing more material to the nucleus. Below we will show that the hydrodynamic force plays a key role.

3.5.2 Inflow Mechanisms

The inflows just described are driven by three different mechanisms: clump-driven inflow, ram-pressure sweeping, and mode-driven inflow. Figure 3.9 illustrates all three mechanisms, with clump-driven, ram pressure, and mode-driven inflow on the left, middle and right panels, respectively.

In order for inflow to occur, the gas must lose angular momentum via torques which we can calculate directly from the particle configuration. To study these torques, we defined a Lagrangian volume of particles (as in Barnes & Hernquist (1991)) which lie within the nucleus ($R \leq 0.0125$, shown in purple in Figure 3.9) at the time, prior to second pericenter, when the inflow curves end in Figures 3.6 - 3.8. This ensures that we have allowed sufficient time, after the first interaction, to maximize the mass of gas in the nucleus prior to second encounter.

Clump-Driven Inflow

Figure 3.10 shows our key example: the torques on the direct disk of encounter D1. Here, and in subsequent plots, torques have been normalized by dividing values by the Lagrangian volume's initial angular momentum, L_0, implying that the vertical units on these plots are inverse time. The total torque, $\tau(t)$, calculated directly from the net gravitational and hydrodynamic forces acting on the Lagrangian volume, is shown in red. For comparison, we also plot the numerical derivative of the volume's angular momentum, $\mathrm{d}L/\mathrm{d}t$ (blue dots); residuals between $\tau(t)$ and $\mathrm{d}L/\mathrm{d}t$ are shown in the bottom panel. On the whole, the residuals are small and fluctuate around zero; this gives us confidence that our techniques for centering and calculating torque are correct (see Appendix A for details).

In addition, Figure 3.10 also shows partial torques due to the direct galaxy's gravity (solid black), the inclined galaxy's gravity (dashed black), the direct galaxy's stellar disk (grey), and the net hydrodynamic force (purple). This shows how various components conspire to drive gas inward. Near first encounter, angular momentum is lost to the companion by gravitational torques. In contrast, hydrodynamic forces at

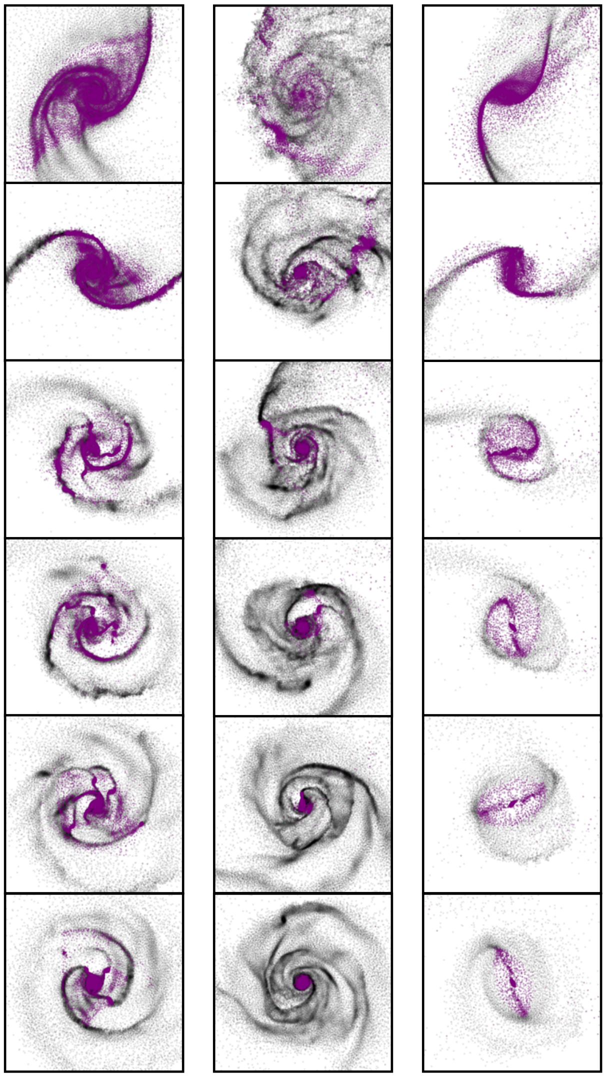

Figure 3.9 *Left:* Clump-induced inflow (encounter A1) gradually delivers material to the nucleus. *Middle:* Ram-pressure sweeping (encounter $D1_r$) dominates only in retrograde disks. *Right:* Mode-driven inflow (encounter E3') rapidly drives gaseous material into the galaxy's centre. Plotted in purple are gas particles in the Lagrangian volume. The remaining gas is displayed in greyscale. All snapshots are 0.6x0.6 length units in size and represent evenly spaced time intervals between $t - t_{peri} = 0.25 - 1.5$. Note that the number of purple particles plotted remains the same in each snapshot of a given encounter. The particles within this Lagrangian volume become much more centrally concentrated as time goes on so they become visually less dominant.

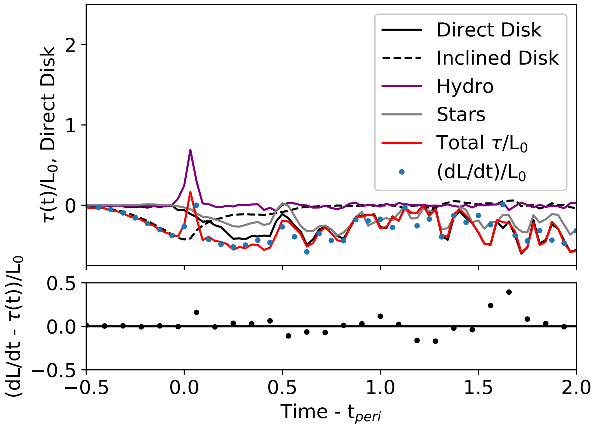

Figure 3.10 Measured and estimated torques on the direct disk of our canonical encounter: D1. This shows the total torque in red, which is made up of components due to the direct galaxy (black), the inclined galaxy (black dashed), and the hydrodynamic force (purple). Residuals, or the difference between the measured total torque (i.e., including all gravitational and hydrodynamic forces) and the time derivative of the angular momentum, are displayed immediately below the corresponding torque plot.

first pericenter briefly increase the angular momentum. By about 0.5 time units after pericenter, much of the material in the Lagrangian volume has fragmented into clumps which are losing angular momentum to their host stellar disk (and also the bulge and halo, as they have some nontrivial contributions to the overall torque on the gas) via gravitational interactions. Comparing back to Figure 3.6, we saw that there is almost no increase in nuclear material between first pericenter and $t - t_{peri} = 1.5$, which is when the first clump reaches the centre.

In §3.5.1 we noted that the direct disk in encounter A1 produces nearly twice as much inflow as the corresponding disk in encounter D1. Figure 3.11 shows the torques acting on the Lagrangian volume for the A1 encounter, and it is clear why the resulting inflow is so much larger. The initial hydrodynamic torque, which opposes inflow, is significantly weaker, and the magnitude of the direct disk's self-gravitational torque is larger in comparison. As in the example above, the total torque in the A1 direct disk appears to be dominated by stellar material early on. However, there are other sources of torque in operation, as the stellar disk accounts for only about half of the net torque measured at later times.

Figure 3.12 provides a close-up of clump formation following a strong tidal interaction. Shocks form just after first pericentric passage, creating filaments of gaseous material which become Jeans-unstable. The resulting clumps orbit the centre of their host galaxy, and eventually spiral to the centre as a result of gravitational torques. Clumps have been seen before in simulations (e.g., Li et al. 2004, 2005), but were observed in both isolated (control) and merging disks, indicating that those disks were less stable than the

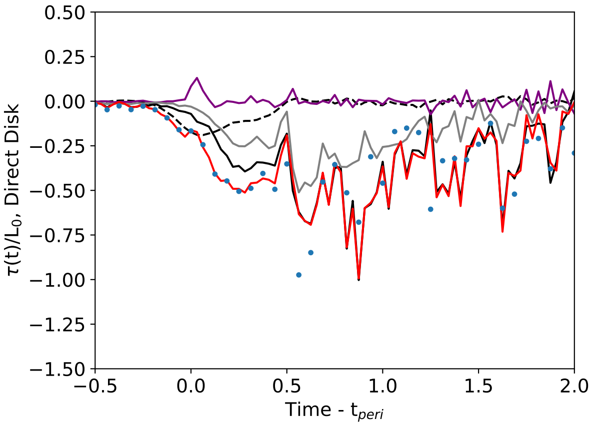

Figure 3.11 Here, we show the torques experienced by the Lagrangian volume in the direct galaxy of the A1 encounter.

ones presented here. In this earlier work, the clumps were considered the progenitors of globular clusters. The clumps seen in our simulations are on average about 0.001 mass units, 0.0033 length units in radius and have lifetimes around 0.1 time units, or in physical units, $m_c \approx 10^8 \mathrm{M}_\odot$, $r_c \approx 100$pc, and $t_c \approx 25$ Myr, roughly consistent with potential progenitors of globular clusters (e.g., Elmegreen et al. 2005).

Figures 3.10 and 3.11 show explicitly that the hydrodynamic force is *not* responsible for torquing material inward. Instead, the stellar distribution is responding to the gas clumps. In Figure 3.12, it is clear to see that there is a wake of trailing stellar material behind the prominent gas clumps. Stellar overdensities gravitationally drag the clumps, removing orbital energy and angular momentum, thereby forcing them to spiral toward the centre. This is an example of dynamical friction, also discussed briefly in Duc et al. (2004) as a way by which clumps may migrate inward. Figures 3.10 and 3.11 show that the torques measured from the stellar distribution are in fact the cause of the gas migrating toward the centre.

Ram-Pressure Sweeping

A good foil to the A1 encounter is the closer A4 encounter, shown in Figure 3.13. As Figure 3.6 reports, the direct disk of this encounter has relatively little inflow, unlike D1 and A1. The much-closer passage results in a rather strong but very brief hydrodynamic torque, while at later times the gravity of the stellar component becomes the main source of torque. This suppresses inflow because the direct disk gains angular momentum as a result of hydrodynamic forces. Thus, it is undergoing a large ram-pressure effect.

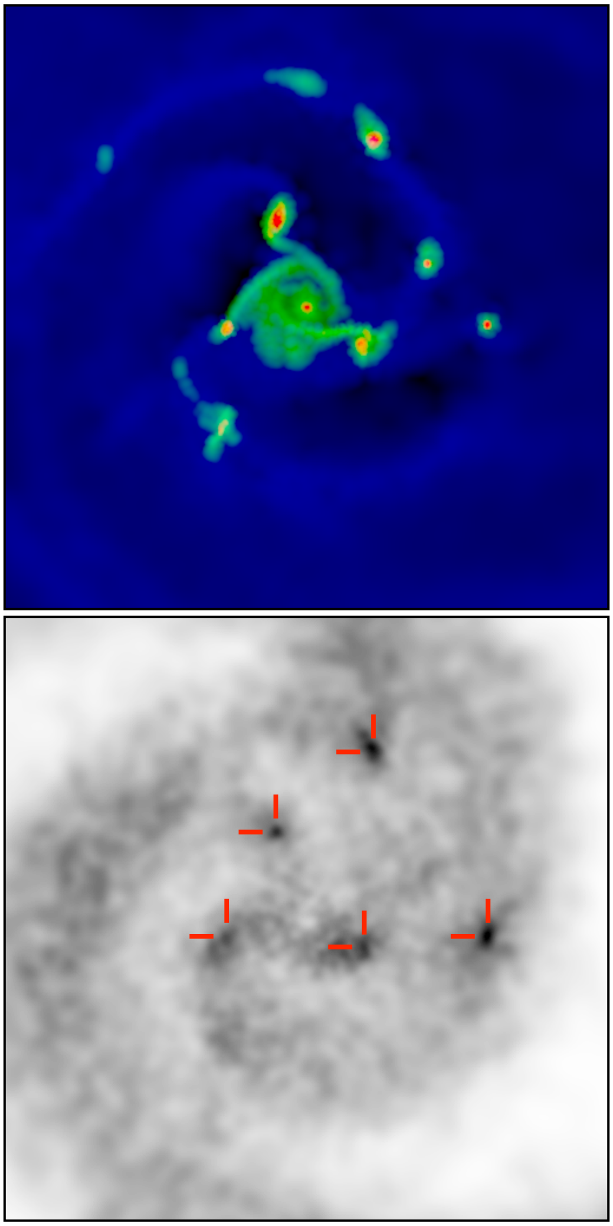

Figure 3.12 A close-up of clump formation, corresponding to $t - t_{peri} = 0.91$, with 0.25x0.25 length units on a side. *Top:* Gas density map to show clump formation at this time. *Bottom:* The stellar distribution, normalized as a function of radius to show density enhancements due to clump formation. Red crosshairs mark the location of the clumps in the gas density. The simulation represented here is fundamentally similar to A1, but with four times as many stellar particles to improve the stellar mass resolution. Note how clumps create localized overdensities in the stellar distribution. This is direct evidence of dynamical friction at work.

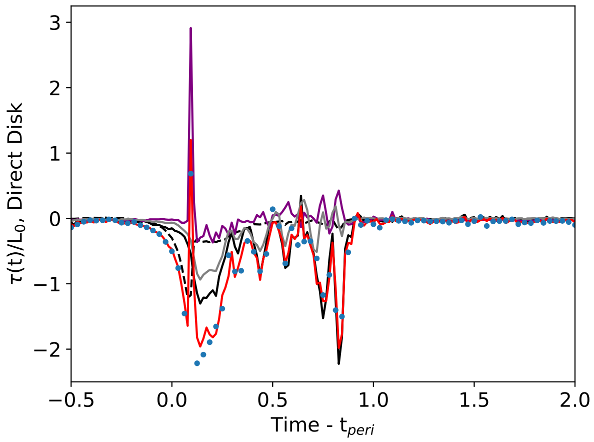

Figure 3.13 Similar to Figure 3.11, but for encounter A4. The line and symbol styles match the legend of Figure 3.10. The evolutionary timescale is compressed since this relatively close encounter merges more rapidly than the other cases described here.

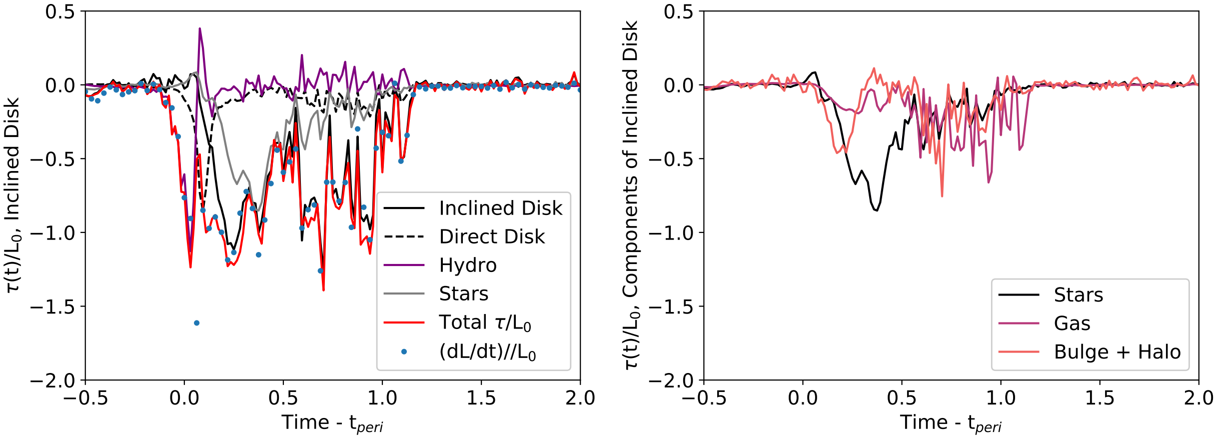

Figure 3.14 This shows the torques on the inclined disk of encounter A4. In addition, the right panel shows the different components of the galaxy: stars, gas (gravitational), bulge and halo. With this, we can pick apart the main source of the torque.

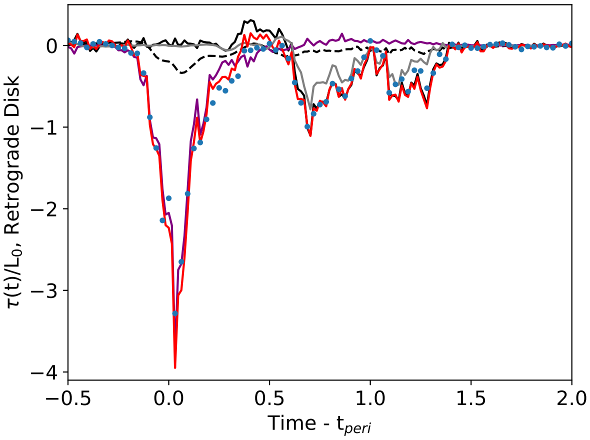

Figure 3.15 Similar to the left panels of Figures 3.11, and 3.13, but for the retrograde galaxy of encounter D1$_r$. The line and symbol styles match the legend of Figure 3.10. Note that the torque due to the hydrodynamic interaction dominates here, whereas in previous examples other components of the galaxy were the main drivers of inflow.

Comparing back once more to Figure 3.6, we found that the inclined disk of encounter A4 experiences nearly three times as much inflow as the direct disk. As Figure 3.14 shows, the inclined A4 disk experiences a very strong hydrodynamic torque, which, in this particular geometry, *subtracts* angular momentum and consequently transports gas inward. The right panel of Figure 3.14 analyses the gravitational torques due to the individual components of the galaxy. We see that the stellar component dominates the torque after first pericenter, and is overtaken by the gaseous component at later times. This plot shows a large contribution due to the bulge and halo components of the galaxy's total torque, which drives more material into the nucleus over a long period of time compared to its direct counterpart. The strong initial hydrodynamic response of the inclined disk produces more clumps, which in turn spiral into the nucleus via dynamical friction, and deliver a larger amount of material than in the direct A4 disk.

This is a good example of how the two disks in a given encounter may have significantly different inflow mechanisms. While the A4 direct disk's inflow was primarily driven by clumps (with a small contribution from ram-pressure sweeping), the A4 inclined disk inflow was almost completely a result of ram-pressure sweeping. However, neither the direct nor the inclined disk produced as much inflow as their counterpart in the widest passage. Studies such as Di Matteo et al. (2007) have shown that the star formation efficiency is anti-correlated with pericentric passage, perhaps due to the negative impact of this ram-pressure effect on inflow production.

Ram-pressure sweeping is also at play in our two retrograde encounters, $A1_r$ and $D1_r$. In the $D1_r$ case, the hydrodynamic torque resulting from the deep retrograde encounter of the two extended gas disks is responsible for over half of the angular momentum loss, as can be seen in Figure 3.15. The geometry of the gas disks enables a strong hydrodynamic interaction, which in turn initiates the encounter-induced inflow. This phenomenon has been noted before, as an alternative route to nuclear fueling (e.g., Capelo & Dotti 2017; Barnes 2002). In the case of $D1_r$, dynamical friction becomes important at late times; the gravitational torques are acting on a rather large gas clump which forms in the immediate aftermath of the encounter.

It is worth noting that hydrodynamic torques often play a supporting role in transporting gas inward in inclined (as in A4) and/or retrograde disks. In inclined prograde encounters (e.g, Figure 3.14), we find hydrodynamic forces initially acting to move gas inward, while at later times, gravitational torques predominate. While these initial torques are not strong enough to drive gas all the way to the nucleus, they transport gas to smaller radii where it can more effectively couple to the stellar disk, creating conditions which then enable gravitational torques to drive gas into the nucleus. Hydrodynamic torques can also work in the opposite sense in direct disks, preventing material from flowing to the centre via a transfer of angular momentum from one disk to the other.

Mode-Driven Inflow

The right panel of Figure 3.9 shows a familiar scenario (e.g., Barnes & Hernquist 1991; Mihos & Hernquist 1996): modes form as a result of the interaction, and rapidly drive inflow to the centre of the host galaxy. Modes are produced by any non-axially symmetric structure. As an example, barred systems produce organized large-scale flows which misalign the stellar and gaseous bars and consequently generate a torque on the gas. The stellar bar acts to slow down the gas bar, which in turn draws gas inwards.

In Figure 3.8, we saw that these mode-driven inflows are rapid and continuous, contrasting with the arrival of clumps seen in Figures 3.6 - 3.7. The legacy models are thus mode-dominated, and induce continuous flow, instead of fragmenting into gas clumps. Figure 3.16 shows the torques on the direct disk of the E3’ encounter. The stellar component dominates the total torque after first pericenter, but prior to that time, the inclined disk significantly torques the direct disk. Figure 3.8 also showed that there is a significant difference in inflow between the direct and inclined galaxies, similar to the reaction of the A4 encounter. This is because the inclined disk does not experience the hydrodyanmic impulse.

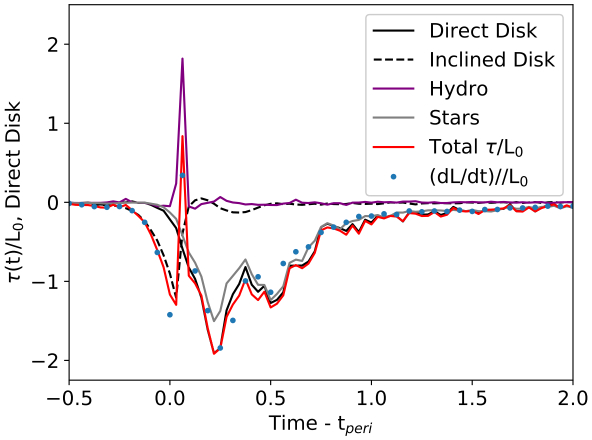

Figure 3.16 Similar to Figures 3.11 and 3.13 direct galaxy of encounter E3'. Bars form as a result of this encounter.

3.6 Discussion

A great deal of the development of our understanding of gas dynamics in the last two decades has been based on isothermal models (e.g., Hernquist & Katz 1989; Barnes & Hernquist 1991). This work has picked up where they left off. It is important to realize, however, that these simulations are limited in multiple ways: resolution effects; the treatment of the ISM equation of state; and the absence of additional subgrid physics including star formation and feedback. In this section, we will address these limitations and provide a deeper context for our simulations.

3.6.1 Previous Descriptions of Clumps

It is important to note that this is not the first time clumps have been observed in simulations. In work such as Di Matteo et al. (2007), the authors see clumps form, and mention that these structures are the cites of off-nuclear star formation. However, the authors do not attempt to quantify these clumps in any way. Clump formation has been studied within the context merger simulations (e.g., Dekel et al. 2009; Teyssier et al. 2010; Bournaud et al. 2011; Renaud et al. 2014), but never to the level of detail as discussed here. For example, Dekel et al. (2009) found that their clumps contain a significant fraction of the gas mass, and convert to stars on roughly the same time scale that they migrate in on, thus building up the bulge. This does imply that the clumps, at least in their simulations, survive the inclusion of star formation and stellar feedback. Renaud et al. (2014) attempted to connect the structure of the interstellar medium to inter-galactic dynamics, and concluded that a clumpy interstellar medium is a byproduct of turbulence. Bournaud et al. (2011) went one step further and included clumps into their initial gas distributions, in an attempt to accurately represent encounters of galaxies at high redshift, which are often observed to be clumpy (e.g., Elmegreen et al. 2005; Ceverino et al. 2010).

3.6.2 Resolution Considerations

Smoothing a gravitational potential serves to weaken that potential. Similarly, altering the number of gas particles included within a single SPH kernel changes the pressure that each particle exerts. Early work, such as Bate & Burkert (1997), stressed the importance of matching these two resolutions when dealing with Jeans fragmentation.

The Jeans length can be written as

$$\lambda_J = c_s\sqrt{\frac{\pi}{G}}\rho^{-1/2} \tag{3.6}$$

where c_s is the sound speed, given by $c_s = \sqrt{(\gamma - 1)u_{int}}$, and ρ is the SPH density. Similarly, the Jeans mass can be given by the expression

$$M_J = \frac{4\pi}{3}\rho\left(\frac{\lambda_J}{2}\right)^3 = \frac{\pi^{5/2}}{6}\frac{c_s^3}{G^{3/2}\rho^{1/2}} \tag{3.7}$$

By equating λ_J to the gravitational smoothing length, ϵ, and M_J to the mass of an SPH smoothing volume, $40M_{SPH}$, we can derive critical densities, $\rho_{\rm crit}$, at which Jeans fragmentation can be resolved. If the $\rho_{\rm crit}$ derived from $\lambda_J = \epsilon$ is smaller than that derived from $M_J = 40M_{SPH}$, then fragmentation will dominate the disk. On the other hand, if the $\rho_{\rm crit}$ derived from M_J is smaller, then fragmentation will be suppressed, resulting in a more (perhaps artificially) smoothed gas distribution. Ultimately, the relative magnitude of the $\rho_{\rm crit}$'s derived from λ_J and M_J depends on the science goal.

Using $\epsilon = 0.0025$, $40M_{SPH} = 3.815 \times 10^{-5}$, $\gamma = 5/3$ (as for a monatomic gas) and $u_{int} = 0.014$, we can derive the critical densities for the majority of our simulations. We find that

$$\rho_{crit,grav} \approx 4690 \qquad \text{and} \qquad \rho_{crit,SPH} \approx 4750 \tag{3.8}$$

The insight to be gained here is that there is a minimum mass and size scale that we can resolve given the fluid element mass and smoothing length chosen. The characteristic scale of clumps derived from these two quantities is likely a lower-limit to the size of clumps produced in our simulations. Thus, clump formation and its eventual migration is likely a generic mechanism, but the characteristic scales are sensitive to the resolution choices we make in the simulations.

Teyssier et al. (2010) posited that large-scale inflows of gas were in fact an artefact of a poorly resolved interstellar medium. More recent work (i.e., Maji et al. 2017) has investigated how star cluster properties differ in SPH codes and meshless codes. They also discuss the limitations of SPH codes, and the importance of considering the resolution when interpreting results.

Inadequate mass resolution in the stellar disk may potentially influence the formation of clumps (e.g., Wetzstein et al. 2007). We have run one version of encounter A1 with four times the number of gas particles, and another version with four times the number of stellar particles, to test the effect of improving both the gas and stellar mass resolutions. Not only do clumps still form in these simulations, but the improved mass resolution of the stellar distribution makes it much easier to identify how the clumps migrate into the centre of the galaxy. Density fluctuations in the stellar distribution trail behind clumps in the gas, implying that the clumps we see are indeed being driven into the nucleus via dynamical friction. This does not necessarily contradict the Wetzstein et al. (2007) work, as they were studying the creation of clumps in tidal tails, which is a much more rarefied environment than the disk of an interacting galaxy.

3.6.3 Missing Subgrid Physics

There has been a significant amount of work recently (e.g., Mihos & Hernquist 1996; Li et al. 2004; Chien & Barnes 2010; Hopkins et al. 2013; Hayward et al. 2014; Li & Bryan 2014b,a; Behrendt et al. 2016; Kim et al. 2017; Mandelker et al. 2017; Oklopčić et al. 2017) on the effects of star formation and feedback on gas disks, both in isolation and in mergers. For example, Hopkins et al. (2013) found that much of the gas in their resolved giant molecular clouds (GMC's) transitioned to stars, leaving a small amount of gas still gravitationally bound to the GMC to spiral in toward the centre. It may very well be that the clumps we see in this work would dissipate as a result of star formation. This could result in off-nuclear star formation, for which there is a wealth of observational evidence (e.g., Hagiwara 2007; Evans et al. 2008; Cortijo-Ferrero et al. 2011). If these clumps do wind up staying bound as star clusters, then they may spiral inward via the same process discussed here to get bulge growth, without having to form stars at the nucleus. Any remaining gas within these clusters could also fuel AGN.

High redshift galaxies are known to be very clumpy, perhaps as a result of violent disk instability (Dekel et al. 2009). Mandelker et al. (2017) looked at high redshift disks in cosmological simulations, with and without feedback from radiation pressure, which serves to reduce the amount of gas available to star formation. They found that this kind of feedback reduces the mass of the clumps by nearly an order of magnitude, and thus reduces their lifetimes significantly. Kim et al. (2017) attempted to locate candidates for globular clusters within the FIRE simulation. They suggest that mergers at high redshift might be the perfect environment for these objects to form.

3.7 Conclusions

In this paper, we have disclosed multiple paths by which gas can arrive at the centre of galaxies as a result of major mergers. We highlight the different mechanisms which drive inflow by exploring the parameter space of encounters. Figure 3.17 summaries the results of our many simulations graphically. Concentric circles show the range of pericentric separations; the inclination angles are indicated by their position on the unit circle; the diameter of each point corresponds to the final nuclear mass of each run; the color of each point corresponds to the mass model indicated. The bottom panel shows a side-view of the top; each layer corresponds to a different $\alpha_\star/\alpha_g$. From this, we can clearly see that there is an intricate relationship between inclination angle, pericentric separation, and resulting nuclear inflow. Further, this relationship is dependent upon mass model, gas fraction and gravitational smoothing. Our results pose important implications for how interactions might affect nuclear activity. Our conclusions are as follows:

1. From the outset, we expected to see bars form and drive material into the nucleus. Our original goal was to find out what happens to the inflow when the stellar bar is much smaller than the gas disk. However, we found that the modal mechanism is not the only way to get nuclear inflows, and may not be the most important way. Shock fronts form just after first pericentric passage, producing filaments of gaseous material which become Jeans-unstable, eventually forming massive, dense clumps. In our simulations, these appear to be the main drivers of material into the central regions of the galaxy and do so via dynamical friction.

2. Simulations such as those in Barnes & Hernquist (1991) posited that bars were the main drivers of inflow; however we have found that the bar formation in that case was in fact a result of a high smoothing parameter and low gas fraction. When non-axially symmetric structures, such as bars do form, it is

highly dependent upon gas fraction (that is, lower gas fraction typically leads to the formation of a stronger bar).

3. The efficiency of inflow is intricately dependent upon the encounter geometry. That is, the size of the gas disk, inclination of the encounter, and pericentric separation all conspire to affect the process of inflow. For prograde encounters, inflow is most efficient in small disks that come in on wide orbits. Retrograde encounters seem to have more efficient inflow in a large gas disk.

4. Clump driven inflow and mode-driven inflow have different timescales for nuclear delivery. Bars promptly deliver a large amount of gas, while clumps intermittently deliver material over a longer period of time.

5. Encounter geometry is a very important factor for inflow. Depending on the circumstances, inclined disks may actually experience a larger inflow than direct disks, contrary to what was previously understood (e.g., Barnes & Hernquist 1996; Mihos & Hernquist 1996).

6. Inflow is strongest when the gas and stellar disks are the same size. More extended gas disks retain too much of their original angular momentum and are not well coupled to the stellar material, thus providing less inflow. It is therefore plausible that previous simulations using stellar and gas disks of comparable size have over-estimated the amount of inflow, and perhaps, the star formation rate.

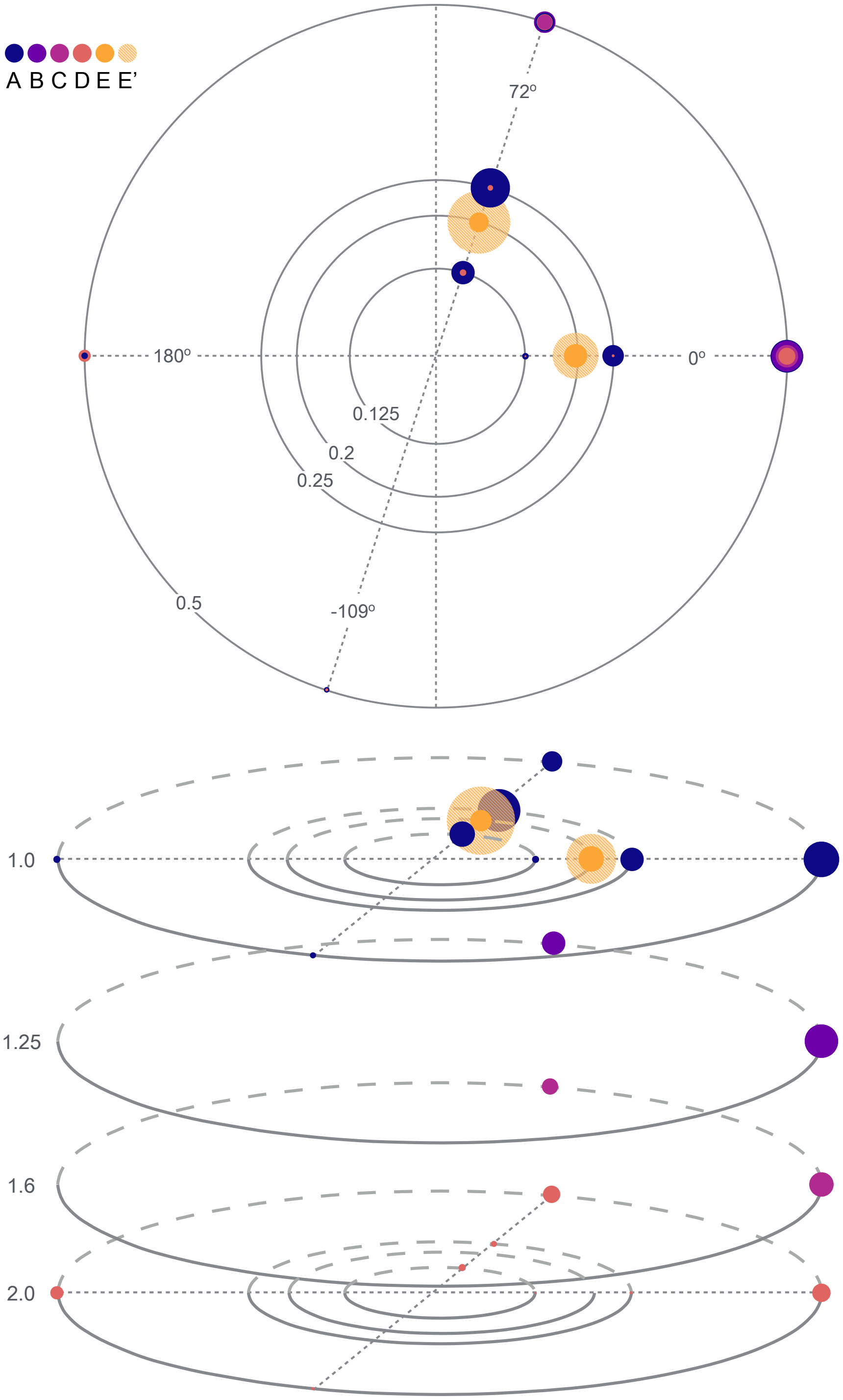

Figure 3.17 Here we graphically summarize our results. Concentric circles show the range of pericentric separations; the inclination angles are indicated by their position on the unit circle. The diameter of each point corresponds to the final nuclear mass of each run. The bottom figure shows a side-view of the top; each layer corresponds to a different $\alpha_\star/\alpha_g$.

References

Aarseth, S. J. 1963, MNRAS, 126, 223

Alonso-Herrero, A., Rieke, G. H., Rieke, M. J., & Scoville, N. Z. 2000, ApJ, 532, 845

Barnes, J. E. 2002, MNRAS, 333, 481

—. 2004, MNRAS, 350, 798

—. 2012, MNRAS, 425, 1104

—. 2016, MNRAS, 455, 1957

Barnes, J. E. & Hernquist, L. 1996, ApJ, 471, 115

Barnes, J. E. & Hernquist, L. E. 1991, ApJ, 370, L65

Bate, M. R. & Burkert, A. 1997, MNRAS, 288, 1060

Behrendt, M., Burkert, A., & Schartmann, M. 2016, ApJ, 819, L2

Bournaud, F., Chapon, D., Teyssier, R., Powell, L. C., Elmegreen, B. G., Elmegreen, D. M., Duc, P.-A., Contini, T., Epinat, B., & Shapiro, K. L. 2011, ApJ, 730, 4

Broeils, A. H. & Rhee, M.-H. 1997, A&A, 324, 877

Capelo, P. R. & Dotti, M. 2017, MNRAS, 465, 2643

Ceverino, D., Dekel, A., & Bournaud, F. 2010, MNRAS, 404, 2151

Chien, L.-H. & Barnes, J. E. 2010, MNRAS, 407, 43

Cortijo-Ferrero, C., González Delgado, R. M., & Pérez, E. 2011, in Stellar Clusters & Associations: A RIA Workshop on Gaia, 379–380

Dekel, A., Sari, R., & Ceverino, D. 2009, ApJ, 703, 785

Di Matteo, P., Combes, F., Melchior, A.-L., & Semelin, B. 2007, A&A, 468, 61

Duc, P.-A., Bournaud, F., & Masset, F. 2004, A&A, 427, 803

Elmegreen, D. M., Elmegreen, B. G., & Ferguson, T. E. 2005, ApJ, 623, L71

Evans, A. S., Vavilkin, T., Pizagno, J., Modica, F., Mazzarella, J. M., Iwasawa, K., Howell, J. H., Surace, J. A., Armus, L., Petric, A. O., Spoon, H. W. W., Barnes, J. E., Suer, T. A., Sanders, D. B., Chan, B., & Lord, S. 2008, ApJ, 675, L69

Gaspari, M., Ruszkowski, M., & Oh, S. P. 2013, MNRAS, 432, 3401

Hagiwara, Y. 2007, AJ, 133, 1176

Hayward, C. C., Torrey, P., Springel, V., Hernquist, L., & Vogelsberger, M. 2014, MNRAS, 442, 1992

Hernquist, L. & Katz, N. 1989, ApJS, 70, 419

Hopkins, P. F., Cox, T. J., Hernquist, L., Narayanan, D., Hayward, C. C., & Murray, N. 2013, MNRAS, 430, 1901

Hopkins, P. F. & Quataert, E. 2010, MNRAS, 407, 1529

Jaffe, W. 1983, MNRAS, 202, 995

Kim, J.-h., Ma, X., Grudić, M. Y., Hopkins, P. F., Hayward, C. C., Wetzel, A., Faucher-Giguère, C.-A., Kereš, D., Garrison-Kimmel, S., & Murray, N. 2017, ArXiv e-prints

Kormendy, J. & Gebhardt, K. 2001, in American Institute of Physics Conference Series, Vol. 586, 20th Texas Symposium on relativistic astrophysics, ed. J. C. Wheeler & H. Martel, 363–381

Larson, K. L., Sanders, D. B., Barnes, J. E., Ishida, C. M., Evans, A. S., U, V., Mazzarella, J. M., Kim, D.-C., Privon, G. C., Mirabel, I. F., & Flewelling, H. A. 2016, ApJ, 825, 128

Li, Y. & Bryan, G. L. 2014a, ApJ, 789, 54

—. 2014b, ApJ, 789, 153

Li, Y., Mac Low, M.-M., & Klessen, R. S. 2004, ApJ, 614, L29

—. 2005, ApJ, 620, L19

Maji, M., Zhu, Q., Li, Y., Charlton, J., Hernquist, L., & Knebe, A. 2017, ApJ, 844, 108

Mandelker, N., Dekel, A., Ceverino, D., DeGraf, C., Guo, Y., & Primack, J. 2017, MNRAS, 464, 635

Marinacci, F., Vogelsberger, M., Pakmor, R., Torrey, P., Springel, V., Hernquist, L., Nelson, D., Weinberger, R., Pillepich, A., Naiman, J., & Genel, S. 2018, MNRAS, 480, 5113

Mihos, J. C. & Hernquist, L. 1996, ApJ, 464, 641

Naiman, J. P., Pillepich, A., Springel, V., Ramirez-Ruiz, E., Torrey, P., Vogelsberger, M., Pakmor, R., Nelson, D., Marinacci, F., Hernquist, L., Weinberger, R., & Genel, S. 2018, MNRAS, 477, 1206

Navarro, J. F., Frenk, C. S., & White, S. D. M. 1996, ApJ, 462, 563

Nelson, D., Pillepich, A., Springel, V., Weinberger, R., Hernquist, L., Pakmor, R., Genel, S., Torrey, P., Vogelsberger, M., Kauffmann, G., Marinacci, F., & Naiman, J. 2018, MNRAS, 475, 624

Oklopčić, A., Hopkins, P. F., Feldmann, R., Kereš, D., Faucher-Giguère, C.-A., & Murray, N. 2017, MNRAS, 465, 952

Pillepich, A., Nelson, D., Hernquist, L., Springel, V., Pakmor, R., Torrey, P., Weinberger, R., Genel, S., Naiman, J. P., Marinacci, F., & Vogelsberger, M. 2018, MNRAS, 475, 648

Planck Collaboration, Ade, P. A. R., Aghanim, N., Armitage-Caplan, C., Arnaud, M., Ashdown, M., Atrio-Barandela, F., Aumont, J., Baccigalupi, C., Banday, A. J., & et al. 2014, A&A, 571, A16

Querejeta, M., Meidt, S. E., Schinnerer, E., García-Burillo, S., Dobbs, C. L., Colombo, D., Dumas, G., Hughes, A., Kramer, C., Leroy, A. K., Pety, J., Schuster, K. F., & Thompson, T. A. 2016, A&A, 588, A33

Renaud, F., Bournaud, F., Kraljic, K., & Duc, P.-A. 2014, MNRAS, 442, L33

Rich, J. A., Kewley, L. J., & Dopita, M. A. 2015, ApJS, 221, 28

Springel, V., Di Matteo, T., & Hernquist, L. 2005a, ApJ, 620, L79

—. 2005b, MNRAS, 361, 776

Springel, V., Pakmor, R., Pillepich, A., Weinberger, R., Nelson, D., Hernquist, L., Vogelsberger, M., Genel, S., Torrey, P., Marinacci, F., & Naiman, J. 2018, MNRAS, 475, 676

Springel, V. & White, S. D. M. 1999, MNRAS, 307, 162

Teyssier, R., Chapon, D., & Bournaud, F. 2010, ApJ, 720, L149

Toomre, A. & Toomre, J. 1972, ApJ, 178, 623

Wetzstein, M., Naab, T., & Burkert, A. 2007, MNRAS, 375, 805

Chapter 4

Galaxy interactions in IllustrisTNG-100, I: The power and limitations of visual identification

4.1 Preamble

This chapter contains the figures and text of my paper which has been submitted to the Monthly Notices of the Royal Astronomical Society, entitled Galaxy interactions in IllustrisTNG-100, I: The power and limitations of visual identification. I have received comments on this manuscript from a referee, about a third of which have been addressed at the moment of this writing.

4.2 Abstract

We present a sample of 446 galaxy pairs constructed using the cosmological simulation IllustrisTNG-100 at $z = 0$, with $\mathrm{M}_{\mathrm{FoF,\,dm}} = 10^{11} - 10^{13.5}\ \mathrm{M}_{\odot}$. We produce ideal mock SDSS g-band images of all pairs to test the reliability of the morphological schema employed to produce samples of interacting galaxies. We visually classify each image as interacting or not based on the projected separation, the presence of stellar debris fields, disturbed discs, and/or tidal features. By inspecting the trajectories of the pairs, we determine that these indicators correctly identify interacting galaxies ~45% of the time. We subsequently split the sample into the visually identified interacting pairs (VIP; 38 pairs) and those which are interacting but are not visually identified (nonVIP; 47 pairs). Although the VIP and nonVIP have similar gas contents, the VIP experience a more intense starburst at their most recent pericenter. The VIP sit in haloes that are approximately 2.5 times as massive, in environments nearly 2 times as dense, and are almost a factor of 10 more affected by

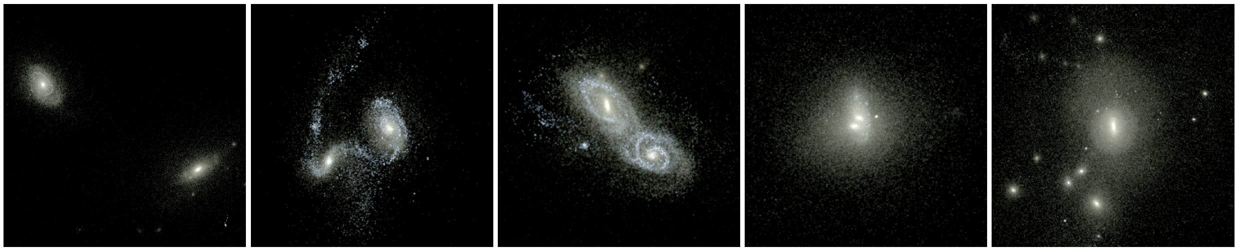

Figure 4.1 The typical view of the merger sequence includes, from left to right: (1) two galaxies coming in on their initial approach, (2) just after the first pericentric passage, when tidal features are prominent, (3) near second pericentric passage, when there are significant disruptions to the discs and still-visible tidal features, (4) prior to final coalescence when the galaxies' nuclei are nearly completely overlapping, and (5) a post-merger remnant, featuring clear tidal shells. These simulated three-color composite images are produced via the same procedure described in §4.4.2 utilising SDSS g, r and i magnitudes.

the tidal forces of their surroundings than the nonVIP. We also find that VIP have undergone a close passage nearly twice as recently as the nonVIP. These factors conspire to increase the observability of tidal features and disturbed morphologies, making the VIP more likely to be identified. Thus, merger rate calculations which rely on stellar morphologies are likely to be significantly biased toward massive galaxy pairs which have recently undergone a close passage.

4.3 Introduction

Galaxy encounters have been used to explain the presence of peculiar galaxies (e.g., Arp 1966), and facilitate our understanding of galaxy evolution in a number of ways. Figure 4.1 illustrates the typical merger sequence, from initial approach (far left) to final coalescence (far right). These encounters lead to significant changes in stellar and gas morphology (e.g., Mihos 1995; Mihos et al. 1995; Malin & Hadley 1997; Côté et al. 1998; Knierman et al. 2003; Lotz et al. 2008; Wen & Zheng 2016; Tapia et al. 2017), including the production of non-axisymmetric torques which enable gaseous inflows (e.g., Duc et al. 2004; Blumenthal & Barnes 2018), which may feed the central black hole, producing heightened activity of the nucleus (e.g., Cutri & McAlary 1985; Dahari 1985; Heckman et al. 1986a,b; Ellison et al. 2011; Hewlett et al. 2017; Trakhtenbrot et al. 2017). Interacting and merging galaxies have been shown to host heightened rates of star formation (e.g., Joseph & Wright 1985; Kennicutt et al. 1987; Whitmore & Schweizer 1995; Vigroux et al. 1996; Mirabel et al. 1998; Bridge et al. 2007; Scudder et al. 2012; Rich et al. 2015). In the Local Universe, gas-rich mergers manifest themselves as (ultra)luminous infrared galaxies (e.g., Sanders et al. 1988; Hopkins et al. 2008). Until the James Webb Space Telescope begins operations, our knowledge of these objects at high redshifts will remain severely limited. However, indirect measurements such as the observation that early discs are dominated by large clumps of gas and dust (e.g., Lotz et al. 2006; Ravindranath et al. 2006; Whitaker et al. 2015) and that many early ellipsoids are very compact (e.g., Buitrago et al. 2008; Williams et al. 2014; Barro et al. 2013), have led some to postulate that mergers were much more common in the Early Universe (e.g., Conselice et al. 2004; Genzel et al. 2008; Bezanson et al. 2009; Bournaud & Elmegreen 2009; Dekel et al. 2009). These findings are consistent with ΛCDM cosmology, which dictates that the hierarchical structure of the universe arises from sequential mergers throughout cosmic time (e.g., White & Rees 1978).

A fundamental component of galaxy evolution, and by extension hierarchical growth, is the galaxy merger rate. In its simplest form, the galaxy merger rate is calculated by dividing the fraction of galaxies undergoing a merger by the typical time a galaxy interaction will be observable. The merger fraction is often determined by counting the number of morphologically disturbed (both automatically or by visual inspection, e.g., Lotz et al. 2008; Jogee et al. 2009; Shi et al. 2009; Lotz et al. 2010b; Bluck et al. 2012), or the number of galaxies in close pairs (projected or 3D, e.g., Bundy et al. 2004; Kartaltepe et al. 2007; Bundy et al. 2009; Robotham et al. 2014; Mundy et al. 2017; Snyder et al. 2017). The observability timescale is also variable, and may depend on the orbital parameters and initial conditions (e.g., Conselice 2006; Lotz et al. 2010a,b), the observational method used to characterize the merger (e.g., Lotz et al. 2008), and the redshift of the interaction (e.g., Snyder et al. 2017). Due to the breadth of observational methods used to derive these quantities, the calculated merger rate varies widely (e.g., Lotz et al. 2011). However, cosmological simulations are providing insight into the limitations of purely observational studies (e.g., Rodriguez-Gomez et al. 2015).

In this paper, we set out to answer the following questions that are fundamental to the calculation of the galaxy merger rate across cosmic time:

1. Does the stellar morphology of a merging pair reliably indicate its dynamical history?
2. What makes an interaction "visible"?
3. Are merger catalogs derived solely from optical observations biased?

a Lotz et al. (2011) use small-scale hydrodynamic simulations of binary galaxy pairs to derive a realistic observability timescale. They find that applying this parameter to observational data causes the widely divergent merger rates to converge. Simons et al. (2019) use synthetic galaxy images from zoom simulations to determine how frequently galaxies are confused for discs in merger catalogues. These interlopers confuse the disc/spheroid ratio that is often used to define merger rates, a trend the authors found was dependent upon stellar mass. More recently there has been a push to apply deep learning (e.g., Bottrell et al. *in prep*; Snyder et al. 2018; Pearson et al. 2019) techniques to synthetic galaxy image catalogues to assess the completeness of observationally derived catalogues.

In this work we utilize the IllustrisTNG simulation with a volume of $\sim 100^3$ Mpc^3 (hereafter TNG100-1), one of the three main runs of the IllustrisTNG cosmological suite (Marinacci et al. 2018; Naiman et al. 2018; Nelson et al. 2018; Pillepich et al. 2018a; Springel et al. 2018). The IllustrisTNG model (Weinberger et al. 2017; Pillepich et al. 2018b) employs state-of-the-art prescriptions for star formation, chemical evolution, and feedback due to active galactic nuclei. Recent work has shown that the IllustrisTNG model matches important observational benchmarks in the chemical and metallicty evolution of galaxies (e.g., Naiman et al. 2018; Torrey et al. 2017), the quasar luminosity function and black hole mass relationships (e.g., Weinberger et al. 2018), and the overall morphologies of galaxies (e.g., Rodriguez-Gomez et al. 2019). Using a sample of galaxy pairs from TNG100-1, we generate ideal mock SDSS images to identify what fraction of the interacting pairs are "observable."

This chapter is structured as follows: in Section 5.3 we discuss the cosmological simulation used, the methods associated with its data products, and the pair sample preparation; in Section 5.4 we present our results and compare the TNG100-1 sample of major mergers at the present-day to the pairs' last pericentric passage; finally, in Section 5.7, we present our conclusions and briefly describe our future and ongoing work.

4.4 Methods

4.4.1 IllustrisTNG

IllustrisTNG is a set of N-body/magnetohydrodynamic cosmological simulations with dark and baryonic matter. Gravity is solved using a Tree-PM algorithm, which uses a particle mesh on large scales and a tree code on small scales. Gas is treated as an ideal fluid on an unstructured mesh (AREPO; SPRINGEL 2010) that incorporates an ideal treatment of magnetohydrodynamics (Pakmor et al. 2011, 2016). Gas is allowed to cool via metal-lines and radiation, and can also heat radiatively by exposure to a redshift-dependent radiation field (e.g., Katz et al. 1996; Faucher-Giguère et al. 2009). High density gas can self-shield (Vogelsberger et al. 2013), under the appropriate optical depth conditions. The interstellar medium (ISM) is modeled with an effective two phase model, following Springel & Hernquist (2003): cool clouds are in pressure equilibrium with the hot diffuse medium. These simulations cannot describe the ISM structure in detail, but do include mass exchange via cooling, star formation, and the evaporation of clouds by supernovae. This acts to harden the equation of state of the star forming gas, and also stabilizes gas against instability. Our ISM prescription does not reach low (high) enough temperatures (densities) to properly describe the molecular gas component. These simulations do not include modeling of cosmic rays nor explicit radiative transfer.

Each star particle represents a stellar population, not an individual star, based on empirical models that include stellar evolution, enrichment, mass and metal returns and supernova rates (Pillepich et al. 2018b). Star formation and supernovae drive outflows in galaxies. Gas mass is ejected from star forming regions such that the wind velocity is proportional to the dark matter velocity dispersion. Due to resolution limitations, outflowing material is initially hydrodynamically decoupled, and is re-coupled at a density threshold. The winds carry a sufficient metal content out of the galaxy, to approximately match the mass-metallicity (or, M-Z) relation (for further details, see Pillepich et al. 2018b).

Black holes - and the feedback due to active galactic nuclei (AGN) - are a key part of this simulation, in particular the production of quiescent galaxies. Given the resolution of the simulation, black hole formation cannot be self-consistently modeled, so once a galactic halo reaches a certain mass, a seed black hole particle is inserted at its centre, which then acts as a sink particle. The black hole is thus tied to the potential minimum and grows by subsequent mass accretion via Eddington-limited Bondi-Hoyle accretion (Springel et al. 2005). The channel of AGN feedback (Sijacki et al. 2007; Weinberger et al. 2017) depends upon the accretion rate. At low accretion rates, the galaxy experiences a wind (or, kinetic mode), wherein kinetic energy is deposited into the gas around the black hole. The duty cycle then ensures star formation remains suppressed. At high accretion rates, the galaxy enters the thermal (or, quasar) mode; the strength of this feedback mode is a function of the black hole mass. Full details of the IllustrisTNG BH feedback model available in Weinberger et al. (2017). For more information regarding the computational methods employed by IllustrisTNG, refer to Ch. 2.4.3.

IllustrisTNG vs. Illustris

The IllustrisTNG model differs from its earlier counterpart, Illustris (Vogelsberger et al. 2014a,b; Genel et al. 2014; Sijacki et al. 2015), in several ways: (1) it includes isotropic winds with velocities that scale according to the halo virial mass; (2) the supernova energy has two components (thermal and kinetic) which are applied to winds; (3) the wind energy is metallicity-dependent; (4) the supernova mass limit has been set to 8 $M_\odot$, and the yield tables have been updated (Naiman et al. 2018); (5) it includes an ideal treatment of magnetohydrodynamics. Further, the IllustrisTNG model was run at three different volumes to generate a simulation series that spans a wide dynamical range: TNG50 (Nelson et al. 2019; Pillepich et al. 2019), TNG100 and TNG300. Each of these runs was initialized with three (TNG100 and TNG300) or four (TNG50) sets of initial conditions, often indicated as e.g., TNG100-1. For more information on the simulation series structure, see Appendix A. In this work, we utilize the run TNG100-1 for several reasons: (1) it has the same set of initial conditions as the original Illustris run; (2) it has the largest number of resolution elements for its volume; and (3) the volume is large enough to contain many examples of interacting galaxies (c.f., TNG50), but not too large that these galaxies are poorly resolved (c.f., TNG300, which has a mass resolution roughly an order of magnitude larger than that in TNG100).

Many parameters and model choices of the IllustrisTNG model were calibrated using observational scaling relations and galaxy properties (Pillepich et al. 2018b). Several works outline the successes of this model. Nelson et al. (2018) shows that the color bimodality, which was absent in the original Illustris, possibly due to the previous implementation of black hole feedback, was present in both TNG100 and TNG300. Rodriguez-Gomez et al. (2019) compares synthetic images from TNG100 to an analogous sample from Pan-STARRS. They find TNG100 to be a significant improvement over the original Illustris suite, particularly with respect to the galaxy morphologies. Additionally, chemical evolution (Naiman et al. 2018), galaxy mass-metallicity relations (Torrey et al. 2017), and the present day quasar luminosity function (Weinberger et al. 2018) are shown to be broadly consistent with observations. Despite its relative success, there are still areas of contention between the IllustrisTNG model and the observed universe. For example, TNG100 may underproduce bulge-dominated galaxies, and may overproduce red discs and blue spheroids (e.g., Huertas-Company et al. 2019; Rodriguez-Gomez et al. 2019). The high-redshift quasar luminosity function, driven by the feedback mechanisms employed by supermassive black holes, may be in tension with observations (Habouzit et al. 2018; Weinberger et al. 2018). Additionally, it has been suggested that there is contention between the observed and simulation H_2 content in high redshift galaxies Popping et al. (2019).

Friends-of-Friends Groups and Subhalos

Friends-of-Friends (hereafter FoF) groups are constructed using a percolation algorithm (Davis et al. 1985) which links together dark matter particles based on their mean inter-particle separation. This linking length,

b, corresponds to a density threshold, below which particles are not considered associated. IllustrisTNG uses a linking length of $b = 0.2$, which means that the most massive FoF groups will have an inter-particle spacing equal to 0.2 times the average distance between all particles at that snapshot. The baryonic (gas and stars) material is assigned to a particular FoF group based on the membership of the nearest dark matter particle. Subhalos, on the other hand, are identified via the SUBFIND algorithm (Springel et al. 2001a). This iteratively strips away particles that are unbound from the central structure, until a bound system above a certain size remains. In many cases, as in this work, subhalos are considered galaxies, while FoF groups may contain pairs or groups of galaxies.

4.4.2 Galaxy Pair Samples

Parent Sample

We select FoF haloes in the most recent snapshot (i.e., $z = 0$) with a FoF group total dark matter mass between 10^{11} and $10^{13.5}$ $M_\odot$. Additionally, subhalos are required to have a total dark matter mass between $10^{10.5}$ and 10^{13} $M_\odot$. These mass cuts ensure that we limit ourselves to well-resolved galaxies and halos; that we avoid systems in which visual features are driven by environmental, non-merger related processes. Subhalos with a total dark halo mass less than $10^{10.5}$ $M_\odot$ are likely to be poorly resolved in both the dark and baryonic material. To ensure the proper mass resolution of the stars, we place a final limit on the subhalo total stellar mass such that both subhalos in the pair have a total stellar mass above 10^9 $M_\odot$. No limit is placed on the distance between the subhalos, although they are required to belong to the same FoF halo. We do not consider pairs that straddle two FoF haloes (as in, e.g., Moreno 2012; Moreno et al. 2013), and note that these systems are not only relatively rare, but are likely to be unbound (and as such, not orbiting one another). We consider only pairs of galaxies with a stellar mass ratio between unity and 1:4 ("major merger") at the present day. Lastly, the majority of observations (e.g., Bridge et al. 2010; Ellison et al. 2010; Larson et al. 2016; Ventou et al. 2017; Mantha et al. 2018) and idealised simulations (e.g., Toomre & Toomre 1972; Barnes & Hernquist 1991, 1996; Di Matteo et al. 2008; Lotz et al. 2008; Rupke et al. 2010; Bournaud et al. 2011; Hopkins et al. 2013) of galaxy mergers typically assume the system is composed of only two galaxies. In order to approximate this assumption, we required that any tertiary subhalo in the FoF group be at most 1/16 the stellar mass of the primary (or, most massive) halo. It should be noted, however, that this restriction will not exclude recent minor mergers. As such, there may be systems with strong tidal features at the present day due to these low mass ratio interactions. However, current minor mergers are removed from the set of ongoing interactions, as we manually exclude visual groups of galaxies. Note too that some recent work has been done to relax the binary merger assumption (e.g., Moster et al. 2014; Sparre & Springel 2016; Pontzen et al. 2017). Our final set of galaxies contains 446 binary galaxy pairs at $z = 0$.

Ideal Mock SDSS Images

We generate ideal mock SDSS images for each of the 446 galaxy pairs in our sample. TNG100 provides magnitudes in eight bands for each star particle, which are calculated using Bruzual & Charlot (2003) (assuming no dust). These include SDSS g, r, i, z, Buser U, B, V, and Palomar K. Here, we generate ideal mock SDSS g-band images using all star particles bound to a FoF group. This band was chosen to facilitate future comparisons with wide-field observational surveys. To calculate the luminosity of each star particle, we determine the true SDSS g magnitude

$$M_{\text{true}} = M_{\text{obs}} - \chi k_{\text{filter}} \tag{4.1}$$

where M_{obs} is the TNG100 SDSS g-band absolute magnitude, k_{filter} is the filter-dependent first order extinction correction, and χ is the airmass, assumed to be 1.3 for all SDSS bands in TNG100. The apparent magnitudes are needed to derive the flux:

$$m_{\text{true}} = M_{\text{true}} + \mu \tag{4.2}$$

The distance modulus, μ, is calculated for each set of galaxy pairs using a set distance of 35 Mpc for every system. The flux is then

$$f = 10^{0.4(m_{\text{true}} - m_{\text{zp}})} \tag{4.3}$$

where m_{zp} is the zero-point of the desired filter. For our images, we use $k_{\text{filter}} = 0.15$, $\chi = 1.3$, and $m_{\text{zp}} = 25.11$ (Stoughton et al. 2002). We project the three-dimensional distribution of particles onto a flat two-dimensional plane, and apply a 2D Gaussian smoothing function with FWHM equal to the radius of a sphere enclosing the 32 nearest star particles, following Torrey et al. (2015). For simplicity, we use the x and y coordinates to define this plane, and do not assume a location or viewing angle for an observer. Thus the sample represents a random set of orientations with no preferred observing direction. Further the images include no treatment of dust attenuation, a convolution with the SDSS resolution, nor the inclusion of a realistic sky background (e.g. Bottrell et al. 2017). This affords us optimal conditions to "observe" any tidal features in the mocks. Figure 4.1 contains five (rgb) examples of our ideal mock observations. For the full postage stamp collection of the interacting pairs, refer to Appendix B.2.

Visual Classification Scheme

The merger sequence is defined by the presence (or absence) of tidal features. Larson et al. (2016) devised a merger stage classification scheme that includes non-interacting single galaxies (s), minor mergers (m) and major mergers, ranging from before first pericentric passage through final coalescence and post-merger remnant (M1−M5) of Ultra-Luminous Infrared Galaxies (ULIRGs). Their major merger sequence is as follows (Figure 4.1):

M1 - Galaxies are well separated and appear to be on their initial approach.

M2 - Tidal features (bridges and tails) are clearly visible, and likely just after the first close passage.

M3 - Two individual nuclei are visible in highly disturbed overlapping discs. The tidal tails are still well defined.

M4 - The two nuclei have now coalesced, but the tidal tails are still visible.

M5 - A post-merger remnant, with a diffuse outer shell, and little-to-no evidence of tidal tails.

Using this merger stage classification as a guide, three of the authors independently classified the pairs as either interacting (roughly, stage M2-M5) or not interacting (s-M1). Visual cues including the projected distance, tidal features, and stellar debris were used. Following Galaxy Zoo (Lintott et al. 2008), we took the group consensus (2 out of 3) to be the morphological classification for a pair.

Identifying merger stage in this way may be subject to many pitfalls. For example, the production of tidal features such as bridges and tails is dependent upon encounter geometry, and can, in some retrograde encounters, be completely absent (e.g., Toomre & Toomre 1972; Di Matteo et al. 2007). Further, galaxies that sit deep inside their gravitational potential wells are less likely to form prominent, long-lasting tidal features (e.g., Barnes & Hernquist 1992). Thus, a schema which depends entirely on tidal features in the stellar material might be severely biasing the kinds of interactions we capture. One of the main goals of this paper is to test how well these morphology-based classifications identify interacting systems.

	Visual ID: Yes	Visual ID: No
Trajectory: Yes	**38**	**47**
Trajectory: No	18	214

Recently entered the same group	97
Group	22
Not Orbiting	10
Total Pairs	446

Table 4.1 A complete description of the classifications for all pairs in the parent sample. In the top section, we report the results of the combined visual and trajectory schema, including the VIP and nonVIP which are the subsamples used in this paper. The middle section reports the number of pairs which were manually eliminated from the sample.

Trajectory Classification

Using the Sublink merger tree (Rodriguez-Gomez et al. 2015), we extract the 3D orbital motion of the secondary with respect to the primary. A pair is considered "interacting" if it has had at least one close passage, the pair is at or nearing an apocenter (i.e., there is an apparent turnover in the relative separation), and there is apparent orbit decay (i.e., sequentially deeper pericentric passages). For pairs which have had only one close passage, we require the pericentric distance be less than ~150 kpc. In considering the full trajectories, we more reliably remove those galaxies which have merely flown past one another. Whilst it could be argued that such systems have *interacted*, they are not *currently interacting*, and are thus not part of our sample.

Sample Selection Summary

In Table 4.1, we provide a full account of the results of our various classification schema. Some pairs were manually removed from the sample. This includes systems with multiple prominent subhalos, which comprised only ~5 per cent of the total pairs sample. Pairs were also discounted if they have only been in the same group for less than 1 Gyr (~22 per cent). These are exclusively subhalos determined not to be interacting, based on the aforementioned criteria. Finally, there are a small number of subhalos (~2 per cent) which appear to be interacting based on their morphologies in the mock images and/or their trajectories, but were not orbiting one another. Namely, their orbits appear to be dominated by structures outside the FoF group. The majority (~48 per cent) of our parent sample are not interacting are not visually identified as mergers. However, there is a small fraction (~4 per cent) of the non-interacting sample which were misidentified as mergers. Pairs which were visually identified as mergers and were found to be interacting

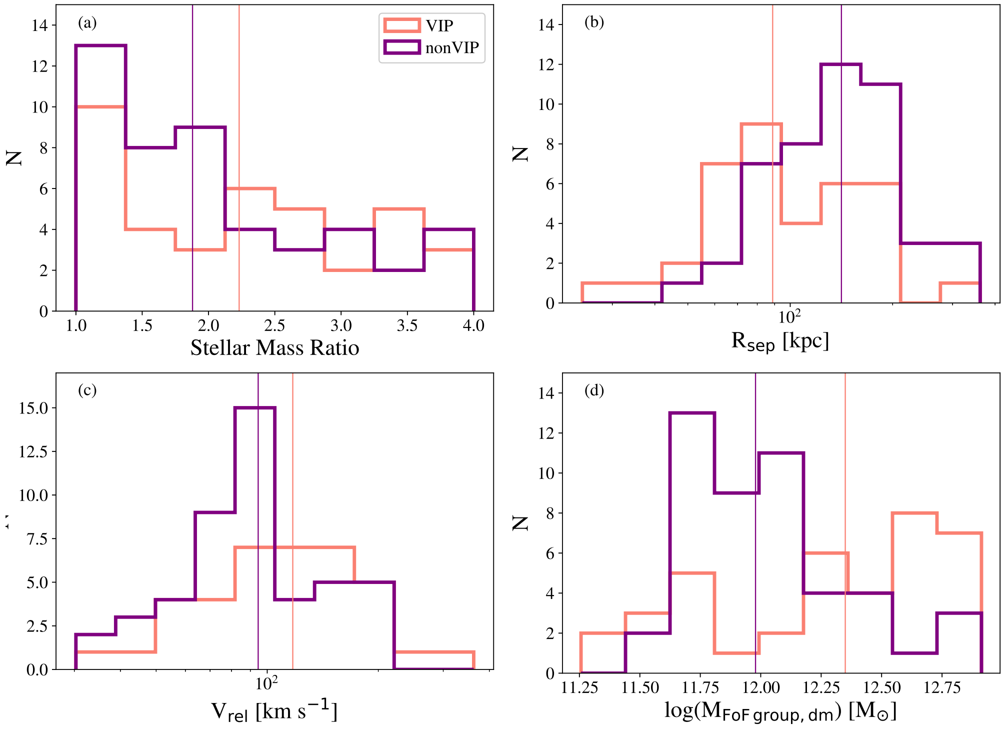

Figure 4.2 Galaxy-pair property distributions for the Visually Identified Pairs (VIP; salmon) and the non-visually identified pairs (nonVIP; purple). The panels show: (a) the current ($z = 0$) stellar mass ratio, (b) $z = 0$ 3D separations, (c) relative velocity, and (d) FoF group dark matter mass. The vertical colored lines correspond to the medians of each sample.

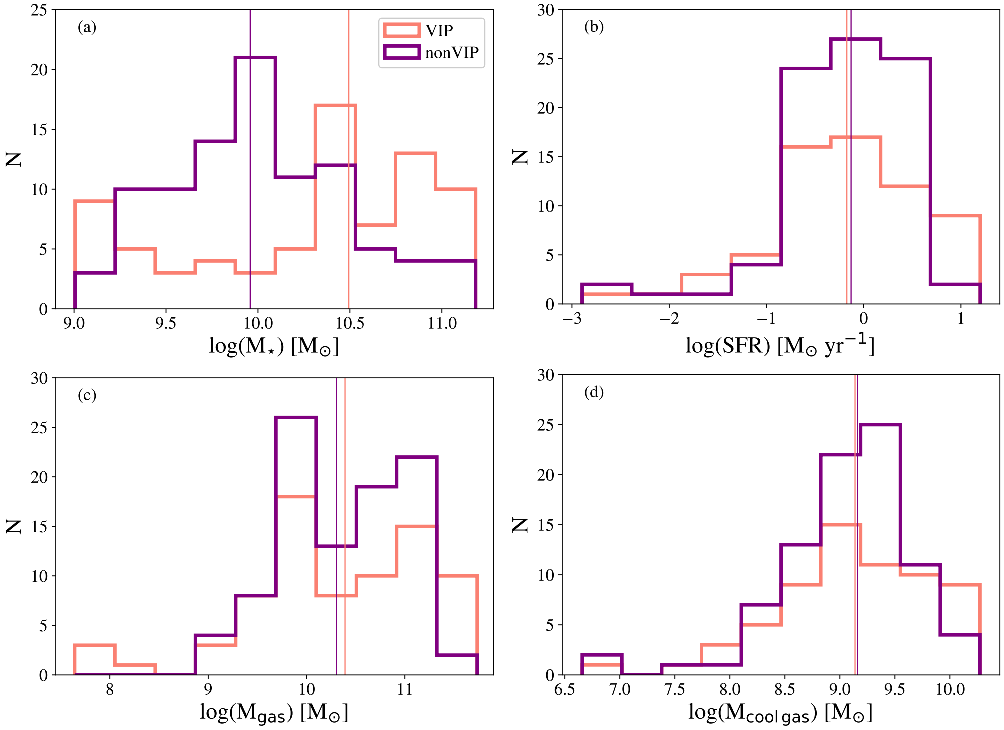

Figure 4.3 Individual galaxy distributions for the Visually Identified Pairs (VIP; salmon) and the non-visually identified pairs (nonVIP; purple). The panels show: (a) stellar mass, (b) star formation rate, (c) total gas mass, and (d) the star forming gas. The vertical colored lines correspond to the medians of each sample.

are hereafter referred to as Visually Identified Pairs, or VIP. The nonVIP, then, are those pairs which are interacting, but were not selected visually.

4.5 Results and Discussion

4.5.1 The VIP and nonVIP Samples

Present-day ($z = 0$) Properties

Panel (a) of Figure 4.2 shows that the distribution in stellar mass ratio peaks at unity and peters out toward larger mass ratios for both samples, with the VIP having a slightly larger median stellar mass ratio. Though we do see this trend with the median values, the VIP and nonVIP stellar mass ratios are not distinct distributions: a two-sided KS test indicates ($p \approx 0.3$) that these are drawn from the same sample. Panel (b) shows the present-day ($z = 0$) 3D separation, with the VIP having separations shifted to smaller values (here, the two-sided KS test indicates that VIP and nonVIP relative separations are in fact drawn from distinct distributions: $p \approx 2\text{e}{-3}$). Interacting pairs at wider projected separations may be overlooked in preparing samples of merging galaxies. However, previous work has indicated that interacting galaxies may exhibit heightened rates of star formation, even with separations as large as 150 kpc (e.g. Patton et al. 2013). In panel (c), we present the relative velocity distributions (i.e. the difference between the subhalo velocities); the VIP and nonVIP samples attain low velocities, facilitating their interaction and eventual merging. The VIP do appear to be moving faster on average than the nonVIP ($p \approx 0.05$), which hints at their local dynamics. That is, the relative velocities of these galaxies may be significantly affected by their environment, as discussed in Section 4.5.6. Finally, panel (d) displays the VIP and nonVIP FoF group dark matter mass distributions. This indicates that the VIP inhabit slightly more massive FoF halos ($p \approx 4\text{e}{-4}$).

In Figure 4.3, panel (a) shows that VIP galaxies tend to have higher stellar masses than the nonVIP ($p \approx 1.3\text{e}{-6}$). Because visual classification is based on tidal disruptions in the stellar material, we might predict that VIP galaxies have a higher stellar mass (i.e., more stars to disrupt) on average. In fact we do find the VIP median stellar mass is about one-half dex greater than the nonVIP, consistent with the findings in panel (d) of Figure 4.2. Panel (b) shows that the present-day star formation rate (SFR) is relatively consistent for both samples (this is confirmed by a two-sided KS test with $p \approx 0.33$). Panels (c) and (d) show the total gas mass and the cool (star forming) gas mass, respectively. The present-day contribution due to cool gas

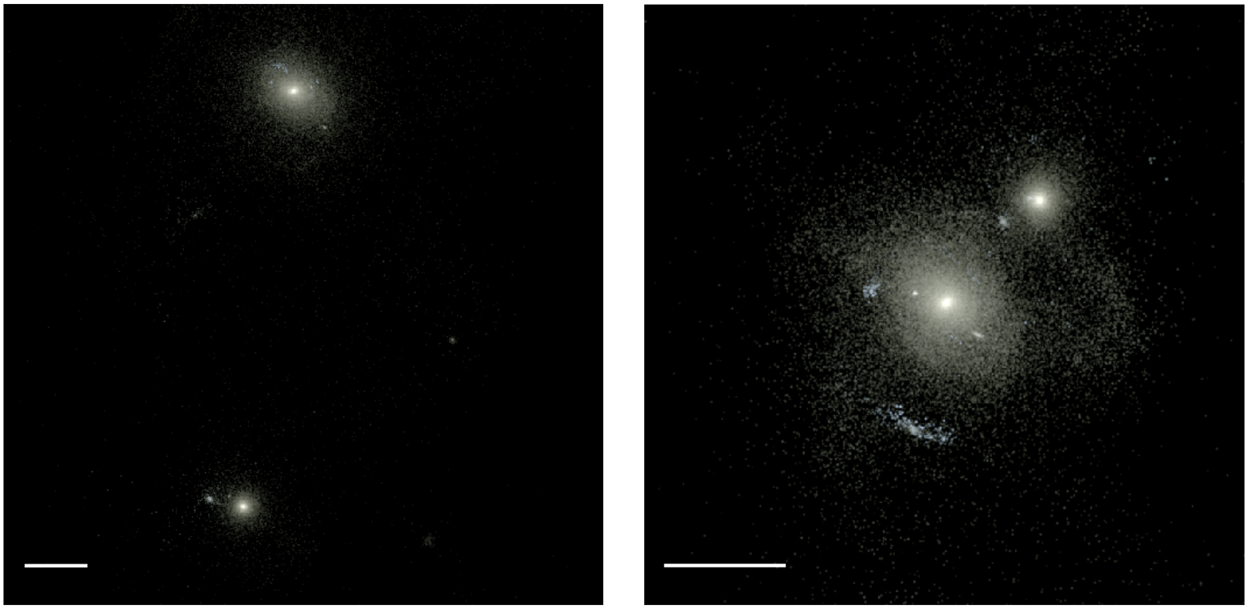

Figure 4.4 Here we show a (nonVIP) pair at the present day (left) and at its last pericenter (right), which occurred about 1.3 Gyr prior. The stellar mass ratio has stayed at ~3:1 over this period. Bars in the bottom left corner of each image indicate 50 kpc.

appears to be nearly the same for both samples ($p \approx 0.23$). This suggests that the gas reservoir available for star formation is not significantly different for the VIP or nonVIP, consistent with the findings of panel (b).

Properties at Last pericentric (LP) passage

We additionally utilize merger trees to study the pairs at the time of their last pericentric passage (LP) – a local maximum in the strength of their interaction. We note that the pairs do not all reach their respective LP events at the same time, but are at a dynamically similar moment in their histories. This way, we analyze all pairs at a point in time when the effects of their interaction are at a near a peak. Figure 4.4 shows a nonVIP galaxy image at the present-day (left), and at its last pericenter (right). At this pair's LP, there is a clear tidal debris field with several star forming regions in the primary galaxy. The LP's span a range of ages relative to the present day of 70 Myr to 5.66 Gyr (Figure 4.5). The VIP have more recently undergone a close passage than the nonVIP by nearly a factor of two ($p \approx 0.01$).

4.5.2 Galaxy pair dynamics

Figure 4.6 focuses on the dynamical properties of the VIP (salmon diamonds) and nonVIP (purple circles) at the present day. In line with panels (b) and (c) of Figure 4.2, the top panel of Figure 4.6 shows the

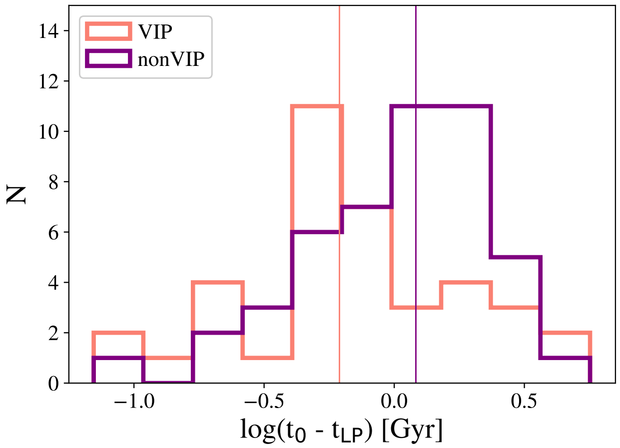

Figure 4.5 Time since last pericenter (t_0 - t_{LP}) distribution and median values (vertical lines) for the VIP (salmon) and the nonVIP (purple). The VIP have more recently undergone a close passage.

VIP and nonVIP are offset from one another: the VIP have smaller 3-dimensional separations, and move with slightly faster relative velocities than the nonVIP. Figure 4.5 shows that the VIP have more recently undergone a pericentric passage. Thus, their separations will naturally be smaller at the present day, and as they are closer to a pericenter, the VIP should have higher velocities than the nonVIP, which are typically closer to an apocenter. The bottom panel of Figure 4.6 shows a moderate linear trend between the dynamical mass and relative velocity. This is expected if the relative velocity traces the virial velocity, and the orbits are parabolic: $V = \sqrt{2\mathrm{GM_{dyn}/R}}$ (e.g., Moreno et al. 2013), where the dynamical mass $\mathrm{M_{dyn}}$ is defined as the sum of the galaxies' dark matter masses. This relation is shown for both the VIP (dashed salmon) and nonVIP (dashed purple) samples, using their corresponding median separations at the present day ($\overline{\mathrm{R}}_{\mathrm{VIP}}$ = 88.8 kpc; $\overline{\mathrm{R}}_{\mathrm{nonVIP}}$ = 141.4 kpc). The solid lines indicate lines of best fit for each subsample. Note that their slopes (most notably, that of the VIP) differ significantly from the parabolic case. There is a substantial amount of scatter in these samples, particularly at the high mass end, where a subset of the VIP dip to lower relative velocities. That these galaxies have lower relative velocities than what might be expected based on their dynamical mass may be indicative of their visual identification.

Figure 4.7 shows the VIP and nonVIP at last pericenter (colored points), compared with their positions at z = 0 (gray points). The interacting sample at LP are significantly closer together, and are moving much faster (left panel) than they are at z = 0. This is expected: an interacting pair should reach a local maximum in its relative velocity at each pericentric passage (or conversely, should reach a local minimum in its velocity at each apocenter, e.g., Figure 4 of Moreno et al. 2019). Similarly, the bottom panel of Figure 4.7 shows

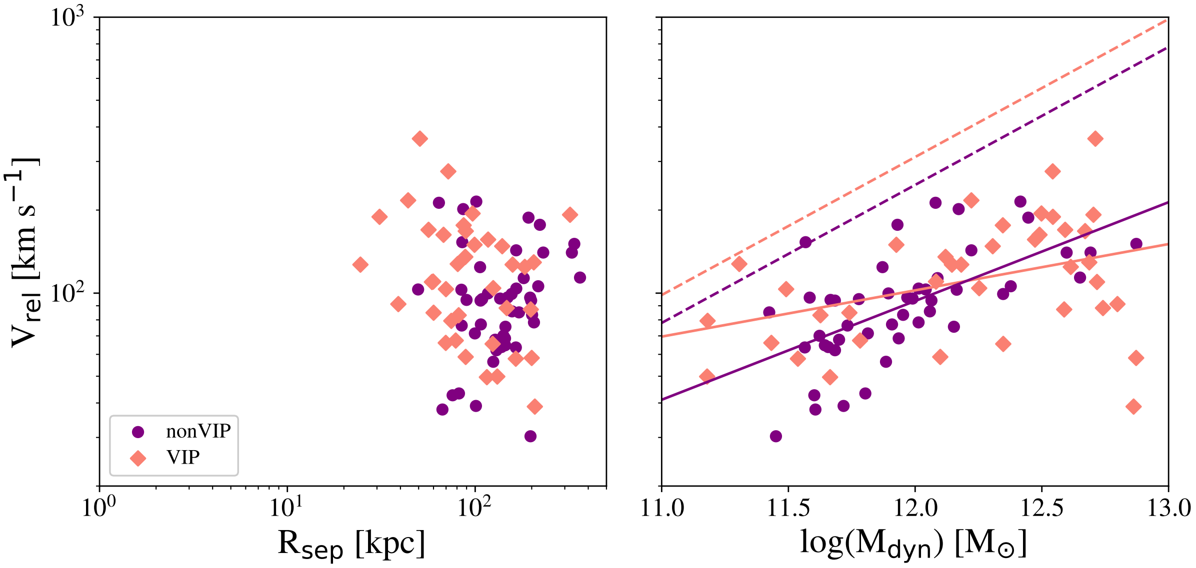

Figure 4.6 The dynamics of the interacting pairs at $z = 0$: relative velocity as a function of pair separation (left) and of dynamical mass (right) for the VIP (salmon diamonds) and the nonVIP (purple circles) sample. The dashed lines in the right panel indicate the trend expected from a parabolic trajectory, whilst the solid lines are a fit to the data.

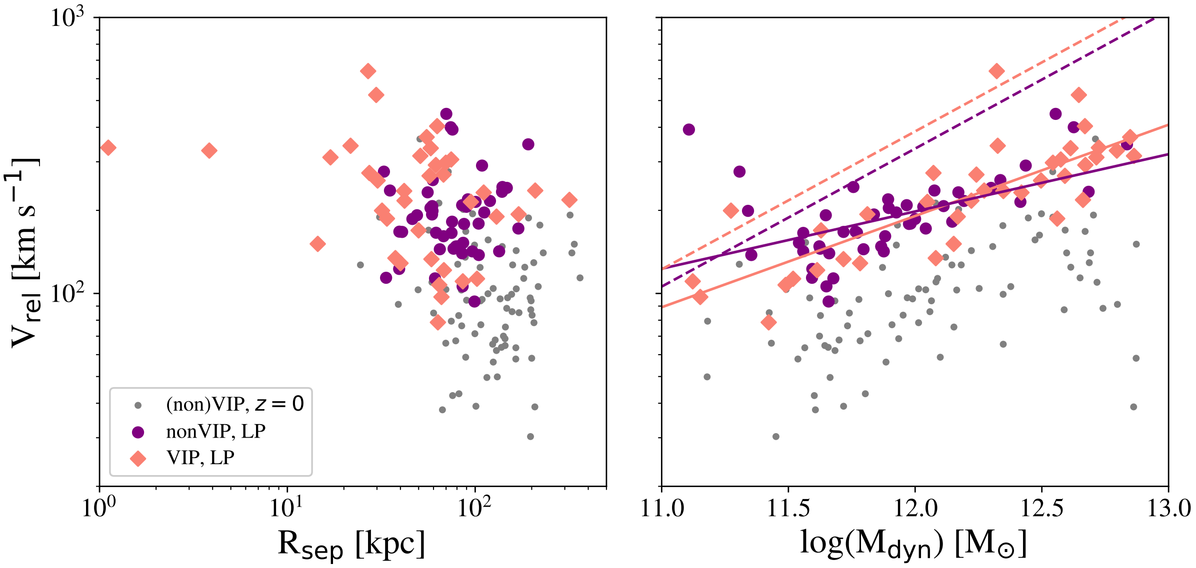

Figure 4.7 Analogous to Figure 4.6, but at last pericenter. Values are reported in color for the VIP and nonVIP (salmon diamonds and purple circles, respectively), and in gray points for comparison with $z = 0$ values.

that the the $M_{\rm dyn} - V_{\rm rel}$ relationship is much tighter at LP than at $z = 0$. The lines of best fit (solid) and the parabolic lines (dashed) are also very different at this time. The parabolic trends are predictably elevated from the $z = 0$ case, as the median separation values used are $\overline{\rm R}_{\rm VIP} = 57.63$ kpc and $\overline{\rm R}_{\rm nonVIP} = 76.73$ kpc. Although the best-fitting lines are still notably different, the VIP slope is now more consistent with the dashed lines. Contrary to their $z = 0$ behavior, the nonVIP appear to have greater scatter, particularly at the low mass end, where a subset achieve higher velocities than their dynamical mass might suggest.

4.5.3 Star Formation Main Sequence

The star formation main sequence (e.g., Noeske et al. 2007; Daddi et al. 2007; Elbaz et al. 2007; Salim et al. 2007; Rodighiero et al. 2011; Bluck et al. 2016, 2019; Donnari et al. 2019, hereafter SFMS) defines a general trend of all star forming galaxies: the star formation rate is tightly correlated with the stellar mass. That this relationship holds for a wide range of redshifts (e.g., Noeske et al. 2007; Lee et al. 2015), several orders of magnitude in stellar mass, and a relatively small spread in star formation rate implies that star forming galaxies behave in a self-regulatory manner with a fairly consistent star formation history throughout cosmic time (e.g., Bouché et al. 2010; Lilly et al. 2013). Outliers above the SFMS (starbursts) are thought to represent an important stage (that is, mergers) in galaxy evolution, though their relative contribution to the star formation density is still debated (e.g., Cox et al. 2008; Rodighiero et al. 2011; Hung et al. 2013; Brennan et al. 2015; Willett et al. 2015; Brennan et al. 2017; Ellison et al. 2018). Quiescent galaxies lie in a so-called “red cloud” below the SFMS, with a “green valley” of transitioning galaxies between the two. Merging and interacting galaxies, which themselves are examples of starbursting systems, have been shown to lie above the SFMS (e.g., Puech et al. 2014; Willett et al. 2015). In particular, Hung et al. (2013) show that for $z \sim 0.4$ galaxies, distance above the SFMS is correlated with disturbed morphologies. However, other studies (Willett et al. 2015; Brennan et al. 2017) are unable to to confirm this morphological dependence.

Figure 4.8 shows the star formation main sequence for all galaxies at $z = 0$ which meet the same mass criteria as the pairs (grayscale hexagons; the black dashed line shows our fiducial SFMS fit), the VIP (diamonds, outlined in black), and the nonVIP (circles). The interacting samples are colored by the change in the log of their star formation rates from the present day to LP. These colors enable mapping from $z = 0$ to LP, and show how the galaxies have evolved since their last close passage. Blue colors indicate that a galaxy has increased its rate of forming stars since LP, whilst red colors indicate a decrease in SFR since LP. The bottom panel of Figure 4.8 shows the VIP and nonVIP distances, defined as Δlog(SFR) = log(SFR)

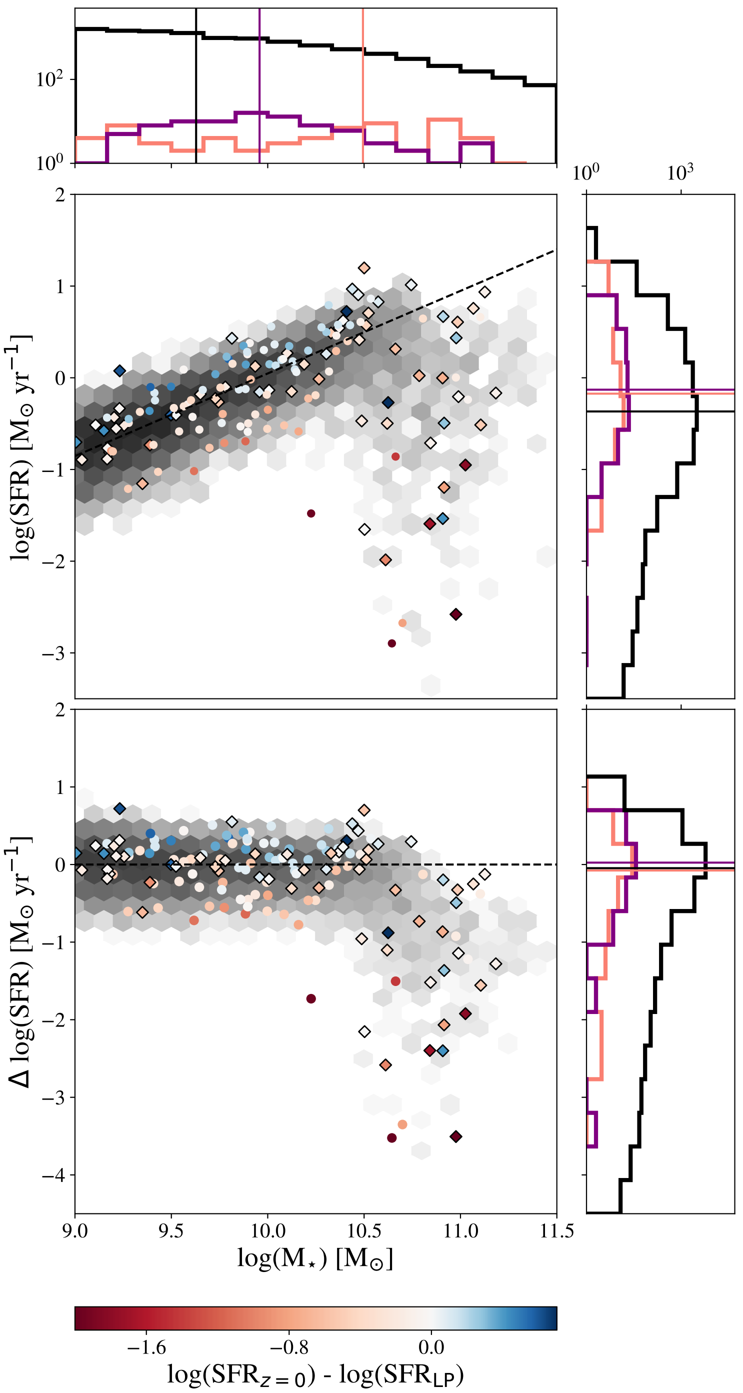

Figure 4.8 *Top:* The SFMS at the present day. The positions of all TNG100-1 galaxies at $z = 0$ which meet the same mass criteria as the pairs are shown in the grayscale hexagons, with the fiducial fit to that SFMS indicated by the black dashed line. The VIP (diamonds, outlined in black) and nonVIP (circles) are colored by the log in the change of their SFR. *Bottom:* Distance from the SFMS fiducial line, Δlog(SFR) for the same samples as above. Despite the fact that the (non)VIP are interacting systems, there is no apparent offset *above* the star formation main sequence, though they are offset from the median value of the total TNG100-1 sample (black solid line). The VIP have more scatter in Δlog(SFR), perhaps indicating that their interaction has triggered a dramatic change in morphology, toward compact quiescent spheroids.

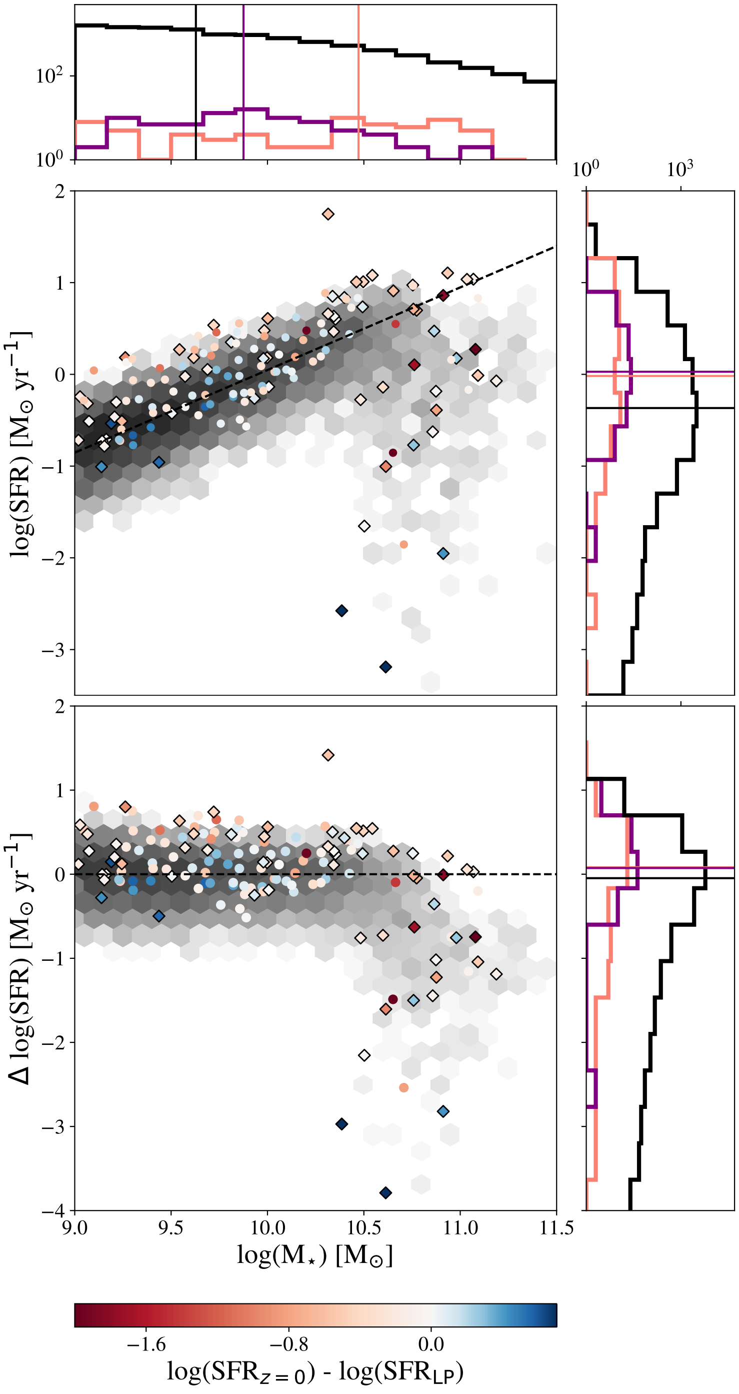

Figure 4.9 The axes and background galaxies are the same as Figure 4.8, but shown here are the VIP and nonVIP at their last close passage. Compared to the present day values, the pairs sit slightly higher on the MS, and fewer of them lie in the green valley.

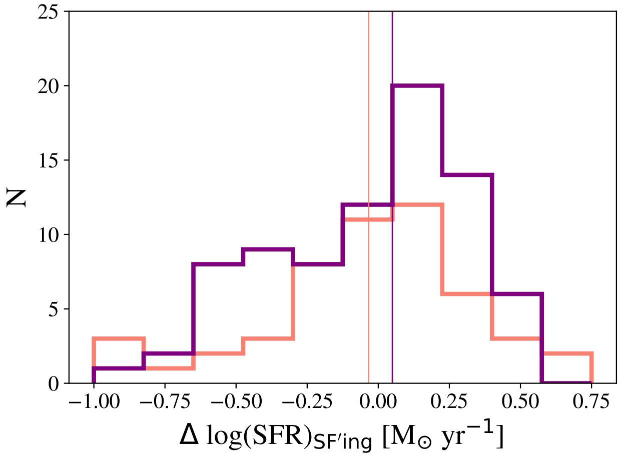

Figure 4.10 The distribution of Δlog(SFR) for all star forming galaxies; median values of the VIP and nonVIP are marked by vertical lines. The star forming VIP appear to have a *lower* median Δlog(SFR).

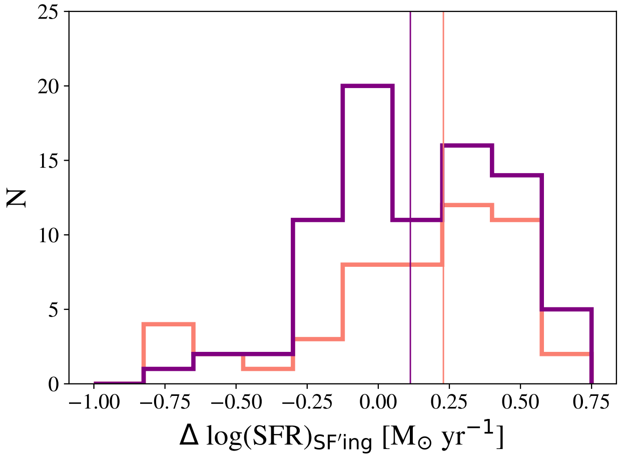

Figure 4.11 At LP, the star forming VIP galaxies have a stronger boost in SFR than the nonVIP, contrary to what was seen at the present day in Figure 4.10.

- log(SFR$|_{\rm MS}$), from the fiducial SFMS line as a function of stellar mass. First, we note that the VIP and nonVIP are consistent with the entire set of local TNG100-1 galaxies. The nonVIP appear to exhibit a tight scatter around the SFMS fiducial line, whilst the VIP display a larger spread. The stellar mass appears to increase with increasing FoF group mass, as is expected from abundance matching (e.g., Colín et al. 1999; Kravtsov & Klypin 1999; Kravtsov et al. 2004; Vale & Ostriker 2004; Conroy & Wechsler 2009; Behroozi et al. 2010; Guo et al. 2010; Moster et al. 2010). That there are more VIP at higher stellar and halo masses (see also Figures 4.2 and 4.3) may indicate the VIP experience a dramatic change in morphology, perhaps toward compact quiescent spheroids (e.g., Ellison et al. 2018).

Regardless of the orbital geometry, the tidal interaction at a pericentre will invariably draw material from the outskirts of each galaxy toward the center (e.g., Barnes & Hernquist 1996; Mihos & Hernquist 1996; Rupke et al. 2010; Moreno et al. 2015; Blumenthal & Barnes 2018). In the case of prograde interactions, a significant amount of gas can be funneled toward the galaxy's nucleus, sparking a burst of star formation (e.g., Alonso-Herrero et al. 2000; Barnes 2004; Evans et al. 2008; Chien & Barnes 2010; Moreno et al. 2015; Larson et al. 2016). Thus, "observing" the VIP and nonVIP at the time of their most recent pericenters would naturally push the points in Figure 4.8 up to higher star formation rates. This is evidenced by Figure 4.9, which shows the star formation main sequence for the pairs at their last pericenters (top), in addition to the distance from the main sequence fiducial line (Δlog(SFR); bottom). The colors in both of these panels are the same as in Figure 4.8. Using these colors, we note that there are some galaxies which appear to move out of the bottom right part of the SFMS (the so-called "red and dead" galaxies) between LP and the present day. This may imply that membership in the various regions of the SFMS is fluid: galaxies might undergo periods of starbursts and relative quiescence (e.g., Forbes et al. 2014a,b).

Figure 4.10 shows the distribution of Δlog(SFR) (that is, the distance above the main sequence line at a fixed stellar mass) for only the star forming VIP and nonVIP. Following observational practices (e.g., Bluck et al. 2014), we define pairs to be "star forming" if they exhibit a Δlog(SFR) $\geq$ -1. The vertical lines indicate the median values of each sample, as before. Interestingly, the nonVIP have a very slightly higher median Δlog(SFR) than the VIP at the present day (~0.05 and ~-0.033, respectively). In Figure 4.11, we show the Δlog(SFR) for the star forming pairs at LP: the star forming VIP galaxies are boosted to higher star formation rates than the star forming nonVIP galaxies. This is most clear when comparing the median values from $z = 0$ to LP: the VIP appear to experience a ~700 per cent boost in Δlog(SFR), whereas the nonVIP

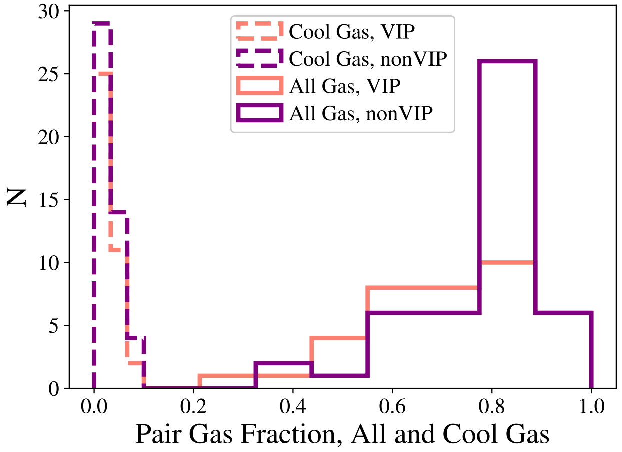

Figure 4.12 Gas fractions for the pairs, split up by the VIP (salmon) and interacting, nonVIP (purple). The cool gas bins are ~0.3 the width of the total gas bins to highlight the structure of the distribution. A dry merger is typically defined as one which has a pair (all) gas fraction of less than 20 per cent; there are no dry mergers in this sample.

Δlog(SFR) increase only by $\sim$ 230 per cent. We note, however, that more work is necessary to quantify the statistical significance of this apparent trend seen in the median values.

The pairs' shift above the main sequence from the present day to LP cannot be explained by the vertical translation of the SFMS with increasing redshift (e.g., Noeske et al. 2007; Lee et al. 2015) alone. If that were true, the VIP should have systematically lower Δlog(SFR) than the nonVIP in Figure 4.9. That this is not the case implies the difference in the merger-driven starbursts is mediated by the strength of the interaction, which we have shown is significantly boosted in the VIP. This is supported by the observation that the VIP have higher stellar masses than the nonVIP (Figure 4.3), and inhabit FoF groups with more massive dark matter haloes (Figure 4.2). Studies have shown (e.g., Sobral et al. 2011) a connection between the stellar mass, star formation rate, and density of environment. In later sections (§4.5.6), we will show that the VIP environment – partially as measured by the total FoF group mass – is marginally more dense than that of the nonVIP.

4.5.4 Gas Content

Figure 4.3 (c) and (d) show that all pairs in the sample contain a significant amount of gas, particularly in the cool phase. We define the pair gas fraction as $f_{\text{gas, pair}} = M_{\text{gas, tot}}/(M_{\text{allgas, tot}} + M_{\star,\text{ tot}})$, following Khochfar & Silk (2009). Figure 4.12 shows the distribution of gas fractions for each galaxy in the VIP, and the nonVIP for both the cool gas (dashed) and all gas (solid). The cool and total gas content tell different stories. In terms of the total gas, there are no dry mergers ($f_{\rm gas,\,pair} \leq 20$ per cent; e.g., Bournaud et al. 2008) in this sample; all pairs have total gas fractions above ~25 per cent. The VIP have a broader (less peaked) distribution than the nonVIP, suggesting that gas-dominated systems are less likely to be captured by a merger scheme based on stellar morphologies. It is plausible (but beyond the scope of this paper) that a merger identification scheme based on the gas-phase morphologies of this sample would have yielded a much higher success rate. From the perspective of the cool gas, however, the VIP and nonVIP appear to have roughly equivalent distributions, which implies that these two samples have similar reservoirs for star formation.

4.5.5 Tidal features

There have been many studies on the production and lifetime of tidal features. For example, Hood et al. (2018) find that gas poor galaxies (defined as $M_{\rm gas}/M_{\star} < 0.1$) are less likely to host tidal features than their gas rich counterparts. The authors note that if a gas poor galaxy does have tidal features, it is likely to reside in a massive halo, to have a high stellar mass, and be close to a neighbour in the same group. Thus, they find that tidal response depends not only on gas content, but on the stellar mass and environment.

Dubinski et al. (1996); Mihos et al. (1998); Barnes & Sanders (1999); Dubinski et al. (1999); Springel & White (1999); Barnes (2016) performed systematic theoretical studies on the tidal response of interacting galaxies, spanning a wide range of galaxy structures. They find that the visibility of tidal features depends heavily on the internal structure of a galaxy (particularly the dark halo mass and concentration); that in some cases, a pair of galaxies may show no obvious signs of interaction. Further, Lotz et al. (2008) have leveraged GADGET (Springel et al. 2001b) simulations of interacting galaxies to determine quantitative morphological metrics, including $G_{\rm ini}$, asymmetry, and M_{20} (e.g., Lotz et al. 2004). The authors use this information to determine when, during the course of an interaction, the tidal response and subsequent morphological disruption is greatest. They find that galaxies tend to exhibit strong tidal features at first pericentre and near final coalescence, whilst the morphologies at intermediate passes may not deviate from a control sample of isolated galaxies.

It is easier to see tidal features shortly after a close passage, when they are at their strongest. The VIP have had a close passage about twice as recently as the nonVIP (Figure 4.5), have higher stellar masses (Figure 4.3), and sit in more massive haloes (Figure 4.2). Further, in the next section, we will show that the VIP reside in denser environments (Figure 4.13). Thus, part of the distinction between the VIP and nonVIP must be due to their tidal features' visibility.

The Failures of Morphological Identification

In ~55 per cent of the pairs here identified, it was unclear if an interaction was underway. There are a number of reasons why morphological identification schema may fail:

1. Due to the finite resolution of the simulations, star particles have relatively large masses. This may inhibit our ability to resolve the fine-grained structures indicative of tidal interactions.

2. The stellar material may not be the best indicator of a tidal interaction (discussed as the "internal properties" in e.g., Darg et al. 2010). The gas disc has been shown to be as large, if not larger than the stellar disc (e.g., Broeils & Rhee 1997). Thus, gas discs are much more likely to be perturbed by one another, even in the case of wide pericentric distances. Integral Field Unit surveys (e.g., Croom et al. 2012; Sánchez et al. 2012; Bundy et al. 2015) of interacting galaxies may be necessary to get a realistic measurement of the local merger rate.

3. The present-day separations (Figure 4.2) are larger than expected from observationally motivated merger catalogues. What observers assume to be the first passage may, in many cases, be the second (e.g., Patton et al. 2013).

4. If encounters are sufficiently wide, tidal forces may not be strong enough to produce visible (i.e. observable) bridges and tails.

5. If an encounter has occurred within the last Gyr, it is more likely to host obvious tidal features. As time passes, material from the bridge and tails settles back into the discs, and is able to phase-mix with the surrounding material (e.g., Lotz et al. 2008, 2010b).

4.5.6 Environment

There is no universal definition of galactic environment (e.g., Muldrew et al. 2012, and references therein). Many studies attempt to compare the various definitions of this fundamental property (e.g., Cooper et al. 2005; Gallazzi et al. 2009; Wilman et al. 2010; Haas et al. 2012; Shattow et al. 2013; Fossati et al. 2017). Parameterizations used to characterize the environment include the local number density (e.g., Dressler 1980; Lewis et al. 2002; Cooper et al. 2005; Shattow et al. 2013), measurements of galaxy clustering (e.g., Skibba et al. 2013, 2015; Gunawardhana et al. 2018), and placement within cosmic structures (e.g., Yang et al. 2007; Darvish et al. 2014; Kuutma et al. 2017; Liao & Gao 2018).

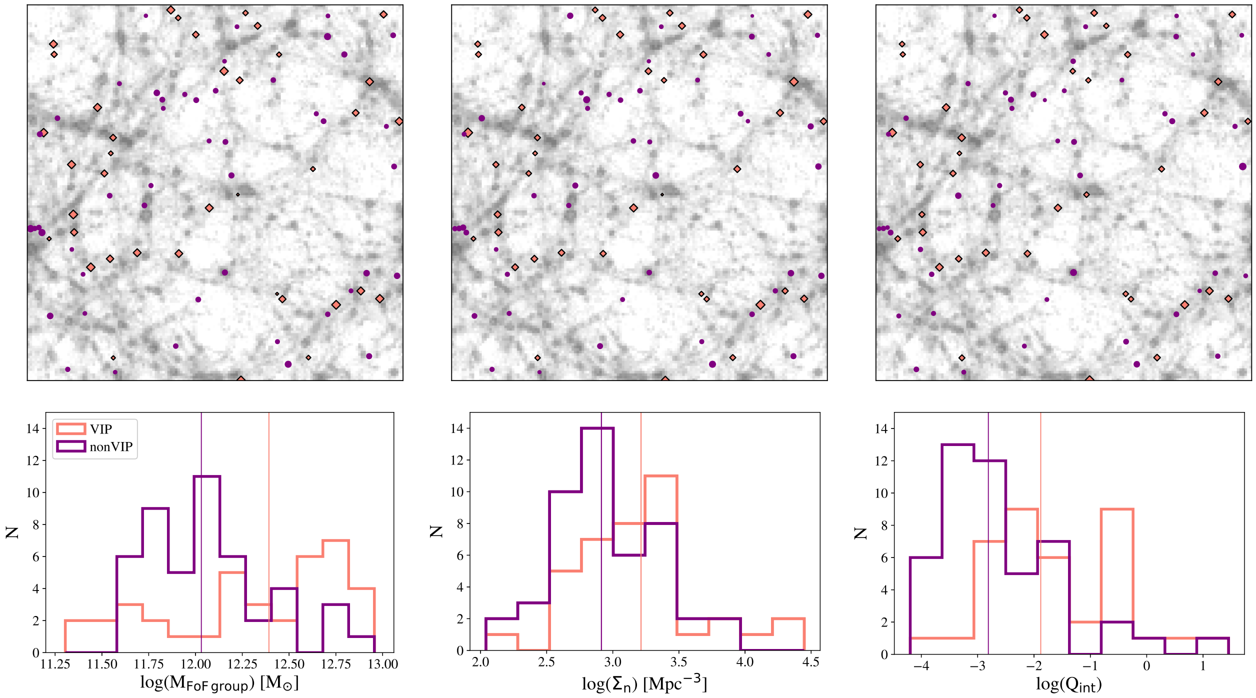

Figure 4.13 *Top:* Placement of the nonVIP (purple circles) and VIP (salmon diamonds) in the TNG100-1 cosmic web. The point sizes are scaled by the total group mass ($M_{\mathrm{FoF\,group}}$, left), nearest neighbour statistic (Σ_n, centre), and the interaction strength (Q_{int}, right). *Bottom:* We also show the distributions of the three environmental measures for the VIP (salmon) and nonVIP (purple), as before. Vertical lines indicate the median values for both subsamples. The VIP sit in significantly more massive haloes, in denser environments and are more affected by their surroundings than the nonVIP.

The top panels of Figure 4.13 show the placement of the VIP (salmon diamonds) and nonVIP (purple circles) samples in the TNG100-1 cosmic web, as traced by all subhalos in the $z = 0$ slice. Qualitatively, the VIP typically lie in denser regions than the nonVIP (which seem to mostly occupy voids). The marker sizes in each of the three panels scale linearly with the log of three independent measures of environment: the total FoF group mass (left, §4.5.6), the $\mathrm{n^{th}}$ nearest neighbor, Σ_n (e.g., Dressler 1980; Lewis et al. 2002, middle, §4.5.6), and the interaction strength, Q_int (e.g., Verley et al. 2007, right, §4.5.6). The structure of the cosmic web is defined by the location of haloes containing individual, groups and clusters of galaxies. Thus, the mass of a halo is indicative of its placement within this structure. The nearest neighbor statistic measures environment based on the number density of nearby galaxies, regardless of mass. On the other hand, the interaction strength measures the balance of external tidal forces from all galaxies within an aperture with the binding force of the galaxy. Whilst it can be difficult to discern any trends from the cosmic web panels, the bottom panels of Figure 4.13 show the subsequent distributions for each of these environmental metrics.

FoF Group Mass

The bottom right panel of Figure 4.13 shows the distribution of FoF group total masses for the VIP (salmon) and nonVIP (purple). This indicates that the VIP sit in preferentially more massive halos ($p \approx 4\mathrm{e}{-4}$), surpassing the nonVIP by nearly half an order of magnitude. This is consistent with the fact that most massive halos are likely to sit in nodes or at intersections of filamentary structures (e.g., Bond et al. 1996; Joachimi et al. 2015, and sources therein).

n^{th} Nearest Neighbour

The $\mathrm{n^{th}}$ nearest neighbour statistic is a number density measurement that uses the distance to the $\mathrm{n^{th}}$ nearest neighbor, $\mathrm{r_n}$, to define the volume. That is,

$$\Sigma_n = \frac{n-1}{\frac{4}{3}\pi \mathrm{r}_n^3} \tag{4.4}$$

where the numerator n−1 is used to discount the central (or, primary) galaxy. (Note that here we employ a three-dimensional version of what is typically used by observers.) Thus, centrals with larger Σ_n sit in denser environments. For the purposes of this paper, we adopt n= 5. The bottom left panel of Figure 4.13 shows that the VIP lie in preferentially denser environments than the nonVIP ($p \approx 0.07$).

Interaction Strength

One major drawback of the Σ_n measure is that it does not account for the mass of neighbouring galaxies. The interaction strength, Q_int, thus serves a useful counterpoint to Σ_n in its careful accounting of the tidal effect of nearby galaxies. Verley et al. (2007) defined the interaction strength as the ratio of the cumulative tidal forces tugging on the galaxy from all neighboring galaxies within a set aperture, and the binding force keeping the central together:

$$Q_{int} \equiv \frac{F_{tidal}}{F_{bind}} \ , \ F_{tidal} = \frac{M_n D_c}{R_{nc}^3} \ , \ F_{bind} = \frac{M_c}{D_c^2} \tag{4.5}$$

where M_n is the mass of the neighbor, R_nc is the distance from the central galaxy to that neighbor, M_c is the mass of the central, and D_c is the diameter of the central. Following observational studies (for which this metric was developed), we take all masses to be the total mass within twice the stellar half-mass radius, and the diameter of the central galaxy which corresponds to that mass (that is, four times the stellar half-mass radius). This value is calculated in a number of different ways in Verley et al. (2007), including using a fixed and infinite aperture (that is, all galaxies within a fixed volume). They find that there was very little difference between the two, as distant galaxies will contribute only a small amount to the tidal field of the central. To accommodate the large present-day separations of some of our interacting pairs, we use an aperture of 5 Mpc (Figure 4.13, bottom right). The VIP are affected by the tidal effects of their neighbors nearly ten times as much as the nonVIP ($p \approx$ 7e−4).

The Effects of Environment

In the previous subsections, we demonstrated that the VIP belong to more massive FoF haloes, sit in denser environments, and are more affected by interactions with their neighbors than the nonVIP. Here we disentangle the effects of mass and environment and show that although the (more massive) VIP are in systematically more dense environments, there is no statistically significant difference between the Δlog(SFR) of the nonVIP and VIP, when controlling for stellar mass.

Figure 4.14 shows the Δlog(SFR) as a function of stellar mass (similar to Figures 4.10 and 4.11). The stellar mass distribution is split into three bins: $9.0 \leq \log(\mathrm{M}_\star) < 9.75$, $9.75 \leq \log(\mathrm{M}_\star) < 10.5$, and $\log(\mathrm{M}_\star) \geq 10.5$. These mass increments were chosen to separately analyze “normal” star forming galaxies ($\log(\mathrm{M}_\star) < 10.5$) from those which have begun to dip below the main sequence ($\log(\mathrm{M}_\star) \geq 10.5$). Environment is considered independently within each of these bins. Different colors indicate the galaxies which sit in a relatively low (light colors) or high (dark colors) density environment. The median environmental measure in each mass bin is used to delineate between low and high densities. We present this in Figure 4.14 for the $\mathrm{M_{FoF\,group}}$ (top), Σ_n (middle) and $\mathrm{Q_{int}}$ (bottom). As before, the VIP and nonVIP are distinguished by diamond and circle markers, respectively. Centrals and satellites are indicated by the marker size (large and small, respectively). The median Δlog(SFR) values for both environment bins within each mass bin are displayed as stars with error bars indicating the first and third quartiles (that is, the width of the distribution). For comparison, the median value of Δlog(SFR) of the underlying TNG100-1 distribution is displayed by the X's.

The first two mass bins of all three environmental metrics shown in Figure 4.14 show no clear trend with environment. That is, not only do they show no distinction between high and low density environments, but they are consistent with the background distribution of all TNG100-1 galaxies (colored X's). Only in the largest mass bin do we see any significant difference between the low and high density environments across all samples. In the largest mass bin of the top panel ($\mathrm{M_{FoF\,group}}$), the less massive FoF groups have systematically higher Δlog(SFR) than the high mass FoF groups, as these are likely quenched or are in the process of quenching. It should be noted however that in this panel, the interacting pair sample (and its individual components) are consistent with the background.

The middle and bottom panels of Figure 4.14 indicate that denser environments foster higher star formation rates only within the highest mass bin. Whereas before, the interacting galaxies behaved similarly to the background TNG100-1 galaxies, in the Σ_n and $\mathrm{Q_{int}}$ panels, the interacting pairs diverge significantly from the background TNG100-1 galaxies. Further, that the environmental dependence of Δlog(SFR) only becomes appreciable at higher masses – when AGN activity and quenching begin to dominate a galaxy's evolution – implies environment plays a larger role in suppressing quenching than it does in boosting star formation.

Though there is no clear distinction between the VIP and nonVIP at any mass bin (except for the highest mass bin of $\mathrm{Q_{int}}$), the satellites and centrals appear to have divergent evolutionary pathways. The centrals dip low in Δlog(SFR) at high masses whereas the satellites are only moderately affected. This implies that centrals are likely to quench before their satellites. It may be that the evolution of satellites is more sensitive to environment, whilst the evolution of centrals is depends more strongly upon mass; perhaps an example of the interplay between "environment quenching" and "mass quenching" (e.g., Peng et al. 2010; Bluck et al.

2016). Thus, the relative importance of environment and stellar mass depends upon which component of the interaction is the subject of inquiry.

4.6 Conclusions

In this paper, we identify a set of paired galaxies from the $z = 0$ snapshot of the TNG100-1 simulation of IllustrisTNG (Marinacci et al. 2018; Naiman et al. 2018; Nelson et al. 2018; Pillepich et al. 2018a; Springel et al. 2018). We generate ideal mock SDSS g-band images of all pairs and visually classify each as interacting or not interacting. We then confirm using the information from the Sublink merger tree, and find that of the 85 interacting pairs, we correctly identify 38 (the Visually Identified Pairs, or VIP) and miss 47 (the Non-Visually Identified Pairs, or nonVIP). Our analysis includes a detailed study of the pairs' present day properties, as well as their properties at their respective last pericenters.

Our primary findings are as follows:

1. Stellar morphologies are not ideal for identifying interactions. The gas phase morphology may well prove more illustrative.

2. Using the merger trees, we trace the interacting pairs back to their time of last pericentric (LP) passage. Compared to the present day, the VIP experience a starburst at their LP that is nearly three times stronger than the nonVIP.

3. The VIP have more recently undergone a close passage than the nonVIP by about a factor of two. As a result, their tidal features are easier to observe. Merger classifications are thus biased toward recent interactions.

4. Compared with the nonVIP, the VIP sit in very different environments. The VIP are: in groups which are nearly 2.5 times as massive; in nearly twice as dense surroundings; and are affected by interactions with their neighbors by nearly an order of magnitude more than the nonVIP. Classification schema based on stellar morphologies are biased toward dense environments within the adopted $\mathrm{M_{FoF}}$ regime.

5. Though the VIP sit in distinct environments from the nonVIP, the visibility of a pair does not depend strongly on environment, when correcting for stellar mass.

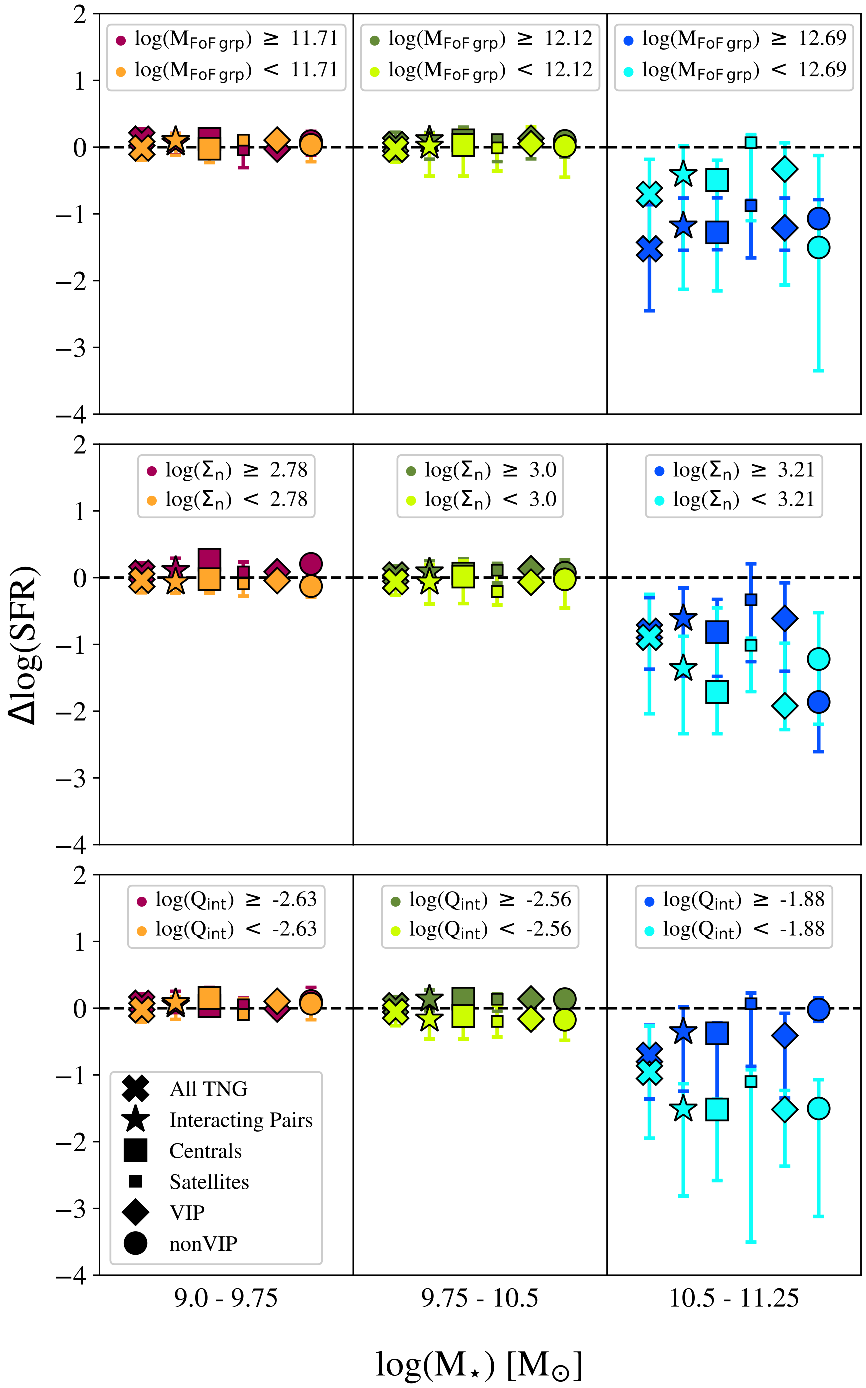

Figure 4.14 We separate the stellar mass into three bins, and further split the subsample into two environmental bins based on the median environmental measure in that mass bin. Stars indicate the median value of Δlog(SFR) for all interacting pairs within each mass bin with “error bars” that correspond to the 25th and 75th percentiles. Markers represent the the median Δlog(SFR) for the galaxies within that mass bin. This is shown for the FoF group mass (top), Σ_n (middle), and Q_{int} (bottom). X’s represent the background distribution of all TNG100-1 galaxies. Stars indicate the sample of interacting pairs (that is, the VIP and nonVIP together). As before, the nonVIP and VIP are indicated by circles and outlined diamonds, respectively. Satellites and centrals are also shown, and are distinguished by symbol size: small and large, respectively.

6. Care should be taken when interpreting these results within the context of large observational catalogues, as the mass range covered in this work is relatively limited. The roughly 45% merger recovery rate that we present above should *not* be taken as a completeness correction. To arrive at such a correction would require a much larger survey of cosmological pairs (perhaps that go back to $z = 0.1$) that span a wide range in masses and environmental properties.

In addition to the intrinsic and dynamic properties of galaxies, the production of tidal features depends on the interaction geometry. In the next chapter, (Blumenthal et al. *in prep*), we investigate the orbital characteristics of the interacting pairs sample. This work will provide a realistic set of parameters from which to produce the initial conditions of future idealized simulations, including the eccentricities, inclinations, and first pericentric separations. Additionally, we will assess orbital stability and the validity of the Keplerian approximation.

References

Alonso-Herrero, A., Rieke, G. H., Rieke, M. J., & Scoville, N. Z. 2000, ApJ, 532, 845

Arp, H. 1966, The Astrophysical Journal Supplement Series, 14, 1

Barnes, J. E. 2004, MNRAS, 350, 798

—. 2016, MNRAS, 455, 1957

Barnes, J. E. & Hernquist, L. 1992, Annual Review of Astronomy and Astrophysics, 30, 705

—. 1996, ApJ, 471, 115

Barnes, J. E. & Hernquist, L. E. 1991, ApJ, 370, L65

Barnes, J. E. & Sanders, D., eds. 1999, Proc. IAU Symposium, Vol. 186, Galaxy Interactions at Low and High Redshift, ed. J. E. Barnes & D. Sanders

Barro, G., Faber, S. M., Pérez-González, P. G., Koo, D. C., Williams, C. C., Kocevski, D. D., Trump, J. R., Mozena, M., McGrath, E., van der Wel, A., Wuyts, S., Bell, E. F., Croton, D. J., Ceverino, D., Dekel, A., Ashby, M. L. N., Cheung, E., Ferguson, H. C., Fontana, A., Fang, J., Giavalisco, M., Grogin, N. A., Guo, Y., Hathi, N. P., Hopkins, P. F., Huang, K.-H., Koekemoer, A. M., Kartaltepe, J. S., Lee, K.-S., Newman, J. A., Porter, L. A., Primack, J. R., Ryan, R. E., Rosario, D., Somerville, R. S., Salvato, M., & Hsu, L.-T. 2013, ApJ, 765, 104

Behroozi, P. S., Conroy, C., & Wechsler, R. H. 2010, ApJ, 717, 379

Bezanson, R., van Dokkum, P. G., Tal, T., Marchesini, D., Kriek, M., Franx, M., & Coppi, P. 2009, ApJ, 697, 1290

Bluck, A. F. L., Bottrell, C., Teimoorinia, H., Henriques, B. M. B., Mendel, J. T., Ellison, S. L., Thanjavur, K., Simard, L., Patton, D. R., Conselice, C. J., Moreno, J., & Woo, J. 2019, MNRAS, 363

Bluck, A. F. L., Conselice, C. J., Buitrago, F., Grützbauch, R., Hoyos, C., Mortlock, A., & Bauer, A. E. 2012, ApJ, 747, 34

Bluck, A. F. L., Mendel, J. T., Ellison, S. L., Moreno, J., Simard, L., Patton, D. R., & Starkenburg, E. 2014, MNRAS, 441, 599

Bluck, A. F. L., Mendel, J. T., Ellison, S. L., Patton, D. R., Simard, L., Henriques, B. M. B., Torrey, P., Teimoorinia, H., Moreno, J., & Starkenburg, E. 2016, MNRAS, 462, 2559

Blumenthal, K. A. & Barnes, J. E. 2018, MNRAS, 479, 3952

Bond, J. R., Kofman, L., & Pogosyan, D. 1996, Nature, 380, 603

Bottrell, C., Torrey, P., Simard, L., & Ellison, S. L. 2017, MNRAS, 467, 2879

Bouché, N., Dekel, A., Genzel, R., Genel, S., Cresci, G., Förster Schreiber, N. M., Shapiro, K. L., Davies, R. I., & Tacconi, L. 2010, ApJ, 718, 1001

Bournaud, F., Chapon, D., Teyssier, R., Powell, L. C., Elmegreen, B. G., Elmegreen, D. M., Duc, P.-A., Contini, T., Epinat, B., & Shapiro, K. L. 2011, ApJ, 730, 4

Bournaud, F., Duc, P. A., & Emsellem, E. 2008, MNRAS, 389, L8

Bournaud, F. & Elmegreen, B. G. 2009, ApJ, 694, L158

Brennan, R., Pandya, V., Somerville, R. S., Barro, G., Bluck, A. F. L., Taylor, E. N., Wuyts, S., Bell, E. F., Dekel, A., Faber, S., Ferguson, H. C., Koekemoer, A. M., Kurczynski, P., McIntosh, D. H., Newman, J. A., & Primack, J. 2017, MNRAS, 465, 619

Brennan, R., Pandya, V., Somerville, R. S., Barro, G., Taylor, E. N., Wuyts, S., Bell, E. F., Dekel, A., Ferguson, H. C., McIntosh, D. H., Papovich, C., & Primack, J. 2015, MNRAS, 451, 2933

Bridge, C. R., Appleton, P. N., Conselice, C. J., Choi, P. I., Armus, L., Fadda, D., Laine, S., Marleau, F. R., Carlberg, R. G., Helou, G., & Yan, L. 2007, ApJ, 659, 931

Bridge, C. R., Carlberg, R. G., & Sullivan, M. 2010, ApJ, 709, 1067

Broeils, A. H. & Rhee, M.-H. 1997, A&A, 324, 877

Bruzual, G. & Charlot, S. 2003, MNRAS, 344, 1000

Buitrago, F., Trujillo, I., Conselice, C. J., Bouwens, R. J., Dickinson, M., & Yan, H. 2008, ApJ, 687, L61

Bundy, K., Bershady, M. A., Law, D. R., Yan, R., Drory, N., MacDonald, N., Wake, D. A., Cherinka, B., Sánchez-Gallego, J. R., Weijmans, A.-M., Thomas, D., Tremonti, C., Masters, K., Coccato, L., Diamond-Stanic, A. M., Aragón-Salamanca, A., Avila-Reese, V., Badenes, C., Falcón-Barroso, J., Belfiore, F., Bizyaev, D., Blanc, G. A., Bland- Hawthorn, J., Blanton, M. R., Brownstein, J. R., Byler, N., Cappellari, M., Conroy, C., Dutton, A. A., Emsellem, E., Etherington, J., Frinchaboy, P. M., Fu, H., Gunn, J. E., Harding, P., Johnston, E. J., Kauffmann, G., Kinemuchi, K., Klaene, M. A., Knapen, J. H., Leauthaud, A., Li, C., Lin, L., Maiolino, R., Malanushenko, V., Malanushenko, E., Mao, S., Maraston, C., McDermid, R. M., Merrifield, M. R., Nichol, R. C., Oravetz, D., Pan, K., Parejko, J. K., Sanchez, S. F., Schlegel, D., Simmons, A., Steele, O., Steinmetz, M., Thanjavur, K., Thompson, B. A., Tinker, J. L., van den Bosch, R. C. E., Westfall, K. B., Wilkinson, D., Wright, S., Xiao, T., & Zhang, K. 2015, ApJ, 798, 7

Bundy, K., Fukugita, M., Ellis, R. S., Kodama, T., & Conselice, C. J. 2004, ApJ, 601, L123

Bundy, K., Fukugita, M., Ellis, R. S., Targett, T. A., Belli, S., & Kodama, T. 2009, ApJ, 697, 1369

Chien, L.-H. & Barnes, J. E. 2010, MNRAS, 407, 43

Colín, P., Klypin, A. A., Kravtsov, A. V., & Khokhlov, A. M. 1999, ApJ, 523, 32

Conroy, C. & Wechsler, R. H. 2009, ApJ, 696, 620

Conselice, C. J. 2006, ApJ, 638, 686

Conselice, C. J., Grogin, N. A., Jogee, S., Lucas, R. A., Dahlen, T., de Mello, D., Gardner, J. P., Mobasher, B., & Ravindranath, S. 2004, ApJ, 600, L139

Cooper, M. C., Newman, J. A., Madgwick, D. S., Gerke, B. F., Yan, R., & Davis, M. 2005, ApJ, 634, 833

Côté, P., Marzke, R. O., & West, M. J. 1998, ApJ, 501, 554

Cox, T. J., Jonsson, P., Somerville, R. S., Primack, J. R., & Dekel, A. 2008, MNRAS, 384, 386

Croom, S. M., Lawrence, J. S., Bland-Hawthorn, J., Bryant, J. J., Fogarty, L., Richards, S., Goodwin, M., Farrell, T., Miziarski, S., Heald, R., Jones, D. H., Lee, S., Colless, M., Brough, S., Hopkins, A. M., Bauer, A. E., Birchall, M. N., Ellis, S., Horton, A., Leon-Saval, S., Lewis, G., López-Sánchez, Á. R., Min, S.-S., Trinh, C., & Trowland, H. 2012, MNRAS, 421, 872

Cutri, R. M. & McAlary, C. W. 1985, ApJ, 296, 90

Daddi, E., Dickinson, M., Morrison, G., Chary, R., Cimatti, A., Elbaz, D., Frayer, D., Renzini, A., Pope, A., Alexander, D. M., Bauer, F. E., Giavalisco, M., Huynh, M., Kurk, J., & Mignoli, M. 2007, ApJ, 670, 156

Dahari, O. 1985, The Astrophysical Journal Supplement Series, 57, 643

Darg, D. W., Kaviraj, S., Lintott, C. J., Schawinski, K., Sarzi, M., Bamford, S., Silk, J., Andreescu, D., Murray, P., Nichol, R. C., Raddick, M. J., Slosar, A., Szalay, A. S., Thomas, D., & Vandenberg, J. 2010, MNRAS, 401, 1552

Darvish, B., Sobral, D., Mobasher, B., Scoville, N. Z., Best, P., Sales, L. V., & Smail, I. 2014, ApJ, 796, 51

Davis, M., Efstathiou, G., Frenk, C. S., & White, S. D. M. 1985, ApJ, 292, 371

Dekel, A., Sari, R., & Ceverino, D. 2009, ApJ, 703, 785

Di Matteo, P., Bournaud, F., Martig, M., Combes, F., Melchior, A. L., & Semelin, B. 2008, A&A, 492, 31

Di Matteo, P., Combes, F., Melchior, A.-L., & Semelin, B. 2007, A&A, 468, 61

Donnari, M., Pillepich, A., Nelson, D., Vogelsberger, M., Genel, S., Weinberger, R., Marinacci, F., Springel, V., & Hernquist, L. 2019, MNRAS, 485, 4817

Dressler, A. 1980, ApJ, 236, 351

Dubinski, J., Mihos, J. C., & Hernquist, L. 1996, ApJ, 462, 576

—. 1999, ApJ, 526, 607

Duc, P.-A., Bournaud, F., & Masset, F. 2004, A&A, 427, 803

Elbaz, D., Daddi, E., Le Borgne, D., Dickinson, M., Alexander, D. M., Chary, R. R., Starck, J. L., Brandt, W. N., Kitzbichler, M., MacDonald, E., Nonino, M., Popesso, P., Stern, D., & Vanzella, E. 2007, A&A, 468, 33

Ellison, S. L., Patton, D. R., Mendel, J. T., & Scudder, J. M. 2011, MNRAS, 418, 2043

Ellison, S. L., Patton, D. R., Simard, L., McConnachie, A. W., Baldry, I. K., & Mendel, J. T. 2010, MNRAS, 407, 1514

Ellison, S. L., Sánchez, S. F., Ibarra-Medel, H., Antonio, B., Mendel, J. T., & Barrera-Ballesteros, J. 2018, MNRAS, 474, 2039

Evans, A. S., Vavilkin, T., Pizagno, J., Modica, F., Mazzarella, J. M., Iwasawa, K., Howell, J. H., Surace, J. A., Armus, L., Petric, A. O., Spoon, H. W. W., Barnes, J. E., Suer, T. A., Sanders, D. B., Chan, B., & Lord, S. 2008, ApJ, 675, L69

Faucher-Giguère, C.-A., Lidz, A., Zaldarriaga, M., & Hernquist, L. 2009, ApJ, 703, 1416

Forbes, J. C., Krumholz, M. R., Burkert, A., & Dekel, A. 2014a, MNRAS, 438, 1552

—. 2014b, MNRAS, 443, 168

Fossati, M., Wilman, D. J., Mendel, J. T., Saglia, R. P., Galametz, A., Beifiori, A., Bender, R., Chan, J. C. C., Fabricius, M., Bandara, K., Brammer, G. B., Davies, R., Förster Schreiber, N. M., Genzel, R., Hartley, W., Kulkarni, S. K., Lang, P., Momcheva, I. G., Nelson, E. J., Skelton, R., Tacconi, L. J., Tadaki, K., Übler, H., van Dokkum, P. G., Wisnioski, E., Whitaker, K. E., Wuyts, E., & Wuyts, S. 2017, ApJ, 835, 153

Gallazzi, A., Bell, E. F., Wolf, C., Gray, M. E., Papovich, C., Barden, M., Peng, C. Y., Meisenheimer, K., Heymans, C., van Kampen, E., Gilmour, R., Balogh, M., McIntosh, D. H., Bacon, D., Barazza, F. D., Böhm, A., Caldwell, J. A. R., Häußler, B., Jahnke, K., Jogee, S., Lane, K., Robaina, A. R., Sanchez, S. F., Taylor, A., Wisotzki, L., & Zheng, X. 2009, ApJ, 690, 1883

Genel, S., Vogelsberger, M., Springel, V., Sijacki, D., Nelson, D., Snyder, G., Rodriguez-Gomez, V., Torrey, P., & Hernquist, L. 2014, MNRAS, 445, 175

Genzel, R., Burkert, A., Bouché, N., Cresci, G., Förster Schreiber, N. M., Shapley, A., Shapiro, K., Tacconi, L. J., Buschkamp, P., Cimatti, A., Daddi, E., Davies, R., Eisenhauer, F., Erb, D. K., Genel, S., Gerhard, O., Hicks, E., Lutz, D., Naab, T., Ott, T., Rabien, S., Renzini, A., Steidel, C. C., Sternberg, A., & Lilly, S. J. 2008, ApJ, 687, 59

Gunawardhana, M. L. P., Norberg, P., Zehavi, I., Farrow, D. J., Loveday, J., Hopkins, A. M., Davies, L. J. M., Wang, L., Alpaslan, M., Bland- Hawthorn, J., Brough, S., Holwerda, B. W., Owers, M. S., & Wright, A. H. 2018, MNRAS, 479, 1433

Guo, Q., White, S., Li, C., & Boylan-Kolchin, M. 2010, MNRAS, 404, 1111

Haas, M. R., Schaye, J., & Jeeson-Daniel, A. 2012, MNRAS, 419, 2133

Habouzit, M., Volonteri, M., Somerville, R. S., Dubois, Y., Peirani, S., Pichon, C., & Devriendt, J. 2018, arXiv e-prints, arXiv:1810.11535

Heckman, T. M., Beckwith, S., Blitz, L., Skrutskie, M., & Wilson, A. S. 1986a, ApJ, 305, 157

Heckman, T. M., Smith, E. P., Baum, S. A., van Breugel, W. J. M., Miley, G. K., Illingworth, G. D., Bothun, G. D., & Balick, B. 1986b, ApJ, 311, 526

Hewlett, T., Villforth, C., Wild, V., Mendez-Abreu, J., Pawlik, M., & Rowlands, K. 2017, MNRAS, 470, 755

Hood, C. E., Kannappan, S. J., Stark, D. V., Dell'Antonio, I. P., Moffett, A. J., Eckert, K. D., Norris, M. A., & Hendel, D. 2018, ApJ, 857, 144

Hopkins, P. F., Cox, T. J., Hernquist, L., Narayanan, D., Hayward, C. C., & Murray, N. 2013, MNRAS, 430, 1901

Hopkins, P. F., Hernquist, L., Cox, T. J., & Kereš, D. 2008, The Astrophysical Journal Supplement Series, 175, 356

Huertas-Company, M., Rodriguez-Gomez, V., Nelson, D., Pillepich, A., Bernardi, M., Domínguez-Sánchez, H., Genel, S., Pakmor, R., Snyder, G. F., & Vogelsberger, M. 2019, arXiv e-prints, arXiv:1903.07625

Hung, C.-L., Sanders, D. B., Casey, C. M., Lee, N., Barnes, J. E., Capak, P., Kartaltepe, J. S., Koss, M., Larson, K. L., Le Floc'h, E., Lockhart, K., Man, A. W. S., Mann, A. W., Riguccini, L., Scoville, N., & Symeonidis, M. 2013, ApJ, 778, 129

Joachimi, B., Cacciato, M., Kitching, T. D., Leonard, A., Mandelbaum, R., Schäfer, B. M., Sifón, C., Hoekstra, H., Kiessling, A., Kirk, D., & Rassat, A. 2015, Space Sci. Rev., 193, 1

Jogee, S., Miller, S. H., Penner, K., Skelton, R. E., Conselice, C. J., Somerville, R. S., Bell, E. F., Zheng, X. Z., Rix, H.-W., Robaina, A. R., Barazza, F. D., Barden, M., Borch, A., Beckwith, S. V. W., Caldwell, J. A. R., Peng, C. Y., Heymans, C., McIntosh, D. H., Häußler, B., Jahnke, K., Meisenheimer, K., Sanchez, S. F., Wisotzki, L., Wolf, C., & Papovich, C. 2009, ApJ, 697, 1971

Joseph, R. D. & Wright, G. S. 1985, MNRAS, 214, 87

Kartaltepe, J. S., Sanders, D. B., Scoville, N. Z., Calzetti, D., Capak, P., Koekemoer, A., Mobasher, B., Murayama, T., Salvato, M., Sasaki, S. S., & Taniguchi, Y. 2007, The Astrophysical Journal Supplement Series, 172, 320

Katz, N., Weinberg, D. H., & Hernquist, L. 1996, ApJS, 105, 19

Kennicutt, Robert C., J., Keel, W. C., van der Hulst, J. M., Hummel, E., & Roettiger, K. A. 1987, AJ, 93, 1011

Khochfar, S. & Silk, J. 2009, MNRAS, 397, 506

Knierman, K. A., Gallagher, S. C., Charlton, J. C., Hunsberger, S. D., Whitmore, B., Kundu, A., Hibbard, J. E., & Zaritsky, D. 2003, AJ, 126, 1227

Kravtsov, A. V., Berlind, A. A., Wechsler, R. H., Klypin, A. A., Gottlöber, S., Allgood, B., & Primack, J. R. 2004, ApJ, 609, 35

Kravtsov, A. V. & Klypin, A. A. 1999, ApJ, 520, 437

Kuutma, T., Tamm, A., & Tempel, E. 2017, A&A, 600, L6

Larson, K. L., Sanders, D. B., Barnes, J. E., Ishida, C. M., Evans, A. S., U, V., Mazzarella, J. M., Kim, D.-C., Privon, G. C., Mirabel, I. F., & Flewelling, H. A. 2016, ApJ, 825, 128

Lee, N., Sanders, D. B., Casey, C. M., Toft, S., Scoville, N. Z., Hung, C.-L., Le Floc'h, E., Ilbert, O., Zahid, H. J., Aussel, H., Capak, P., Kartaltepe, J. S., Kewley, L. J., Li, Y., Schawinski, K., Sheth, K., & Xiao, Q. 2015, ApJ, 801, 80

Lewis, I., Balogh, M., De Propris, R., Couch, W., Bower, R., Offer, A., Bland-Hawthorn, J., Baldry, I. K., Baugh, C., Bridges, T., Cannon, R., Cole, S., Colless, M., Collins, C., Cross, N., Dalton, G., Driver, S. P., Efstathiou, G., Ellis, R. S., Frenk, C. S., Glazebrook, K., Hawkins, E., Jackson, C., Lahav, O., Lumsden, S., Maddox, S., Madgwick, D., Norberg, P., Peacock, J. A., Percival, W., Peterson, B. A., Sutherland, W., & Taylor, K. 2002, MNRAS, 334, 673

Liao, S. & Gao, L. 2018, arXiv e-prints, arXiv:1805.10944

Lilly, S. J., Carollo, C. M., Pipino, A., Renzini, A., & Peng, Y. 2013, ApJ, 772, 119

Lintott, C. J., Schawinski, K., Slosar, A., Land, K., Bamford, S., Thomas, D., Raddick, M. J., Nichol, R. C., Szalay, A., Andreescu, D., Murray, P., & Vandenberg, J. 2008, MNRAS, 389, 1179

Lotz, J. M., Jonsson, P., Cox, T. J., Croton, D., Primack, J. R., Somerville, R. S., & Stewart, K. 2011, ApJ, 742, 103

Lotz, J. M., Jonsson, P., Cox, T. J., & Primack, J. R. 2008, MNRAS, 391, 1137

—. 2010a, MNRAS, 404, 590

—. 2010b, MNRAS, 404, 575

Lotz, J. M., Madau, P., Giavalisco, M., Primack, J., & Ferguson, H. C. 2006, ApJ, 636, 592

Lotz, J. M., Primack, J., & Madau, P. 2004, AJ, 128, 163

Malin, D. & Hadley, B. 1997, Publications of the Astronomical Society of Australia, 14, 52

Mantha, K. B., McIntosh, D. H., Brennan, R., Ferguson, H. C., Kodra, D., Newman, J. A., Rafelski, M., Somerville, R. S., Conselice, C. J., Cook, J. S., Hathi, N. P., Koo, D. C., Lotz, J. M., Simmons, B. D., Straughn, A. N., Snyder, G. F., Wuyts, S., Bell, E. F., Dekel, A., Kartaltepe, J., Kocevski, D. D., Koekemoer, A. M., Lee, S.-K., Lucas, R. A., Pacifici, C., Peth, M. A., Barro, G., Dahlen, T., Finkelstein, S. L., Fontana, A., Galametz, A., Grogin, N. A., Guo, Y., Mobasher, B., Nayyeri, H., Pérez-González, P. G., Pforr, J., Santini, P., Stefanon, M., & Wiklind, T. 2018, MNRAS, 475, 1549

Marinacci, F., Vogelsberger, M., Pakmor, R., Torrey, P., Springel, V., Hernquist, L., Nelson, D., Weinberger, R., Pillepich, A., Naiman, J., & Genel, S. 2018, MNRAS, 480, 5113

Mihos, J. C. 1995, ApJ, 438, L75

Mihos, J. C., Dubinski, J., & Hernquist, L. 1998, ApJ, 494, 183

Mihos, J. C. & Hernquist, L. 1996, ApJ, 464, 641

Mihos, J. C., Walker, I. R., Hernquist, L., Mendes de Oliveira, C., & Bolte, M. 1995, ApJ, 447, L87

Mirabel, I. F., Vigroux, L., Charmandaris, V., Sauvage, M., Gallais, P., Tran, D., Cesarsky, C., Madden, S. C., & Duc, P.-A. 1998, A&A, 333, L1

Moreno, J. 2012, MNRAS, 419, 411

Moreno, J., Bluck, A. F. L., Ellison, S. L., Patton, D. R., Torrey, P., & Moster, B. P. 2013, MNRAS, 436, 1765

Moreno, J., Torrey, P., Ellison, S. L., Patton, D. R., Bluck, A. F. L., Bansal, G., & Hernquist, L. 2015, MNRAS, 448, 1107

Moreno, J., Torrey, P., Ellison, S. L., Patton, D. R., Hopkins, P. F., Bueno, M., Hayward, C. C., Narayanan, D., Kereš, D., Bluck, A. F. L., & Hernquist, L. 2019, MNRAS, 485, 1320

Moster, B. P., Macciò, A. V., & Somerville, R. S. 2014, MNRAS, 437, 1027

Moster, B. P., Somerville, R. S., Maulbetsch, C., van den Bosch, F. C., Macciò, A. V., Naab, T., & Oser, L. 2010, ApJ, 710, 903

Muldrew, S. I., Croton, D. J., Skibba, R. A., Pearce, F. R., Ann, H. B., Baldry, I. K., Brough, S., Choi, Y.-Y., Conselice, C. J., Cowan, N. B., Gallazzi, A., Gray, M. E., Grützbauch, R., Li, I. H., Park, C., Pilipenko, S. V., Podgorzec, B. J., Robotham, A. S. G., Wilman, D. J., Yang, X., Zhang, Y., & Zibetti, S. 2012, MNRAS, 419, 2670

Mundy, C. J., Conselice, C. J., Duncan, K. J., Almaini, O., Häußler, B., & Hartley, W. G. 2017, MNRAS, 470, 3507

Naiman, J. P., Pillepich, A., Springel, V., Ramirez-Ruiz, E., Torrey, P., Vogelsberger, M., Pakmor, R., Nelson, D., Marinacci, F., Hernquist, L., Weinberger, R., & Genel, S. 2018, MNRAS, 477, 1206

Nelson, D., Pillepich, A., Springel, V., Pakmor, R., Weinberger, R., Genel, S., Torrey, P., Vogelsberger, M., Marinacci, F., & Hernquist, L. 2019, arXiv e-prints, arXiv:1902.05554

Nelson, D., Pillepich, A., Springel, V., Weinberger, R., Hernquist, L., Pakmor, R., Genel, S., Torrey, P., Vogelsberger, M., Kauffmann, G., Marinacci, F., & Naiman, J. 2018, MNRAS, 475, 624

Noeske, K. G., Weiner, B. J., Faber, S. M., Papovich, C., Koo, D. C., Somerville, R. S., Bundy, K., Conselice, C. J., Newman, J. A., Schiminovich, D., Le Floc'h, E., Coil, A. L., Rieke, G. H., Lotz, J. M., Primack, J. R., Barmby, P., Cooper, M. C., Davis, M., Ellis, R. S., Fazio, G. G., Guhathakurta, P., Huang, J., Kassin, S. A., Martin, D. C., Phillips, A. C., Rich, R. M., Small, T. A., Willmer, C. N. A., & Wilson, G. 2007, ApJ, 660, L43

Pakmor, R., Bauer, A., & Springel, V. 2011, MNRAS, 418, 1392

Pakmor, R., Springel, V., Bauer, A., Mocz, P., Munoz, D. J., Ohlmann, S. T., Schaal, K., & Zhu, C. 2016, MNRAS, 455, 1134

Patton, D. R., Torrey, P., Ellison, S. L., Mendel, J. T., & Scudder, J. M. 2013, MNRAS, 433, L59

Pearson, W. J., Wang, L., Trayford, J. W., Petrillo, C. E., & van der Tak, F. F. S. 2019, arXiv e-prints, arXiv:1902.10626

Peng, Y.-j., Lilly, S. J., Kovač, K., Bolzonella, M., Pozzetti, L., Renzini, A., Zamorani, G., Ilbert, O., Knobel, C., Iovino, A., Maier, C., Cucciati, O., Tasca, L., Carollo, C. M., Silverman, J., Kampczyk, P., de Ravel, L., Sanders, D., Scoville, N., Contini, T., Mainieri, V., Scodeggio, M., Kneib, J.-P., Le Fèvre, O., Bardelli, S., Bongiorno, A., Caputi, K., Coppa, G., de la Torre, S., Franzetti, P., Garilli, B., Lamareille, F., Le Borgne, J.-F., Le Brun, V., Mignoli, M., Perez Montero, E., Pello, R., Ricciardelli, E., Tanaka, M., Tresse, L., Vergani, D., Welikala, N., Zucca, E., Oesch, P., Abbas, U., Barnes, L., Bordoloi, R., Bottini, D., Cappi, A., Cassata, P., Cimatti, A., Fumana, M., Hasinger, G., Koekemoer, A., Leauthaud, A., Maccagni, D., Marinoni, C., McCracken, H., Memeo, P., Meneux, B., Nair, P., Porciani, C., Presotto, V., & Scaramella, R. 2010, ApJ, 721, 193

Pillepich, A., Nelson, D., Hernquist, L., Springel, V., Pakmor, R., Torrey, P., Weinberger, R., Genel, S., Naiman, J. P., Marinacci, F., & Vogelsberger, M. 2018a, MNRAS, 475, 648

Pillepich, A., Nelson, D., Springel, V., Pakmor, R., Torrey, P., Weinberger, R., Vogelsberger, M., Marinacci, F., Genel, S., van der Wel, A., & Hernquist, L. 2019, arXiv e-prints, arXiv:1902.05553

Pillepich, A., Springel, V., Nelson, D., Genel, S., Naiman, J., Pakmor, R., Hernquist, L., Torrey, P., Vogelsberger, M., Weinberger, R., & Marinacci, F. 2018b, MNRAS, 473, 4077

Pontzen, A., Tremmel, M., Roth, N., Peiris, H. V., Saintonge, A., Volonteri, M., Quinn, T., & Governato, F. 2017, MNRAS, 465, 547

Popping, G., Pillepich, A., Somerville, R. S., Decarli, R., Walter, F., Aravena, M., Carilli, C., Cox, P., Nelson, D., Riechers, D., Weiss, A., Boogaard, L., Bouwens, R., Contini, T., Cortes, P. C., da Cunha, E., Daddi, E., Díaz-Santos, T., Diemer, B., González-López, J., Hernquist, L., Ivison, R., Le Fevre, O., Marinacci, F., Rix, H.-W., Swinbank, M., Vogelsberger, M., van der Werf, P., Wagg, J., & Yung, L. Y. A. 2019, arXiv e-prints, arXiv:1903.09158

Puech, M., Hammer, F., Rodrigues, M., Fouquet, S., Flores, H., & Disseau, K. 2014, MNRAS, 443, L49

Ravindranath, S., Giavalisco, M., Ferguson, H. C., Conselice, C., Katz, N., Weinberg, M., Lotz, J., Dickinson, M., Fall, S. M., Mobasher, B., & Papovich, C. 2006, ApJ, 652, 963

Rich, J. A., Kewley, L. J., & Dopita, M. A. 2015, ApJS, 221, 28

Robotham, A. S. G., Driver, S. P., Davies, L. J. M., Hopkins, A. M., Baldry, I. K., Agius, N. K., Bauer, A. E., Bland-Hawthorn, J., Brough, S., Brown, M. J. I., Cluver, M., De Propris, R., Drinkwater, M. J., Holwerda, B. W., Kelvin, L. S., Lara-Lopez, M. A., Liske, J., López-Sánchez, Á. R., Loveday, J., Mahajan, S., McNaught-Roberts, T., Moffett, A., Norberg, P., Obreschkow, D., Owers, M. S., Penny, S. J., Pimbblet, K., Prescott, M., Taylor, E. N., van Kampen, E., & Wilkins, S. M. 2014, MNRAS, 444, 3986

Rodighiero, G., Daddi, E., Baronchelli, I., Cimatti, A., Renzini, A., Aussel, H., Popesso, P., Lutz, D., Andreani, P., Berta, S., Cava, A., Elbaz, D., Feltre, A., Fontana, A., Förster Schreiber, N. M., Franceschini, A., Genzel, R., Grazian, A., Gruppioni, C., Ilbert, O., Le Floch, E., Magdis, G., Magliocchetti, M., Magnelli, B., Maiolino, R., McCracken, H., Nordon, R., Poglitsch, A., Santini, P., Pozzi, F., Riguccini, L., Tacconi, L. J., Wuyts, S., & Zamorani, G. 2011, ApJ, 739, L40

Rodriguez-Gomez, V., Genel, S., Vogelsberger, M., Sijacki, D., Pillepich, A., Sales, L. V., Torrey, P., Snyder, G., Nelson, D., Springel, V., Ma, C.-P., & Hernquist, L. 2015, MNRAS, 449, 49

Rodriguez-Gomez, V., Snyder, G. F., Lotz, J. M., Nelson, D., Pillepich, A., Springel, V., Genel, S., Weinberger, R., Tacchella, S., Pakmor, R., Torrey, P., Marinacci, F., Vogelsberger, M., Hernquist, L., & Thilker, D. A. 2019, MNRAS, 483, 4140

Rupke, D. S. N., Kewley, L. J., & Barnes, J. E. 2010, ApJ, 710, L156

Salim, S., Rich, R. M., Charlot, S., Brinchmann, J., Johnson, B. D., Schiminovich, D., Seibert, M., Mallery, R., Heckman, T. M., Forster, K., Friedman, P. G., Martin, D. C., Morrissey, P., Neff, S. G., Small, T., Wyder, T. K., Bianchi, L., Donas, J., Lee, Y.-W., Madore, B. F., Milliard, B., Szalay, A. S., Welsh, B. Y., & Yi, S. K. 2007, The Astrophysical Journal Supplement Series, 173, 267

Sánchez, S. F., Kennicutt, R. C., Gil de Paz, A., van de Ven, G., Vílchez, J. M., Wisotzki, L., Walcher, C. J., Mast, D., Aguerri, J. A. L., Albiol-Pérez, S., Alonso-Herrero, A., Alves, J., Bakos, J., Bartáková, T., Bland-Hawthorn, J., Boselli, A., Bomans, D. J., Castillo-Morales, A., Cortijo-Ferrero, C., de Lorenzo-Cáceres, A., Del Olmo, A., Dettmar, R. J., Díaz, A., Ellis, S., Falcón-Barroso, J., Flores, H., Gallazzi, A., García-Lorenzo, B., González Delgado, R., Gruel, N., Haines, T., Hao, C., Husemann, B., Iglésias-Páramo, J., Jahnke, K., Johnson, B., Jungwiert, B., Kalinova, V., Kehrig, C., Kupko, D., López-Sánchez, Á. R., Lyubenova, M., Marino, R. A., Mármol- Queraltó, E., Márquez, I., Masegosa, J., Meidt, S., Mendez-Abreu, J., Monreal-Ibero, A., Montijo, C., Mourão, A. M., Palacios-Navarro, G., Papaderos, P., Pasquali, A., Peletier, R., Pérez, E., Pérez, I., Quirrenbach, A., Relaño, M., Rosales-Ortega, F. F., Roth, M. M., Ruiz-Lara, T., Sánchez-Blázquez, P., Sengupta, C., Singh, R., Stanishev, V., Trager, S. C., Vazdekis, A., Viironen, K., Wild, V., Zibetti, S., & Ziegler, B. 2012, A&A, 538, A8

Sanders, D. B., Soifer, B. T., Elias, J. H., Madore, B. F., Matthews, K., Neugebauer, G., & Scoville, N. Z. 1988, ApJ, 325, 74

Scudder, J. M., Ellison, S. L., & Mendel, J. T. 2012, MNRAS, 423, 2690

Shattow, G. M., Croton, D. J., Skibba, R. A., Muldrew, S. I., Pearce, F. R., & Abbas, U. 2013, MNRAS, 433, 3314

Shi, Y., Rieke, G., Lotz, J., & Perez-Gonzalez, P. G. 2009, ApJ, 697, 1764

Sijacki, D., Springel, V., Di Matteo, T., & Hernquist, L. 2007, MNRAS, 380, 877

Sijacki, D., Vogelsberger, M., Genel, S., Springel, V., Torrey, P., Snyder, G. F., Nelson, D., & Hernquist, L. 2015, MNRAS, 452, 575

Simons, R. C., Kassin, S. A., Snyder, G. F., Primack, J. R., Ceverino, D., Dekel, A., Hayward, C. C., Mandelker, N., Mantha, K. B., Pacifici, C., de la Vega, A., & Wang, W. 2019, ApJ, 874, 59

Skibba, R. A., Coil, A. L., Mendez, A. J., Blanton, M. R., Bray, A. D., Cool, R. J., Eisenstein, D. J., Guo, H., Miyaji, T., Moustakas, J., & Zhu, G. 2015, ApJ, 807, 152

Skibba, R. A., Sheth, R. K., Croton, D. J., Muldrew, S. I., Abbas, U., Pearce, F. R., & Shattow, G. M. 2013, MNRAS, 429, 458

Snyder, G. F., Lotz, J. M., Rodriguez-Gomez, V., Guimarães, R. d. S., Torrey, P., & Hernquist, L. 2017, MNRAS, 468, 207

Snyder, G. F., Rodriguez-Gomez, V., Lotz, J. M., Torrey, P., Quirk, A. C. N., Hernquist, L., Vogelsberger, M., & Freeman, P. E. 2018, arXiv e-prints

Sobral, D., Best, P. N., Smail, I., Geach, J. E., Cirasuolo, M., Garn, T., & Dalton, G. B. 2011, MNRAS, 411, 675

Sparre, M. & Springel, V. 2016, MNRAS, 462, 2418

Springel, V. 2010, MNRAS, 401, 791

Springel, V., Di Matteo, T., & Hernquist, L. 2005, MNRAS, 361, 776

Springel, V. & Hernquist, L. 2003, MNRAS, 339, 289

Springel, V., Pakmor, R., Pillepich, A., Weinberger, R., Nelson, D., Hernquist, L., Vogelsberger, M., Genel, S., Torrey, P., Marinacci, F., & Naiman, J. 2018, MNRAS, 475, 676

Springel, V. & White, S. D. M. 1999, MNRAS, 307, 162

Springel, V., White, S. D. M., Tormen, G., & Kauffmann, G. 2001a, MNRAS, 328, 726

Springel, V., Yoshida, N., & White, S. D. M. 2001b, New A, 6, 79

Stoughton, C., Lupton, R. H., Bernardi, M., Blanton, M. R., Burles, S., Castand er, F. J., Connolly, A. J., Eisenstein, D. J., Frieman, J. A., Hennessy, G. S., Hindsley, R. B., Ivezić, Ž., Kent, S., Kunszt, P. Z., Lee, B. C., Meiksin, A., Munn, J. A., Newberg, H. J., Nichol, R. C., Nicinski, T., Pier, J. R., Richards, G. T., Richmond, M. W., Schlegel, D. J., Smith, J. A., Strauss, M. A., SubbaRao, M., Szalay, A. S., Thakar, A. R., Tucker, D. L., Vand en Berk, D. E., Yanny, B., Adelman, J. K., Anderson, John E., J., Anderson, S. F., Annis, J., Bahcall, N. A., Bakken, J. A., Bartelmann, M., Bastian, S., Bauer, A., Berman, E., Böhringer, H., Boroski, W. N., Bracker, S., Briegel, C., Briggs, J. W., Brinkmann, J., Brunner, R., Carey, L., Carr, M. A., Chen, B., Christian, D., Colestock, P. L., Crocker, J. H., Csabai, I., Czarapata, P. C., Dalcanton, J., Davidsen, A. F., Davis, J. E., Dehnen, W., Dodelson, S., Doi, M., Dombeck, T., Donahue, M., Ellman, N., Elms, B. R., Evans, M. L., Eyer, L., Fan, X., Federwitz, G. R., Friedman, S., Fukugita, M., Gal, R., Gillespie, B., Glazebrook, K., Gray, J., Grebel, E. K., Greenawalt, B., Greene, G., Gunn, J. E., de Haas, E., Haiman, Z., Haldeman, M., Hall, P. B., Hamabe, M., Hansen, B., Harris, F. H., Harris, H., Harvanek, M., Hawley, S. L., Hayes, J. J. E., Heckman, T. M., Helmi, A., Henden, A., Hogan, C. J., Hogg, D. W., Holmgren, D. J., Holtzman, J., Huang, C.-H., Hull, C., Ichikawa, S.-I., Ichikawa, T., Johnston, D. E., Kauffmann, G., Kim, R. S. J., Kimball, T., Kinney, E., Klaene, M., Kleinman, S. J., Klypin, A., Knapp, G. R., Korienek, J., Krolik, J., Kron, R. G., Krzesiński, J., Lamb, D. Q., Leger, R. F., Limmongkol, S., Lindenmeyer, C., Long, D. C., Loomis, C., Loveday, J., MacKinnon, B., Mannery, E. J., Mantsch, P. M., Margon, B., McGehee, P., McKay, T. A., McLean, B., Menou, K., Merelli, A., Mo, H. J., Monet, D. G., Nakamura, O., Narayanan, V. K., Nash, T., Neilsen, Eric H., J., Newman, P. R., Nitta, A., Odenkirchen, M., Okada, N., Okamura, S., Ostriker, J. P., Owen, R., Pauls, A. G., Peoples, J., Peterson, R. S., Petravick, D., Pope, A., Pordes, R., Postman, M., Prosapio, A., Quinn, T. R., Rechenmacher, R., Rivetta, C. H., Rix, H.-W., Rockosi, C. M., Rosner, R., Ruthmansdorfer, K., Sandford, D., Schneider, D. P., Scranton, R., Sekiguchi, M., Sergey, G., Sheth, R., Shimasaku, K., Smee, S., Snedden, S. A., Stebbins, A., Stubbs, C., Szapudi, I., Szkody, P., Szokoly, G. P., Tabachnik, S., Tsvetanov, Z., Uomoto, A., Vogeley, M. S., Voges, W., Waddell, P., Walterbos, R., Wang, S.-i., Watanabe, M., Weinberg, D. H., White, R. L., White, S. D. M., Wilhite, B., Wolfe, D., Yasuda, N., York, D. G., Zehavi, I., & Zheng, W. 2002, AJ, 123, 485

Tapia, T., Eliche-Moral, M. C., Aceves, H., Rodríguez-Pérez, C., Borlaff, A., & Querejeta, M. 2017, A&A, 604, A105

Toomre, A. & Toomre, J. 1972, ApJ, 178, 623

Torrey, P., Snyder, G. F., Vogelsberger, M., Hayward, C. C., Genel, S., Sijacki, D., Springel, V., Hernquist, L., Nelson, D., Kriek, M., Pillepich, A., Sales, L. V., & McBride, C. K. 2015, MNRAS, 447, 2753

Torrey, P., Vogelsberger, M., Marinacci, F., Pakmor, R., Springel, V., Nelson, D., Naiman, J., Pillepich, A., Genel, S., Weinberger, R., & Hernquist, L. 2017, arXiv e-prints, arXiv:1711.05261

Trakhtenbrot, B., Lira, P., Netzer, H., Cicone, C., Maiolino, R., & Shemmer, O. 2017, ApJ, 836, 8

Vale, A. & Ostriker, J. P. 2004, MNRAS, 353, 189

Ventou, E., Contini, T., Bouché, N., Epinat, B., Brinchmann, J., Bacon, R., Inami, H., Lam, D., Drake, A., Garel, T., Michel-Dansac, L., Pello, R., Steinmetz, M., Weilbacher, P. M., Wisotzki, L., & Carollo, M. 2017, A&A, 608, A9

Verley, S., Leon, S., Verdes-Montenegro, L., Combes, F., Sabater, J., Sulentic, J., Bergond, G., Espada, D., García, E., Lisenfeld, U., & Odewahn, S. C. 2007, A&A, 472, 121

Vigroux, L., Mirabel, F., Altieri, B., Boulanger, F., Cesarsky, C., Cesarsky, D., Claret, A., Fransson, C., Gallais, P., Levine, D., Madden, S., Okumura, K., & Tran, D. 1996, A&A, 315, L93

Vogelsberger, M., Genel, S., Sijacki, D., Torrey, P., Springel, V., & Hernquist, L. 2013, MNRAS, 436, 3031

Vogelsberger, M., Genel, S., Springel, V., Torrey, P., Sijacki, D., Xu, D., Snyder, G., Bird, S., Nelson, D., & Hernquist, L. 2014a, Nature, 509, 177

Vogelsberger, M., Genel, S., Springel, V., Torrey, P., Sijacki, D., Xu, D., Snyder, G., Nelson, D., & Hernquist, L. 2014b, MNRAS, 444, 1518

Weinberger, R., Springel, V., Hernquist, L., Pillepich, A., Marinacci, F., Pakmor, R., Nelson, D., Genel, S., Vogelsberger, M., Naiman, J., & Torrey, P. 2017, MNRAS, 465, 3291

Weinberger, R., Springel, V., Pakmor, R., Nelson, D., Genel, S., Pillepich, A., Vogelsberger, M., Marinacci, F., Naiman, J., Torrey, P., & Hernquist, L. 2018, MNRAS, 479, 4056

Wen, Z. Z. & Zheng, X. Z. 2016, ApJ, 832, 90

Whitaker, K. E., Franx, M., Bezanson, R., Brammer, G. B., van Dokkum, P. G., Kriek, M. T., Labbé, I., Leja, J., Momcheva, I. G., Nelson, E. J., Rigby, J. R., Rix, H.-W., Skelton, R. E., van der Wel, A., & Wuyts, S. 2015, ApJ, 811, L12

White, S. D. M. & Rees, M. J. 1978, MNRAS, 183, 341

Whitmore, B. C. & Schweizer, F. 1995, AJ, 109, 960

Willett, K. W., Schawinski, K., Simmons, B. D., Masters, K. L., Skibba, R. A., Kaviraj, S., Melvin, T., Wong, O. I., Nichol, R. C., Cheung, E., Lintott, C. J., & Fortson, L. 2015, MNRAS, 449, 820

Williams, C. C., Giavalisco, M., Cassata, P., Tundo, E., Wiklind, T., Guo, Y., Lee, B., Barro, G., Wuyts, S., Bell, E. F., Conselice, C. J., Dekel, A., Faber, S. M., Ferguson, H. C., Grogin, N., Hathi, N., Huang, K.-H., Kocevski, D., Koekemoer, A., Koo, D. C., Ravindranath, S., & Salimbeni, S. 2014, ApJ, 780, 1

Wilman, D. J., Zibetti, S., & Budavári, T. 2010, MNRAS, 406, 1701

Yang, X., Mo, H. J., van den Bosch, F. C., Pasquali, A., Li, C., & Barden, M. 2007, ApJ, 671, 153

Chapter 5

Galaxy interactions in IllustrisTNG, II: Orbit characterization and lessons for idealized simulations

5.1 Abstract

In the previous chapter, we have shown that merger catalogues constructed by looking primarily at tidal features are biased toward short-lived encounters of massive galaxies. These are, in part, used to inform the initial conditions of idealized simulations of galaxy mergers. Although these simulations have improved over the years, they still employ some major oversimplifications regarding the structure of galaxy models, and the galaxy orbits themselves. Cosmological simulations, such as IllustrisTNG, can serve as self-consistent checks of these assumptions. In this chapter, we provide cosmologically motivated initial conditions for future idealized simulations. We additionally test the validity of the Keplerian Approximation, and present a case study in the framework of idealized galaxy merger simulations with one of the 85 interacting pairs from Chapter 4. We find that, under certain circumstances, the idealized prescription with appropriate initial conditions yields results that match the cosmological trajectory, and generally reproduce the tidal features that are "observed" in the cosmological simulation.

5.2 Introduction

Galaxy mergers – both major and minor – are a fundamental driver of galaxy formation and evolution. In addition to building up the structures we see at the present day (e.g., White & Rees 1978; Miller 1983; Burkey et al. 1994; De Propris et al. 2005; Bluck et al. 2012), tidal interactions strongly affect the galaxies' gas (e.g., Hagiwara 2007; Evans et al. 2008; Cortijo-Ferrero et al. 2011; Larson et al. 2016). This not only results in the massive bursts of star formation that are generally associated with merging galaxies (e.g., Alonso-Herrero et al. 2000; Evans et al. 2008), but also redistributes gas, creating a complicated system of self-regulating processes which drive the evolution of the merger remnant (e.g., Springel et al. 2005; Hopkins & Quataert 2010; Rich et al. 2015).

Much of our understanding of the phenomena involved in galaxy interactions is based on idealized simulations, the framework for which was developed by Toomre & Toomre (1972). This early work distributed massless test particles in concentric rings surrounding a point mass potential. When collided toward one another, the disks of test particles experience the gravitational potential of both galaxies. Toomre & Toomre (1972) found that as a result of this collision, tidal "tails" and "bridges" formed. Their work investigated the effects of geometry on these features. As computational and observational resources have advanced, so too has the sophistication of idealized simulations and our grasp of galaxy evolution theory (e.g., Hernquist & Katz 1989; Hopkins et al. 2006; Bryan et al. 2014; Emerick et al. 2019).

Though the last forty years have brought real improvements in numerical methods, most idealized simulations are still highly schematic. For example, initial orbits are assumed to be Keplerian and often exactly parabolic; galaxies, though now modeled as a composite system of stars, gas and dark matter, are still initialized as equilibrated objects; and the distributions of gas and stars are not necessarily representative of the real universe (e.g., Broeils & Rhee 1997; Blumenthal & Barnes 2018). The most far-reaching failure of idealized simulations is the assumption of isolation: galaxies are not considered within their cosmological context (however, recent work on cosmological zoom simulations has begun to alleviate this issue; e.g., Oñorbe et al. 2014; Sparre & Springel 2016; Fitts et al. 2017). Ultimately, idealized simulations are built upon a series of assumptions that limit their ability to explain some of the most fundamental questions in cosmology, and there has yet been no attempt to test these assumptions.

Modern cosmological simulations (e.g., Genel et al. 2014; Vogelsberger et al. 2014a,b; Schaye et al. 2015; Weinberger et al. 2017; Pillepich et al. 2018b), on the other hand, utilize initial conditions derived from the well-established physics of the early universe. Their success is measured by their ability to produce structures that evolve in their environmental context and eventually produce universes that closely match observational data (e.g., Hopkins et al. 2014; Torrey et al. 2017; Naiman et al. 2018; Weinberger et al. 2018; Rodriguez-Gomez et al. 2019). However, idealized simulations are still needed to test the models of "sub-grid" phenomena which underline the cosmological simulations. It is thus important to approach galaxy modeling in a two-handed way, wherein we consider the advantages of both cosmological and idealized simulations.

In this work, we use a sample of simulated interactions introduced in Blumenthal et al. (2019, Chapter 4), identified from the cosmological simulation IllustrisTNG (Marinacci et al. 2018; Naiman et al. 2018; Nelson et al. 2018; Pillepich et al. 2018a; Springel et al. 2018). We identify the moment of first interaction ("infall") and calculate orbital parameters, halo and stellar profiles, and perform a series of tests which examine the validity of the idealized method. The primary goals of this chapter are as follows:

1. Provide a systematic test of the myriad assumptions involved in idealized simulations of galaxy encounters,
2. Evaluate the validity of the Keplerian approximation,
3. Present a primer for future idealized simulations.

In Section 5.3, we describe the cosmological simulation used, give a brief overview of the findings of Chapter 4, and detail some key definitions. We discuss the Keplerian approximation in Section 5.5, and motivate the need for cosmologically informed initial conditions. In Section 5.4 we present the initial conditions (that is, the infall configuration) for the pairs sample, including the dark matter and stellar profile fits, the halo shapes, and orbital elements. Additionally, we present a test case in remodeling one of our pairs in Section 5.6 (this case study is represented in all plots as short grey lines in histograms and outlined x's as in scatter plots), with further details provided in Appendix C.1. Finally, we summarize our conclusions in Section 5.7.

5.3 Methods

5.3.1 IllustrisTNG

IllustrisTNG (Marinacci et al. 2018; Naiman et al. 2018; Nelson et al. 2018; Pillepich et al. 2018a; Springel et al. 2018) is a suite of N-body/magnetohydrodynamic cosmological simulations, comprised of three different volumes, each with a dark-only component and a full-physics counterpart. In this work, we utilize the $\sim 100^3$ Mpc^3 volume, hereafter TNG100-1. The full-physics simulations are run with the IllustrisTNG model (Weinberger et al. 2017; Pillepich et al. 2018b), featuring state-of-the-art prescriptions for star

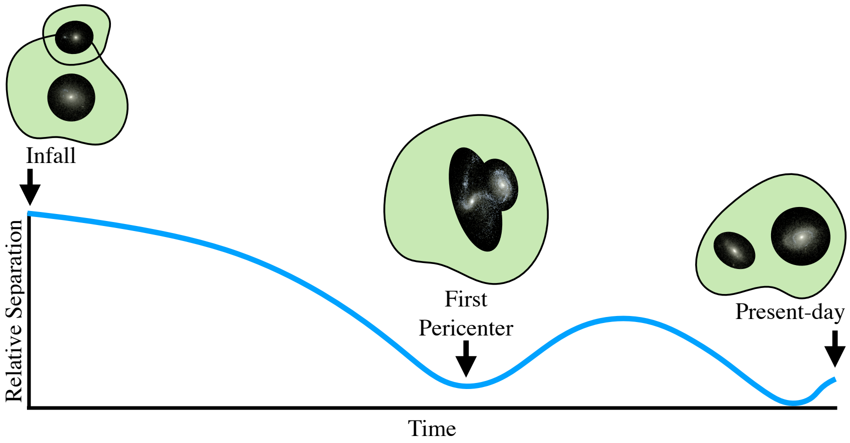

Figure 5.1 A cartoon representation highlighting the definitions presented in §5.3.3. FoF group halos are represented by green shapes which contain the subhalos (galaxies) that are shown as composite images from Chapter 4. The plot shown indicates the relative separation of the subhalos (galaxies) as a function of time. At infall, the moment when the two galaxies enter into the same FoF group, they are at their farthest distance in the interaction. The galaxies will fall toward one another, eventually reaching their first closest: first pericenter. Subsequent pericenters will occur, but perhaps not before the end of the simulation: the present-day.

formation, chemical evolution, and feedback due to active galactic nuclei. For a more detailed overview of TNG100-1 and the IllustrisTNG model, please refer to the aforementioned works.

5.3.2 Overview of Chapter 4

In Chapter 4, we generate a sample of ongoing major mergers, selected from galaxies in the $z = 0$ snapshot of IllustrisTNG100-1. Table 5.1 lists the dark matter and stellar mass limits placed on subhalos and Friends-of-Friends groups to arrive at the galaxy binary pair sample. Following this series of mass cuts, the truly interacting pairs were identified based on their trajectories throughout the volume. This resulted in a sample of 85 ongoing interactions. For more information on the sample selection process, please refer to Chapter 4.

The goals of this work are similar to those of Khochfar & Burkert (2006), who derive orbital parameters for a set of merging halos in the dark matter only simulation, GIF (Kauffmann et al. 1999). Though we follow the formalism laid out by Khochfar & Burkert (2006), this work differs in several ways. Namely, the cosmological simulation used here (and discussed below) includes both dark and baryonic material, enabling us to look directly at disks, and not just parameterize their halos. The FoF halo mass limits presented in Table 5.1 include the mass range covered by Khochfar & Burkert (2006), and roughly one order of magnitude below. In this work, we similarly investigate isolated major mergers, and note that because our mass ratios

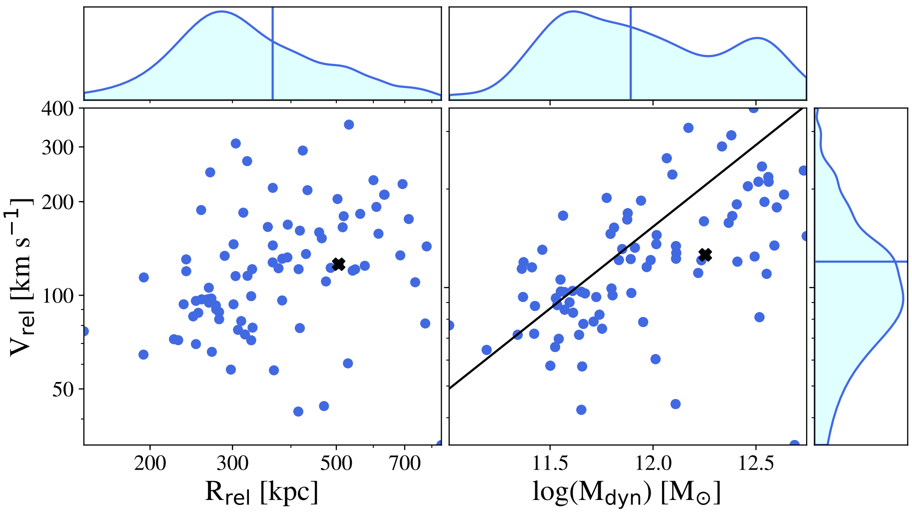

Figure 5.2 Dynamics of the 85 pairs at their individual infall times: the relative velocity as a function of separation (left), and as a function of the dynamical mass (that is, $M_{\rm DM,p}$ + $M_{\rm DM,s}$; right). The solid black line on the right panel indicates the velocity of a parabolic orbit as a function of dynamical mass: $v = \sqrt{2GM_{\rm dyn}/\bar{R}}$, where $\bar{R}$ = 365.6 kpc is the median relative separation.

Mass Limits
$10^{11} < M_{\rm FoF,DM} \leq 10^{13.5}$ $M_\odot$
$10^{10.5} < M_{\rm Sub,DM} \leq 10^{13}$ $M_\odot$
10^9 $M_\odot \geq M_{{\rm Sub},\star}$
$M_{s\star}$ / $M_{p\star} \geq$ 1:4
$M_{t\star}$ / $M_{p\star} \leq$ 1:16

Table 5.1 An overview of the mass cuts placed on the TNG100-1 $z = 0$ galaxies from Chapter 4. Here, $M_{[p,s,t]\star}$ refers to the stellar mass of the primary, secondary, and any tertiary subhalo, respectively.

are based on stellar mass, this definition may be slightly different depending on the abundance matching (e.g., dark to stellar mass mapping) prescription used (Behroozi et al. 2010).

Just as in Chapter 4, we present the dynamics of the pairs in Figure 5.2 but now at the time of infall, as defined below. The relative velocity experiences a moderate linear trend with both the relative separation, and the dynamical mass (i.e. $M_{\rm DM,p}$ + $M_{\rm DM,s}$). In the righthand plot, the black line represents the velocity as a function of dynamical mass for a parabolic orbit, adopting a relative separation equal to the median of our sample, $\bar{R}$ = 365.6 kpc.

5.3.3 Definitions

Friends-of-Friends Groups and Subhalos

Many modern cosmological simulations use Friends-of-Friends groups as the top-most structure for the particle representation of data (see Knebe et al. 2011, for an extensive list). Friends-of-Friends (hereafter FoF) groups are constructed via a percolation algorithm (Davis et al. 1985) which links together dark matter particles based on their inter-particle separation. The baryonic (gas and stars) material is assigned to a particular FoF group based on the membership of the nearest dark matter particle. Subhalos are the next structure down from FoF groups, and are identified via the SUBFIND algorithm (Springel et al. 2001). This iteratively strips away particles that are unbound from the central structure, until a bound system above a certain size remains. In many cases, as in this work, subhalos are considered galaxies, while FoF groups may contain pairs or groups of galaxies.

Infall

We define "infall" as the moment when two subhalos have entered into the same FoF group. We require that these two halos have not, independently, undergone an interaction with another subhalo in the last Gyr. An alternative choice in definition would be to take one snapshot prior to the aforementioned instance. However, this would result in inconsistent timings across the sample, as the moment of infall for each pair of galaxies is different, and the TNG100-1 snapshot sampling is variable, such that snapshots are closer together near the present-day.

A cartoon schematic is shown in Figure 5.1 that visually describes the distinction between FoF groups (green blobs with a dashed outline), subhalos (galaxy images outlined in white), "infall" (beginning of the time axis), "first pericenter" (middle arrow along the time axis), and the "present day" (end of the time axis, and end of the simulation). As these interactions are all ongoing, they will not reach final coalescence by the present day.

5.4 Cosmologically Motivated Initial Conditions

In the section above, we detailed ways in which the Keplerian approximation fails. In addition, Ch 4 shows that morphologically-based catalogues of merging galaxies, which have been historically used to motivate the initial conditions of idealized simulations, are likely to be incomplete, as the stellar mass of the interacting galaxies will bias the visibility of tidal features toward more massive systems. Additional factors, such as the orientation of the galaxies with respect to each other, and to the observer, will also have an impact. As such, we provide a series of distributions for initial conditions that are cosmologically motivated.

5.4.1 Galaxy Structure

Dark Matter Profiles

The earliest theoretical studies of dark matter halos posited that these objects form out of gravitational collapse, and as a result, exhibit isothermal density profiles ($\rho \sim r^{-2}$; e.g., Gunn & Gott 1972). Subsequent observational evidence (e.g., Blumenthal et al. 1986; Moore 1994; Flores & Primack 1994) and theoretical work (e.g., Dubinski & Carlberg 1991) show that the isothermal sphere model is too simplified for realistic halos. The most commonly utilized dark matter profile is the NFW profile (Navarro et al. 1994, 1995b,a, 1997), which was devised for objects – originally hot X-ray emitting clusters – in approximate equilibrium. This has had much success in reproducing the velocity profiles of galaxies and providing accurate predictions for gravitational lensing events, however there are some drawbacks to this model: (1) the mass derived from the NFW profile is divergent, and so it must be artificially truncated (typically at R_{200}, defined to be the radial distance from the galaxy center at which the local density is equal to 200 times the critical density); and (2) the profile shape is assumed to be universal, depending only on mass and central concentration.

The Einasto profile (Einasto 1965), introduced nearly three decades before the NFW profile, and has recently been recognized as a useful alternative. In fact, Navarro et al. (2004, 2010) show that the Einasto profile is a better fit than the NFW profile for cosmological halos and in particular, more faithfully reproduces the inner structure of dark matter halos. The form is nearly identical to the Sérsic profile, which is typically used to model the surface brightness of galaxies (see §5.4.1 below). The Einasto profile employs three free parameters: the scale radius, r_s, the density at that radius, ρ_s, and a variable that controls the shape of the function, α. The Einasto profile is

$$\rho_{\text{Einasto}} = \rho_s \exp\left\{-\frac{2}{\alpha}\left[\left(\frac{r}{r_s}\right)^{\alpha} - 1\right]\right\} \tag{5.1}$$

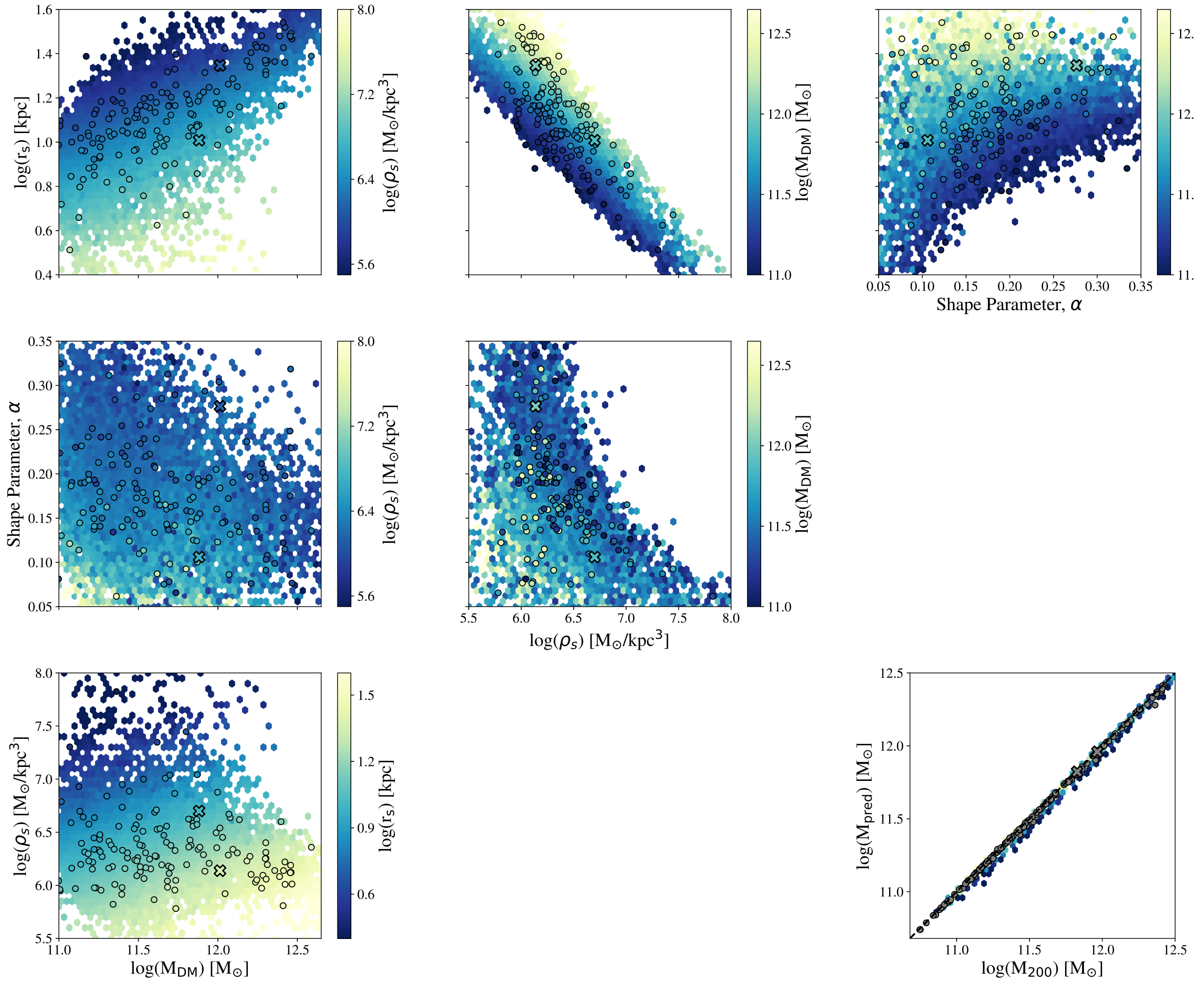

Figure 5.3 The fit parameters for the Einasto profile of isolated TNG100-1 FoF halos at the median infall time ($z \approx 0.3$; hexbin background) and the interacting pairs sample at infall (colored points outlined in black). Two-sided t tests for all halo parameters produce p-values > 0.35, implying that our interacting pairs arise from the same underlying distribution as the isolated TNG100-1 FoF groups. This is not true of the parameter sets at the present day. The interaction between the pairs leads to halo properties that are distinct from the isolated sample. The bottom right hand plot shows how well the fit Einasto profiles reproduce the halo mass when integrated over the fitting range: within this region, the profile fits the density profile well. However, care should be taken not to over-interpret these fits, as the predicted *total* mass is always over-estimated.

with an associated slope

$$\frac{\mathrm{d}\ln\rho}{\mathrm{d}\ln r} = -2\left(\frac{r}{r_s}\right)^{\alpha} \tag{5.2}$$

Thus, as α approaches zero, the density of Equation 5.1 has a constant slope, whereas if $\alpha = 1$, Equation 5.1 reduces to a simple exponential function with a knee located at the scale radius, r_s. In the shape parameter, α, cosmological halos are typically in the range $0.1 \lesssim \alpha \lesssim 0.25$ (e.g., Gao et al. 2008).

We use COLOSSUS (Diemer 2018), a versatile dark halo fitter and general-purpose cosmology toolkit, to fit the dark matter particle data for all interacting pairs at infall. To avoid resolution issues, we set the inner boundary of the profile fit at $3\epsilon_{\mathrm{DM}}$, and cut off the fit at an upper bound defined by an approximate iterative calculation of R_{200} for each subhalo. With this outer boundary, we successfully avoid overfitting significantly less-bound particles that blend into the Friends-of-Friends (FoF) group halo or those particles which are perturbed by the surrounding material. It should be noted that this is not an accurate measurement of R_{200}, as this quantity is ill-defined for subhalos which sit within the larger FoF structure. However, this value serves as a sufficient first approximation to the halo upper limit. We attempt to fit both Einasto and NFW functional forms to the subhalo dark matter density data, and find that the former is a better fit for most galaxies, consistent with previous findings (e.g. Navarro et al. 2004; Pedrosa et al. 2009; Navarro et al. 2010; Chua et al. 2019).

The resultant Einasto parameters are shown in Figure 5.3. In addition to the interacting pairs (shown in Figure 5.3 as coloured circles outlined in black), we also generate a set of Einasto fits for a sample of isolated FoF halos which match the dark matter mass limits placed upon the interacting pairs. These background galaxies are considered at the median infall time ($z \approx 0.3$; in Figure 5.3, these are represented as the background colored hexbin distribution). Two-sided t tests for all three fit parameters have p-values > 0.35: the halos of isolated and interacting galaxies are constructed from the same distribution of parameters. This illustrates that the interacting pair (subhalo) sample have similar halo properties to isolated FoF halos. That is, our pair sample at infall is consistent with the TNG100-1 population of galaxies as a whole, and are not unique systems predestined for interaction.

In addition to the profile fit parameters, we also show the predicted dark matter halo mass ($\mathrm{M}_{\mathrm{pred}}$) against the corresponding true halo mass (M_{DM}) for the TNG100-1 isolated FoF background (colors qualitatively indicate the number of objects in each bin, with a higher count corresponding to lighter colurs) and the interacting pair sample (grey circles). The black dashed line indicates what would be perfect agreement

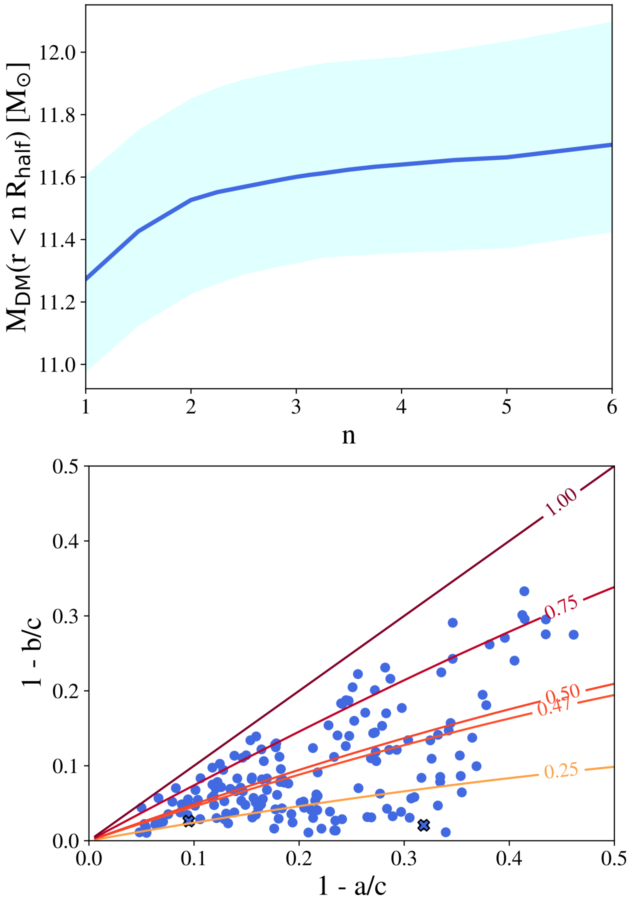

Figure 5.4 *Top:* To avoid issues with the SUBFIND algorithm misidentifying subhalo membership, we redefine the subhalo dark matter particles to include all those which lie $3R_{half}$ from the subhalo centre. The value of n was chosen based on this bottom plot, which shows how the mass interior to r changes as r increases by nR_{half}, and the apparent turnover at n~3. *Bottom:* Similar to Figure 1 of Franx et al. (1991), this shows the derived halo axis lengths ($a < b < c$) in ratio (blue circles), with lines of constant triaxiality overlaid (yellow to red colored lines, ranging from 0.25 to 1.0). Perfectly spherical halos would cluster in the lower left corner (a/c = b/c = 1).

between the mass determinations. Note however that this is only the mass enclosed by the fitted range of radii, and not the total mass of the system. As such, the fitting procedure should not be extrapolated to large radii. The parameters presented in Figure 5.3 should not be interpreted as resulting from a physical fit, but rather only as the result of a numerical regression to match the density data between $3\epsilon_{DM}$ and R_{200}.

Halo Shapes

We measure the three-dimensional shapes of the individual galaxies in our pairs sample. Following e.g., Schneider et al. (2012) and Bose et al. (2016), we utilize the dark matter shape tensor, which has ij components of the form:

$$I_{ij} = \sum_n \frac{x_{n,i}\, x_{n,j}}{R_n^2} \tag{5.3}$$

Each of these components is summed over n particles, at their ij positions: $x_{n,i}$ and $x_{n,j}$. The normalization R_n is the elliptic radius, or $R_n = (x_n/a)^2 + (y_n/b)^2 + (z_n/c)^2$, where a, b, and c are the primary axes of the ellipsoid and x_n, y_n, and z_n are the ellipsoidal coordinates of the n^{th} particle. The eigenvalues of the inertia tensor are simply related to the principal axes of the halo, $a, b, c = \sqrt{\lambda_{a,b,c}}$. We adopt the convention that $a < b < c$: that the minor axis lies along the x-axis.

There are several ways to solve for the eigenvectors and values using the inertia tensor of a set of particles (e.g., Bailin & Steinmetz 2005; Zemp et al. 2011). In this work, we initially assume a perfectly spherical halo with a radius equal to the dark matter half-mass radius. We then diagonalize Equation 5.3 and rotate into a frame defined by the derived principal axes. We calculate the quantities

$$q_c = \frac{(q' - q)^2}{q^2} \text{and} s_c = \frac{(s' - s)^2}{s^2} \tag{5.4}$$

where q' and s' are $q = b/c$ and $s = a/c$ from the previous iteration. We iterate on this process, keeping a fixed volume, until it reaches convergence (i.e., $q_c + s_c < \epsilon$, where $\epsilon = 5e - 3$).

It has been shown that the derived shape of dark halos depends significantly on the radius within which the shape is measured (e.g., Zemp et al. 2011). Further, the SUBFIND algorithm is known to occasionally misappropriate particles from one subhalo to another (e.g., Knebe et al. 2013). To alleviate these and subsequent complications, we redefine the subhalo dark matter halo to ensure the constituent particles belong to the appropriate halo. To consistently achieve this for all pairs, we determine the mass enclosed within a radius n-times the subhalo's dark matter half-mass radius, $\mathrm{R_{half}}$, using all FoF group particles centered about the position of the subhalo's most bound particle. The results of this test are shown in the top panel of Figure 5.4: there is an apparent turnover in the enclosed mass starting at n=3. As such, we redefine each subhalo's dark matter halo to consist of only those particles which lie within $3\mathrm{R_{half}}$.

The overall three-dimensional shape of the halos can be inferred from the ratio of the principal axes. For example, the bottom panel of Figure 5.4 shows $1 - a/c$ against $1 - b/c$. In this parameter space (as in Figure 1 of Franx et al. 1991), oblate spheroids lie along the x-axis, prolate spheroids along the diagonal, elliptic discs along the y-axis, and perfect spheres at the origin. We also indicate the triaxiality parameter

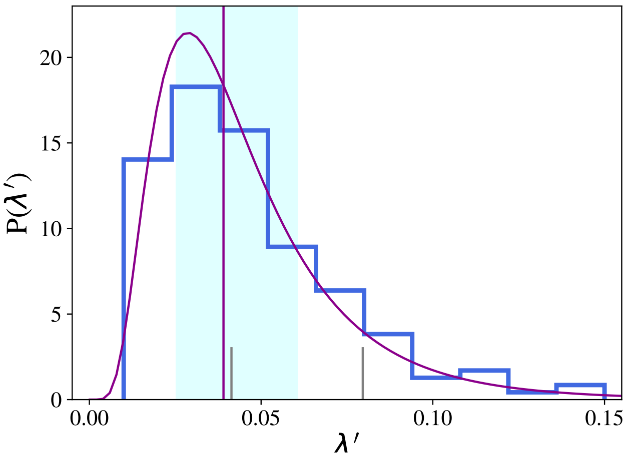

Figure 5.5 The galaxy halo spin parameter, λ', indicates what fraction of the halo angular momentum is a result of rotation. That the median value (magenta vertical line at 0.039) is close to zero indicates that rotation is not responsible for the angular momentum content of the dark halo. This distribution is well fit by a power law, following e.g., Bullock et al. (2001), shown in purple.

(e.g. Franx et al. 1991), defined as

$$T = \frac{c^2 - b^2}{c^2 - a^2} \tag{5.5}$$

Lines of constant triaixiality fill the space in the lower half of this figure, and increase with increasing $1 - b/c$. Several such contours are shown in the bottom panel of Figure 5.4, including the median triaxiality, T~ 0.47. This value increases with increasing n until n~3, at which point the measurement becomes stable. The reported values shown in the bottom panel of Figure 5.4 span a range of halo shapes from nearly spherical close to the origin, to nearly completely prolate just below the diagonal, to almost totally oblate along the x-axis.

Halo Spins

Angular momentum of dark halos is widely considered to be a byproduct of tidal torques, the accretion of satellites, and more generally, hierarchical structure formation (e.g. Blumenthal et al. 1984; White 1984; Barnes & Efstathiou 1987). Thus, as interactions spin up halos, there can be drastic effects on the evolution of the gas and stellar discs within, particularly as the merger history becomes more developed. The renormalized spin parameter, λ' (Bullock et al. 2001), is based on the formulation from Peebles (1969) and

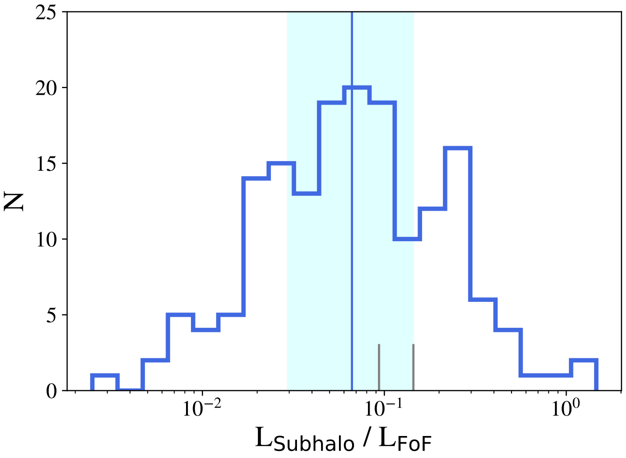

Figure 5.6 The magnitude of the total angular momentum (i.e. the total contribution due to all particle types) of the subhalo, $L_{Subhalo}$, in ratio with the magnitude of the total FoF group angular momentum, L_{FoF}. Idealized simulations typically ignore galaxies' angular momenta, however this figure shows that there are many cases in which the angular momentum is a nontrivial fraction of the whole. The median value of this ratio is ~ 0.08; the corresponding confidence interval is shown in the light blue region.

is a parameterization of the dark halo angular momentum. It is given by the expression

$$\lambda' = \frac{L}{\sqrt{2} M V_{circ} R} \tag{5.6}$$

where L, M, and $V_{\rm circ}$ are the angular momentum, the mass of the halo contained within R, and the velocity of a circular orbit at that radius. The λ' parameter indicates what fraction of the halo is supported by rotation, as it is the ratio of the total halo angular momentum to the halo's rotational angular momentum. The median value for various sets of simulated halos is consistently ~ 0.03 (e.g., Bullock et al. 2001; D'Onghia et al. 2006; D'Onghia & Navarro 2007). That this parameter is so close to zero indicates that the halo asphericity (as seen in §5.4.1) is a fundamental consequence of the halo velocity structure, and not merely a result of rotation.

Figure 5.5 shows the probability density distribution of λ' for the sample of interacting pairs, measured for all FoF group particles within $3R_{\rm half}$ of each subhalo's most bound particle. This distribution follows a log-normal power law as in e.g., Bullock et al. (2001) (magenta curve), with $\lambda'_{\rm med} = 0.039$ (vertical purple line; the 25th to 75th percentiles are indicated by the light blue shaded region). Though mergers are typically thought to be a source of angular momentum in halos (e.g., Vitvitska et al. 2002), D'Onghia & Navarro (2007) show that this is true only in non-equilibrium systems near final coalescence of a major merger or accretion event. The halo will gradually spin down as it virializes. The internal angular momentum of the pairs sample at infall are much like isolated galaxy halos. This is further evidence that interacting galaxies are not drawn from a special subset of the galaxy population.

Additionally, we show the subhalo total (i.e., including particles of all types) angular momentum as a fraction of its parent FoF group total angular momentum in Figure 5.6. Many idealized simulations assume that the individual galaxies have nearly zero initial angular momentum. Figure 5.6 shows that this is not the case. The internal angular momentum of many galaxies is a significant fraction of the whole. Depending on the trajectory and relative orientation of the interacting galaxies, nonzero angular momenta may yield noticeable and nontrivial deviations from the expected tidal response based solely on their orbital elements. While many have investigated the impact of stellar and gas angular momentum on merger remnants, several groups (e.g., Rodriguez-Gomez et al. 2017) have recently begun to look at the impact of the halo angular momentum.

Baryon Profiles

Bottom-up theories of galaxy formation indicate that galaxies build up through the merger of early star clusters and small dwarf galaxies, which form first. These structures will gravitationally attract one another, eventually forming a massive galaxy, much like the ones observed at the present day. Through angular momentum conservation, the gas and stars will settle into disks near to the center of the halo. Observational studies of galaxies have shown that stellar discs can often be described by an exponential profile (e.g., Pohlen & Trujillo 2006), however the relative size of these discs and the inner profile of the gas have been shown to vary depending on the gas tracer used to probe the distribution (e.g., La Barbera et al. 2010; Holwerda et al. 2011; Vulcani et al. 2014).

Idealized simulations typically assume that the gas and stars are organised into equal-size exponential discs (e.g., Springel & Hernquist 2005; Cox et al. 2006; Moreno et al. 2015, 2019). However, in addition to observational evidence indicating that gas is frequently more extended than the stellar material (e.g., Broeils & Rhee 1997), there are often additional structures to both the gas and stars, including a stellar bulge, spiral arms, and stellar and/or gaseous bar. How these components interact with one another plays an intricate role in shaping the star formation history of the galaxy (e.g., Cheung et al. 2013; Méndez-Abreu et al. 2014; Sachdeva et al. 2015; Spinoso et al. 2017; Blumenthal & Barnes 2018). Cosmological simulations such as Illustris and IllustrisTNG underproduce bars (Peschken & Łokas 2019). We can, however, reliably look at the total distribution of the baryonic material of our interacting pairs sample.

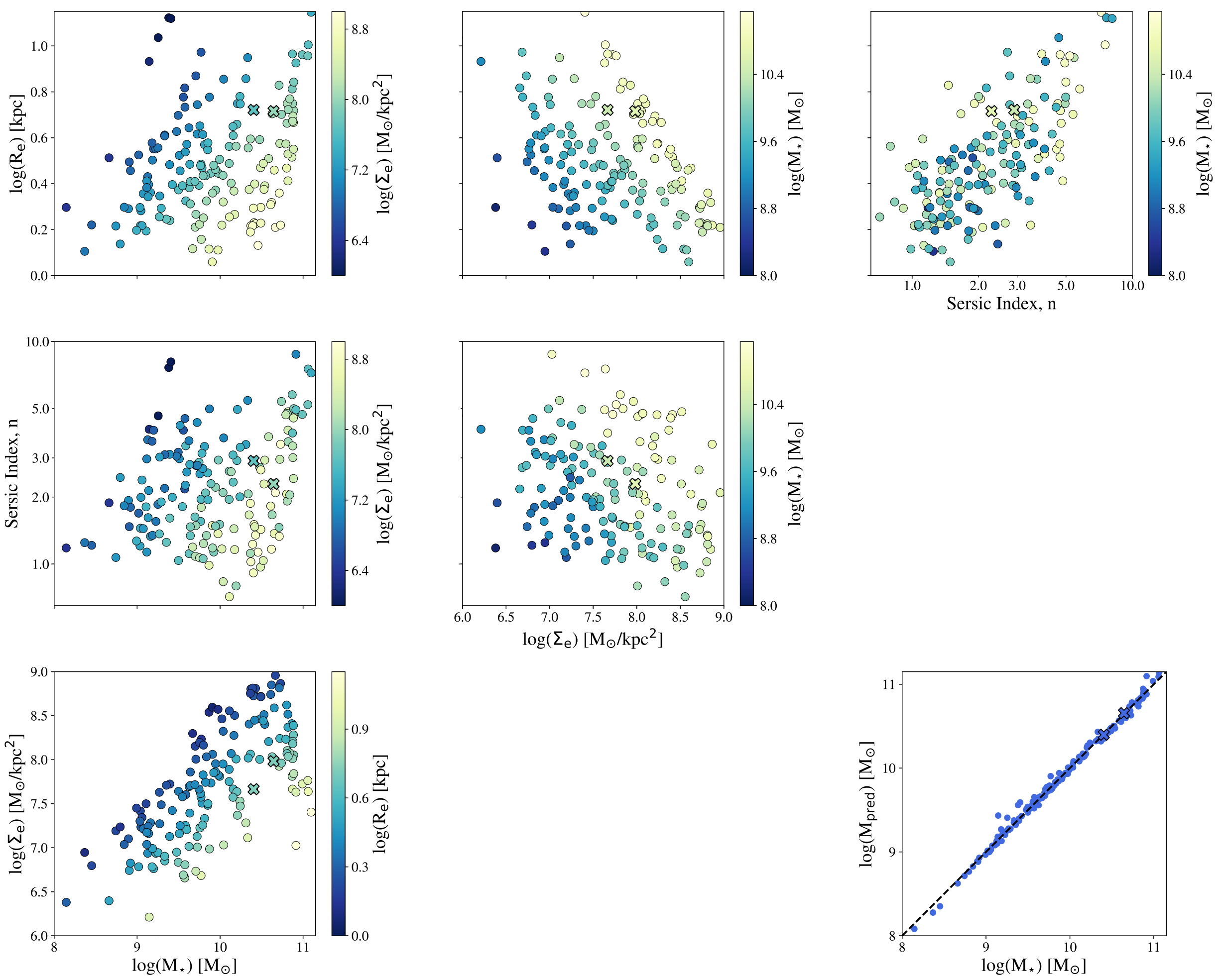

Figure 5.7 We use the stellar material to fit a generic Sérsic profile. This has three parameters: the effective radius, R$_e$, the surface mass density at that radius Σ$_e$, and the Sérsic index n. Here we show the results of this fitting process for all galaxies in our pairs sample, their interdependencies, and the relationship with stellar mass. Most notably, the Sérsic index spans a wide range of values, and displays a tight correlation with the effective radius. This model-independent trend has been seen before (e.g., Trujillo et al. 2001), and implies that as the stellar material becomes more concentrated (that is, *n* increases), the physical size of the distribution increases.

While much of the gaseous material lies in a plane, in many cases the gas disc is greatly disrupted (e.g., exhibits larges holes, broken discs) even at infall, making it impossible to fit a single axisymmetric profile to all galaxies. As a result, we do not attempt to fit the gas discs, nor perform a bulge- or bar-disc decomposition of the stellar material; instead, we fit a single generic Sérsic profile to the entire stellar distribution.[1]

Following the formalism described below in Section 5.4.3, we derive the angular momentum vector of the stellar disc and use this to enter into a frame of reference in which the vertical axis looks down onto the disc plane. In this configuration, we perform a fit of a Sérsic profile to all stellar particles following the form

$$\Sigma(r) = \Sigma_{\rm e} \exp\left\{-b_n\left(\left(\frac{r}{R_e}\right)^{1/n} - 1\right)\right\} \tag{5.7}$$

where Σ_e is the surface density at the effective radius, R_e, and n is the Sérsic index. This functional form reduces in three cases: $n = 0.5$ gives rise to a Gaussian distribution, $n = 1$ is a simple exponential profile, and $n = 4$ corresponds to a de Vaucouleurs profile, which is typically used for elliptical galaxies. The constant b_n is linked to the incomplete gamma function and the Sérsic index: $\Gamma(2n) = 2\gamma(2n, b_n)$, or equivalently $b_n = \gamma^{-1}(2n, \frac{1}{2})$.

The results of our fits are shown in Figure 5.7. Clearly, not all stellar discs are well described by the exponential profile, as the Sérsic index n ranges from $\sim 0.6 - 10$ (e.g., Vulcani et al. 2014). There is a fair amount of scatter in all relations shown in Figure 5.7, particularly in the effective radius and Sérsic index with stellar mass. Previous work has shown that there is an intrinsic (i.e., model-independent) relationship between the Sérsic index n and the effective radius (e.g., Trujillo et al. 2001), something which is also seen in our results. It has also been shown that n can be considered a proxy for concentration; as a galaxy increases in size, it becomes more centrally concentrated, which drives up the Sérsic index. Similar trends have also been noted with $\Sigma_{\rm e}$ and $\mathrm{R}_{\rm e}$ (e.g., Trujillo et al. 2001). Just as in Section 5.4.1 (Figure 5.3), we include a scatter plot of the total stellar mass predicted from the profile to the true total stellar mass. Unlike the Einasto fits in Section 5.4.1, these Sérsic fits converge to nearly the exact total stellar mass, and as such we can consider these fits to be accurate physical representations of the underlying stellar distribution.

The stellar mass ratio, or the ratio of the two galaxies' total stellar masses, is often used to delineate between major and minor mergers. Our pairs sample was selected such that the galaxies exhibited a stellar

---

[1] It is interesting to note that the Sérsic index is often used to distinguish between disc-dominated (low n) and bulge-dominated (high n) galaxies (e.g., Blanton et al. 2003; Hogg et al. 2004; Luparello et al. 2015). The question as to whether this delineation holds is well-suited for the high resolution of TNG50.

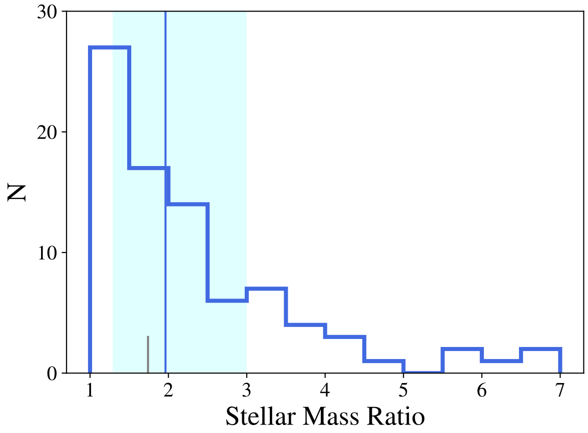

Figure 5.8 The stellar mass ratio measured at infall. The vertical blue line indicates the median value at 1.96, with the confidence interval shown as the light blue shaded region. Note that these pairs were selected at the present-day to be major mergers with a mass ratio < 1:4. That there are pairs which initially did not meet this criterion implies that the galaxies must undergo some change in mass between infall and the present day.

mass ratio of less than or equal to 1:4 – the typical mass ratio of a "major merger." Figure 5.8 shows the stellar mass ratio as measured at infall: what might be considered the initial condition for the total stellar mass of an idealized simulation. While the majority of these pairs also have stellar mass ratios ranging from unity to 1:4, there is a small fraction of pairs which have much higher mass ratios. Therefore, as discussed in Section 5.5.2, there must be some amount of growth (or loss) that occurs between and within these galaxies from infall to the present day. This may manifest as simply a byproduct of star formation which results from the interaction, or perhaps from mass exchange with the local environment and with each other.

5.4.2 Orbital Characterization

In the reduced two body problem, extended halos are assumed to be accurately represented by the position and velocity of their most bound particle (in IllustrisTNG, this is by definition the location of the supermassive black hole at the center of the galaxy). Here, we define the most massive galaxy in the pair as the primary, denoted by a subscript p, and the second most massive galaxy as the secondary, similarly denoted by a subscript s. For consistency in all that follows, vectors will be in boldface font, and their norms will be in regular typeface. The orbital parameters are defined as in Toomre & Toomre (1972).

We continue with the equivalent one body problem of the reduced two body problem by defining a frame of reference for the pair that is dependent upon the position and velocity of the primary and secondary (as in, e.g., Khochfar & Burkert 2006). In this frame, the positional vector is the separation of the two galaxies,

$\mathbf{R} = \mathbf{r}_s - \mathbf{r}_p$, and the velocity is similarly the difference of their average velocities, $\mathbf{V} = \mathbf{v}_s - \mathbf{v}_p$. In this framework, there is a test particle of mass μ_r, orbiting at a distance $R = |\mathbf{R}|$. The equation of motion if this "particle" is

$$\mu_r \ddot{\mathbf{R}} = -G \frac{M_p M_s}{R^2} \frac{\mathbf{R}}{R} \tag{5.8}$$

where μ_r is the reduced mass of the system, defined as

$$\mu_r = \frac{M_p M_s}{M_p + M_s} \tag{5.9}$$

The total energy this orbit is

$$E = \frac{1}{2} \mu_r V^2 - \frac{G M_p M_s}{R} \tag{5.10}$$

with an orbital angular momentum of

$$\mathbf{L} = \mu_r \mathbf{R} \times \mathbf{V} \tag{5.11}$$

With these, quantities, we can compute the parameters that describe the orbit. In particular, the Keplerian eccentricity is

$$e = \sqrt{1 + \frac{2EL^2}{\mu_r (G M_p M_s)^2}} \tag{5.12}$$

The *vis-viva* equation follows directly from conserving Equation 5.10, and describes the orbital motion of a body with any eccentricity:

$$V^2 = G(M_p + M_s) \left(\frac{2}{R} - \frac{1}{a} \right) \tag{5.13}$$

where a is the semi-major axis of the orbit.

Note that there is an implicit time dependence in all of the above equations. Before first pericenter, the orbital angular momentum and the eccentricity are expected to stay roughly constant. As the interaction continues, however, this will change. The orbit will decay through gravitational friction as the dark matter halos torque on one another. This will cause the two galaxies to spiral inward, and eventually merge. Naturally, at this stage, the orbital parameters change rapidly.

In §5.4.1, we motivated using a $3\mathrm{R}_{\mathrm{half}}$ aperture for the FoF dark matter particles in defining the halo shape and angular momentum. Similarly, the issues with SUBFIND may affect the subhalo velocity, and consequentially, all orbital parameters. To ensure we capture only the motions of the subhalo, we redefine

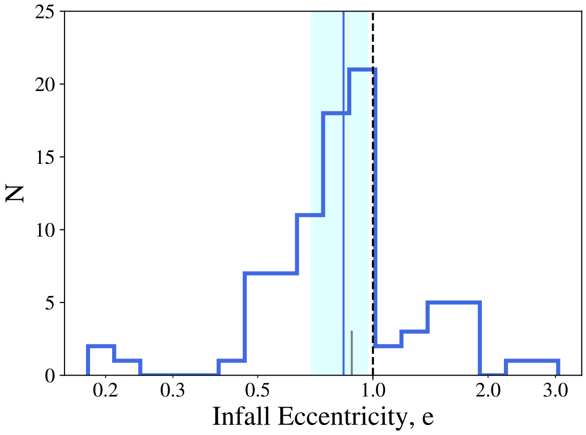

Figure 5.9 The interacting pairs sample have a median eccentricity at e~0.84, marked by the vertical blue line and its subsequent confidence interval is shown by the light blue shaded region. The vertical dashed black line indicates e= 1, a perfectly parabolic orbit, and the typical choice for many idealized simulations.

the subhalo velocity using the mass-weighted average of all dark matter particles within $R_{\rm half}$. We use a smaller volume here to ensure that we capture the bulk motion of the subhalo, and not its inner structures. Though the difference in the TNG100-1 reported velocity and our redefined velocity is typically not large (the median absolute difference is $\sim$ 3km s^{-1}), this substitution is necessary to ensure that the contribution due to misplaced particles does not effect the orbital properties of the pair.

Eccentricity

Typically, galaxies' initial orbits are assumed to be Keplerian and exactly parabolic (e.g., Barnes 1988; Barnes & Hernquist 1992; Springel 2000; Springel et al. 2005; Cox et al. 2006; Blumenthal & Barnes 2018), with few, but notable, exceptions (e.g., Borne 1988; Mihos & Hernquist 1996; Di Matteo et al. 2007; Cox et al. 2008; Bournaud et al. 2011; Moreno et al. 2015; Solanes et al. 2018; Moreno et al. 2019). Cosmological simulations allow us to test this assumption of a large sample of galaxies. We calculate the eccentricity of the pairs sample at infall using Eqn. 5.12. The results, shown in Figure 5.9, indicate a median value of $e \approx 0.84$ (marked in a blue vertical line, and consistent with the findings of Khochfar & Burkert (2006)). To guide the eye, we also include a dashed black line indicating the eccentricity of a parabolic orbit ($e = 1$).

Pre-processing, or some degree of gravitational interaction with nearby objects, must play an important role in the dynamical history of these galaxies. Assuming orbits are initially parabolic requires that the merging galaxies have not encountered another object prior to the current interaction. This not only ignores

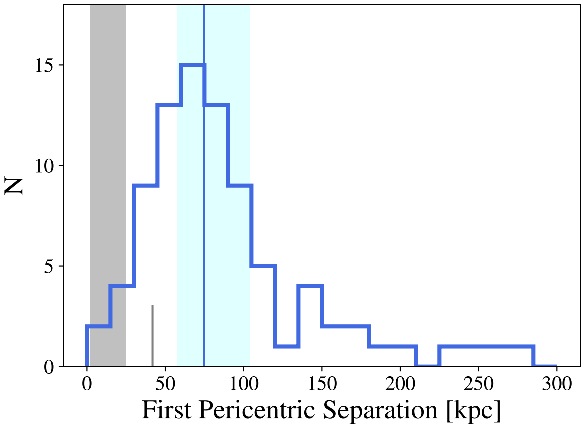

Figure 5.10 The distribution of first pericentric separations of the interacting pairs sample has a median of 74.85 kpc with the confidence interval shown in the light blue shaded region, as before. The shaded region indicates roughly where idealized simulations often set their first pericentric distances: between 2 and 25 kpc. These values are completely encompassed by the tail of the true distribution.

the cosmological context, but also diminishes the role of structure formation on the continuing evolution of the system. In reality, galaxy orbits are constantly perturbed by nearby material, through gravitational harassment or prior mergers, which conspire to circularize the orbits of galaxies once they enter into a merging pair.

Pericentric Parameters

Idealized simulations of galaxy encounters tend to assume that the first pericentric separation is below 30kpc (e.g., Taylor & Babul 2001; Cox et al. 2008; Moreno et al. 2015, 2019, and shown in the grey shaded region of Figure 5.10). There are two primary reasons why this is the case: (1) it takes considerably less time between first pericenter and coalescence if the targeted separations are smaller, and (2) it is typically considered necessary to assume a small first pericentric passage, with deeply interpenetrating discs, in order to produce the tidal features seen in systems like The Antennae (NGC 4038/39, e.g. Barnes & Hernquist 1996; Karl et al. 2008; Renaud et al. 2015). Though these assumptions may be appropriate for a small subset of interacting systems, there is no assurance that they will capture the diversity observed in the real universe.

We determine the pericentric separations from interpolated position data as the snapshot output of TNG100-1 is too coarse to reliably capture the depth of a close passage. As such, we perform a cubic spline over the snapshot positions with a new time resolution of 2.5 Myr, mimicking the full TNG100-1 resolution near $z = 0$, where the snapshot resolution is the highest. As shown in Figure 5.10, we find a broad distribution of pericentric separations at first passage, between about 1 and 300 kpc.

The peak of this distribution is nearly 75 kpc, which is roughly 2-3 times larger than what is typically used in idealized simulations of galaxy interactions (again, indicated in Figure 5.10 by the shaded region between 2 and 25 kpc). This may have a significant impact on the star formation histories of galaxies; if passages are typically wider, then the gravitational torques which drive inflows will be weaker, and star formation may not be triggered until much later in the merger history. To that end, systems which are assumed to be at first or second pericentric passage from observational data, may actually be much further along in their dynamical evolution. That is, Figure 5.10 suggests galaxies often initially have very wide, yet still bound, orbitals which decay to smaller separations at late times.

5.4.3 Encounter Geometry

Inclinations can be defined for material which sits in a disc-like plane. Whereas in Section 5.4.1 we could only reliably use the stellar material, here we utilize both the gas and stars. For the stars, we isolate the stellar disc by targeting only those particles inside the median stellar radius, and that exhibit transverse velocities two or more times greater than their radial velocities. This removes particles on plunging orbits, and ensures that the presumed disc particles are on orbits about the rotation axis. We define the gas disc plane in a similar way, but additionally require that all gas disc particles are either star forming or have temperatures below 10^4 K, as warmer material is more likely to be in a hot halo. Note that the IllustrisTNG effective equation of state has a temperature floor at 10^4K, meaning that the temperature is not well-defined for star forming gas cells.

The angular momentum of the gas (stellar) disc, $\mathbf{L}_{\mathbf{g},\star\mathbf{disc}}$, is thus the sum of the individual angular momenta of the gas (star) particles. Projected onto a unit sphere, the three principle axes of the angular momentum vector of each gas (star) particle will cluster in the case of a true disk (that is, all particles' angular momenta will point roughly in the same direction). If there is a warp, then the angular momenta of the particles will trace out patterns (typically closed loops) on the unit sphere. Particles in pressure-supported systems, on the other hand, will exhibit randomly oriented angular momenta. In this way, we identify which galaxies host gaseous and stellar discs, warped discs, and spheroids. Inclinations are only reported for well-defined discs.

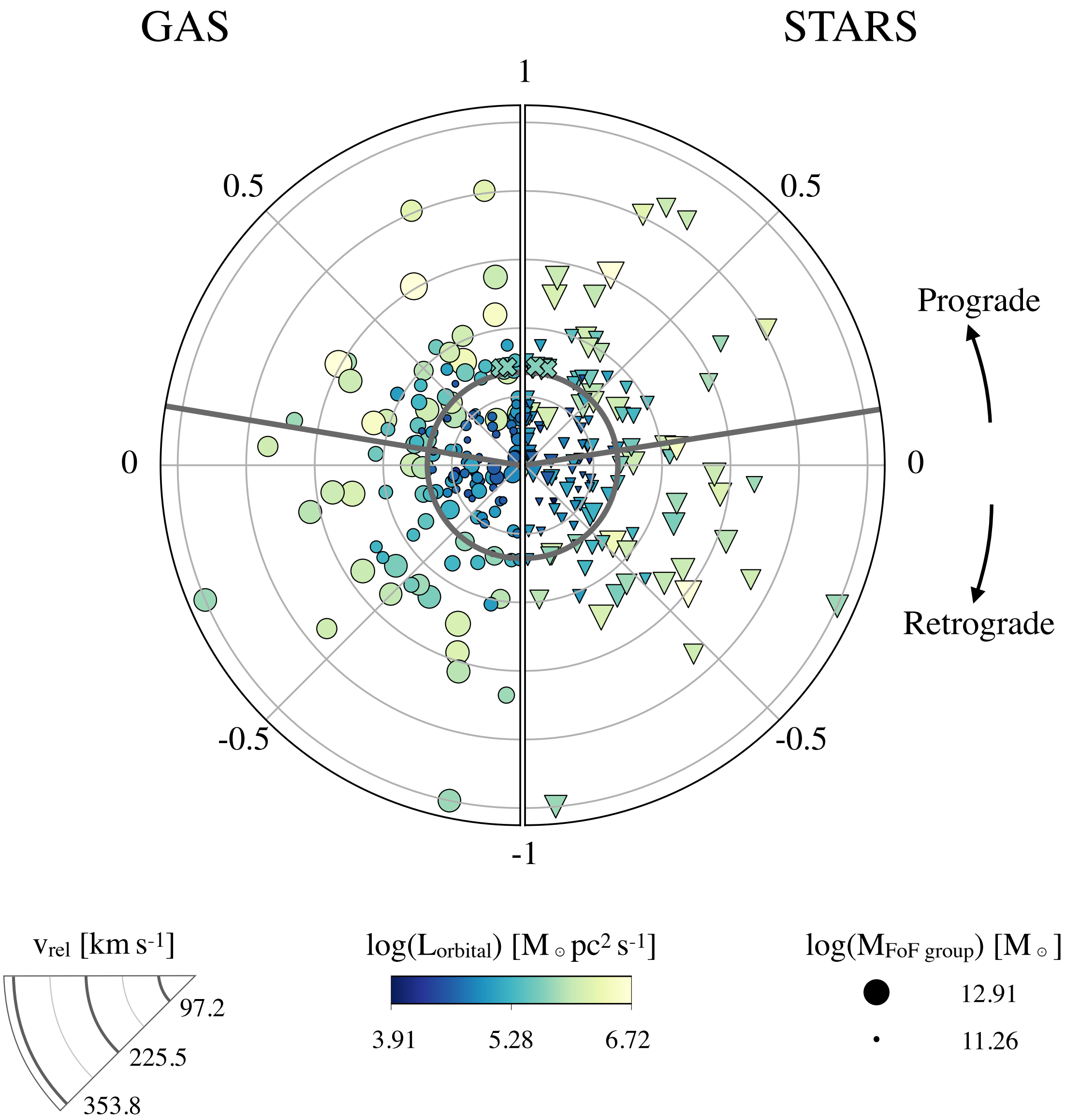

Figure 5.11 The inclinations of the gas (left, circles) and stellar (right, downward facing triangles) discs are not uniformly distributed. The inclination is given along the polar direction, relative velocity increases with increasing distance from the centre, color indicates the magnitude of the orbital angular momentum, and the size of the symbol scales with the FoF group mass, a proxy for environment. Both the stellar and gaseous discs are slightly biased toward prograde (the thick grey lines indicate the median of the stellar and gas disc inclination: 0.0994 and 0.105 respectively). The grey semicircles show the radial position of the median velocity of the full sample of pairs, at $v_{rel} \sim 120$km s^{-1}.

The inclination, i, is the angle between the gas (stellar) disc angular momentum and the vector normal to the orbital plane (as defined in §5.5.1). Here, we report the inclination as the cosine of i, $\cos i$, such that a disc with $\cos i = 1$ lies exactly in the orbital plane, and $\cos i = -1$ has an angular momentum exactly antiparallel to the normal of the orbital plane. In this way, $\cos i > 0$ indicates a prograde disc, while $\cos i < 0$ indicates a retrograde disc. Figure 5.11 shows the gas (left semicircle; circle markers) and stellar (right semicircle; inverted triangle markers) disc inclinations, with the median values indicated by grey radial lines on either side. In the radial direction, the relative velocity increases from $\sim$33 km s^{-1} to $\sim$353.8 km s^{-1}, as indicated by the scale in the lower left corner. In addition, colour shows the magnitude of the orbital angular momentum (Eqn. 5.11), and marker size indicates the FoF group mass, a proxy for environment (e.g., Chapter 4).

Both the gas and stellar discs show a slight preference toward prograde encounters, however the two distributions produce slightly different results in a KS test against a uniform distribution: the stellar inclinations exhibit $p \approx 0.13$ whereas the gas disks show $p \approx 0.09$. Though different conclusions might be drawn from these data, a two-sided KS test indicates that they are drawn from the same distribution ($p \approx 0.998$). It is thus necessary to sample more interacting pairs in order to definitively say whether the trends seen in our TNG100-1 pairs sample are indicative of all encounter geometries. Regardless, historical implementations of idealized encounters have assumed galaxy inclinations are random. However, it has been suggested that at larger cosmological scales than the one presented here (e.g., Hu et al. 2006, and references therein), galaxies are not randomly oriented, but are in fact aligned with structures in their environment (e.g., filaments, groups, and nearby massive galaxies). In Figure 5.11, we see a clear trend between the FoF group mass, relative velocity and the magnitude of the orbital angular momentum. Though the inclinations of our interacting galaxies do not appear to show a dependence on environment, the final quadrant ($-0.5 < \cos i < -1$) of both the gas and stellar disc inclinations is relatively underpopulated. Those discs that do have very retrograde inclinations tend to have larger angular momenta, indicating that perhaps this inclination range is only accessible by extreme systems.

5.5 Testing the Keplerian Approximation

The dynamics of idealized simulations are based on the premise that before halos overlap, the two galaxies involved in an interaction can be treated as separate objects. To the extent that this is true, galaxies should adhere to the following:

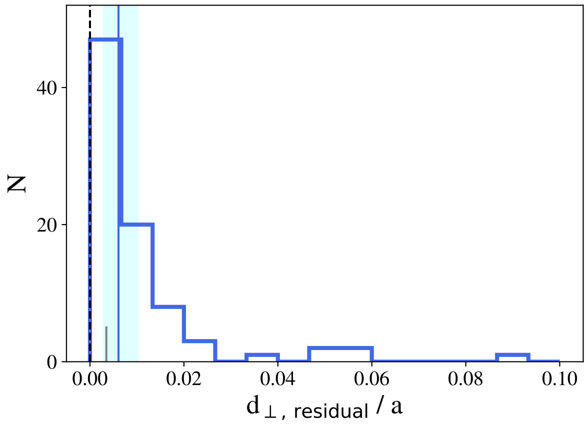

Figure 5.12 The median perpendicular distance above or below the fit orbital plane, $d_\perp$, is shown as a fraction of the semimajor axis, a, as measured at infall. If the trajectory of all orbits sat perfectly in a plane, then the perpendicular deviation would be zero (black dashed line). The median is shown at the location of the blue vertical line, where $d_\perp/a = 0.006$, and the confidence interval of the 25th to 75th percentiles is indicated by the light blue shaded region.

1. Galaxy orbits lie in a single plane.
2. The total mass is constant as a function of time.
3. The orbital elements remain constant between infall and first pericenter.

In the following section, we investigate the validity of these statements. We find that although orbital planes are very stable throughout the entire interaction, the exchange of material between the galaxies and their environments (that is, a non-constant mass) causes the interaction to speed up or slow down, likely due to the details of the transfer. In short, galaxy interactions cannot be considered otherwise isolated.

5.5.1 Conserving the Orbital Plane

In the Keplerian prescription, galaxies merge on a single orbital plane. We take the positions of the interacting galaxies at each snapshot between infall and the present day and fit a plane of the form $ax + by + cz = d$. The coefficients a, b, and c form the normal to the plane, $\hat{n}$. For all interacting systems in our sample, there is very little deviation from the best-fit plane. The top panel of Figure 5.12 shows the median perpendicular distance from the best fit plane divided by the semimajor axis measured at infall. This is an indication of how significant the deviation from the plane is: the vast majority of the pairs stay very close to the orbital plane, with a maximum deviation of under 10% the semimajor axis.

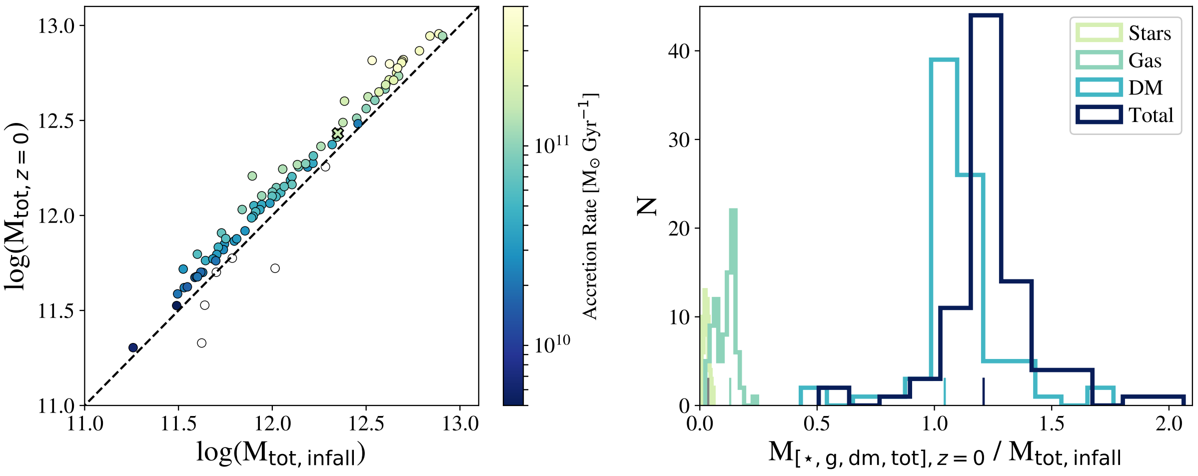

Figure 5.13 We show the mass increase of the FoF group from infall to the present day. *Left*: Total mass of the FoF group at the present day (y−axis) and at infall (x−axis). Each marker is colorized by the accretion rate, calculated as the difference in mass divided by the elapsed time between infall and the present day. Unfilled circles correspond to those systems which lose mass during this time. *Right*: A series of histograms corresponding to the mass increase from infall to the present day, corresponding to the y values of the left panel. If the majority of the mass gain were due to star formation triggered by the interaction, the fractional increase in the total mass would be on the order of a few percent. However, the median value in these interacting pairs indicates a > 20% increase in mass. Thus, the galaxies must be accreting material from their surroundings, which we show to likely be in the form of gaseous filaments.

5.5.2 Mass Accretion and Ejection

The effects of environment on galaxies are varied, and include the transfer of torque, angular momentum, and mass from nearby structures onto the halos. In the Keplerian approximation, it is assumed that the total mass stays constant throughout the orbit, however cosmic flows deposit a significant amount of material onto halos (e.g., Davé et al. 2011; Pichon et al. 2011; Wetzel & Nagai 2015; Borzyszkowski et al. 2017). Figure 5.13 shows how the total FoF group mass changes from infall to the present day for each interacting pair. The color in the left panel indicates that more massive halos have higher rates of accretion. The dashed line in the lefthand panel indicates a steady state wherein the mass lost and gained between infall and the present day is constant. Points that lie above this line have experienced some amount of accretion (e.g., inflow from the cosmic web). The right panel shows how the mass increase is broken up into components: the stars, gas, dark matter, and total. The majority of galaxies are more massive at the present day than they were at infall, by nearly 23%. It is clear that the stellar material accounts for a negligible fraction of the growth. This is expected; star formation triggered by the interaction is likely to account for only a few percent of any mass increase. Thus, there must be inflows of gas and dark matter from the cosmic web onto the system throughout the course of the interaction. This change in mass will affect the interaction in significant ways. For a demonstration of the relative importance of mass accretion, refer to Section 5.6.

5.5.3 Predicting First Pericenter

If the Keplerian prescription for an orbit is accurate, and we accept all the assumptions listed above, then the time between pericenter ($t_{\text{peri}} = 0$) and a subsequent position along an elliptical orbit ($e < 1$) is

$$t = (E - e \sin E)\sqrt{\frac{a^3}{\mu}} \tag{5.14}$$

and along a hyperbolic orbit ($e > 1$) is

$$t = (e \sinh F - F)\sqrt{\frac{|a|^3}{\mu}} \tag{5.15}$$

where a is the semi-major axis, $\mu = G(M_p + M_s)$ is the standard gravitational parameter, and E and F are the eccentric and hyperbolic anomaly, respectively. For details about the derivation of these orbital parameters, refer to Section 5.4.2. We first orient the system such that $\hat{z}$ is aligned with the orbital angular momentum, and $\hat{x}$ is aligned with the eccentricity vector. We manipulate a series of equations which describe the orbit to arrive at values for E, F, and a. In a similar fashion, we can define the predicted pericentric distance from the orbital parameters for both an elliptical and hyperbolic orbit:

$$\mathrm{R}_{\mathrm{Kep}} = a(1 - e) \tag{5.16}$$

In Figure 5.14, we compare the derived Keplerian time between infall and first pericenter ($\mathrm{t}_{\mathrm{Kep}}$) with the time as measured directly from TNG100-1 ($\mathrm{t}_{\mathrm{TNG}}$) on the left, and additionally show a comparison of the derived ($\mathrm{R}_{\mathrm{Kep}}$) and measured ($\mathrm{R}_{\mathrm{TNG}}$) pericentric distances on the right. In the left panel, each marker is colored according to its eccentricity, and in the right panel markers are colored by the measured time between infall and pericenter (the $y-$axis of the left panel) to facilitate matching between the two. Stars indicate the pairs which are initially on hyperbolic orbits. In both panels, the black dashed line indicates perfect agreement between the axes.

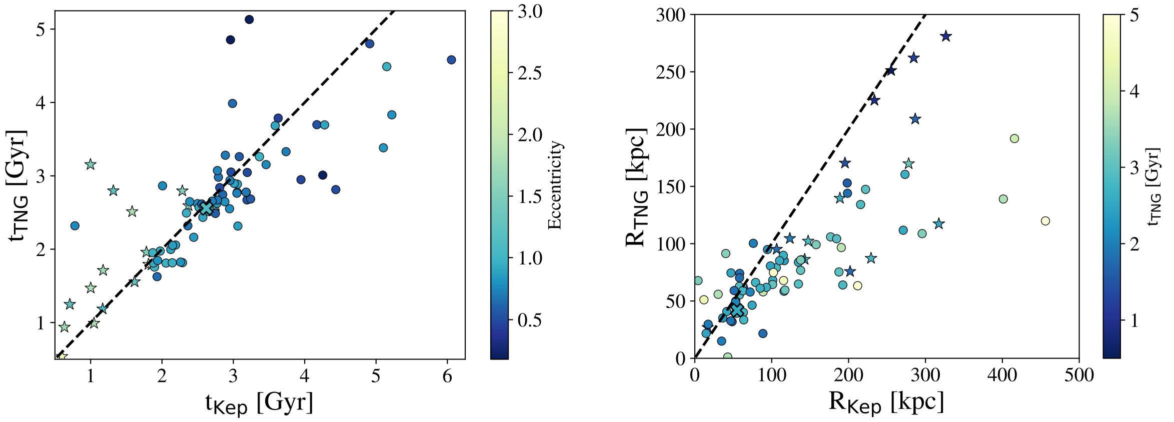

Figure 5.14 Here we show two plots comparing the measured and derived time between infall and pericenter (left) and pericentric distance (right). On the left, the markers are colored by the eccentricity, while on the right panel, markers are colored by the measured time until pericenter, t_{TNG}, to facilitate matching between the panels. In both panels, stars indicate the systems with initially hyperbolic orbits. Many of these pairs agree within ±1 Gyr, with the largest deviations typically seen in orbits with the longest t_{TNG}.

In the left panel, there appears to be good agreement between the derived and measured pericentric times; about 75% of interactions occur within 500 Myr of the derived t_{Kep}. The amount of time between infall and first pericenter appears to be correlated with the eccentricity, such that higher eccentricities are often associated with faster interaction times (defined as $t_{1^{st}peri}$ - t_{infall}). If there is a long amount of time between infall and first pericenter ($\gtrsim$ 3.5Gyr), then the scatter between t_{Kep} and t_{TNG} greatly increases. Long interaction times provide a longer amount of time for perturbative forces (e.g., interactions with the environment, mass and/or momentum transfer) to alter the orbit of the interacting bodies.

This is also true of the measured and derived first pericentric separation (Figure 5.14, right panel). While there are some exceptions, nearly all instances of large deviation occur in systems where there is $\gtrsim$ 3.5 Gyr of orbital evolution before the first pericentric passage occurs. Interestingly, below $R_{TNG} \sim 100$ kpc, the Keplerian orbital elements frequently underestimate the true pericentric distance, and above this threshold, R_{Kep} typically overestimates this parameter.

5.6 Idealized Interactions: a Case Study

The most straightforward way to test whether idealized simulations can reproduce the cosmological outcome is by performing such an idealized simulation. We chose the system in Figure 5.15 for its obvious tidal features, as many idealized simulations aim to reproduce the strong tidal response of specific systems. In

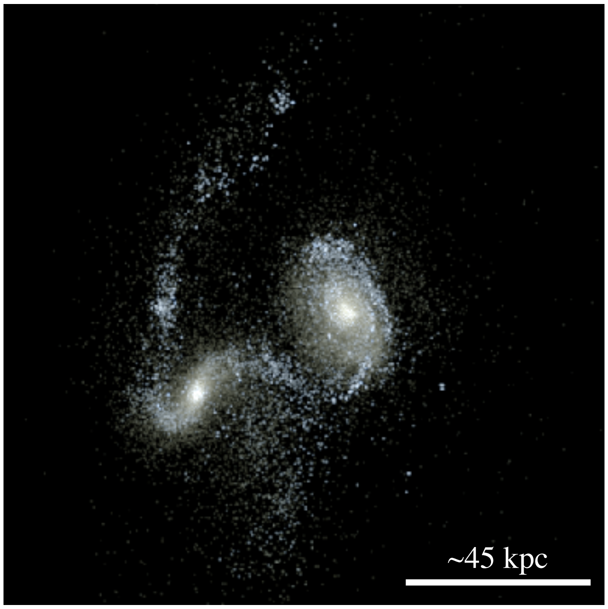

Figure 5.15 The subject of our case study: the Shuixiu System. This three-color image (from Chapter 4) is constructed at the present-day.

other respects, this system is not an outlier: its relative velocity, eccentricity, and stellar mass are all close to the median of their respective distributions, as are the properties of the two galaxies making up this system. Both galaxies' gas and stellar discs are prograde, though slightly less inclined to the orbital plane than the median. Their halo and stellar profile fit parameters are well within the broad distributions presented above. Throughout the chapter, we have used short grey lines in histograms and outlined x's as indicators of where the system lies with respect to the rest of the TNG100-1 pairs sample. We nicknamed this the Shuixiu system because its curving tidal features, which prove to be associated with the secondary galaxy, resemble the flowing "water sleeves" (shui xiu) of Chinese opera.

We use three techniques to simulate the encounter and eventual merger of the two galaxies:

1. "Reconstituted" models use the actual positions and velocities of bodies in the infall FoF halo;
2. "Idealized equilibrium" models use N-body realizations of spherical Einasto profiles for the initial galaxies;
3. "Idealized non-equilibrium" models artificially truncate an equilibrium N-body realization to generate galaxies with virial ratio $T/U < -0.5$.

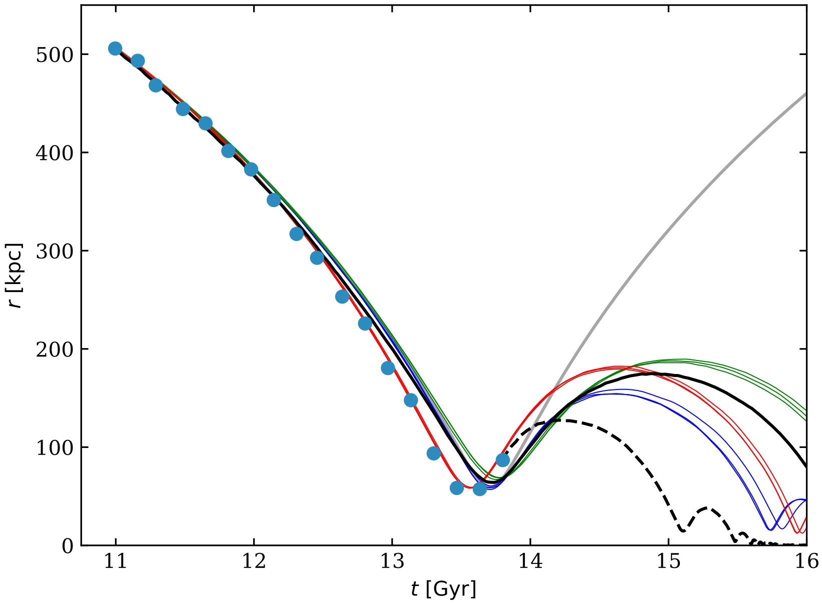

Figure 5.16 Separation as a function of time for different versions of the Shuixiu System. Blue dots show the trajectory reported by the TNG100-1 snapshots. The solid black curve shows reconstituted version of the system based on the infall FoF configuration; likewise, the dashed black curve shows the future evolution of a reconstituted version of the present FoF configuration. The light grey curve shows a Keplerian encounter of two points with the same initial masses, positions, and velocities as the primary and secondary galaxies at infall. Finally, the three sets of color curves show our idealized models: equilibrium models (blue), non-equilibrium (green), and non-equilibrium with 25% extra mass (red).

In all of the above cases, we include only collisionless stellar dynamics. That is, we do not employ any prescription for gas dynamics, star formation, active galactic nuclei, or feedback. For more information regarding the construction and implementation of these models, refer to Appendix C.1.

Figure 5.16 shows the resultant trajectories of the various idealized models of the Shuixiu system, in addition to its actual trajectory from TNG100-1 (blue circles), the future trajectory of the system based on the present-day FoF configuration (black dashed line), and the motion of two point masses (that is, no orbit decay) with the same initial positions, velocities and masses as Shuixiu (light grey line). Each idealized model is run in triplicate to ensure that run-to-run variation does not significantly alter our interpretation.

While all models match reasonably well before about 12.5 Gyr, there is growing deviation between the true trajectory and most of the idealized models. The best match to the actual trajectory results when we artificially inflate the initial masses of the primary and secondary galaxies by 25%. This may be thought of as crudely approximating the additional mass accreted onto the system between infall and the present. It is interesting to note that all models fail to recreate the future evolution of this system, based on the FoF configuration at the present-day. Cosmological zoom simulations are be necessary to determine the cause of this disagreement.

We additionally show, in Figure 5.17, two projections ($x - y$, left and $y - z$, right) of the true TNG100-1 Shuixiu System's present-day stellar material (top), the present-day stellar configuration of a reconstituted system (middle), and the stellar distribution of an idealized model at the present-day (bottom). Though these three models exhibit divergent trajectories, their tidal features are very similar. As such, we may reliably use idealized simulations to study tidal features, broad galaxy-scale structures, and the general dynamics of interactions.

5.7 Conclusions

In this work, we explore the limits of the Keplerian approximation. Though it is known that orbital elements (e.g., eccentricity, inclination) change rapidly after first pericenter, we find that the orbital elements change even before the first pericenter occurs. This is likely a result of mass exchange between the systems and their cosmological surroundings. In spite of this, the orbital plane stays very nearly constant throughout the entire interaction. Thus, it seems that there are components of the Keplerian approximation that are reasonable, and components that are a significant over-simplification.

It is therefore important to utilize cosmologically motivated initial conditions for idealized interactions of two galaxies. Here, we provide ranges for the following parameters: initial and first pericentric separations, initial velocity, stellar mass ratio, eccentricity, and inclinations. We also include "numerical" Einasto profile fits for the dark matter halos of the interacting pairs sample and a sample of isolated TNG100-1 galaxies that meet the same mass criteria as our primary pairs sample. It is important to note that the dark halo fits do not accurately reproduce the *total* mass of the halo, but are good representations of the material within the fitted range of radii ($3\epsilon_{\rm DM}$–R_{200}). This is true both of the pairs sample and the TNG100-1 isolated control systems. In fact, there is remarkable agreement between the fit parameter distributions of these samples. This, along with the spin-prime parameter distribution (Figure 5.5), indicate that the interacting pairs are not drawn from a unique sample of galaxies.

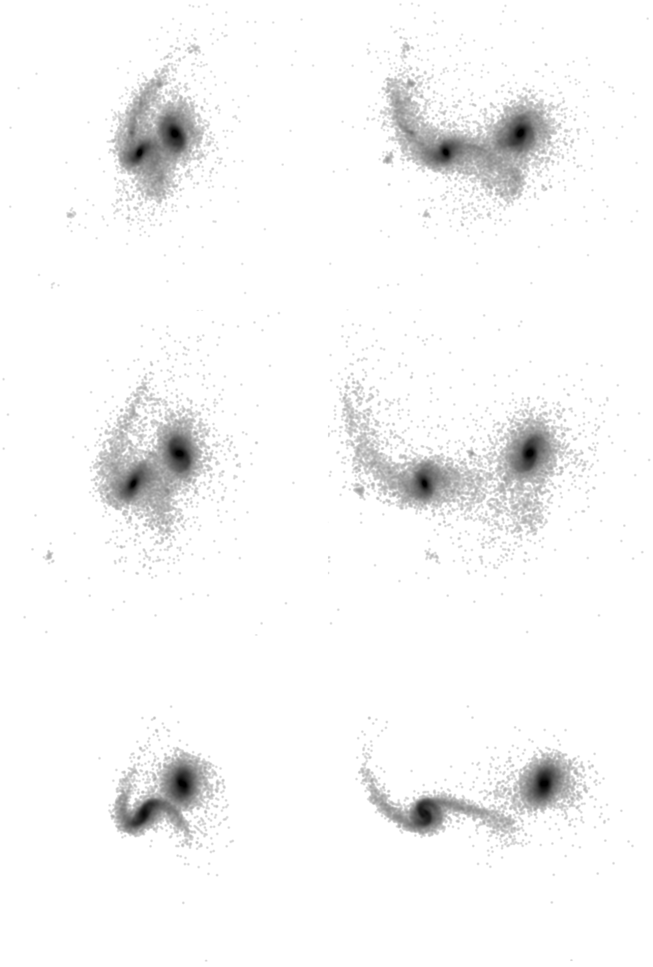

Figure 5.17 Greyscale images of the Shuixiu System. Left: (x, y) projections; right: (z, y) projections. Top row shows actual TNG100-1 results at present ($t = 13.79\,\mathrm{Gyr}$). Middle row shows the "reconstituted" model at $t = 13.92\,\mathrm{Gyr}$. Bottom row shows an idealized model at $t = 13.79\,\mathrm{Gyr}$.

	Median	CI=[25^{th},75^{th}]%ile	
$M_{tot,z=0}/M_{tot,infall}$	1.23	[1.17, 1.3]	
R_{sep}	365.6	[276.5, 502.9]	kpc
V_{rel}	119.99	[87.84, 161.4]	km s^{-1}
$L_{Subhalo}/L_{FoF}$	0.07	[0.03, 0.15]	
Stellar Mass Ratio	1.96	[1.29, 3.0]	
e	0.838	[0.69, 0.97]	
$\cos i_g$	0.105	[-0.34, 0.61]	
$\cos i_\star$	0.0994	[-0.36, 0.65]	
R_{peri}	74.85	[57.82, 104.31]	kpc

Table 5.2 Here we provide the median values and the corresponding confidence intervals (25th to 75th percentiles) of the most salient parameters discussed above.

Though the Einasto profile is an improvement over the NFW profile, both assume that the halos have spherical symmetry. We calculate the three-dimensional halo shapes within $3R_{half}$, and find that halos are generally very triaxial. This will generate non-spherical potential fields, which may approximate to spherically symmetric when the halo are far from one another, but near pericentric passages this deviation from sphericity could have a significant impact on the evolution of the interaction.

In nearly every galaxy in our sample, the gas is coplanar, but very disrupted even at infall. As such, we could not systematically fit a generic Sérsic profile to each galaxy, and instead we present only fits for the stellar material. Contrary to the dark matter profiles, these can be described as “physical” fits: the extrapolated total stellar mass is nearly exactly the reported value from TNG100-1. Thus, these are not only good fits to the data, but are accurate representations of the physical system.

We characterized the orbits of the interacting pairs at the time of infall, and determine several parameters which may prove useful for future idealized galaxy interaction simulations. The medians are presented in Table 5.2, along with the confidence intervals (CI) corresponding to the distributions' 25th to 75th percentiles.

In this chapter, we have shown multiple ways in which the assumptions of idealized simulations may yield inaccurate representations of the observed universe. Namely:

1. There is a nontrivial amount of mass accretion (though some systems appear to undergo tidal stripping) between the FoF group halo and the local environment in the time spanning infall and the present day. If the mass is not constant, then the Keplerian approximation is no longer valid. This could impact the orbital history in a variety of ways. For example, this will affect the interaction time, introduce changes in angular momentum and torque, and potentially confuse interpretations of the star formation history.

2. The total angular momentum of galaxies is not negligible in comparison to their parent FoF group halo. More exploration is required to understand the impact on orbital history, morphology, and remnant substructure.

3. Eccentricities span a wide range, from nearly circular to hyperbolic, but most are between $0.7 \lesssim e \lesssim 0.97$. This is indicative of pre-processing; the dynamical history of galaxies is not forgotten before a new encounter occurs.

4. First pericentric passages span about two orders of magnitude. The median value for our interacting pairs is roughly 2-3 times larger than what is typically used in idealized simulations of galaxy mergers. By choosing small values for the separation at first pericenter, other work is biased toward interactions that occur on short timescales. This distribution of separations may impact merger rates, as wide orbits are underrepresented in observational catalogues.

5. Inclinations are slightly biased toward prograde for both the gas and stellar discs. However, the results of KS tests for both samples are contradictory and inconclusive. It is thus necessary to expand this work to a larger mass range, and/or a higher redshift (e.g., $z \approx 0.1$). Looking only at the median values, the trends seen here indicate that galaxy orientations are slightly biased toward prograde. It has been shown that direct prograde encounters produce the strongest tidal response (e.g. Toomre & Toomre 1972), which logically leads to the highest rate of star formation. If galaxy inclinations are more frequently prograde, then idealized simulations may be underestimating the fraction of the star formation density due to mergers.

These parameters are presented to be used for realizing idealized simulations. As a test of the efficacy of this suggestion, we reconstructed (and remodeled) one interacting pair: the Shuixiu System. From this exercise, we find that simple idealized simulations can be used to look at the broad structural features (e.g., tidal tails) and general dynamics of an interacting pair. However, the mass accreted between infall and the present-day has an important impact on the evolution of the system that should not be ignored.

References

Alonso-Herrero, A., Rieke, G. H., Rieke, M. J., & Scoville, N. Z. 2000, ApJ, 532, 845

Bailin, J. & Steinmetz, M. 2005, ApJ, 627, 647

Barnes, J. & Efstathiou, G. 1987, ApJ, 319, 575

Barnes, J. E. 1988, ApJ, 331, 699

Barnes, J. E. & Hernquist, L. 1992, Annual Review of Astronomy and Astrophysics, 30, 705

—. 1996, ApJ, 471, 115

Behroozi, P. S., Conroy, C., & Wechsler, R. H. 2010, ApJ, 717, 379

Blanton, M. R., Hogg, D. W., Bahcall, N. A., Baldry, I. K., Brinkmann, J., Csabai, I., Eisenstein, D., Fukugita, M., Gunn, J. E., & Ivezić, Ž. 2003, ApJ, 594, 186

Bluck, A. F. L., Conselice, C. J., Buitrago, F., Grützbauch, R., Hoyos, C., Mortlock, A., & Bauer, A. E. 2012, ApJ, 747, 34

Blumenthal, G. R., Faber, S. M., Flores, R., & Primack, J. R. 1986, ApJ, 301, 27

Blumenthal, G. R., Faber, S. M., Primack, J. R., & Rees, M. J. 1984, Nature, 311, 517

Blumenthal, K. A. & Barnes, J. E. 2018, MNRAS, 479, 3952

Blumenthal, K. A., Moreno, J., Barnes, J. E., Hernquist, L., Torrey, P., Claytor, Z., Rodriguez-Gomez, V., Marinacci, F., & Vogelsberger, M. 2019, MNRAS

Borne, K. D. 1988, ApJ, 330, 61

Borzyszkowski, M., Porciani, C., Romano-Díaz, E., & Garaldi, E. 2017, MNRAS, 469, 594

Bose, S., Hellwing, W. A., Frenk, C. S., Jenkins, A., Lovell, M. R., Helly, J. C., & Li, B. 2016, MNRAS, 455, 318

Bournaud, F., Chapon, D., Teyssier, R., Powell, L. C., Elmegreen, B. G., Elmegreen, D. M., Duc, P.-A., Contini, T., Epinat, B., & Shapiro, K. L. 2011, ApJ, 730, 4

Broeils, A. H. & Rhee, M.-H. 1997, A&A, 324, 877

Bryan, G. L., Norman, M. L., O'Shea, B. W., Abel, T., Wise, J. H., Turk, M. J., Reynolds, D. R., Collins, D. C., Wang, P., Skillman, S. W., Smith, B., Harkness, R. P., Bordner, J., Kim, J.-h., Kuhlen, M., Xu, H., Goldbaum, N., Hummels, C., Kritsuk, A. G., Tasker, E., Skory, S., Simpson, C. M., Hahn, O., Oishi, J. S., So, G. C., Zhao, F., Cen, R., Li, Y., & Enzo Collaboration. 2014, The Astrophysical Journal Supplement Series, 211, 19

Bullock, J. S., Dekel, A., Kolatt, T. S., Kravtsov, A. V., Klypin, A. A., Porciani, C., & Primack, J. R. 2001, ApJ, 555, 240

Burkey, J. M., Keel, W. C., Windhorst, R. A., & Franklin, B. E. 1994, ApJ, 429, L13

Cheung, E., Athanassoula, E., Masters, K. L., Nichol, R. C., Bosma, A., Bell, E. F., Faber, S. M., Koo, D. C., Lintott, C., & Melvin, T. 2013, ApJ, 779, 162

Chua, K. T. E., Pillepich, A., Vogelsberger, M., & Hernquist, L. 2019, MNRAS, 484, 476

Cortijo-Ferrero, C., González Delgado, R. M., & Pérez, E. 2011, in Stellar Clusters & Associations: A RIA Workshop on Gaia, 379–380

Cox, T. J., Jonsson, P., Primack, J. R., & Somerville, R. S. 2006, MNRAS, 373, 1013

Cox, T. J., Jonsson, P., Somerville, R. S., Primack, J. R., & Dekel, A. 2008, MNRAS, 384, 386

Davé, R., Finlator, K., & Oppenheimer, B. D. 2011, MNRAS, 416, 1354

Davis, M., Efstathiou, G., Frenk, C. S., & White, S. D. M. 1985, ApJ, 292, 371

De Propris, R., Liske, J., Driver, S. P., Allen, P. D., & Cross, N. J. G. 2005, AJ, 130, 1516

Di Matteo, P., Combes, F., Melchior, A.-L., & Semelin, B. 2007, A&A, 468, 61

Diemer, B. 2018, ApJS, 239, 35

D'Onghia, E., Burkert, A., Murante, G., & Khochfar, S. 2006, MNRAS, 372, 1525

D'Onghia, E. & Navarro, J. F. 2007, MNRAS, 380, L58

Dubinski, J. & Carlberg, R. G. 1991, ApJ, 378, 496

Einasto, J. 1965, Trudy Astrofizicheskogo Instituta Alma-Ata, 5, 87

Emerick, A., Bryan, G. L., & Mac Low, M.-M. 2019, MNRAS, 482, 1304

Evans, A. S., Vavilkin, T., Pizagno, J., Modica, F., Mazzarella, J. M., Iwasawa, K., Howell, J. H., Surace, J. A., Armus, L., Petric, A. O., Spoon, H. W. W., Barnes, J. E., Suer, T. A., Sanders, D. B., Chan, B., & Lord, S. 2008, ApJ, 675, L69

Fitts, A., Boylan-Kolchin, M., Elbert, O. D., Bullock, J. S., Hopkins, P. F., Oñorbe, J., Wetzel, A., Wheeler, C., Faucher-Giguère, C.-A., & Kereš, D. 2017, MNRAS, 471, 3547

Flores, R. A. & Primack, J. R. 1994, ApJ, 427, L1

Franx, M., Illingworth, G., & de Zeeuw, T. 1991, ApJ, 383, 112

Gao, L., Navarro, J. F., Cole, S., Frenk, C. S., White, S. D. M., Springel, V., Jenkins, A., & Neto, A. F. 2008, MNRAS, 387, 536

Genel, S., Vogelsberger, M., Springel, V., Sijacki, D., Nelson, D., Snyder, G., Rodriguez-Gomez, V., Torrey, P., & Hernquist, L. 2014, MNRAS, 445, 175

Gunn, J. E. & Gott, J. Richard, I. 1972, ApJ, 176, 1

Hagiwara, Y. 2007, AJ, 133, 1176

Hernquist, L. & Katz, N. 1989, ApJS, 70, 419

Hogg, D. W., Blanton, M. R., Brinchmann, J., Eisenstein, D. J., Schlegel, D. J., Gunn, J. E., McKay, T. A., Rix, H.-W., Bahcall, N. A., & Brinkmann, J. 2004, ApJ, 601, L29

Holwerda, B. W., Pirzkal, N., de Blok, W. J. G., Bouchard, A., Blyth, S. L., van der Heyden, K. J., & Elson, E. C. 2011, MNRAS, 416, 2401

Hopkins, P. F., Hernquist, L., Cox, T. J., Di Matteo, T., Robertson, B., & Springel, V. 2006, ApJS, 163, 1

Hopkins, P. F., Kereš, D., Oñorbe, J., Faucher-Giguère, C.-A., Quataert, E., Murray, N., & Bullock, J. S. 2014, MNRAS, 445, 581

Hopkins, P. F. & Quataert, E. 2010, MNRAS, 407, 1529

Hu, F. X., Wu, G. X., Song, G. X., Yuan, Q. R., & Okamura, S. 2006, Ap&SS, 302, 43

Karl, S. J., Naab, T., Johansson, P. H., Theis, C., & Boily, C. M. 2008, Astronomische Nachrichten, 329, 1042

Kauffmann, G., Colberg, J. M., Diaferio, A., & White, S. D. M. 1999, MNRAS, 303, 188

Khochfar, S. & Burkert, A. 2006, A&A, 445, 403

Knebe, A., Knollmann, S. R., Muldrew, S. I., Pearce, F. R., Aragon-Calvo, M. A., Ascasibar, Y., Behroozi, P. S., Ceverino, D., Colombi, S., Diemand, J., Dolag, K., Falck, B. L., Fasel, P., Gardner, J., Gottlöber, S., Hsu, C.-H., Iannuzzi, F., Klypin, A., Lukić, Z., Maciejewski, M., McBride, C., Neyrinck, M. C., Planelles, S., Potter, D., Quilis, V., Rasera, Y., Read, J. I., Ricker, P. M., Roy, F., Springel, V., Stadel, J., Stinson, G., Sutter, P. M., Turchaninov, V., Tweed, D., Yepes, G., & Zemp, M. 2011, MNRAS, 415, 2293

Knebe, A., Pearce, F. R., Lux, H., Ascasibar, Y., Behroozi, P., Casado, J., Moran, C. C., Diemand, J., Dolag, K., & Dominguez-Tenreiro, R. 2013, MNRAS, 435, 1618

La Barbera, F., de Carvalho, R. R., de La Rosa, I. G., Lopes, P. A. A., Kohl-Moreira, J. L., & Capelato, H. V. 2010, MNRAS, 408, 1313

Larson, K. L., Sanders, D. B., Barnes, J. E., Ishida, C. M., Evans, A. S., U, V., Mazzarella, J. M., Kim, D.-C., Privon, G. C., Mirabel, I. F., & Flewelling, H. A. 2016, ApJ, 825, 128

Luparello, H. E., Lares, M., Paz, D., Yaryura, C. Y., Lambas, D. G., & Padilla, N. 2015, MNRAS, 448, 1483

Marinacci, F., Vogelsberger, M., Pakmor, R., Torrey, P., Springel, V., Hernquist, L., Nelson, D., Weinberger, R., Pillepich, A., Naiman, J., & Genel, S. 2018, MNRAS, 480, 5113

Méndez-Abreu, J., Debattista, V. P., Corsini, E. M., & Aguerri, J. A. L. 2014, A&A, 572, A25

Mihos, J. C. & Hernquist, L. 1996, ApJ, 464, 641

Miller, G. E. 1983, ApJ, 268, 495

Moore, B. 1994, Nature, 370, 629

Moreno, J., Torrey, P., Ellison, S. L., Patton, D. R., Bluck, A. F. L., Bansal, G., & Hernquist, L. 2015, MNRAS, 448, 1107

Moreno, J., Torrey, P., Ellison, S. L., Patton, D. R., Hopkins, P. F., Bueno, M., Hayward, C. C., Narayanan, D., Kereš, D., Bluck, A. F. L., & Hernquist, L. 2019, MNRAS, 485, 1320

Naiman, J. P., Pillepich, A., Springel, V., Ramirez-Ruiz, E., Torrey, P., Vogelsberger, M., Pakmor, R., Nelson, D., Marinacci, F., Hernquist, L., Weinberger, R., & Genel, S. 2018, MNRAS, 477, 1206

Navarro, J. F., Frenk, C. S., & White, S. D. M. 1994, MNRAS, 267, L1

Navarro, J. F., Frenk, C. S., & White, S. D. M. 1995a, MNRAS, 275, 720

—. 1995b, MNRAS, 275, 56

—. 1997, ApJ, 490, 493

Navarro, J. F., Hayashi, E., Power, C., Jenkins, A. R., Frenk, C. S., White, S. D. M., Springel, V., Stadel, J., & Quinn, T. R. 2004, MNRAS, 349, 1039

Navarro, J. F., Ludlow, A., Springel, V., Wang, J., Vogelsberger, M., White, S. D. M., Jenkins, A., Frenk, C. S., & Helmi, A. 2010, MNRAS, 402, 21

Nelson, D., Pillepich, A., Springel, V., Weinberger, R., Hernquist, L., Pakmor, R., Genel, S., Torrey, P., Vogelsberger, M., Kauffmann, G., Marinacci, F., & Naiman, J. 2018, MNRAS, 475, 624

Oñorbe, J., Garrison-Kimmel, S., Maller, A. H., Bullock, J. S., Rocha, M., & Hahn, O. 2014, MNRAS, 437, 1894

Pedrosa, S., Tissera, P. B., & Scannapieco, C. 2009, MNRAS, 395, L57

Peebles, P. J. E. 1969, ApJ, 155, 393

Peschken, N. & Łokas, E. L. 2019, MNRAS, 483, 2721

Pichon, C., Pogosyan, D., Kimm, T., Slyz, A., Devriendt, J., & Dubois, Y. 2011, MNRAS, 418, 2493

Pillepich, A., Nelson, D., Hernquist, L., Springel, V., Pakmor, R., Torrey, P., Weinberger, R., Genel, S., Naiman, J. P., Marinacci, F., & Vogelsberger, M. 2018a, MNRAS, 475, 648

Pillepich, A., Springel, V., Nelson, D., Genel, S., Naiman, J., Pakmor, R., Hernquist, L., Torrey, P., Vogelsberger, M., Weinberger, R., & Marinacci, F. 2018b, MNRAS, 473, 4077

Pohlen, M. & Trujillo, I. 2006, A&A, 454, 759

Renaud, F., Bournaud, F., & Duc, P.-A. 2015, MNRAS, 446, 2038

Rich, J. A., Kewley, L. J., & Dopita, M. A. 2015, ApJS, 221, 28

Rodriguez-Gomez, V., Sales, L. V., Genel, S., Pillepich, A., Zjupa, J., Nelson, D., Griffen, B., Torrey, P., Snyder, G. F., Vogelsberger, M., Springel, V., Ma, C.-P., & Hernquist, L. 2017, MNRAS, 467, 3083

Rodriguez-Gomez, V., Snyder, G. F., Lotz, J. M., Nelson, D., Pillepich, A., Springel, V., Genel, S., Weinberger, R., Tacchella, S., Pakmor, R., Torrey, P., Marinacci, F., Vogelsberger, M., Hernquist, L., & Thilker, D. A. 2019, MNRAS, 483, 4140

Sachdeva, S., Gadotti, D. A., Saha, K., & Singh, H. P. 2015, MNRAS, 451, 2

Schaye, J., Crain, R. A., Bower, R. G., Furlong, M., Schaller, M., Theuns, T., Dalla Vecchia, C., Frenk, C. S., McCarthy, I. G., & Helly, J. C. 2015, MNRAS, 446, 521

Schneider, M. D., Frenk, C. S., & Cole, S. 2012, Journal of Cosmology and Astro-Particle Physics, 2012, 030

Solanes, J. M., Perea, J. D., & Valentí-Rojas, G. 2018, A&A, 614, A66

Sparre, M. & Springel, V. 2016, MNRAS, 462, 2418

Spinoso, D., Bonoli, S., Dotti, M., Mayer, L., Madau, P., & Bellovary, J. 2017, MNRAS, 465, 3729

Springel, V. 2000, MNRAS, 312, 859

Springel, V., Di Matteo, T., & Hernquist, L. 2005, MNRAS, 361, 776

Springel, V. & Hernquist, L. 2005, ApJ, 622, L9

Springel, V., Pakmor, R., Pillepich, A., Weinberger, R., Nelson, D., Hernquist, L., Vogelsberger, M., Genel, S., Torrey, P., Marinacci, F., & Naiman, J. 2018, MNRAS, 475, 676

Springel, V., White, S. D. M., Tormen, G., & Kauffmann, G. 2001, MNRAS, 328, 726

Taylor, J. E. & Babul, A. 2001, ApJ, 559, 716

Toomre, A. & Toomre, J. 1972, ApJ, 178, 623

Torrey, P., Vogelsberger, M., Marinacci, F., Pakmor, R., Springel, V., Nelson, D., Naiman, J., Pillepich, A., Genel, S., Weinberger, R., & Hernquist, L. 2017, arXiv e-prints, arXiv:1711.05261

Trujillo, I., Graham, A. W., & Caon, N. 2001, MNRAS, 326, 869

Vitvitska, M., Klypin, A. A., Kravtsov, A. V., Wechsler, R. H., Primack, J. R., & Bullock, J. S. 2002, ApJ, 581, 799

Vogelsberger, M., Genel, S., Springel, V., Torrey, P., Sijacki, D., Xu, D., Snyder, G., Bird, S., Nelson, D., & Hernquist, L. 2014a, Nature, 509, 177

Vogelsberger, M., Genel, S., Springel, V., Torrey, P., Sijacki, D., Xu, D., Snyder, G., Nelson, D., & Hernquist, L. 2014b, MNRAS, 444, 1518

Vulcani, B., Bamford, S. P., Häußler, B., Vika, M., Rojas, A., Agius, N. K., Baldry, I., Bauer, A. E., Brown, M. J. I., & Driver, S. 2014, MNRAS, 441, 1340

Weinberger, R., Springel, V., Hernquist, L., Pillepich, A., Marinacci, F., Pakmor, R., Nelson, D., Genel, S., Vogelsberger, M., Naiman, J., & Torrey, P. 2017, MNRAS, 465, 3291

Weinberger, R., Springel, V., Pakmor, R., Nelson, D., Genel, S., Pillepich, A., Vogelsberger, M., Marinacci, F., Naiman, J., Torrey, P., & Hernquist, L. 2018, MNRAS, 479, 4056

Wetzel, A. R. & Nagai, D. 2015, ApJ, 808, 40

White, S. D. M. 1984, ApJ, 286, 38

White, S. D. M. & Rees, M. J. 1978, MNRAS, 183, 341

Zemp, M., Gnedin, O. Y., Gnedin, N. Y., & Kravtsov, A. V. 2011, ApJS, 197, 30

Chapter 6

Conclusions

The field of galaxy merger simulations is at a crossroads. Along one road lies cosmological simulations, which boast some of the most intricate models for star formation, feedback, and active nuclei. These capture a wealth of information regarding the environmental context of galaxies, and numerical methods are now so sophisticated that individual galaxies can have sub-kiloparsec resolution in a volume of millions of cubic megaparsecs. Down the other road are idealized simulations: much smaller in scope, but typically boast very high spatial and mass resolution. These are often used to access regimes and physics that are inaccessible to large-scale simulations because of their size. As a result, the subgrid physics models used in large-scale cosmological simulations are developed and perfected using these smaller scale simulations. In the era of precision cosmological simulations such as IllustisTNG, idealized simulations can still be valuable, but need to be updated. The primary concern of this thesis is to explore the limitations of the current state of idealized simulations, and provide suggestions to move toward a paradigm more strongly rooted in the physical reality of our universe.

6.1 Overview of this Dissertation

6.1.1 Gas Inflows in Realistic Discs

Observations of isolated galaxies have shown that the gas discs of spirals are always equal in size or larger than their corresponding stellar discs (e.g., Broeils & Rhee 1997). Despite this evidence, nearly every small-scale simulation of galaxy encounters models the gas and stellar distributions as equal-size exponential discs. In Chapter 3 we present a suite of idealized galaxy encounters to show how factors such as the relative size of the gas and stellar disc, disc inclinations, first pericentric distance, galaxy structure, and gas fraction affect the merger-induced nuclear inflow. All of these parameters conspire to impact the inflow. In prograde encounters, we find nuclear inflow to be the most efficient in small discs on wide orbits, while in retrograde encounters, larger gas discs yield relatively more inflow. In general, inflow is strongest in systems with equal-size gas discs; the tight coupling of the gas and stars, in addition to relatively low angular momentum of the gas, facilitates in-spiraling of gaseous material. As also seen in e.g., Renaud et al. (2014) and Di Matteo et al. (2007), the conventional wisdom that the diminished tidal force experienced by inclined discs results in minimal inflow (e.g., Barnes & Hernquist 1996; Mihos & Hernquist 1996) is inconsistent with these simulations: depending on the interaction geometry, inclined discs may experience more inflow than direct discs. The relative size of the gas and stellar discs adds a necessary level of complexity to simulations of galaxy encounters. Previous simulations that overlook parameter may over-estimate inflow, and as a result, the star formation rate.

6.1.2 Galaxy Mergers in IllustrisTNG

The observable universe does not tell us a galaxy's entire dynamical history. Figure 6.1 illustrates this point: though a pair of galaxies may exhibit visual signs of interaction (e.g., disturbed or warped stellar discs; right panel of Figure 6.1), they may not actually be orbiting one another. The inverse is also true; a pair of galaxies which have no obvious signs of interaction (left panel of Figure 6.1) may, in fact, be in the process of merging. Cosmological simulations thus offer a unique opportunity to test the observational methods used to motivate idealized simulations. We use IllustrisTNG to identify and classify 85 pairs of ongoing interactions. Using mock SDSS images, we sort the pairs into two groups – visually identified pairs (VIP) and non-visually identified pairs (nonVIP) – and classify them based on (stellar) morphological indicators typical of observational merger catalogues. We find that ~45% of interacting pairs are easily identifiable as merging systems. There are a number of biases that play into this. First, the VIP have had a close passage more recently than the nonVIP, which speaks to the longevity of tidal features. Second, by three independent environmental measures (the total group mass, the nth nearest neighbor, and the interaction strength), the VIP are in more massive halos, sit in systematically denser environments, and are more significantly effected by their neighbors. Thus, a local merger sample built solely from the presence or absence of stellar tidal features is likely to be incomplete and biased toward specific environments.

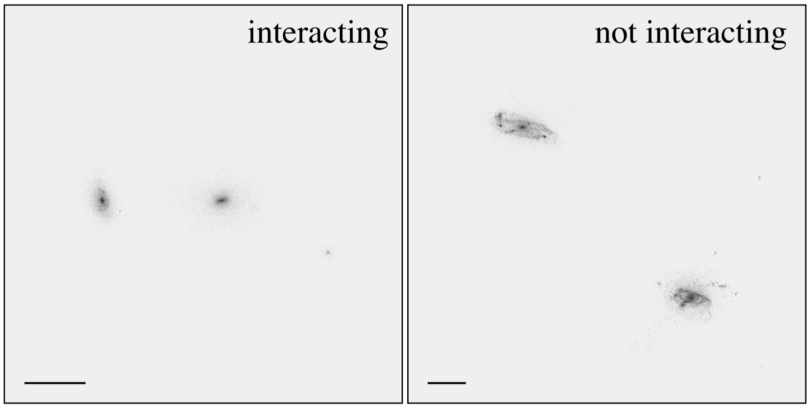

Figure 6.1 Simulations of galaxy mergers are informed by observationally identified systems in the real universe, but the details of the orbit's dynamics often obscure the true history of a merging pair. Shown here are mock SDSS images of binary pairs in the IllustrisTNG $z = 0$ snapshot (bars indicate 50kpc). Despite the disturbed morphologies of the disks on the right, this pair is not interacting. However, the left panel, which shows a pair with no obvious tidal features, has undergone two close passages.

6.1.3 Reevaluating Kepler: A Primer for Idealized Simulations of Galaxy Encounters

The fundamental assumption of a Keplerian orbit is that the bodies on intersecting trajectories can initially be treated as independent and separable systems. This has three primary consequences: (1) the orbital elements are roughly constant between infall and first pericenter, (2) the mass of the system remains constant, and (3) the orbit occurs on a single, well-defined plane. In Chapter 5, we show that in most systems, there is a nontrivial amount of mass and momentum accreted by the FoF group halo in the time between infall and the present day. During this period, the orbital elements change significantly, often resulting in drastic differences between the measured time to pericenter and the time derived from equations that describe the orbit. Despite these inconsistencies with Kepler, we find that the galaxies' trajectories are confined to a plane throughout the entire interaction. Thus, there are ways in which the Keplerian approximation is appropriate, and ways in which it falls short of accurately representing known systems.

To the extent that the Keplerian approximation is valid, we provide cosmologically motivated initial conditions for idealized galaxy interactions that avoid the biases of observational catalogues noted in Chapter 4. There are a number of important consequences of the parameter distributions given in the table at the end of Chapter 5. For example, current galaxy orbits are affected by prior mergers of all sizes, minor gravitational harassments, and flybys. As such, their eccentricities are not parabolic. We also find that galaxy disc orientations are not random, but are in fact biased toward prograde. Compared to retrograde, prograde encounters experience a stronger tidal response, and larger inflow rate. That these inclinations are not randomly distributed may significantly impact predicted rates of star formation. Further, most of the TNG100-1 pairs have first pericenterss that are 2-4 times larger than those assumed by many idealized simulations. This failure to account for wide orbits may affect the interpretation of galaxies' dynamical and star formation histories. In addition to using Einasto profiles to describe the dark matter halos, we note that the stellar distributions cannot all be described by a single exponential profile, but span a range of Sérsic indices. The gas distributions, on the other hand, are too disturbed at infall to fit a single profile.

As a test of the efficacy of these suggestions, we generate simulations of one interacting pair, the Shuixiu System, in three different ways: by reconstructing the galaxies based on the particle positions and velocities at infall, and by generating idealized models of the system with both equilibrium and non-equilibrium spherical Einasto profiles. We find that the best fit to the TNG100-1 trajectories result from non-equilibrium idealized models which have been increased in mass by 25%, as a crude approximation of the additional mass accreted onto the system between infall and the present day.

6.2 Future Work

6.2.1 Improve Observational Merger Catalogues

The Sloan Digital Sky Survey (SDSS) has mapped the universe in remarkable detail for the last 20 years. Its diverse armory of instruments has facilitated nearly every area of research from the structure of the Milky Way to the large-scale structure of the universe. In the coming years, MaNGA (Mapping Nearby Galaxies with APO) will provide integral field unit observations for the nearest 104 SDSS galaxies. In Chapter 4, we show that stellar tidal features are an unreliable indicator of merger activity. However, the gas is much more extended than the stars, and as such will be more affected by tidal interactions. To date, there has yet to be a systematic study of gas phase merger morphology. The MaNGA data will not only provide gas-phase morphologies of these galaxies, but also kinematic information that could better constrain the orbital geometry than stellar morphologies alone. Comparing this observational data with mock IFU observations (e.g., Yajima et al. 2012) of the TNG100-1 interacting pairs sample described in Chapters 4 and 5 will be crucial for understanding the limitations of each. This will not only enable a detailed exploration of the behavior of gas in TNG100-1, but if applied to galaxies at higher redshift, may also prove invaluable for interpreting the output of the James Webb Space Telescope.

6.2.2 The Next Generation of Merger Simulations

The current state of idealized simulations is sufficient to analyze the tidal features and overall dynamics of merging systems. However, great care must be taken not to over-interpret results regarding the internal structure of individual galaxies. Above, and in previous chapters, we have discussed aspects of the Keplerian approximation that need improvement. In Chapter 5 we present a crude way to account for the inflow of dark matter and gas onto a halo from its cosmological surroundings, but this needs to be made more systematic. It would be beneficial to carefully study the 85 interacting pairs discussed in this thesis to understand how, when, and where mass is distributed onto the halos. Additionally, the total angular momentum of galaxies is not negligible in comparison to their parent FoF group halos. More exploration is required to understand the impact this has on orbital history, morphology, and remnant substructure. All halos presented here are triaxial. Though this is not a new result, future idealized simulations must account for departures from sphericity. At large distances, the potential due to the triaxial halo may appear spheroidal, but near pericenter when halos are deeply interpenetrating, the tidal field experienced by each halo will depend significantly on the dark matter distribution. Further, idealized galaxies are constructed using equilibrium halos, an assumption that presumes previous encounters were either very long ago or were relatively minor. This is not the case for the early universe, at which time hierarchical structure is being built up through frequent mergers.

6.2.3 Zoom-in Simulations

Cosmological zoom simulations are valuable for investigating cosmological halos at a much higher resolution. In this framework, a halo found in a large-scale cosmological simulation is reconstructed at a high spatial and mass resolution, while its immediate surroundings are at low resolution. As a result, zoom simulations provide the context (e.g., local tidal field, sources of inflow) of cosmological, and the resolution of idealized simulations. These cannot be used to construct galaxy models from individual components (e.g., to recreate an observed system), as the initial conditions are derived from the full cosmological simulation. Interesting regions, such as the interacting pairs discussed here, can be traced back in time and re-run within a localized region of high resolution. Performing a systematic study of the TNG100-1 pairs sample using zoom simulations would provide the basis for understanding not only the departures from the Keplerian approximation discussed above, but also the future evolution – and eventual merger – of these systems.

6.2.4 Implications for Dwarf Galaxy Physics

In Chapter 3, we demonstrate that inflow is greatly suppressed in massive galaxies with large gas disks. Most models of star formation assume that it is triggered as a result of gaseous inflow, but dwarf galaxies typically have extremely extended gas discs (eg., Pearson et al. 2016; Swaters et al. 2002), and as such should not experience much inflow. However, dwarf galaxies are known to have widespread star formation, which begs the question: how is the star formation mechanism different in low-mass galaxies? At these low mass scales, high resolution and realistic feedback prescriptions are of upmost importance. For example, in massive galaxies, supernovae only locally alter ISM properties, whereas in dwarf galaxies they are far more disruptive. Additionally, dwarf galaxy dark matter halos are typically unique from those of massive galaxies: dwarf galaxies tend to be dark matter dominated, even at the very centre. Thus in many cases, baryons cannot control the internal structure or dynamics of the galaxy. Clearly, detailed simulations (e.g., Bryan et al. 2014; Emerick et al. 2019) of dwarf galaxies is necessary to understand star formation across all mass scales.

References

Barnes, J. E. & Hernquist, L. 1996, ApJ, 471, 115

Broeils, A. H. & Rhee, M.-H. 1997, A&A, 324, 877

Bryan, G. L., Norman, M. L., O'Shea, B. W., Abel, T., Wise, J. H., Turk, M. J., Reynolds, D. R., Collins, D. C., Wang, P., Skillman, S. W., Smith, B., Harkness, R. P., Bordner, J., Kim, J.-h., Kuhlen, M., Xu, H., Goldbaum, N., Hummels, C., Kritsuk, A. G., Tasker, E., Skory, S., Simpson, C. M., Hahn, O., Oishi, J. S., So, G. C., Zhao, F., Cen, R., Li, Y., & Enzo Collaboration. 2014, The Astrophysical Journal Supplement Series, 211, 19

Di Matteo, P., Combes, F., Melchior, A.-L., & Semelin, B. 2007, A&A, 468, 61

Emerick, A., Bryan, G. L., & Mac Low, M.-M. 2019, MNRAS, 482, 1304

Mihos, J. C. & Hernquist, L. 1996, ApJ, 464, 641

Pearson, S., Besla, G., Putman, M. E., Lutz, K. A., Fernández, X., Stierwalt, S., Patton, D. R., Kim, J., Kallivayalil, N., Johnson, K., & Sung, E.-C. 2016, MNRAS, 459, 1827

Renaud, F., Bournaud, F., Kraljic, K., & Duc, P.-A. 2014, MNRAS, 442, L33

Swaters, R. A., van Albada, T. S., van der Hulst, J. M., & Sancisi, R. 2002, A&A, 390, 829

Yajima, H., Li, Y., Zhu, Q., & Abel, T. 2012, MNRAS, 424, 884

Appendix A

Appendix to Chapter 3

A.1 SPH Code

The SPH code used for these simulations incorporates algorithms from TREESPH (Hernquist & Katz 1989) and Gasoline (Wadsley et al. 2004); gravitational forces are calculated using a Tree algorithm (Barnes & Hut 1986). Previous studies using this code include Barnes (2002, 2004); Chien & Barnes (2010).

As in other SPH codes (e.g., Monaghan 1992), gaseous material is represented using discrete particles, and kernel interpolation is used to obtain hydrodynamic variables as functions of position. Gas particles are subject to "hydrodynamic" forces due to pressure gradients as well as shocks; the net acceleration of gas particle i due to such forces is

$$\left(\frac{\nabla P}{\rho}\right)_i^{\mathrm{SPH}} = \sum_{j\neq i} m_j \left(\frac{P_i}{\rho_i^2} + \frac{P_j}{\rho_j^2} + \Pi_{ij}\right) \hat{\mathbf{r}}_{ij} \left.\frac{d\overline{W}}{dr}\right|_{r=r_{ij}}, \tag{A.1}$$

where

$$\frac{d\overline{W}}{dr} = \frac{1}{2}\left[\frac{dW(r,h_i)}{dr} + \frac{dW(r,h_j)}{dr}\right] \tag{A.2}$$

and our notation follows Monaghan (1992) throughout. Likewise, the internal energy u_i of gas particle i is subject to PdV work and shock dissipation:

$$\dot{u}_i^{\mathrm{SPH}} = \sum_{j\neq i} m_j \left(\frac{P_i}{\rho_i^2} + \frac{1}{2}\Pi_{ij}\right) \hat{\mathbf{r}}_{ij} \cdot \mathbf{v}_{ij} \left.\frac{d\overline{W}}{dr}\right|_{r=r_{ij}}. \tag{A.3}$$

If the internal energy u_i is allowed to vary according to Eq. (2), the net energy of a self-gravitating SPH system is

$$E_{\rm net} = U_{\rm grav} + T_{\rm kin} + E_{\rm int}\,. \tag{A.4}$$

where $U_{\rm grav}$ and $T_{\rm kin}$ are the gravitational and kinetic energy, respectively, of the particle system, and

$$E_{\rm int} = \sum_i m_i\, u_i \tag{A.5}$$

is the internal energy of the gas particles. In the absence of numerical errors, $E_{\rm net}$ is conserved. As a slight abuse of terminology, we refer to such an SPH system as "adiabatic" even though Eqs. (B1) and (B2) include non-adiabatic processes (shocks).

When implementing an *isothermal* SPH system, it's tempting to ignore Eq. (B2) altogether and simply set u_i = constant. In this case, however, the quantity $E_{\rm net}$ defined in Eq. (B3) is no longer conserved, and variations in $E_{\rm net}$ cannot be used to diagnose numerical errors. Instead, we imagine that each gas particle is coupled to an external reservoir with constant temperature T and infinite heat capacity. Any PdV work or shock heating is then transferred to the external reservoir, and the internal energy of gas particle i obeys

$$\frac{du_i}{dt} = \dot{u}_i^{\rm SPH} + \dot{u}_i^{\rm EXT}\,, \tag{A.6}$$

where $\dot{u}_i^{\rm EXT} = -\dot{u}_i^{\rm SPH}$ represents energy exchanged with the external reservoir by particle i; thus $du_i/dt = 0$ and the gas is isothermal. The net energy is then

$$E_{\rm net} = U_{\rm grav} + T_{\rm kin} + E_{\rm int} + E_{\rm ext}\,, \tag{A.7}$$

where $E_{\rm ext}$, the energy in the external reservoir, obeys

$$\frac{dE_{\rm ext}}{dt} = \sum_i m_i\, \dot{u}_i^{\rm EXT}\,. \tag{A.8}$$

The net energy $E_{\rm net}$ is conserved and variations can be used to detect numerical errors.

A.2 Measuring Torques

As with the inflow calculations, we took the first 8192 bulge or stellar disc particles (where the particles are sorted by binding energy) to define the positional centroid. However, because torque measurements depend on both position and acceleration, we also determined the acceleration centre using the first 8192 halo particles. If the bulge particles are used to determine the acceleration centre, there is a substantial amount of jitter in the centroid's motion. Similarly, the halo particles do not accurately track the positional centroid of the potential well because the halo particles are diffuse. In all encounters, this method tracks the nuclear material well, and minimizes the motion of the potential's position in phase space.

Torque is the result of a force, $\bar{F}$, applied to a lever arm, $\bar{r}$,

$$\bar{\tau} = \bar{r} \times \bar{F} \tag{A.9}$$

This then produces a change in the angular momentum

$$\bar{\tau} = \frac{\mathrm{d}\bar{L}}{\mathrm{d}t} \tag{A.10}$$

Using the centroiding described above, we calculated the angular momentum at each time step, and took the time derivative of that function to arrive at a derived torque. If we had calculated explicitly the acceleration due to each component (i.e., bulge, gas and stellar discs, halo, etc.) at every time step, then the calculated torque (i.e., the result of the $\bar{r} \times \bar{F}$ calculation) and the derived torque would be the same. However, this was not the case. Hence, there is some residual scatter between these two measurements, as seen in Figure 3.10. Instead, to calculate the force due to each component on the Lagrangian volume, we set up acceleration calculations using the position and velocity information of all particles at each time step, weighted such that we single out individual components. To account for precession, we align the torque and angular momentum vectors.

Appendix B

Appendix to Chapter 4

B.1 Technical Details

B.1.1 Data Structure

The IllustrisTNG model is run at three different volumes (TNG50, TNG100 and TNG5300), each with a dark matter only run, and a dark plus baryonic matter run. Additionally, there are three (TNG100 and TNG300) or four (TNG50) iterations for each simulation that correspond to different initial conditions and resolutions. All simulations contain 100 nearly logarithmically spaced snapshots that span a redshift range of z = [0 – 20]. Particle data is available for all snapshots, and is organised based on three criteria: binding energy, subfind halo membership, and friend-of-friend (FoF) group membership. Subfind haloes (or, 'subhaloes') are defined based on the SUBFIND algorithm (Springel et al. 2001), which links together baryonic and dark matter particles into locally over-dense and bound groups. The FoF haloes (or simply, 'groups') are explicitly defined only for the dark matter particles using the FoF algorithm (Davis et al. 1985) with linking length $b = 0.2$, however baryonic particles' membership to a FoF group is based on the membership of the closest dark matter particle.

B.2 Visual Examples

In this Appendix, we present our ideal mock SDSS g-band images for each of the 85 interacting pairs. These are organized roughly by their FoF group mass, with the most massive haloes at the top of the figure.

Numerical Parameters		Cosmological Parameters	
Volume	110.7^3 Mpc^3	$\Omega_{\rm dm}$	0.3089
$N_{\rm gas}$	1820^3	$\Omega_{\rm baryon}$	0.0486
$N_{\rm dm}$	1020^3	Ω_Λ	0.6911
$m_{\rm baryon}$	1.4×10^6 $M_\odot$	h	0.6744
$m_{\rm dm}$	7.6×10^6 $M_\odot$		
$\epsilon_{\rm baryon}$	0.7 kpc		
$\epsilon_{\rm dm}$	1.4 kpc		

Table B.1 *Left:* Numerical specifications of TNG100-1. *Right:* Cosmological parameters used in the IllustrisTNG model.

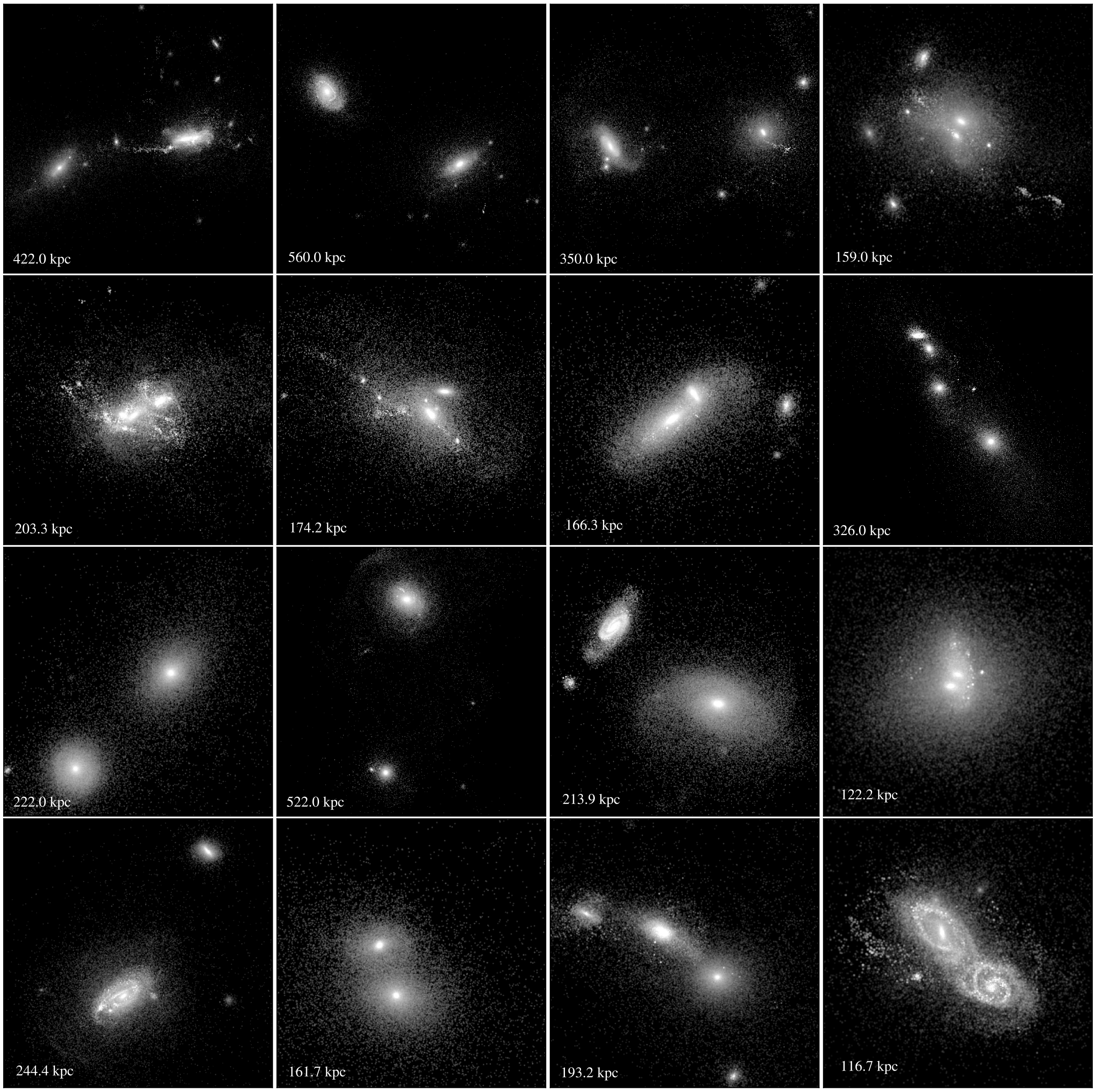

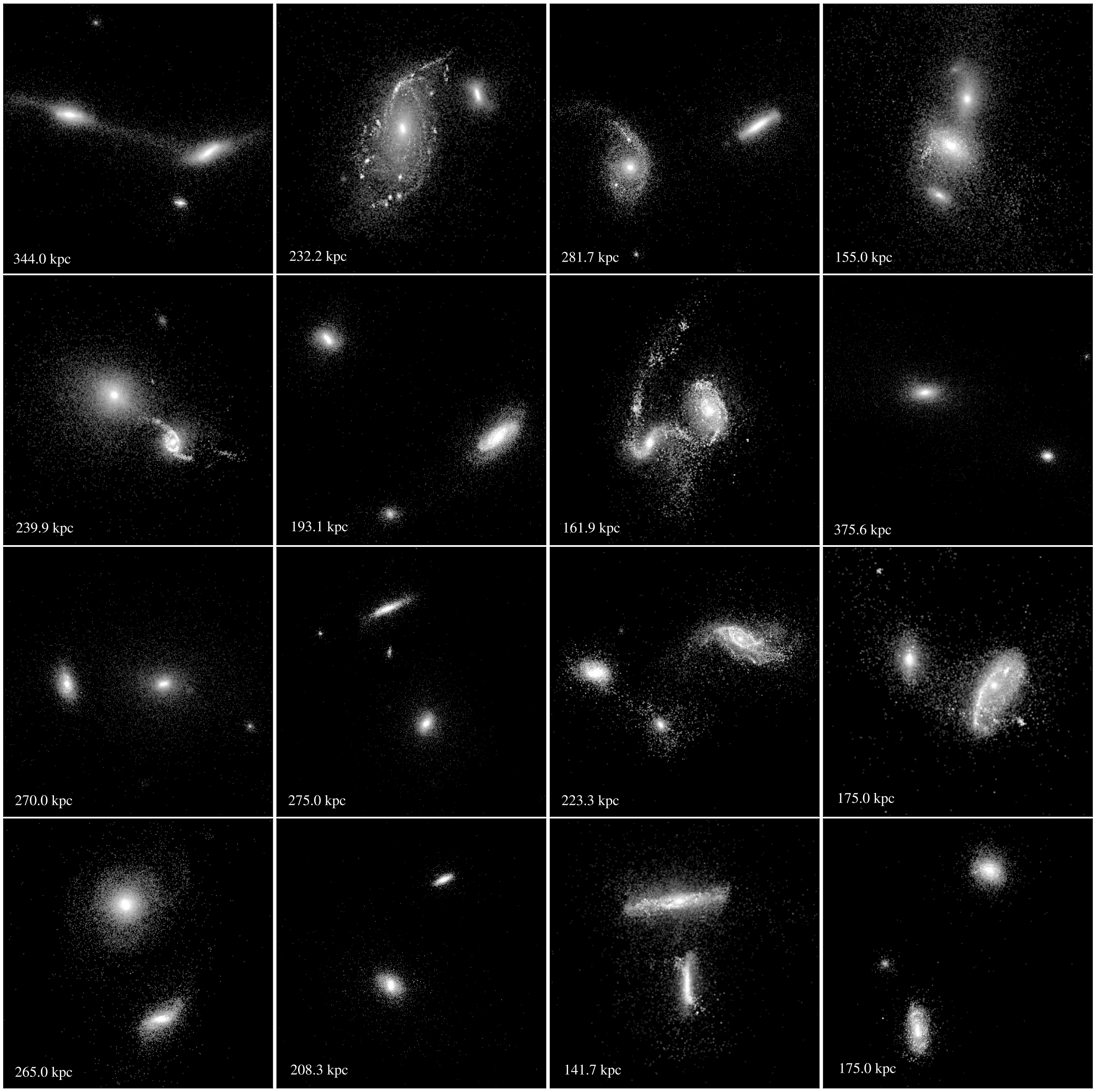

344.0 kpc
232.2 kpc
281.7 kpc
155.0 kpc
239.9 kpc
193.1 kpc
161.9 kpc
375.6 kpc
270.0 kpc
275.0 kpc
223.3 kpc
175.0 kpc
265.0 kpc
208.3 kpc
141.7 kpc
175.0 kpc

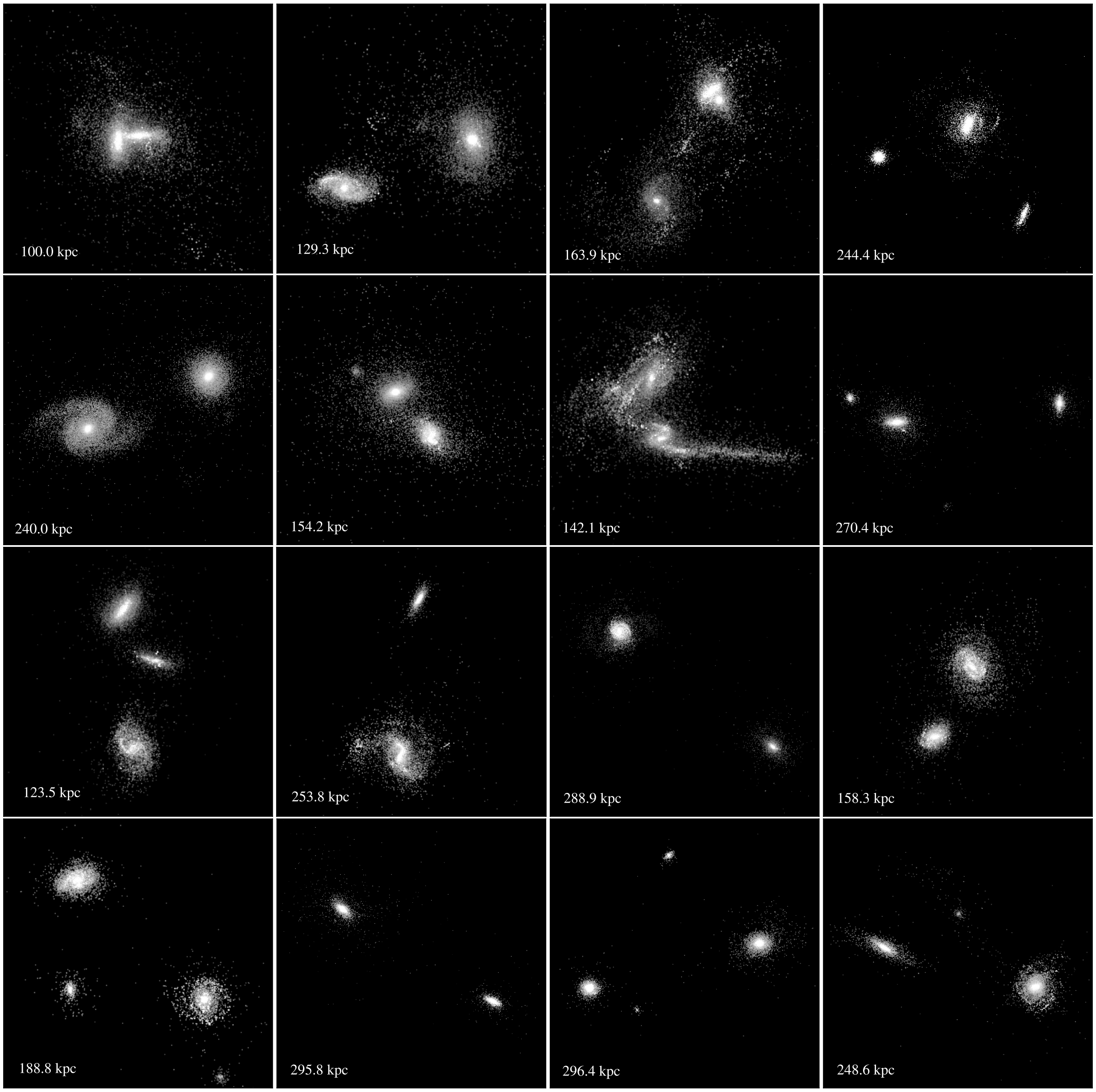
100.0 kpc
129.3 kpc
163.9 kpc
244.4 kpc
240.0 kpc
154.2 kpc
142.1 kpc
270.4 kpc
123.5 kpc
253.8 kpc
288.9 kpc
158.3 kpc
188.8 kpc
295.8 kpc
296.4 kpc
248.6 kpc

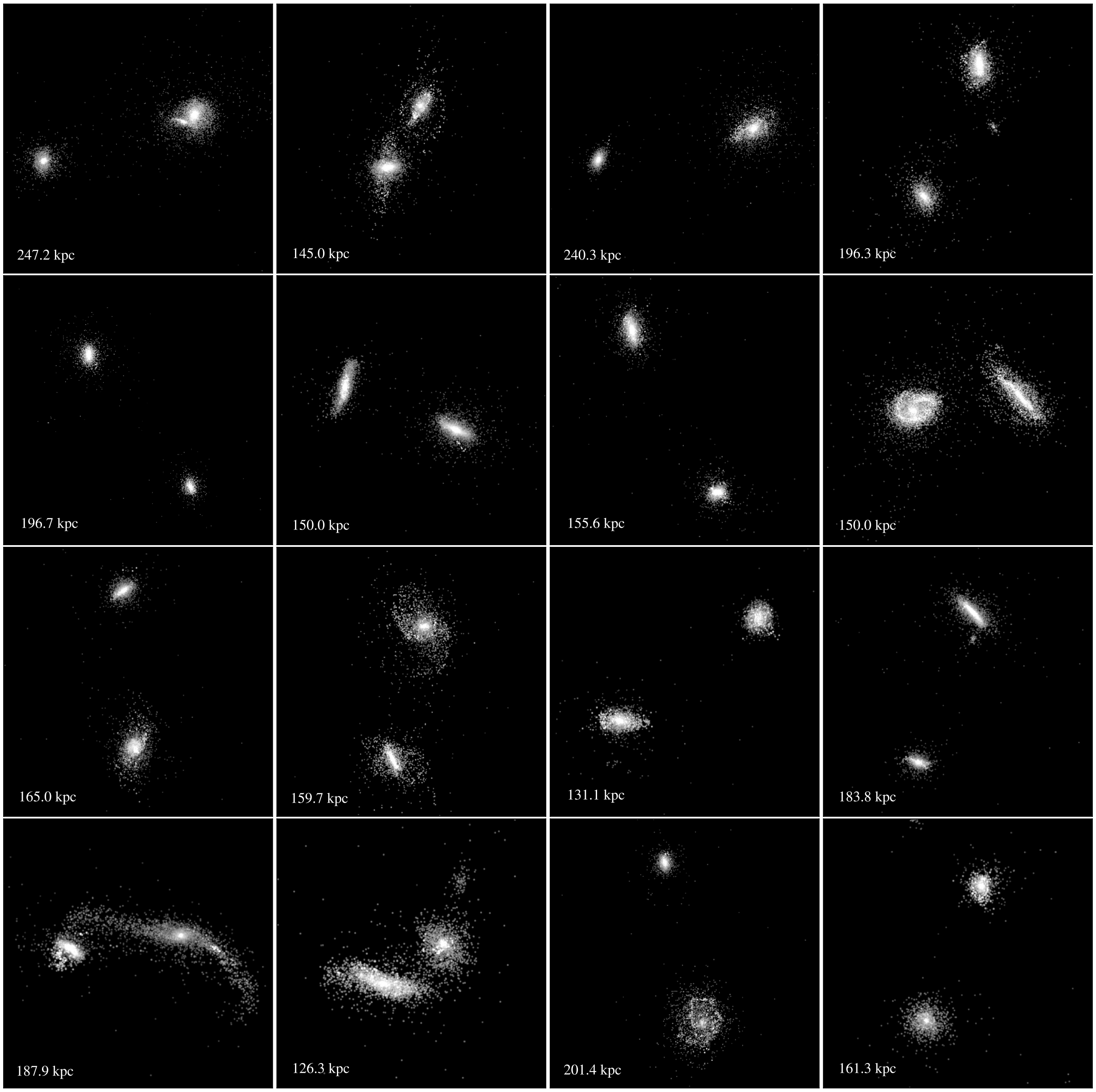
247.2 kpc
145.0 kpc
240.3 kpc
196.3 kpc
196.7 kpc
150.0 kpc
155.6 kpc
150.0 kpc
165.0 kpc
159.7 kpc
131.1 kpc
183.8 kpc
187.9 kpc
126.3 kpc
201.4 kpc
161.3 kpc

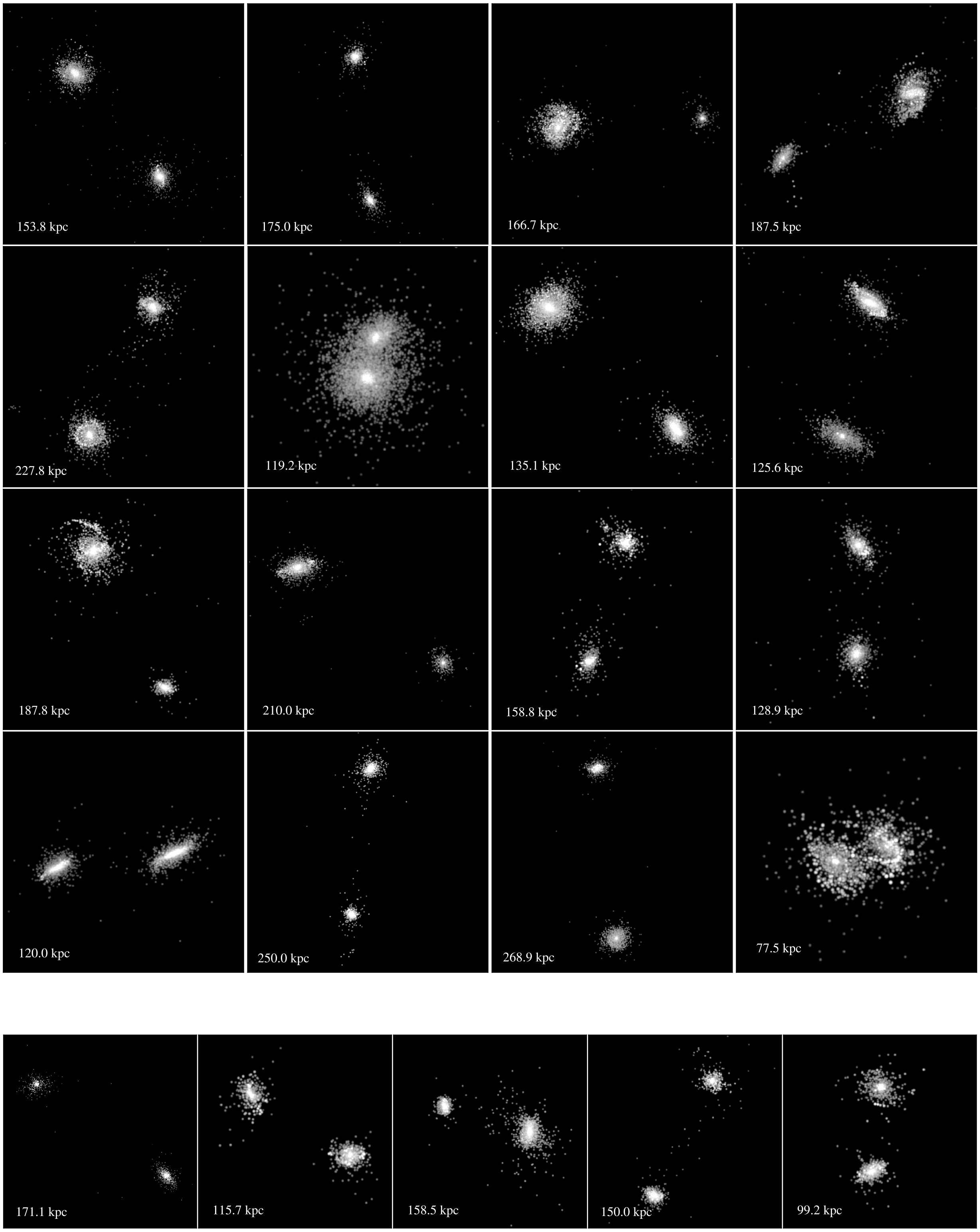

Figure B.1 Ideal mock SDSS images of the 85 TNG100-1 interacting pairs at $z = 0$. Galaxies are ordered roughly by their FoF group mass, with the most massive halos at the beginning, and the less massive halos toward the end.

Appendix C

Appendix to Chapter 5

C.1 The Shiuxiu System, A Case Study

Our models of the Shuixiu System are based on its FoF group configuration at infall ($t = 11.00\,\mathrm{Gyr}$). This configuration is composed of $N_{\mathrm{tot}} = 475647$ bodies, including $N_{\mathrm{bh}} = 2$ black holes, $N_{\mathrm{dm}} = 260374$ dark matter bodies, $N_{\mathrm{st}} = 69318$ stellar bodies, and $N_{\mathrm{gas}} = 145953$ gas bodies; the latter provide a convenient representation of the AREPO (Springel 2010) fluid model. Each body $i = 1, \ldots, N_{\mathrm{tot}}$ has a mass m_i, position vector $\mathbf{r}_i$, velocity vector $\mathbf{v}_i$, and optionally (for gas bodies) a temperature T_i. Positions and velocities are specified in physical (that is, non-comoving) coordinates; we adopted the center of mass of the FoF configuration as the coordinate origin.

After some preliminary tests, we decided not to use the sub-halo information that SUBFIND generated in modeling this system. In the specific case of the Shuixiu System, the SUBFIND algorithm included a number of bodies surrounding the secondary as part of the primary subhalo. To avoid complications arising from these misapportioned bodies, we instead chose to define all bodies within 250 kpc of the black hole at the center of the primary as members of the primary galaxy. Likewise, we defined all bodies within 200 kpc of the secondary's black hole as members of the secondary galaxy. Visual inspection showed these definitions appear reasonable, with the radial cutoffs corresponding closely to the physical extent of the two dark-matter halos. Some 95% of the FoF group mass is assigned to one of the two galaxies.

C.1.1 Reconstituted Models

Before attempting to construct idealized models, we first experimented with reconstituted versions formatted for a simple N-body code which uses a hierarchical force calculation algorithm (Barnes & Hut 1986) and a common-timestep leap-frog integrator. The initial conditions for these experiments use masses, positions and velocities for stellar and dark matter bodies taken directly from the FoF configuration. Each FoF gas body i was replaced by a collisionless equivalent with the same mass and position, but with velocity $\mathbf{v}'_i = \mathbf{v}_i + \mathbf{u}(T_i)$, where $\mathbf{u}(T)$ is drawn from a 3-D Maxwell–Boltzmann velocity distribution with an rms of $23.6\,\mathrm{km/sec} \times \sqrt{T/10^4\,\mathrm{K}}$. In effect, this procedure replaces the thermal energy of the gas bodies with a statistically equal amount of kinetic energy. In addition, each black hole body was replaced by a nuclear cluster of $N_{\mathrm{nc}} = 32$ bodies with the same total mass. We did this because our N-body code had no special provisions to properly handle interactions between the relatively massive black-holes and the rest of the system.

We likewise generated initial conditions for reconstituted versions of the primary and secondary galaxies by first selecting all FoF bodies within the appropriate radius of the primary or secondary black hole, respectively, and then applying the transformations described above.

C.1.2 Idealized Models

To construct initial conditions for an idealized model, we need individual models for the two galaxies, and a specification of their positions and velocities at infall.

Initial coordinates

Initial positions and velocities of the primary and secondary galaxies (respectively, $\mathbf{r}_{\mathrm{pri}}$, $\mathbf{v}_{\mathrm{pri}}$, $\mathbf{r}_{\mathrm{sec}}$, $\mathbf{s}_{\mathrm{sec}}$) are required to initialize an idealized encounter. We adopted the aggregate center-of-mass position and velocity of each galaxy as defined above. For the primary galaxy, we set

$$\mathbf{r}_{\mathrm{pri}} = \frac{\sum_i m_i \mathbf{r}_i}{\sum_i m_i} \qquad \text{and} \qquad \mathbf{v}_{\mathrm{pri}} = \frac{\sum_i m_i \mathbf{v}_i}{\sum_i m_i}\,, \tag{C.1}$$

where the index i runs over all bodies in the primary. Analogous expressions are used for the secondary galaxy.

Individual mass models

Our idealized models use spherical mass distributions for the primary and secondary galaxies. A spherical distribution is entirely characterized by the cumulative mass profile $M(r)$, which reports the total mass inside

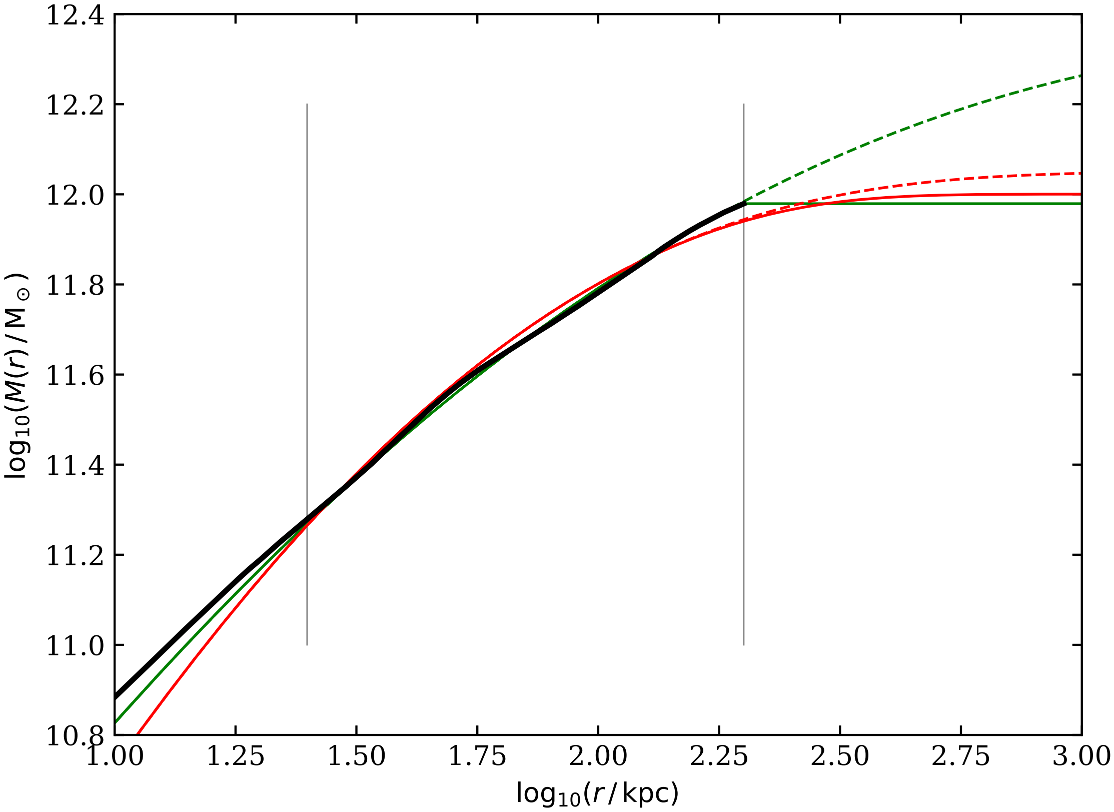

Figure C.1 Cumulative mass profiles for the secondary galaxy in the Shuixiu System. The black curve is the actual mass profile measured from the infall FoF group configuration. The solid red curve shows our equilibrium model, which employs an Einesto profile, modified to converge more rapidly as r increases; the dashed red curve is an unmodified Einasto profile. The solid green curve shows our non-equilibrium model, which is abruptly truncated ar $r = 200$ kpc; the dashed green curve again shows a unmodified Einasto profile.

radius r. The actual mass profiles for the two galaxies were measured by centering on their respective black holes and binning the mass of all bodies – including stars and gas – in spherical shells $\Delta r = 1$ **kpc** thick. In Fig. C.1, the black curve shows the resulting $M(r)$ curve for the secondary galaxy. We will use the secondary galaxy as an example in what follows, but the primary galaxy can be modeled by the same procedures.

Equilibrium models are defined by fitting a modified Einasto profile to the actual mass profile. This modified profile matches a standard Einasto (Eqn. 5.1) model for $r < r_{\mathrm{taper}} = 100$ kpc, while at larger radii the density smoothly tapers off (see § 4 of Barnes 2012 for details), thereby converging more rapidly to a given total mass as $r \to \infty$. In Fig. C.1, the solid red curve shows the equilibrium model for the secondary

Galaxy	**Type**	n	M_{fit}	r_{s}	r_{taper}	r_{trunc}
			$[10^{12} M_{\odot}]$	[kpc]	[kpc]	[kpc]
primary	equilib.	2.80	1.235	85	100	
secondary	equilib.	3.20	1.001	80	100	
primary	non-equ.	8.50	2.881	300		200
secondary	non-equ.	8.25	2.383	300		200

Table C.1 Parameters for individual galaxy models.

galaxy. This profile is constrained to have total mass $M_{\text{fit}} = 1.05 M_{\text{sec}}$, where M_{sec} is the total mass of the secondary within $r = 200$ kpc. The 5% additional mass improves the fit within 200 kpc without significantly perturbing the encounter dynamics. The other parameters for this model were chosen by hand to obtain a good fit for 25 kpc $\leq r \leq$ 200 kpc, indicated by the grey vertical lines. For comparison, the red dashed curve shows the same Einasto profile with no taper; it converges to $\sim 1.18 M_{\text{sec}}$ as $r \to \infty$.

Once the parameters for a model are determined, we construct an N-body realization by (1) calculating the gravitational potential $\Phi(r)$ from the density $\rho(r)$; (2) using the Eddington (1916) formula to find the isotropic distribution function $f(E)$; (3) sampling the distribution function to obtain positions $\mathbf{r}_i$ and velocities $\mathbf{v}_i$ for N bodies, each of mass $m_i = M_{\text{fit}}/N$.

We created non-equilibrium models by generating equilibrium N-body realizations of Einasto profiles and keeping only bodies within $r < r_{\text{trunc}} = 200$ kpc. This somewhat ad-hoc approach was motivated by experiments with reconstituted versions of the individual galaxies, which appear to be truncated by the outer limits of the FoF configuration. In Figure C.1, the dotted green curve shows a standard Einasto profile, constrained to have $M_{\text{fit}} = 2.5 M_{\text{sec}}$. The solid green curve shows the mass profile after truncation at r_{trunc}. Note that this fit is appreciably better than the fit used for the equilibrium model because it uses a more linear (in the $\log r$ vs $\log M(r)$ plane) portion of the Einasto profile.

Table C.1 collects model parameters for the individual galaxy mass models.

Embedded discs

We used massless bodies to model the discs in the primary and secondary galaxies. Massless discs are easy to implement, and do an adequate job of reproducing the essentially kinematic development of tidal features (Toomre & Toomre 1972). The mass of the actual discs has already been included in the cumulative mass profile $M(r)$.

The stellar distributions in the FoF configuration may be fit using Sérsic profiles with indices $n \simeq 3$ (see Figure 5.7). We modeled the disc components of the primary and secondary galaxies using exponential profiles with inverse scale lengths of 0.28 kpc^{-1} and 0.2 kpc^{-1}, respectively. These scales were chosen to roughly match the half-mass radii of the stellar discs. The disc component in the primary galaxy is quite thick, indicating a high velocity dispersion; we therefore gave each disc body a random velocity of $0.3v_\mathrm{c}$, where v_c is the local circular velocity in each velocity coordinate. Likewise, the thinner secondary disc was modeled with a velocity dispersion of $0.1v_\mathrm{c}$ in each velocity coordinate. We determined the disc angular momentum (and thus, the inclination of the stellar discs) without using the restrictions above. However, because the discs of the primary and secondary galaxies are very well defined, these values are nearly identical.

References

Barnes, J. & Hut, P. 1986, Nature, 324, 446

Barnes, J. E. 2002, MNRAS, 333, 481

—. 2004, MNRAS, 350, 798

Chien, L.-H. & Barnes, J. E. 2010, MNRAS, 407, 43

Davis, M., Efstathiou, G., Frenk, C. S., & White, S. D. M. 1985, ApJ, 292, 371

Eddington, A. S. 1916, MNRAS, 76, 572

Hernquist, L. & Katz, N. 1989, ApJS, 70, 419

Monaghan, J. J. 1992, ARA&A, 30, 543

Nelson, D., Pillepich, A., Genel, S., Vogelsberger, M., Springel, V., Torrey, P., Rodriguez-Gomez, V., Sijacki, D., Snyder, G. F., Griffen, B., Marinacci, F., Blecha, L., Sales, L., Xu, D., & Hernquist, L. 2015, Astronomy and Computing, 13, 12

Rodriguez-Gomez, V., Genel, S., Vogelsberger, M., Sijacki, D., Pillepich, A., Sales, L. V., Torrey, P., Snyder, G., Nelson, D., Springel, V., Ma, C.-P., & Hernquist, L. 2015, MNRAS, 449, 49

Springel, V. 2010, ARA&A, 48, 391

Springel, V., White, S. D. M., Tormen, G., & Kauffmann, G. 2001, MNRAS, 328, 726

Toomre, A. & Toomre, J. 1972, ApJ, 178, 623

Wadsley, J. W., Stadel, J., & Quinn, T. 2004, New A, 9, 137